Studies on Optoelectronic and Structural Properties of MoO_{3-x} Thin Films and Fabrication of Dopant Free Single Side MoO_{3-x}/c-Si(n) Solar Cells

A thesis submitted

by

Juhi Kumari

Roll No. 166151008

In partial fulfillment of the requirement for the award of the degree of

Doctor of Philosophy

School of Energy Science and Engineering
Indian Institute of Technology Guwahati
Guwahati-781039, India

November 2023

DECLARATION

The work contained in this thesis entitled "**Studies on Optoelectronic and Structural Properties of MoO_{3-x} Thin Films and Fabrication of Dopant Free Single Side MoO_{3-x}/c-Si(n) Solar Cells"** has been carried out by me under the supervision of Dr. Pratima Agarwal, Professor, Department of Physics and School of Energy Science and Engineering, Indian Institute of Technology, Guwahati, Assam, India. This thesis does not contain any materials previously submitted for the award of any degree or diploma. I further confirm that if any third-party owned material is incorporated in my thesis and requires formal permission from the copyright owners, I have obtained all necessary rights from the respective copyright owners and acknowledged these in my thesis.

Juhi Kumari

Date: 08-11-2023

Juhi Kumari
Roll No: 166151008
School of Energy Science and Engineering
Indian Institute of Technology Guwahati
Guwahati-781039, Assam, India

भारतीय प्रौद्योगिकी संस्थान गुवाहाटी
Indian Institute of Technology Guwahati
North Guwahati, Guwahati
PIN- 781 039, Assam State, INDIA
Phone: +91 361 2583000 Extn 2702, 2582702
Fax: +91 361 2690 762 (Institute), 2582749 (Department)
Fax: +91 361 2690 762 (Institute), 2582749 (Department)

Dr. Pratima Agarwal
Professor
Department of Physics
E-mail:pratima@iitg.ernet.in

Dated: Nov 08, 2023

Certificate

This is certified that the work contained in this thesis entitled "**Studies on Optoelectronic and Structural Properties of MoO_{3-x} Thin Films and Fabrication of Dopant Free Single Side MoO_{3-x}/c-Si(n) Solar Cells"** submitted by Ms. Juhi Kumari, a Ph. D. student at School of Energy Science and Engineering, Indian Institute of Technology, Guwahati, Assam, India, for the award of the degree of Doctor of Philosophy has been carried out under my supervision. This work has not been submitted elsewhere for the award of any degree or diploma.

Pratima Agarwal

(Dr. Pratima Agarwal)

Dedicated
to
My Family and
My Friends

ACKNOWLEDGMENTS

I humbly acknowledge the Almighty for his unwavering support in helping me achieve my academic goal. As I approach another milestone in my academic career, I want to take this opportunity to express my gratitude to everyone who has contributed to this thesis through criticism, remarks, praise and both intellectual and personal encouragement.

First and foremost, I would like to express my sincere gratitude to my supervisor, Prof. Pratima Agarwal, for giving me the opportunity to complete my PhD work under her supervision, believing in me, supporting and encouraging me in my endeavors. She taught me how to approach research challenges, evaluate the findings and present them in an experimentalist's perspective. She has always helped me deal with all the problems, I experienced during my PhD, sometimes behaving as a guardian and sometimes as a mentor. Her unwavering friendliness, cooperation, and kindness, are qualities I would definitely like to cherish and emulate.

I am grateful to my doctoral committee members, Prof. Ashwini Kumar Sharma (Chairperson), Prof. Mahuya De and Late Dr. Harsh Chaturvedi for their timely evaluation, critics and invaluable suggestions, which helped me to enrich my research work and dissertation. I extend my sincere gratitude to the former Head of the School of Energy Science and Engineering, Prof. Pranab Goswami, Prof. Vijay S. Moholkar and present head Prof. Vaibhav V. Goud, for their cooperation and permission to avail the facilities in School throughout my doctoral work. I also acknowledge all the faculty members, specially Dr. Pankaj Kalita and staffs for their constant support and help. I would also like to express my sincere gratitude to the former head of Department of Physics, Prof. P. Poulose, Prof. Subhradip Ghosh and present head Prof. Perumal Alagarsamy for their support in carrying out my research work. I also express my sincere gratitude to former technical officer Dr. Sidananda Sarma and present technical officer Dolly Gogoi and Mr. Basab Bijoy Purkayastha for allowing me to avail the departmental facilities.

I am grateful to the former head of Central Instruments Facility, IIT Guwahati, Prof. G Krishnamoorthy, Prof. Mohammad Qureshi, Prof. G. Pugazhenthi and present head Prof. Gagan Kumar for their constant support and allowing to avail the central facilities. I am

also thankful to Dr. Kula Kamal Senapati, Mr. Madhurjya Borah, Mr. Sujit Kumar Deb and Dr. Ashim Malakar, staffs and other members for helping me to use the central facilities. I would also like to acknowledge the official instruments operators, Mr. Kishore Talukdar, Mr. Bhaskar Hazarika, Mr. Inamul Haque, Mr. Rupak Bordoloi and all student operators for cooperating me in using different instruments facilities to carry out my assigned research objectives.

I want to thank the Ministry of Education of India and the Indian Institute of technology for providing financial assistantship during my PhD tenure.

It was a pleasure to work with my lab seniors Dr. Himanshu S. Jha, Dr. Asha Yadav, Dr. Ramakrishna Madaka, Dr. Venkanna Kanneboina, Dr. Pilik Basumatary and labmates Mr. Manvendra Singh Gangwar, Ms. Jai Shree Bhardwaj, Mr. Himangshu Deka, Mr. Rahul, Mr. Anterdipan Singh, Mr. Tun Naing Aye, Mr. Tulsiram Madkami, Mr. Ashish Kumar Patel, Ms. Keerthana BK and Mr. Biswajit Das. I thank them for their support, suggestions, time and help in performing experiments during my PhD tenure and building a friendly and healthy environment in lab. I would also like to thank my past lab members Mr. Vivek Ghritlahare, Ms. Shubhangi Bhardwaj, Dr. Niharika Gogoi, Mr. Ankit Kumar Singh, Mr. Gaurav Singh, Ms. Ranju Kumari, Mr. Rohan Ghosh and Ms. Vaishnavi Chouksey, Mr. Gaurav Singh, Mr. Rakesh Prasad, Mr. Bhagwat Singh Chouhan, Mr. Dharmendra Singh Samota, Mr. Mahipal Singh Rathore, Ms. Kaushalya Kumari, Mr Kazuki Tanaka, Mr. Nisarg Vyas, Mr. Jay Kumawat, Mr. Dharmendra Viswakarma, Mr. Aditya, Mr. Yogesh, Ms. Nikita, and Ms. Lakshmi, for supporting me with my research work and for creating an encouraging and friendly environment during my doctoral work. I am also grateful to the research scholars of Department of Physics, School of Energy Science and Engineering, Department of Chemistry and Department of Mechanical Engineering for their assistance during my research work.

I specially want to thank my senior/cum friend Dr. Ramakrishna Madaka and Dr. Pilik Basumatary and my junior/cum friend Ms. Jai Shree Bhardwaj, Mr. Rahul, Mr. Anterdipan Singh, Mr. Rohan and Mr. Vivek Ghritlahare for constantly supporting and encouraging me during the most difficult part of my doctoral studies and for making every effort to enable me to complete my research work.

Words cannot convey how much I appreciate my friends of other Department at IIT Guwahati Dr. Ashutosh Kumar Pandey, Dr. Prajna Paramita Mohapatra, Dr. Sasmita Behera, Mr. Abhishek Singh, Mr. Rahul Tiwari, Mr. Sai Santhosh, Ms. Toni, Ms. Pragya Gupta, Ms. Munmi Bhattacharya, Dr. Deepika Bishnoi, Dr. Basu Bhattacharjee, Dr. Suhaib Alam Ansari, Mr. Karan Kumar, MS(R) 2016 class, Dr. Deepa Sachan, Ms. Sonali Gangwar, Dr. Sumit Goswami, Dr. Nagendra Kumar, Dr. Eshita Mal and others for the supportive atmosphere, conversations, and guidance throughout my PhD.

I also want to convey my sincere gratitude to my badminton group Prof. Charudatt Kadolkar, Dr. Indu Kalpa Dihingia, Dr. Ranjan Kalita, Dr. Susmita Rambha, Dr. Prahlad Baruah, Dr. Rahul Kesarwani, Mr. Ankan Bhattacharya, Mr. Vivek Singh Yadav, Mr. Ravi Vashist, Mr. Samarjeet Das, Mr. Devender Kumar, Dr. Dhriti Maurya, Dr. Angana Bhattacharya, Mr. Himanshu Murari, Mr. Sirsendu Ghosal, Mr. Soumya Padhi, Dr. Ravi Kiran Dokala, Mr. Madhav Bhat, Mr. Akanshu Chauhan, Mr. Jegyasu Gupta, Mr. Kalim Khan, Mr. Sailesh Pincha and Mr. Somath Sahu for providing enthusiastic, soothing and enjoyable atmosphere during my PhD duration. Throughout my PhD, badminton always hold a special place in my heart since it gave me the opportunity to interact with a lovely group of people, forget about my difficulties with research and brighten my day.

I'd also like to thank the Canteen workers of Core 3 and Core 4, IIT Guwahati, and the Security team of Core 3 and Core 4, IIT Guwahati, for their assistance throughout my stay at IIT Guwahati.

I must acknowledge my school and college friends Dr. Rifat Mokhtar, Mr. Vivek Tiwari, Ms. Suman Gupta, Ms. Jyotsna Bharti, Ms. Nishu, Md Danish Khan, Mohammad Kaif, Ms. Roshni Singh, Mr. Satyam, Mr. Amit, Ms. Nikita Mehta, Mr. Gaurav Singh, Dr Prashant Malik, Mr. Devrat Agarwal, Mr. Kishan Agarwal, Ms. Lopa Bhattacharya, Ms. Kavisha Shunyo, Ms. Astha Singh, Ms. Sonam Sinha, Ms. Madhavi Singh, Ms. Shruti Sharma, Ms. Prachi Singh, Mr. Pranav Anand, Mr. Deepak Raj, Mr. Vivek Krishnan, Mr. Faraz Uddin, Dr. Kumar Ashwini, Mr. Mukesh Singh Sunni, Ms. Sonia Sasmal, Ms. Shikha, Dr. Ashutosh Pandey, Dr. Adya Isha and all others for their unwavering support and encouragement, which constantly inspired me to be resilient and upbeat during my difficult days of research work.

There are not enough words to convey how grateful I am to my sisters and brother, whose unconditional love I have always cherished at difficult times. I express my sincere gratitude to my elder sister Dr. Vineeta Kumari, Ms. Sweta Kumari and my elder brother Mr. Gyan Shankar for their blessing love, patience, support and understanding throughout my studies. I am very much thankful to my uncle Shri Ramakant Singh and Late Shri Baccha Singh, my aunty Late Smt. Mithilesha Devi and my brother-in-law Dr. Bhibhuti Bhsuhan, Mr. Ashish Mohan and my sister-in-law Ms. Siddhi Shankar and other family members for their motivation, suggestion and support during my PhD. I also want to acknowledge my little cute niece Rashmi, Vasudha, Bhawya, Subhlakshmi, Sudhiksha and Jaishnavi and my nephew Himanshu and Prameet for always being my calming sources during my crucial Ph.D. days.

I would want to thank and honour my parents, Shri Ramjee Singh and Smt. Usha Devi, for fostering in me the courage, forbearance, confidence, and everlasting desire to achieve my goals. They also continually encouraged me to finish my PhD with success. My parents are true role models for me. Their dedication, tireless effort, strength, challenging circumstances and responsibilities tutored me valuable knowledge that I could never have learned anywhere else. I couldn't find the right words to express my gratitude to my parents and family. I believe that the only way to express gratitude is to look after them forever.

With regrets and best wishes, I acknowledge those who are almost listed in this acknowledgment but not included by name. Along with acknowledging their help and encouragement, I also hope they will pardon me.

Juhi Kumari

IIT Guwahati

PREFACE

The solar industry, notably solar photovoltaic (PV), has made a substantial contribution to meeting the increasing energy demands within the field of renewable energy resources. The a-Si:H/c-Si(n) solar cells with an efficiency > 26% are leading in PV field; however, the requirement of capital-intensive fabrication techniques and the use of toxic gases as dopants to prepare n/p a-Si:H layers are encouraging the search for a suitable alternative material to eliminate these factors. Transition metal oxides such as MoO_{3-x} are gaining interest as dopant-free heterocontact, because of the extraordinary performance (>23%) of silicon wafer based solar cells when p-doped a-Si:H is replaced with MoO_{3-x} as hole selective layer. The hole selectivity of MoO_{3-x} depends on the work function of MoO_{3-x}, which is sensitive to the deposition temperature, gaseous environment and post-deposition heat treatments. Thus, sequential adjustment of these deposition conditions is needed to fabricate MoO_{3-x} films suitable for use as a hole selective layer in MoO_{3-x}/c-Si(n) solar cells. The motivation for this thesis was to study the effect of deposition conditions on optoelectronic properties of MoO_{3-x} films, as well as the utilisation of optimised conditions for the fabrication of dopant free single sided MoO_{3-x}/c-Si(n) heterojunction solar cells. Based on this motivation, the objective of the thesis work had been:

- Deposition of MoO_{3-x} films under different conditions such as substrate temperature, gaseous environment and post-deposition conditions to check its influence of the structural, optical and electrical properties.
- Post-deposition oxygen plasma treatment to improve the work function of MoO_{3-x} films.
- Preparation of device quality Indium Tin Oxide thin films.
- Fabrication of dopant free single sided MoO_{3-x}/c-Si(n) solar cells.
- Simulation studies to understand the impact of work function of MoO_{3-x} and thin silicon oxide layer between MoO_{3-x} and c-Si(n) on the performance of MoO_{3-x}/c-Si(n) solar cells using AFORS-HET software.

The present dissertation contains 9 chapters. The first chapter provides a brief overview of carrier selective contacts, features of MoO_{3-x} and progress in dopant free transition metal oxide/c-Si(n) heterojunction solar cells. Chapter 2 presents an overview of the deposition

techniques used for ITO and MoO_{3-x} film deposition and oxygen plasma treatment. This chapter also discusses the characterization techniques used to investigate the various properties of MoO_{3-x} and ITO films. Chapter 3 discusses studies on the structural and optoelectronic properties of MoO_{3-x} films prepared by rf-sputtering technique. The deposition conditions of MoO_{3-x} films are optimised sequentially to prepare coloured and highly conducting MoO_{3-x} films, as well as transparent and resistive MoO_{3-x} films. Chapter 4 discusses the impact of deposition temperature on the structural, optical and work function properties of MoO_{3-x} films deposited by thermal evaporation technique. In addition, post-deposition heat treatment of MoO_{3-x} films deposited at room temperature is performed to investigate its influence on work function and compositional properties of MoO_{3-x}. Chapter 5 focuses on the utilisation of oxygen plasma treatment (OPT) to increase work function of thermally evaporated MoO_{3-x} films. OPT was first performed on thick MoO_{3-x} films, but because we were interested in using MoO_{3-x} for solar cell fabrication, we also performed OPT on thin MoO_{3-x} films and examined its effect on MoO_{3-x}'s work function. Chapter 6 presents the influence of process pressure and substrate temperature on microstructure, morphology, optical and electrical properties of Indium tin oxide (ITO) thin films prepared by rf Sputtering technique. Chapter 7 presents the fabrication of dopant free single sided MoO_{3-x}/c-Si(n) solar cells. The effect of deposition conditions on solar cell performance for the fabrication of transparent conducting oxide layer (ITO) and hole selective layer (MoO_{3-x}) is investigated. In addition, the influence of multiple heat treatments on the properties of MoO_{3-x} and performance of solar cells are also studied in this chapter. Chapter 8 presents the simulation studies carried out using the AFORS-HET software to investigate the effect of MoO_{3-x} work function on the performance of MoO_{3-x}/c-Si(n) solar cells. This chapter also investigates the role of carrier transport through thin SiO_x layer and few pin holes on various solar cell parameters. Chapter 9 presents the overall conclusions and summary of the present thesis work and future scope of this research work.

LIST OF ABBREVIATIONS AND SYMBOLS

Ar	Argon gas
α-MoO_3	Orthorhombic Phase of MoO_3
Ag	Silver
AFR	Argon flow rate
a-Si:H	Hydrogenated amorphous silicon
Al	Aluminium
AFM	Atomic force microscopy
AZO	Aluminium doped Zinc oxide
β-MoO_3	Monoclinic phase of MoO_3
B_2H_6	Diborane
CSC	Carrier Selective Contact
CVD	Chemical vapour deposition
CPD	Contact Potential Difference
c- Si (n)	n-type crystalline Silicon
CG	Corning glass
C	Carbon
DASH	Dopant free asymmetric heterocontact
DI	Deionized
ESL	Electron selective layer
E_c	Conduction band
E_v	Valence band
E_f	Fermi Level
EHT	Electron high tension voltage
EDS	Energy dispersive X-ray spectroscopy
FETEM	Field emission transmission electron microscopy
FESEM	Filed emission scanning electron microscopy
HSL	Hole selective layer
HIT	Heterojunction thin intrinsic layer
h-MoO_3	Hexagonal phase of MoO_3
H_2	Hydrogen gas
HF	Hydrofluoric acid
H_2O_2	Hydrogen Peroxide
HCl	Hydrogen Chloride
HRTEM	High resolution transmission electron microscopy
ITO	Indium Tin Oxide
In	Indium
KPFM	Kelvin probe force microscopy
MoO_3	Molybdenum oxide
MoO_{3-x}	Sub-stoichiometric Molybdenum Oxide
MoO_6	Octahedron
Mo	Molybdenum
MFC	Mass flow controller
NH_4OH	Ammonium hydroxide
O_v	Oxygen Vacancy
O_2	Oxygen gas
O_t	Terminal Oxygen
O_s	Symmetric Oxygen
O_a	Asymmetric Oxygen
OPT	Oxygen Plasma Treatment
O	Oxygen
OFR	Oxygen flow rate
OHT	One time heat treatment
PV	Photovoltaic
RCA	Radio Corporation of America
RT	Room temperature
r_d	Deposition rate
SiO_x	Silicon Oxide
SAED	Selected area electron diffraction
Sn	Tin
SHJ	Silicon heterojunction
TMO	Transition metal Oxide
TiO_2	Titanium oxide
Ta	Tantalum
T_s	Substrate temperature
T_{max}	Maximum Transmission
TCO	Transparent conducting oxide
t_d	Deposition time
THT	Two time heat treatment
UV-Vis	Ultra-Violet Visible

V_2O_5	Vanadium Oxide
WO_3	Tungsten Oxide
W	Tungsten
XRD	X-ray diffraction
XPS	X-ray photoelectron spectroscopy
ZnO	Zinc oxide
FTO	Fluorine doped tin oxide
α	Absorption coefficient
AM	Air Mass
β	Full width at half maxima
B	Size broadening
BE	Binding Energy
°C	Degree Celsius
χ	Electron affinity
d	Thickness
D	Crystallite Size
D_{ph}	Fraction of pin holes
eV	Electron volt
ε	Strain
E_g	Band gap
E_a	Activation Energy
E_{bp}	Energy barrier for holes
E_{bn}	Energy barrier for electrons
η	Efficiency
FF	Fill Factor
h	Plank constant
I	Current
J_{sc}	Short Circuit Current Density
J	Current Density
k_B	Boltzmann Constant
KE	Kinetic Energy
ν	Frequency
λ	Wavelength
Φ	Work function
R_{sheet}	Sheet resistance
R_s	Series resistance
R_{sh}	Shunt resistance
r_e	Rate of evaporation
~	Approximately
σ	Conductivity
σ_d	Dark conductivity
θ	Diffraction angle
V	Voltage
V_{oc}	Open Circuit Voltage

Contents

Chapter 3: Optimization of deposition conditions to tune optoelectronic properties of MoO_{3-x} films prepared by rf-sputtering technique

List of Figures

List of Tables

CHAPTER 1

Introduction

The global demand for energy has experienced a notable increase in recent decades as a result of population growth and advancements in technology. Consequently, there has been a substantial increase in the utilization of conventional energy sources. This poses a potential risk of future scarcities in traditional energy resources, including coal, petroleum, diesel, and others, leading to an imminent energy crisis. The phenomenon of rapid climate change and global warming is currently giving rise to worrying circumstances and exerting a significant impact on the daily lives of individuals. These circumstances have presented an opportunity for researchers to explore other approaches or support systems that could perhaps mitigate this significant problem. Renewable energy sources are considered the most effective solutions of this particular problem. The aforementioned elements have exerted a significant influence on the examination and progression of renewable energy sources. One of the primary attributes inherent to renewable energy (RE) resources is their capacity to refrain from emitting

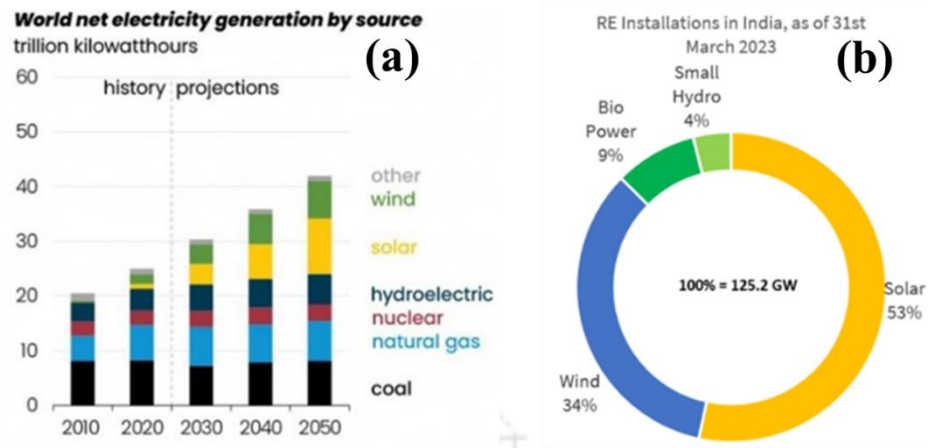

Figure 1.1: *(a) Expected trend in the growth of renewable energy sector to fulfil the energy demand [1] and (b) share of different renewable energy installation up to March 2023 in India [2].*

environmentally detrimental greenhouse gases. Renewable energy supplies are characterized by their cleanliness, abundance and seemingly limitless availability. The International Energy Agency (IEA) predicts that the renewable energy sector, particularly solar and wind energy, will account for almost two-thirds of the global energy demand in the forthcoming years as shown in Figure 1.1a [1]. The Ministry of New and Renewable Energy provided statistics concluding that as of March 2023, the total installed capacity of renewable energy has reached 125.2 GW. Figure 1.1b displays the distribution of installation shares derived from various renewable energy sources. The solar sector, specifically solar photovoltaic (PV), has exhibited a significant contribution towards fulfilling the increasing energy requirements within the realm of renewable energy resources. The positive results obtained from these notable outcomes have served as a catalyst for the photovoltaic community to persist in their pursuit of cost-effective materials and technologies, with the aim of ensuring universal accessibility to solar PV across diverse socioeconomic strata.

1.1. Solar cell and its Progress

The considerable potential of solar energy and its promising prospects have spurred substantial progress in the photovoltaic technology. Solar cells operate based on the fundamental concept

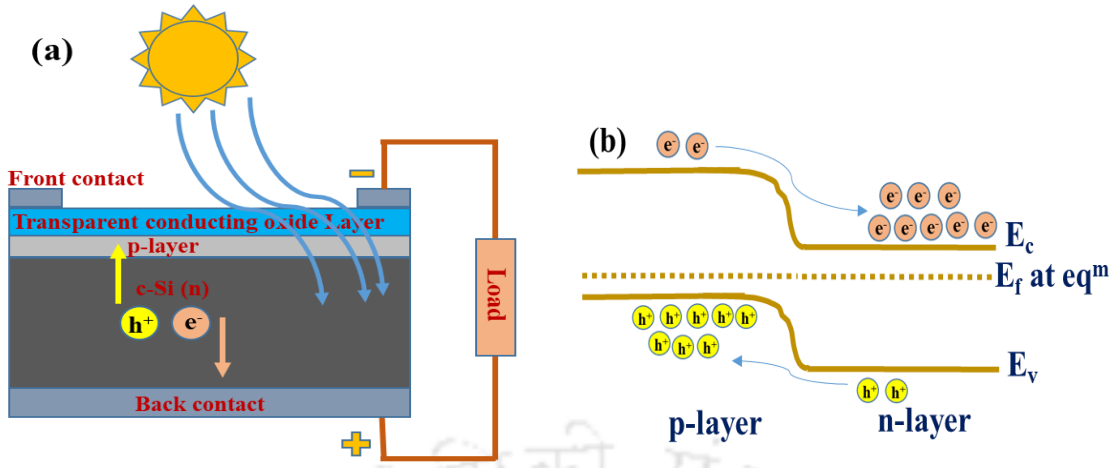

Figure 1.2: *(a) Schematic configuration and (b) energy band diagram of homojunction solar cell.*

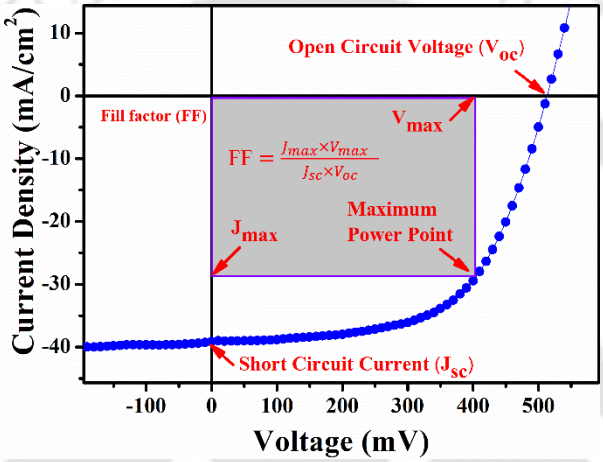

Figure 1.3: *Current density- voltage characteristics of a solar cell.*

known as the photovoltaic effect, wherein the exposure of a photovoltaic cell to sunlight results in the generation of an electric current. The three distinct processes involved in the operation of a solar cell are: generation, separation and collection of charge carriers. When photons with energy above the band gap are absorbed, free charge carriers are produced, leading to the formation of electron-hole pairs. The photogenerated charge carriers are then separated by the electric field due to band bending across the interface followed by the collection of free charge carriers through the front and rear metal contacts. Figure 1.2a depicts the schematic diagram of a p-n junction solar cell. The band bending that occurs at the p-n junction as depicted in Figure 1.2b, makes it easier for minority carriers, specifically electrons to migrate from the p-layer to the n-layer and holes to migrate from the n-layer to the p-layer.

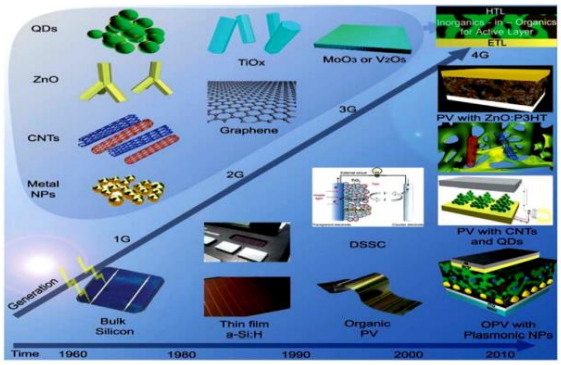

Figure 1.4: *Different generation of solar cells [3].*

The evaluation of a solar cell's performance is conducted by the analysis of its current density vs voltage (*J*-*V*) characteristics, as depicted in Figure 1.3. A solar cell's open circuit voltage (V_{oc}), short circuit current density (J_{sc}) and fill factor (*FF*) are the characteristics that contribute together to determine the efficiency (η) of the cell. There are two primary classifications of solar cells: homojunction and heterojunction solar cells. Homojunction solar cells are made from the identical material with equal band gap but different dopants, whereas heterojunction solar cells are made up of dissimilar materials with varied band gaps. In homojunction solar cells, there is no band discontinuity at the interface, however this imposes certain constraint on solar cell characteristic like limited V_{oc}, limited range of electromagnetic spectrum participating in electron hole pair generation. Nevertheless, heterojunction solar cells effectively address these concerns by facilitating the integration of materials with low and wide band gaps. This integration broadens the range of photons that may be absorbed across several layers, hence enhancing the overall performance of the device.

Silicon (Si) solar cells are currently at the forefront of industrial-level solar photovoltaic due to the advantageous characteristics of silicon, including its low band gap, abundant availability, and cost-effectiveness. Ongoing research endeavours are focused on the exploration of alternative materials and technologies that have the potential to serve as substitutes for silicon-based solar cells. However, the production cost, payback duration and stability of alternative

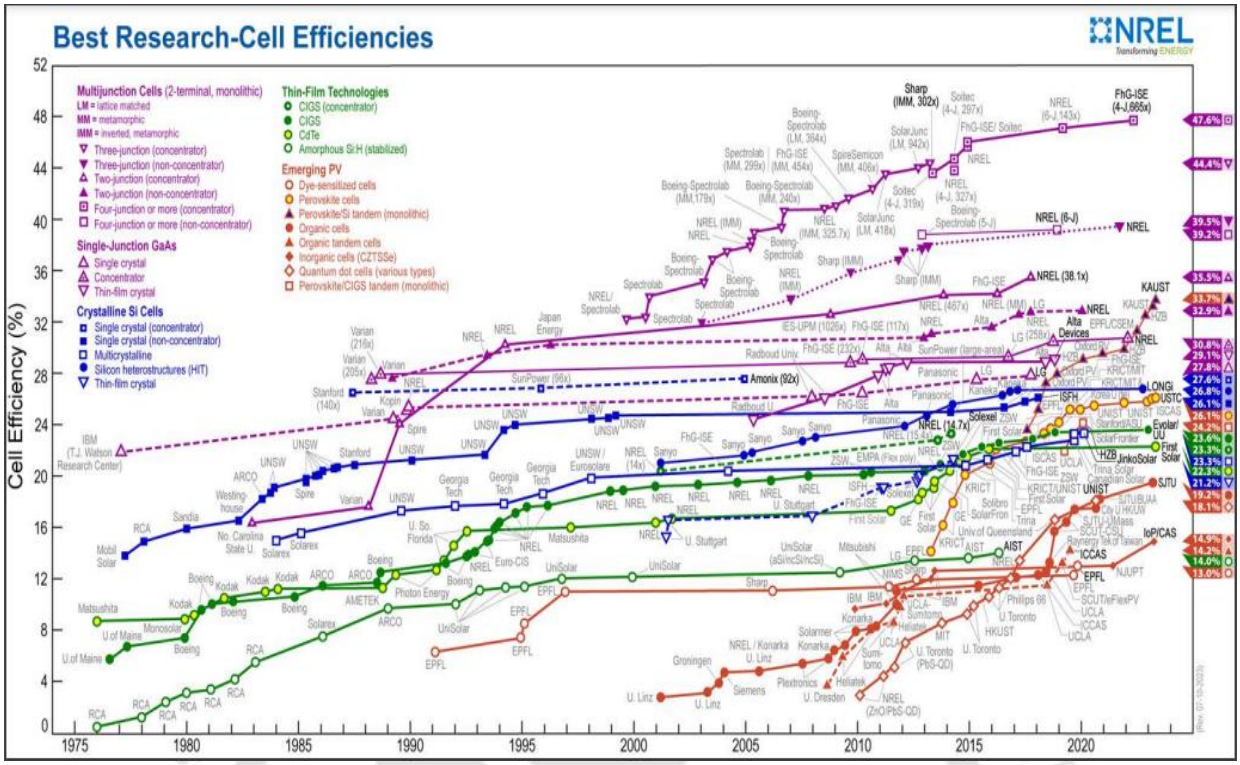

Figure 1.5: *Efficiency chart for different solar technologies [4].*

technologies to silicon solar cells continue to pose significant challenges when used on industrial scale. Figure 1.4 displays various generations of solar cells, whereas Figure 1.5 provides a comprehensive list of state of art efficiencies for different solar cell technologies. [2].

The traditional silicon solar cell necessitates the establishment of a p-n junction, which is achieved by the process of doping distinct regions of a silicon wafer. Figure 1.6a illustrates the schematic structure of a conventional c-Si solar cell. The progressive development of c-Si solar cells has resulted in the development of a solar cells with an efficiency of ~25% [5]. Nevertheless, the utilization of diffusion-based technology for doping in this field is energy intensive due to its time-consuming nature and the high temperature requirement of above 900 °C [6]. The issue has been partially resolved by the advancement of silicon heterojunction solar cells, which include the utilization of a thin layers of doped and intrinsic amorphous silicon (a-Si:H) [7, 8]. Figure 1.6b illustrates the configuration of heterojunction silicon solar cells

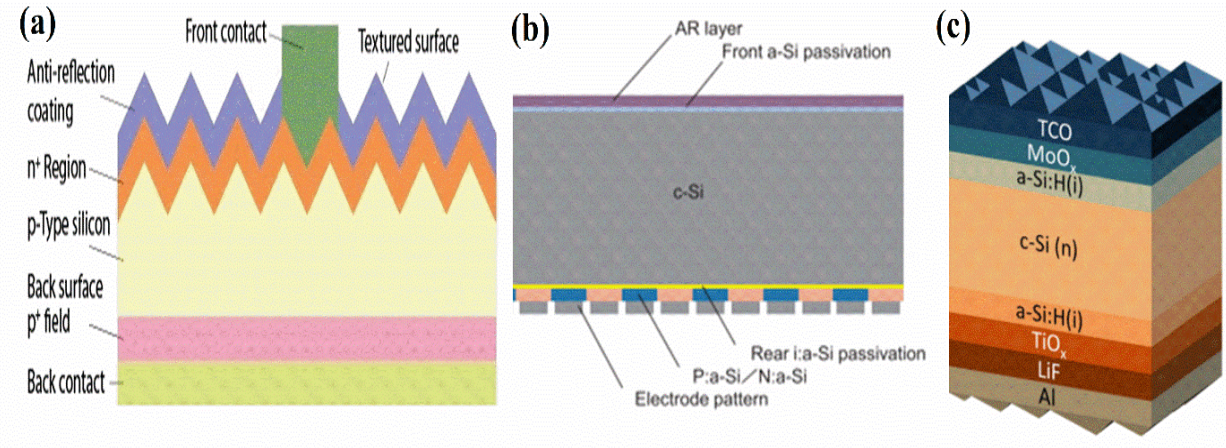

Figure 1.6: *(a) Conventional homojunction Si solar cell [5], (b) Heterojunction thin intrinsic layer Si solar cell [9] and (c) DASH Si solar cells [10].*

featuring a thin intrinsic layer (HIT solar cells). The preparation of a-Si:H layers necessitates a low deposition temperature and much shorter time, thereby expediting the fabrication process of solar cells. However, the widespread adoption of this technology at an industrial scale is hindered by significant capital investment requirements and the utilization of toxic gases such as phosphine (PH_3) for n-doping and diborane (B_2H_6) for p-doping. This development however, has facilitated the exploration of materials that can be synthesized at low temperatures by cost-effective deposition methods, without the need of external dopants to exhibit n/p type characteristics. Carrier selective passivating contacts may serve as a suitable alternative in this context. Materials such as PEDOT: PSS and P3HT, transparent conducting oxides like ITO, and transition metal oxides (TMOs) including Titanium oxide (TiO_2), Molybdenum oxide (MoO_3), Tungsten oxide (WO_3), and Vanadium oxide (V_2O_5) are among the organic polymers and inorganic compounds commonly employed in this context [8, 9]. These materials enhance the separation of photo-generated carriers by promoting the conductivity of one specific charge carrier (such as electrons or holes) while impeding the movement of the opposite type (such as holes or electrons). In a study conducted by Zielke et al., it was shown that the substitution of a doped p layer with PEDOT:PPS in silicon heterojunction solar cells resulted in a efficiency of 20% and an open circuit voltage of 657 mV [10]. Nevertheless, the primary drawback that

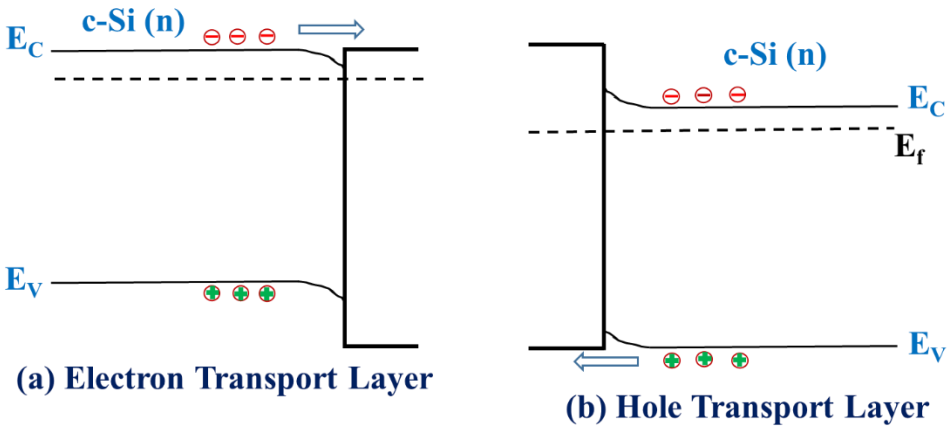

Figure 1.7: *Band diagram of (a) c-Si (n) and electron transport layer and (b) c-Si (n) and hole transport layer.*

hinders the utilization of this material in photovoltaic (PV) systems is its inadequate chemical stability. Transition metal oxides belong to a distinct category of materials that have demonstrated exceptional carrier-selective characteristics due to their distinctive and intriguing optoelectronic capabilities and stability. The aforementioned materials have provided a novel technological advancement in the domain of silicon solar cells, known as Dopant free asymmetric heterocontact (DASH) Si solar cells. The corresponding structure of this particular form of solar cell is depicted in Figure 1.6c.

1.2 Carrier selective contacts (CSCs)

In traditional solar cells, a p-n junction is formed and the electric field developed across the junction is responsible for charge carrier transportation. Basically, the difference in the quasi Fermi levels of n/p Si layers govern the motion of charge carriers. The carriers' separation and transportation are one of the important key parameters to have a good device. Thus, a good contact scheme with low contact resistivity, good passivation effect and carrier selectivity is required. This demands the search for carrier selective contacts which allows the movement of particular charge carrier (i.e. holes or electrons) while blocking the transport of any other charge carrier (i.e. electrons or holes). Recently, the PV community has developed designs based on carrier selective contacts that aid in reducing recombination across the metal-

semiconductor contact [11]. Carriers selective contacts are categorized as an hole transport/selective layer (HTL/HSL) and electron transport/selective layer (ETL/ESL). The selectivity of ETL and HTL is mainly guided by the band offsets across the conduction band (E_c) or valence band (E_v) and work function values [12]. Figure 1.7a shows the energy band diagram for electron transport layer and hole transport layer. For ETL, low ΔE_c offset value and the downward band bending across the interface, facilitates the transport of electron from c-Si (n) to ETL side. In the similar manner for HTL (Figure 1.7b), ΔE_v favours movement of holes across the junction from c-Si (n) towards hole transport layer. Apart from facilitating effective charge carrier movement at the interface, these selective contacts provide good passivation, cost-effective manufacturing, and simple patterning procedures [11]. ETL and HTL are categorized into two types one is doped silicon based (in which doping of silicon is done to tune the work function) and other is dopant free i.e. non-silicon based contacts.

1.2.1 Doped Silicon based carrier selective contacts

To create an electron transport layer/hole transport layer in case of HIT solar cells, intrinsic amorphous silicon films (a-Si:H) need to be externally doped using PH_3 and B_2H_6 for n and p doping respectively. The widely employed carrier selective contacts are doped amorphous silicon and polysilicon layers [11]. The direct deposition of the carrier selective contact on top of a c-Si (n)/c-Si (p) interface results in the creation of defect states across the interface. These interface defects can be reduced using surface passivation techniques such as hydrogen/silane plasma treatment using chemical vapour deposition. Sanyo group is the first to introduce thin intrinsic (i) layer between the doped amorphous silicon layer and the absorber layer (c-Si(n)/c-Si(p)) [7, 8]. The i-layer helps to decrease the surface defects by satisfying the dangling bonds present on the surface. This structure is called heterojunction thin intrinsic layer (HIT) solar cell. Apart from this, other kind of passivation is field effect passivation [13]. In this technique,

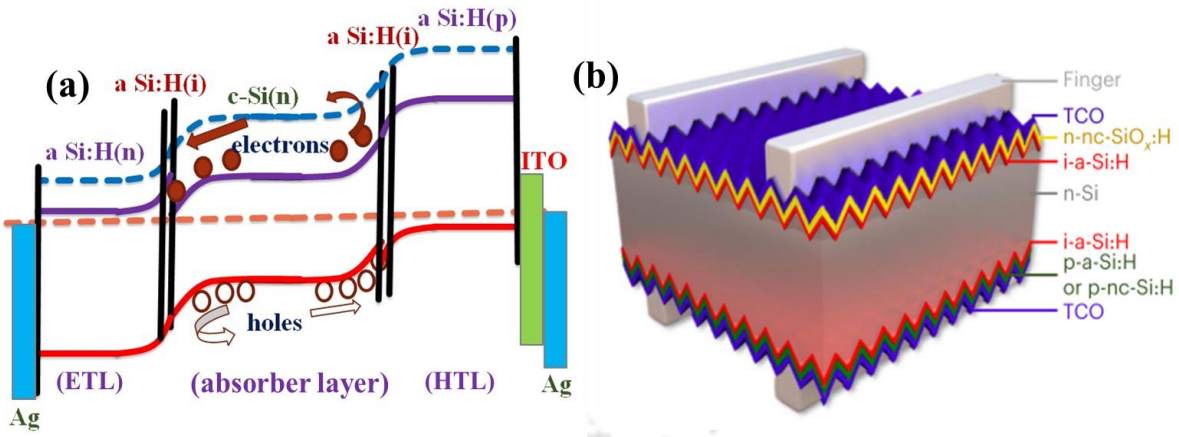

Figure 1.8: *(a) Band diagram of HIT silicon solar cell with doped ETL and HTL and (b) solar cell structure with 26.81% record efficiency [14].*

the amorphous silicon layer is highly doped. This leads either to charge accumulation or inversion on the surface because of the work function difference and presence of fixed charges in the a-Si:H layer. The electric field formed across the interface causes the effective separation of electrons/holes and thus recombination across the amorphous layer and absorber layer is reduced. The difference in the Fermi levels of c-Si and a-Si:H produces band bending across the interface, permitting the transport of only one type of carrier while obstructing another. In this way, doped a-Si:H layers offer carrier selectivity [13]. Figure 1.8a shows the energy band diagram for such device structure. The charge carrier transportation shown here is different from that shown in Figure 1.2b. In heterojunction solar cell, photo generation takes place primarily in absorber layer (c-Si (n)) and photo-generated carriers are transported to respective contacts depending on the band bending taking place across the interface which in governed by the Fermi level position. The work function (Φ), which is defined as the difference between the vacuum and Fermi levels, determines whether a carrier selective contact will be an ETL or HTL. LONGi group reported the record efficiency of 26.81% for HIT silicon solar cell (Figure 1.8b) till 2023 [14].

1.2.2 Dopant free carrier selective contacts

DASH (dopant free asymmetric heterocontacts) are another term for dopant free CSCs [15].

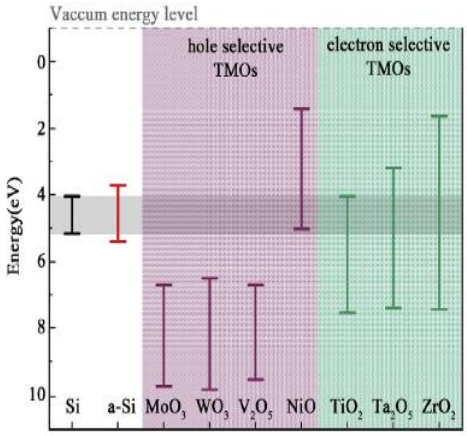

Figure 1.9: *List of TMOs used in optoelectronic devices as HTL and ETL [16].*

The HIT solar cell requires low temperature processing but expensive fabrication techniques and use of toxic gases for doping [17]. Furthermore, silicon-based materials have a limited work function and band gap range. These limitations for silicon based materials have led to the exploration of dopant free carrier selective contacts. Among organic CSCs, Spiro-OMeTAD, poly (3, 4-ethylenedioxythiophene) polystyrene sulfonate (PEDOT: PSS) [11, 18] and among inorganic, transition metal oxides (TMOs) are frequently used CSCs [6]. TMO is composed of a transition metal atom linked to oxygen atoms. Transition metal oxides have wide band gap and variable range of work function (3-7 eV). A large band gap (3.3 eV) allows minimal absorption losses in the HTL or ETL layer, increasing the value of the short circuit current density of solar cells. Work function tunability is viable for TMOs since it is dependent on oxygen vacancies, metal cation concentration and the stoichiometry of oxygen (O) and transition metal. TMO can be insulating, semiconducting, or metallic depending on its stoichiometry. TiO_2, ZnO are frequently utilised as ETL in semiconductor devices due to its low work function. [15]. MoO_3, V_2O_5 and NiO_x are the commonly used HTL in the field of organic or inorganic based solar cells because of high work function (5 to 6 eV) [11, 17]. Figure 1.9 shows the list of TMOs used in optoelectronic devices as HTL and ETL. We shall go into detail on TMO features because inorganic CSCs are our focus.

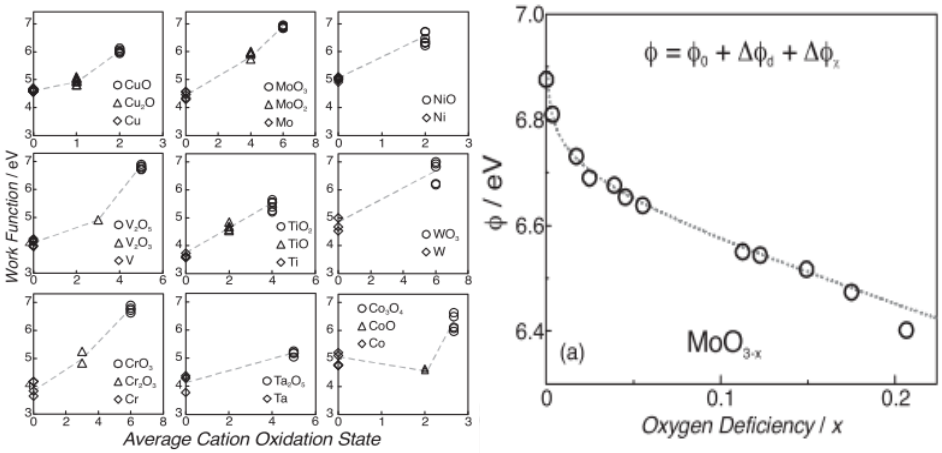

Figure 1.10: *Effect of metal cation oxidation state and oxygen vacancies on work function [19].*

1.2.3 Properties of TMOs

In TMOs, defects can be induced by oxygen vacancy (O_v), metal vacancy and occupancy of interstitial sites by oxygen and metal atoms [19, 20]. Metal vacancies act as p doping and oxygen vacancies form n-doping in TMOs, respectively. However, oxygen vacancies are the dominant defects because of low defect formation energy and are responsible for doping irregularity in TMOs [20]. The conduction band minima lies in close proximity to the defect gap states caused by oxygen vacancies in TMO like MoO_3 [21]. To maintain the charge neutrality, oxygen vacancies also lead to the generation of metal atoms in lower oxidation states [6]. The oxygen vacancy concentration and metal cation oxidation number of TMO determine whether it behaves as an insulator, a semiconductor, or a metal. The conductivity and work function (Φ) of TMOs are thus substantially impacted by oxygen vacancies [19]. Figure 1.10 depicts the influence of metal cation oxidation state and O_v on Φ. The concentration of O_v can be impacted by deposition methods (sputtering/thermal evaporation), thin film depositing parameters (substrate temperature/process pressure/gaseous environment), post-deposition treatments (annealing/oxygen plasma treatment/ultraviolet ozone treatment) and air exposure of films. Thin film of these oxides can be prepared by different techniques like electro-deposition, flash evaporation, chemical vapour deposition, sputtering and thermal evaporation

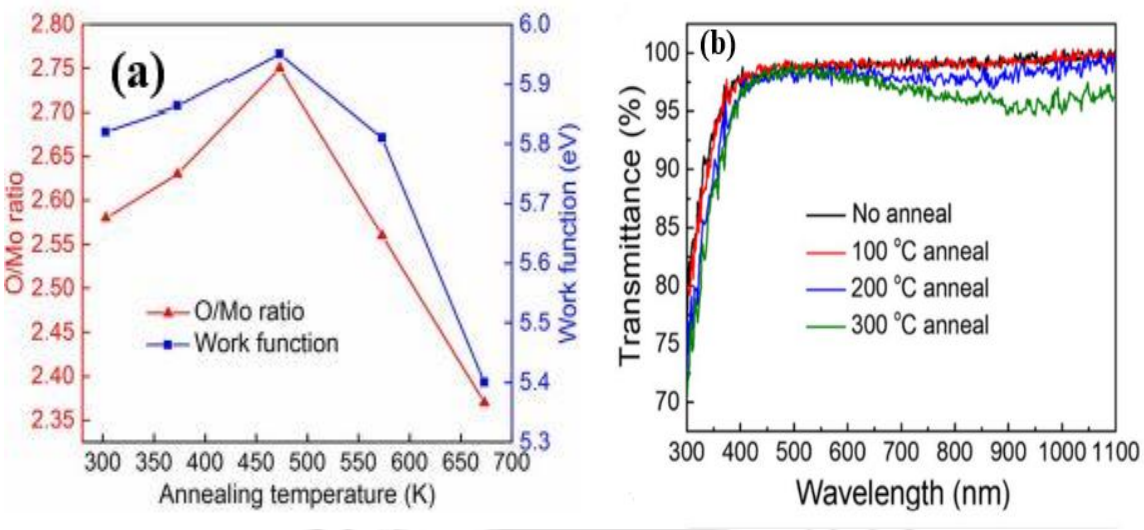

Figure 1.11: *Annealing temperature effect on (a) work function and O/Mo ratio and (b) on transmission spectra* [22, 23].

[24]. Sputtering and thermal evaporation are two of the most frequently used methods [25]. The sputtering offers a diverse set of parameters for optimising the optical and electrical properties of TMOs films [26]. Non-reactive sputtering technique produces conducting films due to the presence of extra oxygen vacancies, whereas reactive sputtering technique produces semiconducting TMOs thin films. Thus, this technique offers good control over the stoichiometric ratio and tuning of TMO properties according to its application [24]. J. Sun et al. compared the films prepared using thermal evaporation and sputtering techniques and observed that thermal evaporation formed more resistant films having high work function [25]. That's why thermal evaporation method is the commonly used method for fabrication of dopant-free asymmetric hetero contacts. But, use of this technique at industrial scale is still challenging. The process pressure, substrate temperature and gaseous environment conditions like Argon gas (Ar), Argon + Hydrogen gases ($Ar+H_2$), Argon + Oxygen gases ($Ar+O_2$) during film preparation have also a great impact on the properties of TMOs [24, 26]. Many groups have also examined how heat treatments like post-annealing alter the band gap, transmission, work function, and stoichiometry ratio of transition metals and oxygen (O) [22, 23, 27, 28]. The work function and transmission variation of TMO films with respect to annealing

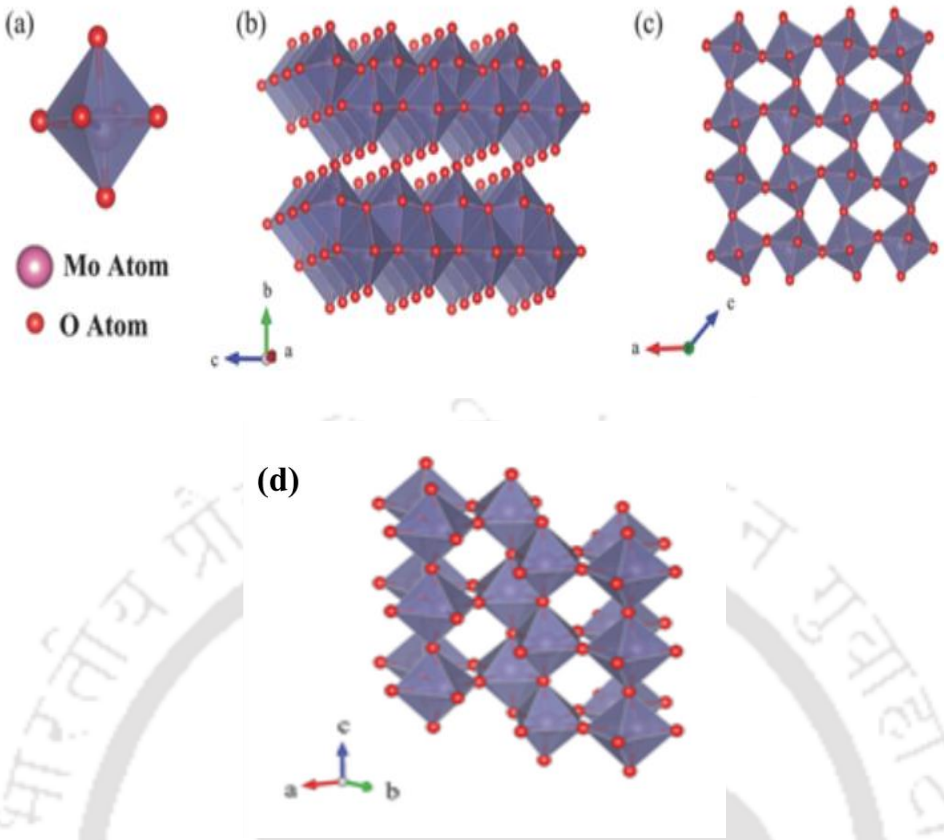

Figure 1.12: *(a) MoO_6 octahedron, (b) α-MoO_3, (c) β-MoO_3, and (d) h-MoO_3 crystal structures [29].*

temperature is presented in Figure 1.11. Increased annealing temperature induces a decrease in the band gap, transmission, and work function because of increase in oxygen vacancies, a decrease in the oxygen/transition metal ratio and the formation of rough TMO thin films. Therefore, both the deposition conditions and the post-treatment must be optimized to make TMO appropriate for usage as a hole-or electron selective layer in optoelectronic devices.

1.2.4 Molybdenum Oxide and its properties

Among all TMOs, MoO_3 is commonly used HTL in organic as well as inorganic optoelectronic devices [30]. The building block of the MoO_3 structure is octahedron MoO_6, as depicted in Figure 1.12a. The oxygen atoms at the edge and corner of MoO_6 are shared with other octahedra in three different ways, resulting in three different crystal phases of MoO_3: (i) the thermodynamically preferred and stable orthorhombic phase (α-MoO_3) (Figure 1.12b); (ii) the metastable monoclinic phase (β-MoO_3) (Figure 1.12c); and (iii) the metastable hexagonal

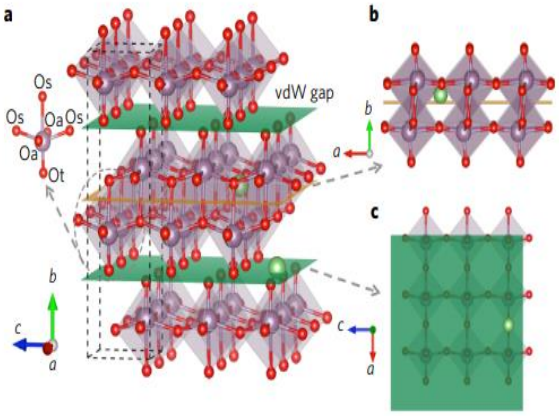

Figure 1.13: *MoO_6 octahedron with O_t, O_a and O_S and layered structure of MoO_3 [31].*

phase (h-MoO_3) (Figure 1.12d). Among three, mixed phases of (α-MoO_3) and (β-MoO_3) are commonly found. The layered structure of the α-MoO_3 makes it different from other phases. As shown in Figure 1.13, the octahedron MoO_6 is comprised of three distinct types of oxygen atoms. O_t (the terminal oxygen) is shared with only one Mo atoms with 1.67Å bond length and O_s (the symmetric oxygen), also called bridging oxygen, forms three bond with Mo atoms, two bonds (1.95 Å) in the same layer and one bond (2.33Å) in neighbouring sub-layer [31]. O_a (the asymmetric oxygen) forms two asymmetric bonds (2.25 Å and 1.73 Å) with two Mo atoms present in the same layer. O_t sites are more favourable to the formation of oxygen vacancies since it requires lesser energy to remove oxygen from this site than other O_a and O_s sites [31]. O_t sites are hence suitable for catalytic processes. The presence of oxygen vacancies in MoO_3 enhances its electrical conductivity and distance between interlayers, thereby improving its electrochemical characteristics. Therefore, increase in O_v makes MoO_3 appropriate for use in catalytic processes and storage devices. In order to attain high work function and adequate conductivity, moderate O_v is required, which makes MoO_3 suitable for its use as the HTL in solar cells.

Thin films of MoO_3 can be synthesized by vapour phase methods and liquid phase methods. Vapour phase synthesis methods are categorized into two techniques, physical vapour

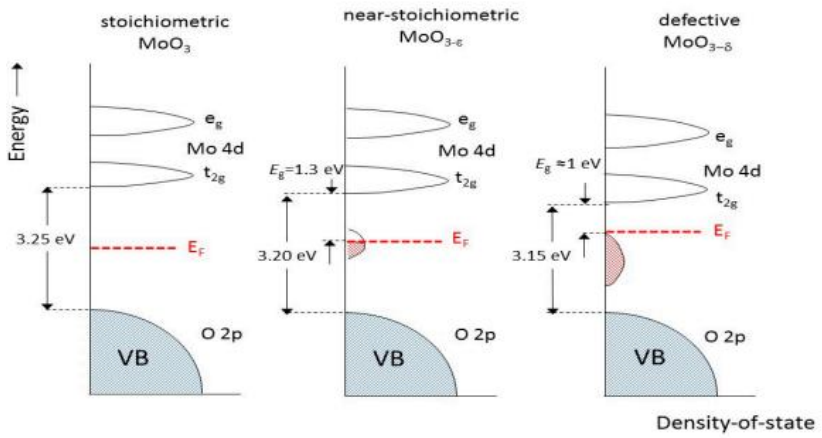

Figure 1.14: *Changes induced in the band structures of molybdenum oxides as an effect of oxygen vacancies [32].*

deposition and chemical vapour deposition [29]. Physical vapour deposition methods include direct current (DC) sputtering/ radio-frequency (rf) magnetron sputtering, pulsed laser deposition, electron beam evaporation and thermal evaporation. Thermal evaporation is the preferred method for depositing MoO_3 films because it forms nearly stoichiometric films and the crystalline stable phase of MoO_3. The chemical vapour deposition approach also provides good control over the formation of stoichiometric MoO_3 films by post-annealing of the films in an oxygen-rich environment. Sol-gel, hydrothermal, spin-coating, and electrochemical deposition are all liquid phase processes used for fabricating MoO_3 films. As MoO_3 has a layered structure, mechanical and liquid phase exfoliation methods are also used to produce MoO_3 films [29].

Molybdenum oxide is an intrinsically n-type high band-gap semiconductor (3-3.5 eV). The maxima of the MoO_3 valence band are generated by oxygen 2p orbitals, whereas the minima of the conduction band are formed by unoccupied Mo 4d states [21, 32, 33]. Metal and oxygen atoms are in bound states at the bottom of the valence band, while non-bonded states are at the top. Conduction band is formed by anti-bonding interaction between oxygen atoms and the transition metal (d orbital). Oxygen vacancies in these oxides create defect states that act like donor levels within the valence band and conduction band [19, 32]. The increased oxygen

vacancies can raise donor levels closer to conduction band and reduce the work function, as shown in Figure 1.14, resulting in the formation of an n-type doped MoO_{3-x} [32, 34]. The work function of molybdenum (Mo) oxide varies from 5.0 to 6.6 eV depending on the oxygen (O) /molybdenum (Mo) stoichiometry and the presence of O_v [35]. The experimentally prepared MoO_3 always deviates from its ideal stoichiometry i.e. 3:1, so its sub-stoichiometric form is represented by MoO_{3-x}. MoO_{3-x} behaves like insulators with a high work function and extremely high resistivity if x is zero (x=0); however, if x is between 3 and 2 (3<x<2), MoO_{3-x} behaves like semiconductors with a reduced work function. MoO_2, having high conductivity and low work function is formed when x=1. Since MoO_{3-x} properties are sensitive to air exposure, thin MoO_{3-x} films exposed to air for a long time exhibit a work function drop of approximately 1 eV [36]. Work function loss is caused by surface contamination and the surface adsorption of ambient oxygen on MoO_{3-x} film surface. Annealing of MoO_{3-x} films in presence of oxygen, post-deposition ultra-violet ozone and oxygen plasma treatments are the methods which can be used to recover the work function of MoO_{3-x} [36, 37].

In addition to possessing a wide band gap and a high Φ, molybdenum oxide also exhibits the chromic effect, which means the external variables can alter its optical properties [38]. This effect is categorized as thermo-chromic, photo-chromic and electro-chromic, where the optical characteristics are sensitive towards temperature, irradiation and applied potential respectively. The transfer of charges between the various oxidation states of molybdenum atoms cause the change in colour of MoO_{3-x} films. These interesting properties make MoO_{3-x} suitable for its use in smart windows [39]. It is still unclear how exactly these chromic effects are obtained.

1.2.5 MoO_{3-x} as HTL in silicon solar cells

Depending on the doping of c-Si (whether it is n doped or p doped), MoO_{3-x} can function as

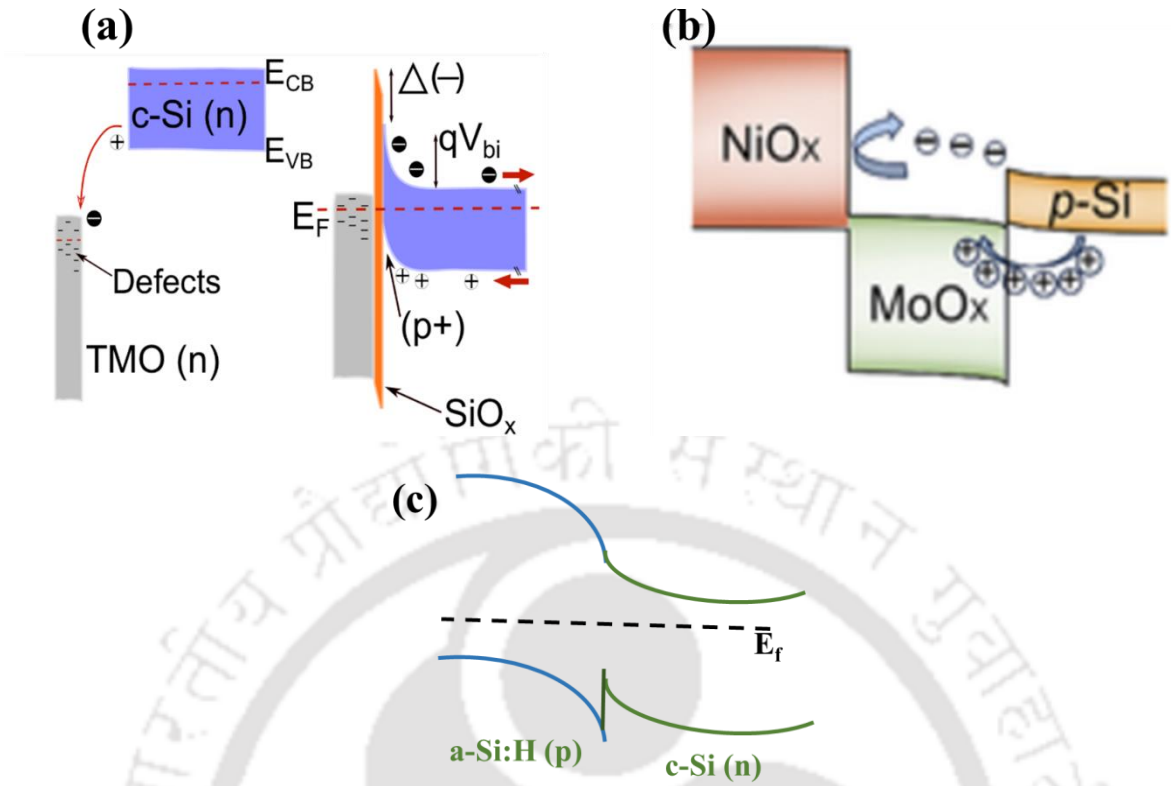

Figure 1.15: *Band diagram showing (a) formation of inversion layer at MoO_{3-x}/c-Si (n) interface, (b) accumulation layer at c-Si (p)/MoO_{3-x} interface and (c) band diagram of a-Si:H (p)/c-Si (n) [40, 41].*

HTL in two distinct manners: the first approach involves forming an inversion layer between MoO_{3-x} and c-Si (n), and the second requires formation of an accumulation layer between MoO_{3-x} and c-Si (p) [12, 40, 42-45]. Figure 1.15a and 1.15b depict the band diagram showing the formation of the inversion layer across the *MoO_{3-x}/c-Si(n)* interface and the accumulation layer across the *c-Si(p)/MoO_{3-x}* interface, respectively. The band alignment for the *MoO_{3-x}/c-Si(n)* junction exhibits the same band bending behaviour as the *a-Si:H(p)/c-Si(n)* junction (Figure 1.15c) [46]. The difference between two is that holes are transported from valence band of c-Si (n) to valence band of a-Si:H (p) across *a-Si:H(p)/c-Si(n)* whereas when MoO_{3-x} is used with c-Si (n), holes move from valence band of c-Si (n) to conduction band of MoO_{3-x} side. At *MoO_{3-x}/c-Si(n)* interface, the reaction between the silicon and MoO_{3-x} results in the formation of a thin layer of SiO_x (1.5 nm–2.8 nm). Figure 1.15a shows band bending with thin silicon oxide (SiO_x) layer formed at MoO_{3-x} and c-Si (n) interface. The ultrathin SiO_x layer that forms

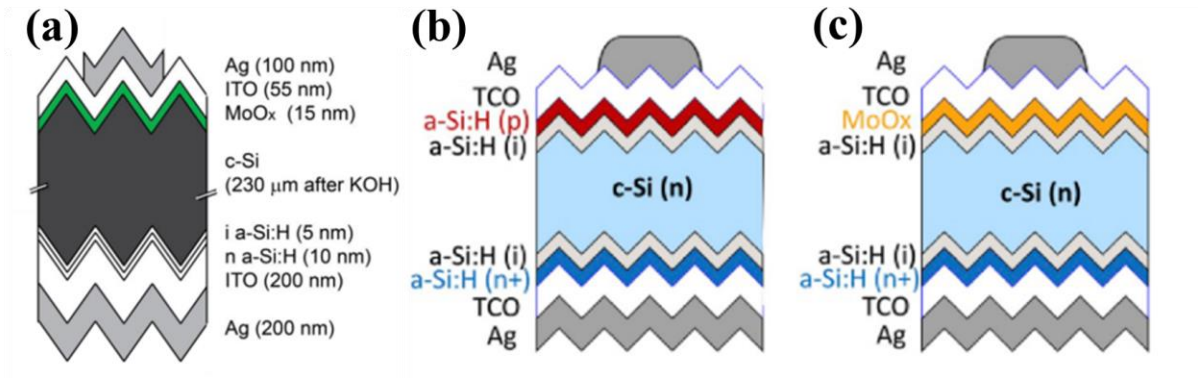

Figure 1.16: *Schematic device structure using (a) unpassivated MoO_{3-x} as HTL, (b) a-Si:H (p) as HTL for reference and (c) with thin a-Si:H (i) layer between MoO_{3-x} and c-Si (n) [47, 48].*

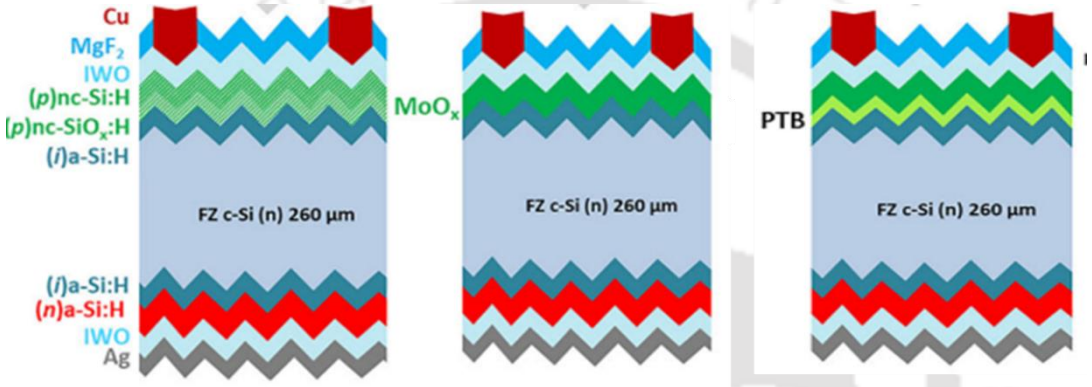

Figure 1.17: *Solar cell structure reported to have record efficiency of 23.83% [49].*

near the interface serves as a surface passivation layer [40]. In the device configuration (*Ag/ITO/MoO_{3-x}/c-Si(n)/a-Si:H(i)/a-Si:H(n)/ITO/Ag*) depicted in Figure 1.16a, V_{oc} of 580 mV, J_{sc} of 37.8 mAcm^{-2}, *FF* of 0.65 and efficiency of 14.5% are achieved, when unpassivated MoO_{3-x} in used as HTL [47]. The efficiency of solar cells (*Ag/IO:H/ITO/MoO_{3-x}/a-Si:H(i)/c-Si(n)/a-Si:H(i)/a-Si:H(n)/ITO/Ag*) has increased to 20.81% with 725 mV V_{oc}, and 0.76 *FF* by adding a thin intrinsic amorphous silicon layer (a-Si:H(i)) between MoO_{3-x} and c-Si (n) [50]. This increase is due to improved passivation effect generated by a-Si:H (i) layer at the MoO_{3-x} and c-Si (n) junction. By employing copper electrodes instead of silver ones, efficiency is increased to 22.5% and the fill factor is increased to 0.80 [50]. These findings encouraged the development of dopant-free TMOs and silicon heterojunction solar cells (SHJ). To obtain strong hole selectivity and passivation effect, J Dreaon and group reduced the thicknesses of the MoO_{3-x} and a-Si:H (i) layers. [48]. A 4 nm thin MoO_{3-x} layer and a 6 nm a-Si:H (i)

passivation layer have been found to improve device performance, with an efficiency of 23.48%, V_{oc} of 733.70 mV, J_{sc} of 39.15 mAcm^{-2}, and *FF* of 0.81 [48]. Figures 1.16b and 1.16c display the reference and *MoO_{3-x}/a-Si:H(i)/c-Si(n)* SHJ solar cell architectures, respectively. The intrinsic a-Si:H layer which is inserted between MoO_{3-x} and c-Si (n) is plasma treated utilising silane, carbon dioxide, hydrogen and diborane gases using a plasma enhance chemical vapour deposition technique, yielding a record efficiency of 23.83% and fill factor of 0.82 [49]. The plasma treatment obstructs the diffusion and reaction of oxygen at MoO_{3-x}/a-Si:H(i) interface and boosts the oxygen content and work function of MoO_{3-x} films deposited using the thermal evaporation technique. The respective solar cell configuration is shown in Figure 1.17. These modifications and efficient device performances are making TMO an emerging alternative to doped carrier selective contacts in SHJ solar cells. These developments have introduced a new kind of photovoltaic device known as DASH solar cells that are entirely free of doped CSCs. The maximum reported efficiency of the DASH solar cell till now is 20.7% [10]. To further increase the efficiency of DASH solar cells, modifications to the device architecture and optimisations of the characteristics of dopant-free CSCs are going on.

The performance of *MoO_{3-x}/c-Si(n)* solar cells are significantly impacted by the both work function and trap states present in MoO_{3-x} film. Depending on work function value and density of defect/trap states, the charge transfer between c-Si (n) (the absorber layer) and MoO_{3-x} (HTL) are possible in two ways: (1) band to band tunnelling (B2B) and (2) trap-assisted tunnelling (TAT). When the work function is > 5.7 eV, direct transport of holes from c-Si (n) to MoO_{3-x} (n) side is possible as shown in Figure 1.18a. This mechanism of holes transfer is called B2B tunnelling [12, 51]. When MoO_{3-x}'s work function is low, the presence of trap states is necessary for effective hole transport and these trap states originate from O_v. As traps are necessary for the efficient conveyance of holes from c-Si (n) to MoO_{3-x}, this method is known

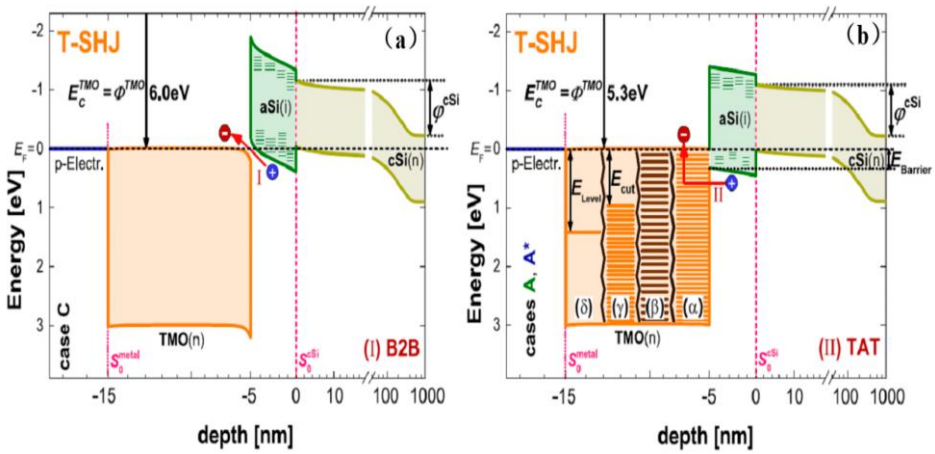

Figure 1.18: *(a) Band to band tunnelling and (b) Trap-assisted tunnelling in MoO_{3-x}/c-Si(n) solar cell [51].*

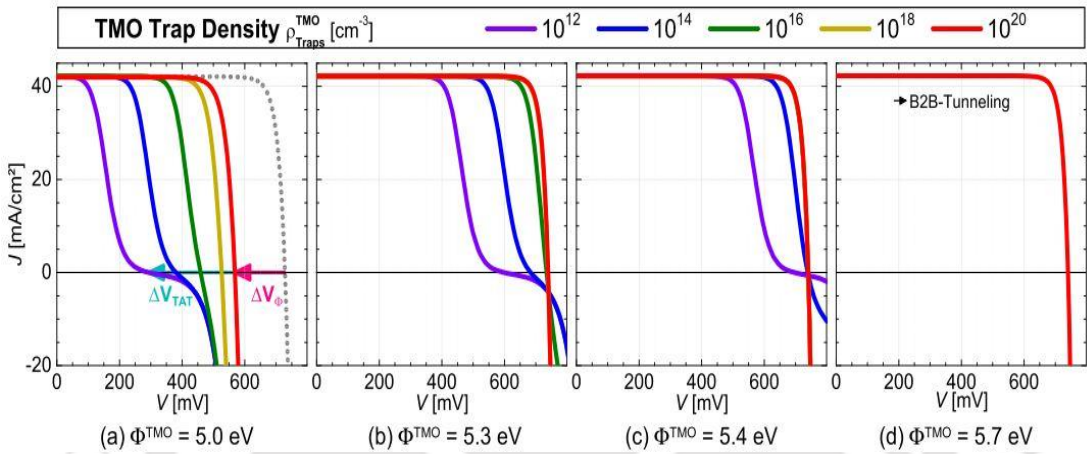

Figure 1.19: *Effect of work function and traps density on J-V characteristics of MoO_{3-x}/c-Si(n) solar cell [12]*

as TAT. Figure 1.18b depicts the TAT mechanism. The impact of MoO_{3-x} work function and density of trap states on the *J-V* characteristics of c-Si(n) heterojunction solar cells with MoO_{3-x} as an HTL is presented in Figure 1.19. Progress report of transition metal oxides and silicon heterojunction solar cells is summarized in Table 1.1.

1.3 Motivations and objectives

As discussed above, MoO_{3-x} is the widely explored TMO finding its integration as suitable substitute of p-doped a-Si:H layer in silicon heterojunction solar cells. *MoO_{3-x}/c-Si(n)* solar cells' promising performance has demonstrated its potential in the field of photovoltaic devices. MoO_{3-x} optoelectronic features like transparency, band gap, work function and conductivity

Table 1. 1: *Progress report of the TMO/c-Si(n) solar cells up to 2023.*

Device Structure	V_{oc} (mV)	J_{sc} (mAcm^{-2})	*FF* (%)	η (%)	Year
**"Ag/ITO/MoO_{3-x}/c-Si(n)/a-Si:H(i)/a-Si:H(n)/ITO/Ag"*	580	37.80	65.00	14.30	2014[47]
**"Ag/IO:H/ITO/ MoO_{3-x} /a-Si:H(i)/c-Si(n)/a-Si:H(i)/a-Si:H(n)/ITO/Ag"*	711	39.4	67.2	18.8	2014[52]
#"Ag/IO:H/ITO/ MoO_{3-x} /a-Si:H(i)/c-Si(n)/a-Si:H(i)/LiF_x/Al"	716.4	37.07	73.15	19.42	2016[53]
**"Ag/IO:H/ITO/ MoO_{3-x} /a-Si:H(i)/c-Si(n)/a-Si:H(i)/a-Si:H(n)/ITO/Ag"*	725	37.46	76.67	20.81	2015[50]
**"Cu/IO:H/ITO/ MoO_{3-x} /a-Si:H(i)/c-Si(n)/a-Si:H(i)/a-Si:H(n)/ITO/Ag"*	725.4	38.60	80.36	22.50	2015[50]
**"Ag/ITO/ MoO_{3-x} /a-Si:H(i)/c-Si(n)/a-Si:H(i)/a-Si:H(n)/ITO/Ag"*	733.7	39.19	81.77	23.48	2020[48]
**"Ag/MgF_2/IWO/MoO_{3-x}/a-Si:H(i)/c-Si(n)/a-Si:H(i)/a-Si:H(n)/IWO/Ag"*	721.10	40.20	82.18	23.83	2022[49]
#"Ag/ITO/MoO_{3-x}/a-Si:H(i)/c-Si(n)/a-Si:H(i)/ TiOx/LiF/Ag"	706	38.40	76.20	20.70	2018[10]
#"Ag/ITO/MoO_{3-x}/c-Si(n)/LiF_x/Al"	575	35.60	75.02	15.36	2019[54]
§"Ag/MoO_{3-x} NSs/c-Si(n)/Ag"	640		66.00	10.74	2023[55]

Note:* Double sided + one dopant free CSC; # Double sided + all dopant free CSCs; §Single sided + all doped CSCs.

rely on the O/Mo ratio, oxygen vacancies and Mo atom's oxidation number. All of these factors are further affected by the approaches used for synthesis, the environment during deposition and the post-deposition treatments performed on MoO_{3-x} films. So, before integration of MoO_{3-x} as HTL in solar cell, sequential optimization of deposition conditions and post-deposition heat treatments are required to prepare device quality films. These observations have inspired us to fabricate MoO_{3-x} films by different vacuum processes and optimize deposition conditions including substrate temperature, process pressure and gaseous environment to produce MoO_{3-x} films with a wide band gap and a high Φ. Thermally evaporated molybdenum oxide films are also subjected to some post-deposition treatments, such as annealing and oxygen plasma treatment, to investigate their effects on various MoO_{3-x} film properties. The motivation of the thesis work is to investigate and optimize the optoelectronic properties of MoO_{3-x} films and fabricate dopant free single-sided *MoO_{3-x}/c-Si(n)* silicon heterojunction solar cells.

To better understand the mechanism of charge carrier transport and band bending formed

across the interface, simulation studies on TMO and c-Si (n) heterojunction solar cells have also been conducted [51]. Sentaurus TCAD and AFORS-HET are the simulation tools that are used most frequently. It assists in directing us toward the best strategy for achieving better device performance and also gives us a clearer understanding of the various factors to be considered during fabricating the actual devices. In this thesis we have used AFORS-HET software to perform simulation studies on *MoO_{3-x}/c-Si(n)* solar cells.

Apart from HTL layer properties, the performance of the device is directly impacted by the transparent conducting oxide (TCO) layer, deposited on top of HTL. The TCO layer serve as the optically transparent electrode at the front of solar cells, allowing photons to enter the solar cell and transporting the photo-generated electrons to the terminals of external devices. Therefore, for the front TCO of solar cell, low sheet resistance and low absorption in UV-Vis-IR region are essential requirements [56]. So, in order to fabricate an efficient device, optimization of TCO layer is also necessary. Very few studies are available which show impact of ITO film preparation parameters directly on the performance of *MoO_{3-x}/c-Si(n)* solar cells.

The main objective of the present dissertation aimed to fabricate dopant free single-sided *MoO_{3-x}/c-Si(n)* heterojunction solar cells. The following objectives were designed to accomplish it:

1. Optimization of deposition conditions (rf power, substrate temperature, gaseous environment) to tune the optoelectronic properties of MoO_{3-x} films deposited by rf-magnetron sputtering and thermal evaporation techniques.
2. Investigation of structural, optical and electrical properties, as well as compositional details of MoO_{3-x} films prepared under varying conditions using several characterization techniques.
3. Oxygen plasma treatment on thick and thin MoO_{3-x} to improve the work function of

thermally evaporated MoO_{3-x} films.

4. Optimisation of deposition parameters (process pressure and substrate temperature) to prepare device quality ITO films using rf-sputtering technique
5. Fabrication of solar cells with optimized individual layer and its characterization by current density-voltage (*J -V*) measurement.
6. Simulation studies to comprehend how the work function affects the transport mechanism and performance of MoO_{3-x}/c-Si(n) solar cells.

1.4 Content of Thesis chapters

There are nine chapters in this thesis. The carrier selective contact and its types are briefly introduced in Chapter 1. A brief introduction to the properties of transition metal oxides, their synthesis methods, and their use in silicon heterojunction solar cells are discussed in this chapter. The literature review on the development of *MoO_{3-x}/c-Si(n)* SHJ solar cells is also summarised in this chapter. In this chapter, the thesis's motivation and objectives are also addressed.

Chapter 2, describes the details of deposition techniques such as the thermal evaporation and rf-puttering that have been utilised for the fabrication of dopant free single sided solar cells and deposition of MoO_{3-x} (HTL) and ITO (TCO layer) films. The description of several characterization techniques used to investigate the morphological, optical, electrical, structural, and compositional properties of molybdenum oxide and performance of *MoO_{3-x}/c-Si(n)* SHJ solar cells are also covered in this chapter.

Chapter 3, presents research conducted on the structural and optoelectronic characteristics of MoO_{3-x} films fabricated by rf-sputtering technique. The optimization of deposition conditions (rf power, substrate temperature and gaseous environment) is carried out in a sequential manner

to study how deposition conditions affect the optoelectronic properties of MoO_{3-x}. High rf power (80 W) and substrate temperature (400 °C) has enabled the formation of MoO_{3-x} films that exhibit uniformity and high conductivity. The incorporation of oxygen gas during deposition has transformed the coloured and conducting MoO_{3-x} films prepared at 400 °C to highly transparent and resistive MoO_{3-x} films, making it suitable for use as a hole selective or emitter layer in solar cells.

Chapter 4 presents the impact of deposition temperature (RT and 100 °C) and heat treatment (vacuum annealing at 130 °C and 150 °C) on the optical, electrical, and structural properties of MoO_{3-x} films deposited by thermal evaporation technique. Decrease in band gap, work function and increases in oxygen vacancies are observed with an increase in deposition and annealing temperatures.

Chapter 5 presents an overview of the research conducted on the effects of oxygen plasma treatment (OPT) on thermally evaporated MoO_{3-x} films. An increase in work function is observed when thick MoO_{3-x} films are subjected to OPT due to the filling of oxygen vacancies with active oxygen atoms produced during OPT. Studies are performed sequentially by varying OPT conditions such as rf power, oxygen flow rate (OFR) and OPT time to optimize the treatment conditions. The 80 W rf power, 30 SCCM OFR, and 10-minute treatment duration increased the work function of 500 nm thick MoO_{3-x} from 4.91 eV (for untreated films) to 5.22 eV. Under optimised conditions, thin films of MoO_{3-x} with thicknesses of 23 nm and 14 nm appropriate for solar cell applications are also subjected to OPT. The work function is improved from 4.47 eV (for No OPT) to 4.99 eV (after OPT) for 23 nm films and from 4.58 eV (for No OPT) to 4.95 eV (after OPT) for 14 nm films. These studies have provided empirical evidence supporting the effectiveness of oxygen plasma treatment, thereby establishing it as a suitable method for enhancing or restoring the work function of molybdenum oxide films.

Chapter 6 contains the detailed studies on the influence of deposition conditions such as process pressure and substrate temperature on the structural, optical and electrical properties of indium tin oxide (ITO) thin films. Low pressure of 3.8×10^{-3} mbar and substrate temperature of 150 °C and 170°C have led to the formation of highly transparent and good quality films having low sheet resistance (11-10 Ω/□).

Chapter 7 presents the influence of back electrodes combinations and conditions for depositing ITO (the TCO layer) on the performance of MoO_{3-x}/c-Si(n) solar cells. Dopant free single sided MoO_{3-x}/c-Si(n) SHJ solar cells (*Ag/ITO/MoO_{3-x}/c-Si(n)/Al/Ag*) are fabricated on both side polished n-type silicon wafer. ITO and MoO_{3-x} films are prepared using thermal evaporation and rf-sputtering, respectively. Cell efficiency has improved from 8.58% to 10.06% with the decrease in process pressure from 5.3×10^{-3} mbar to 3.8×10^{-3} mbar for ITO films deposition. Enhancement in cell efficiency and photovoltaic parameters are due to the high deposition rate of ITO film at low pressure, which reduced the sputter damage between the ITO/MoO_{3-x} interface. The effect of MoO_{3-x} film deposition temperature on the current density-voltage characteristics of MoO_{3-x}/c-Si(n) solar cells is also studied. When MoO_{3-x} film is prepared at room temperature, an efficiency of 11.88% and open circuit voltage of 539 mV are obtained. This chapter also discusses the effect of multiple time heat treatments on the properties of MoO_{3-x} films deposited at RT during device fabrication. During the fabrication of solar cells, two-time heat treatment of MoO_{3-x} films has resulted in increased oxygen vacancies and structural distortion.

Chapter 8 presents the simulation studies performed to understand how the work function of MoO_{3-x} layer in the cell structure MoO_{3-x}/c-Si(n) affect the cell performance using a user-friendly AFORS-HET v-2.5 software. The simulation studies revealed that the increase in the work function of MoO_{3-x} layer from 4.7 eV to 5.2 eV has increased the MoO_{3-x}/c-Si(n) solar

cells' open circuit voltage from 115.7 mV to 605.80 mV, fill factor from 0.52 to 0.83 and overall power conversion efficiency from 2.23% to 19.18%. Furthermore, the effects of tunnelling through the SiO_x layer, SiO_x thickness and transport through pinholes on the efficiency of MoO_{3-x} and silicon solar cells are also investigated in this chapter.

Chapter 9 is the concluding chapter of the thesis, which summarises the discussions of each chapter and concludes the work done in this thesis. The thesis work is wind up with the scope for future research based on the present studies.

1.5 References

[1] H. Karunathilake, S. Witharana, Fossil fuels and global energy economics, Reference Module in Earth Systems and Environmental Sciences, Elsevier 2023.

[2] "India added 12.8 GW solar capacity in FY2023", Available: https://jmkresearch.com/india-added-12-8-gw-solar-capacity-in-fy2023/.

[3] M. Aamir Iqbal, M. Malik, W. Shahid, S. Zaheer Ud Din, N. Anwar, M. Ikram, F. Idrees, Materials for Photovoltaics: Overview, Generations, Recent Advancements and Future Prospects, in: Z. Beddiaf, S. Chander (Eds.) Thin Films Photovoltaics, IntechOpen, Rijeka, 2022.

[4] "Best Research-Cell Efficiency Chart", Available: https://www.nrel.gov/pv/cellefficiency.html.

[5] T. Saga, Advances in crystalline silicon solar cell technology for industrial mass production, NPG Asia Materials, 2 (2010) 96-102.

[6] L. Gerling, S. Mahato, C. Voz, R. Alcubilla, J. Puigdollers, Characterization of Transition Metal Oxide/Silicon Heterojunctions for Solar Cell Applications, Applied Sciences, 5 (2015) 695-705.

[7] K.K. Mikio Taguchi, Sadaji Tsuge,Toshiaki Baba,Hitoshi Sakata,Masashi Morizane, Kenji Uchihashi, Noboru Nakamura, Seiichi Kiyama and OsamuOota, HITTM cells high-efficiency crystalline Si cells with novel structure., Progress in Photovoltaics Research and Applications, 8 (2000) 503-513.

[8] M.T. Makoto Tanaka, Takao Matsuyama, Toru Sawada, Shinya Tsuda, Shoichi Nakano, Hiroshi Hanafusa and Yukinori Kuwano, Development of New a-Si/c-Si Heterojunction Solar Cells: ACJ-HIT (Artificially Constructed Junction-Heterojunction with Intrinsic Thin-Layer), Japanese Journal of Applied Physics, 31 (1992) 3518-3522.

[9] K. Yoshikawa, W. Yoshida, T. Irie, H. Kawasaki, K. Konishi, H. Ishibashi, T. Asatani, D. Adachi, M. Kanematsu, H. Uzu, K. Yamamoto, Exceeding conversion efficiency of 26% by heterojunction interdigitated back contact solar cell with thin film Si technology, Solar Energy Materials and Solar Cells, 173 (2017) 37-42.

[10] J. Bullock, Y. Wan, Z. Xu, S. Essig, M. Hettick, H. Wang, W. Ji, M. Boccard, A. Cuevas, C. Ballif, A. Javey, Stable Dopant-Free Asymmetric Heterocontact Silicon Solar Cells with Efficiencies above 20%, ACS Energy Letters, 3 (2018) 508-513.

[11] Hakim Najeeb-ud-Din, Bisma Bilal, Fundamentals of and Recent Advances in Carrier Selective Passivating Contacts for Silicon Solar Cells, Journal of Electronic Materials, 50 (2021) 3761–3772.

[12] Z. Wang, P. Li, Z. Liu, J. Fan, X. Qian, J. He, S. Peng, D. He, M. Li, P. Gao, Hole selective materials and device structures of heterojunction solar cells: Recent assessment and future trends, APL Materials, 7 (2019) 110701.

[13] Y. Tao, V. Upadhyaya, K. Jones, A. Rohatgi, Tunnel oxide passivated rear contact for large area n-type front junction silicon solar cells providing excellent carrier selectivity, AIMS Materials Science, 3 (2016) 180-189.

[14] H. Lin, M. Yang, X. Ru, G. Wang, S. Yin, F. Peng, C. Hong, M. Qu, J. Lu, L. Fang, C. Han, P. Procel, O. Isabella, P. Gao, Z. Li, X. Xu, Silicon heterojunction solar cells with up to 26.81% efficiency achieved by electrically optimized nanocrystalline-silicon hole contact layers, Nature Energy, 8 (2023) 789-799

[15] J. Bullock, M. Hettick, J. Geissbühler, A.J. Ong, T. Allen, Carolin M. Sutter-Fella, T. Chen, H. Ota, E.W. Schaler, S. De Wolf, C. Ballif, A. Cuevas, A. Javey, Efficient silicon solar cells with dopant-free asymmetric heterocontacts, Nature Energy, 1 (2016) 1-7.

[16] M.A. Hossain, K.T. Khoo, X. Cui, G.K. Poduval, T. Zhang, X. Li, W.M. Li, B. Hoex, Atomic layer deposition enabling higher efficiency solar cells: A review, Nano Materials Science, 2 (2020) 204-226.

[17] Z. Yang, P. Gao, J. Sheng, H. Tong, C. Quan, X. Yang, K.W.A. Chee, B. Yan, Y. Zeng, J. Ye, Principles of dopant-free electron-selective contacts based on tunnel oxide/low work-function metal stacks and their applications in heterojunction solar cells, Nano Energy, 46 (2018) 133-140.

[18] C. Yu, S. Xu, J. Yao, S. Han, Recent Advances in and New Perspectives on Crystalline Silicon Solar Cells with Carrier-Selective Passivation Contacts, Crystals, 8 (2018) 430.

[19] M.T. Greiner, L. Chai, M.G. Helander, W.-M. Tang, Z.-H. Lu, Transition Metal Oxide Work Functions: The Influence of Cation Oxidation State and Oxygen Vacancies, Advanced Functional Materials, 22 (2012) 4557-4568.

[20] D.S. Lambert, S.T. Murphy, A. Lennon, P.A. Burr, Formation of intrinsic and silicon defects in MoO_3 under varied oxygen partial pressure and temperature conditions: an ab initio DFT investigation, RSC Advances, 7 (2017) 53810-53821.

[21] K. Inzani, T. Grande, F. Vullum-Bruer, S.M. Selbach, A van der Waals Density Functional Study of MoO_3 and Its Oxygen Vacancies, The Journal of Physical Chemistry C, 120 (2016) 8959-8968.

[22] B. Han, M. Gao, Y. Wan, Y. Li, W. Song, Z. Ma, Effect of post-annealing on the properties of thermally evaporated molybdenum oxide films: Interdependence of work function and oxygen to molybdenum ratio, Materials Science in Semiconductor Processing, 75 (2018) 166-172.

[23] Y. Jiang, S. Cao, L. Lu, G. Du, Y. Lin, J. Wang, L. Yang, W. Zhu, D. Li, Post-annealing Effect on Optical and Electronic Properties of Thermally Evaporated MoO_x Thin Films as Hole-Selective Contacts for p-Si Solar Cells, Nanoscale Res Lett, 16 (2021) 87.

[24] N. Lopez-Pinto, T. Tom, J. Bertomeu, J.M. Asensi, E. Ros, P. Ortega, C. Voz, Deposition and characterisation of sputtered molybdenum oxide thin films with hydrogen atmosphere, Applied Surface Science, 563 (2021) 150285.

[25] J. Sun, Q. Zheng, S. Cheng, H. Zhou, Y. Lai, J. Yu, Comparing molybdenum oxide thin films prepared by magnetron sputtering and thermal evaporation applied in organic solar cells, Journal of Materials Science: Materials in Electronics, 27 (2015) 3245-3249.

[26] J. Kumari, P. Agarwal, Optimization of deposition conditions to tune optoelectronic properties of MoO_{3-x} films prepared by RF-sputtering technique, Vacuum, 216 (2023) 112485.

[27] R. Sivakumar, M. Jayachandran, C. Sanjeeviraja, Effect of Annealing on Structural, Surface and Optical Properties Of PVD-EBE α-MoO_3 Thin Films For Electrochromic Devices, Surface Engineering, 20 (2013) 385-390.

[28] M.T. Greiner, M.G. Helander, Z.B. Wang, W.M. Tang, Z.H. Lu, Effects of Processing Conditions on the Work Function and Energy-Level Alignment of NiO Thin Films, J Phys Chem C, 114 (2010) 19777-19781.

[29] I.A. de Castro, R.S. Datta, J.Z. Ou, A. Castellanos-Gomez, S. Sriram, T. Daeneke, K. Kalantar-Zadeh, Molybdenum Oxides - From Fundamentals to Functionality, Adv Mater, 29 (2017) 1701619.

[30] S.Q. Hussain, K. Mallem, Y.J. Kim, A.H. Tuan Le, M.Q. Khokhar, S. Kim, S. Dutta, S.

Sanyal, Y. Kim, J. Park, Y. Lee, Young H. Cho, Eun C. Cho, J. Yi, Ambient annealing influence on surface passivation and stoichiometric analysis of molybdenum oxide layer for carrier selective contact solar cells, Materials Science in Semiconductor Processing, 91 (2019) 267-274.

[31] H.S. Kim, J.B. Cook, H. Lin, J.S. Ko, S.H. Tolbert, V. Ozolins, B. Dunn, Oxygen vacancies enhance pseudocapacitive charge storage properties of MoO_{3-x}, Nat Mater, 16 (2017) 454-460.

[32] A. Lakshmi-Narayana, O.M. Hussain, C.V. Ramana, M. Camacho-Lopez, A. Abdel-Ghany, A. Hashem, A. Mauger, C.M. Julien, Molybdenum-Suboxide Thin Films as Anode Layers in Planar Lithium Microbatteries, Electrochem, 1 (2020) 160-187.

[33] H.W. Eng, P.W. Barnes, B.M. Auer, P.M. Woodward, Investigations of the electronic structure of d^0 transition metal oxides belonging to the perovskite family, Journal of Solid State Chemistry, 175 (2003) 94-109.

[34] D. Xiang, C. Han, J. Zhang, W. Chen, Gap states assisted MoO_3 nanobelt photodetector with wide spectrum response, Sci Rep, 4 (2014) 4891.

[35] M. Vasilopoulou, A.M. Douvas, D.G. Georgiadou, L.C. Palilis, S. Kennou, L. Sygellou, A. Soultati, I. Kostis, G. Papadimitropoulos, D. Davazoglou, P. Argitis, The influence of hydrogenation and oxygen vacancies on molybdenum oxides work function and gap states for application in organic optoelectronics, J Am Chem Soc, 134 (2012) 16178-16187.

[36] X. Liu, C. Wang, Irfan, S. Yi, Y. Gao, Effect of oxygen plasma treatment on air exposed MoO_x thin film, Organic Electronics, 15 (2014) 977-983.

[37] J. Kumari, J.S. Bhardwaj, Rahul, P. Agarwal, Oxygen Plasma Treatment of Thermally Evaporated MoO_{3-x} Films: An Approach to Tune the Work Function, ACS Applied Electronic Materials, 5 (2023) 4103–4113.

[38] M. Morita, S. Toyoda, H. Kiuchi, T. Abe, K. Kumagai, T. Saida, K. Fukuda, Chromogenic Amorphous MoO_{3-x} Nanosheets and Their Nanostructured Films for Smart Window Applications, ACS Applied Nano Materials, 4 (2021) 8781-8788.

[39] K. Gesheva, T. Ivanova, G. Bodurov, I.M. Szilágyi, N. Justh, O. Keri, S. Boyadjiev, D. Nagy, M. Aleksandrova, Technologies for deposition of transition metal oxide thin films: application as functional layers in "Smart windows" and photocatalytic systems, Journal of Physics: Conference Series, 682 (2016) 012011.

[40] L.G. Gerling, C. Voz, R. Alcubilla, J. Puigdollers, Origin of passivation in hole-selective transition metal oxides for crystalline silicon heterojunction solar cells, Journal of Materials Research, 32 (2016) 260-268.

[41] Y. Wang, S.T. Zhang, L. Li, X. Yang, L. Lu, D. Li, Dopant-free passivating contacts for crystalline silicon solar cells: Progress and prospects, EcoMat, 5 (2022) e12292.

[42] T.T. Haris Mehmood, Hisham Nasser, Shahzad Hussain and Rasit Turan, Effect of Hole Selective Molybdenum Oxide Work Function and Silicon Wafer Resistivity on Dopant Free Asymmetric Silicon Heterostructure Solar Cell, IEEE Xplore, 2017 International Renewable and Sustainable Energy Conference (IRSEC) 2017, (2017).

[43] J. Bullock, A. Cuevas, T. Allen, C. Battaglia, Molybdenum oxide MoO_x: A versatile hole contact for silicon solar cells, Applied Physics Letters, 105 (2014) 232109.

[44] C. Messmer, M. Bivour, J. Schon, M. Hermle, Requirements for efficient hole extraction in transition metal oxide-based silicon heterojunction solar cells, Journal of Applied Physics, 124 (2018) 085702.

[45] T. Sun, R. Wang, R. Liu, C. Wu, Y. Zhong, Y. Liu, Y. Wang, Y. Han, Z. Xia, Y. Zou, T. Song, N. Koch, S. Duhm, B. Sun, Investigation of MoO_x/n-Si strong inversion layer interfaces via dopant-free heterocontact, physica status solidi (RRL) – Rapid Research Letters, 11 (2017) 1700107.

[46] V. Kanneboina, R. Madaka, P. Agarwal, Stepwise tuning of the doping and thickness of a-Si:H(p) emitter layer to improve the performance of c-Si(n)/a-Si:H(p) heterojunction solar cells, Journal of Materials Science: Materials in Electronics, 32 (2021) 4457-4465.

[47] C. Battaglia, X. Yin, M. Zheng, I.D. Sharp, T. Chen, S. McDonnell, A. Azcatl, C. Carraro, B. Ma, R. Maboudian, R.M. Wallace, A. Javey, Hole selective MoO_x contact for silicon solar cells, Nano letters, 14 (2014) 967-971.

[48] J. Dreon, Q. Jeangros, J. Cattin, J. Haschke, L. Antognini, C. Ballif, M. Boccard, 23.5%-efficient silicon heterojunction silicon solar cell using molybdenum oxide as hole-selective contact, Nano Energy, 70 (2020) 104495.

[49] L. Cao, P. Procel, A. Alcaniz, J. Yan, F. Tichelaar, E. Ozkol, Y. Zhao, C. Han, G. Yang, Z. Yao, M. Zeman, R. Santbergen, L. Mazzarella, O. Isabella, Achieving 23.83% conversion efficiency in silicon heterojunction solar cell with ultra-thin MoO_x hole collector layer via tailoring (i)a-Si:H/MoO_x interface, Progress in Photovoltaics: Research and Applications, (2022) 1-10.

[50] J.W. Jonas Geissbühler, Silvia Martin de Nicolas, Loris Barraud, Aïcha Hessler-Wyser, Matthieu Despeisse, Sylvain Nicolay, Andrea Tomasi, Bjoern Niesen, Stefaan De Wolf and Christophe Ballif, 22.5% efficient silicon heterojunction solar cell with molybdenum oxide hole collector, Applied Physics Letters, 107 (2015) 081601.

[51] C. Messmer, M. Bivour, J. Schon, S.W. Glunz, M. Hermle, Numerical Simulation of Silicon Heterojunction Solar Cells Featuring Metal Oxides as Carrier-Selective Contacts, IEEE Journal of Photovoltaics, 8 (2018) 456-464.

[52] C. Battaglia, S.M. de Nicolás, S. De Wolf, X. Yin, M. Zheng, C. Ballif, A. Javey, Silicon heterojunction solar cell with passivated hole selective MoO_x contact, Applied Physics Letters, 104 (2014) 113902.

[53] J. Bullock, M. Hettick, J. Geissbuhler, A.J. Ong, T. Allen, Carolin M. Sutter-Fella, T. Chen, H. Ota, E.W. Schaler, S. De Wolf, C. Ballif, A. Cuevas, A. Javey, Efficient silicon solar cells with dopant-free asymmetric heterocontacts, Nature Energy, 1 (2016) 1-7.

[54] M. Nayak, K. Singh, S. Mudgal, S. Mandal, S. Singh, V.K. Komarala, Carrier-Selective Contact Based Silicon Solar Cells Processed at Room Temperature using Industrially Feasible Cz Wafers, Phys. Status Solidi A 216 (2019) 1900208.

[55] M. Shahbazi, A. Taherkhani, J. Nasrollah Gavgani, Enhancing the efficiency and short-circuit current of silicon solar cells using MoO_3 as emitter layers, Materials Today Communications, 35 (2023) 106263.

[56] J. Shi, L. Shen, Y. Liu, J. Yu, J. Liu, L. Zhang, Y. Liu, J. Bian, Z. Liu, F. Meng, MoO_x modified ITO/a-Si:H(p) contact for silicon heterojunction solar cell application, Materials Research Bulletin, 97 (2018) 176-181.

CHAPTER 2

Experimental Details and Characterization Techniques

This chapter presents an overview of the techniques used for the synthesis of molybdenum oxide (MoO_{3-x}), indium tin oxide (ITO) films and fabrication of MoO_{3-x}/c-Si (n) solar cells. Various characterization techniques are used for investigating the structural, optical and electrical properties of MoO_{3-x} and ITO films. This chapter presents a brief description of each characterization tool. The objective of this chapter is to give the reader a quick overview of the various experimental setups and the fundamentals of characterization techniques used in this thesis work.

2.1 Film preparation and device fabrication techniques

Molybdenum oxide films can be prepared by several techniques like physical vapour deposition (PVD) and chemical vapour deposition (CVD) techniques. PVD technique includes thermal evaporation [1], electron beam evaporation [2], radio-frequency (rf)/direct current

(DC) sputtering [3, 4] and pulsed laser vapour deposition [5]. Other than these two methods, thin films can also be prepared using exfoliation methods [6] and solution processed techniques like spin coating [7], electro deposition [8]. Our discussion in this thesis will be confined to the thermal evaporation and rf-sputtering techniques, which have been used to prepare MoO_{3-x} films. For oxygen plasma treatment, radio frequency plasma enhanced chemical vapour deposition (rf PECVD) method is used. Indium tin oxide films and silver electrodes are deposited using rf-sputtering technique. Thermal evaporation is used to prepare the aluminium electrodes in MoO_{3-x}/c-Si (n) solar cells. The next section covers a brief overview of these methods.

2.1.1 Rf sputtering

In this thesis, molybdenum oxide films, indium tin oxide (ITO) films and silver (Ag) as back electrodes are deposited on coring 1737 glass and silicon substrates using RF-sputtering. Sputtering is a physical vapour deposition (PVD) method utilised for thin film deposition in plasma environments. The ejection of atoms from the surface of a source material (the target) by bombardment with energetic particles is called sputtering [9]. The ions needed to carry out sputtering are produced by the glow discharge phenomenon in a gas when an electric field is applied between cathode and anode under low pressure. When a specific voltage is supplied, the ionisation of gas occurs, creating the plasma. The positively charged energetic plasma ions are accelerated towards the target which is negatively biased to strike the target surface and eject the target atoms. Sputtered atoms move towards the anode and impinge on the substrate to form thin film. If the target is an insulator, positively charged plasma ions striking the target develops positive charge on the target surface. This charge may reach a level where bombarding ions are repelled and the sputtering process stops. To continue the process, the polarity must be reversed to attract enough electrons from the plasma to eliminate surface

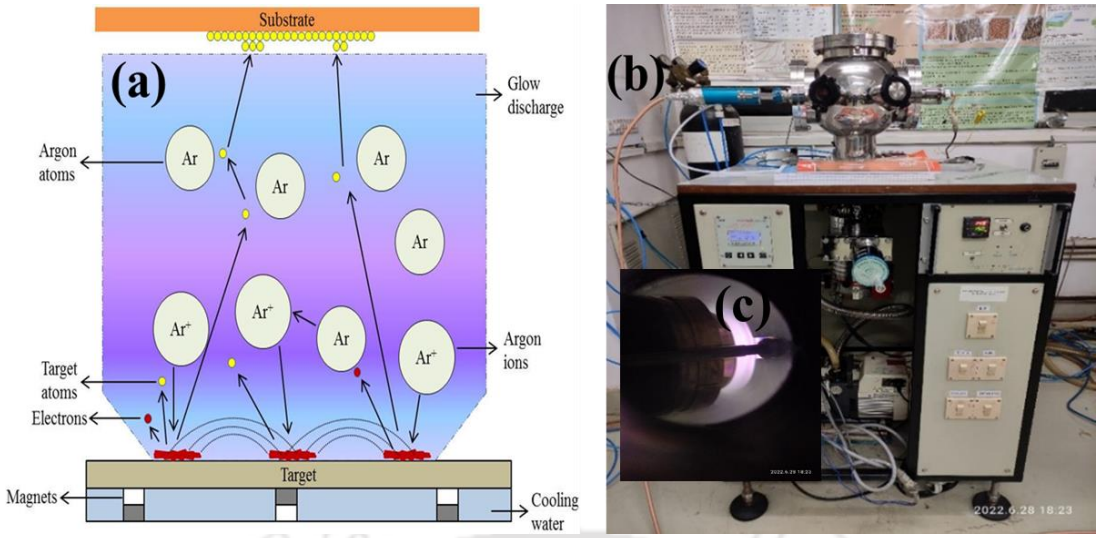

Figure 2.1: *(a) Schematic diagram of rf-sputtering, (b) RF sputtering system in our lab and chamber view during deposition.*

charge. This periodic reversal of polarity is done automatically by applying a radio-frequency (rf) voltage on the target assembly. Thus, this type of sputtering is known as "RF sputtering" [3, 4]. It uses high radio frequency source of 13.56 MHz to generate plasma. The schematic diagram of rf sputtering is shown in Figure 2.1a.

In order to increase the efficiency of the sputtering process, magnets are provided behind the negative cathode to trap electrons over the negatively charged target material. This magnetic field confines the plasma close to the target enabling the plasma to be operated at a higher density. The sputtering set up in our lab is shown in Figure 2.1b. The area of the rf electrode used in our case is 20.25 cm^2 (diameter 2 inch).

In order to avoid any chemical reaction between the sputtered atoms and the sputtering gas, the sputtering gas is usually an inert gas, such as argon. However, in some applications, such as the deposition of oxides, a reactive gas is purposely added to argon so that the deposited film is a chemical compound. This type of sputtering is called "reactive sputtering". Materials that can be sputtered include elements such as pure metals and elemental semiconductors, alloys, and compounds (such as oxides and carbides). Sputtering allows the deposition of films having

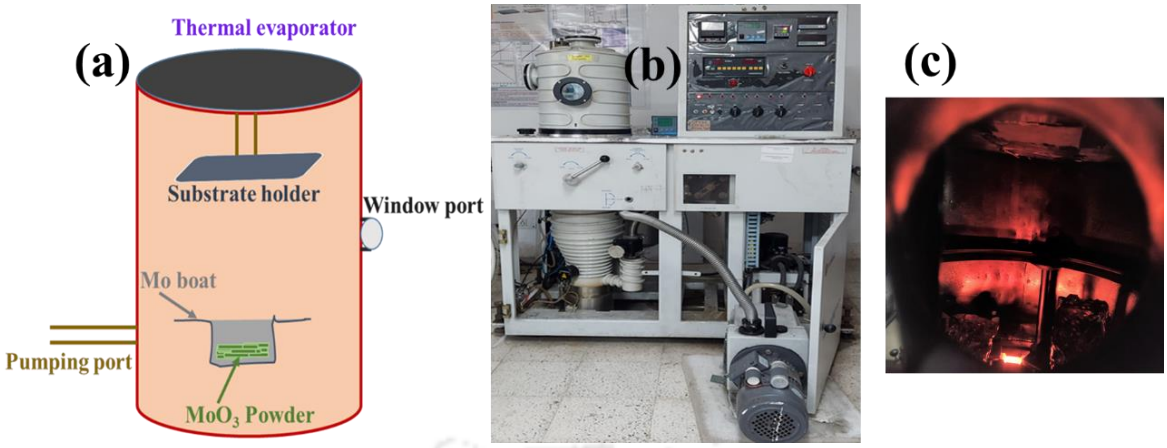

Figure 2.2: *(a) Schematic diagram of thermal evaporator, (b) Thermal evaporation system in our lab and (c) chamber while deposition.*

the same composition as the target source. This is the primary reason for the widespread use of sputtering as a thin-film deposition technique.

2.1.2 Thermal evaporation

Thermal evaporation is a widely used PVD technique in thin film technology. The schematic diagram of thermal evaporation is displayed in Figure 2.2a. This method is employed to deposit thin films of various materials onto solid substrates. The process involves the controlled heating of a source material until it reaches its sublimation temperature, at which point it turns into a vapour. The vaporized material condenses and forms a thin film on the substrate, which is usually held at a lower temperature. The entire process takes place in a vacuum (10^{-6} -10^{-7} mbar) or controlled atmosphere to eliminate the interference of air molecules [10]. The material to be deposited is often referred as the "evaporation material" or "source material" is placed in resistively heated evaporation sources like filament, crucible or boat within an evaporation chamber. The evaporation sources are made of pure/elemental refractory metal such as tantalum (Ta), molybdenum (Mo), tungsten (W). Combinations of ceramic compounds and inert oxide are other materials used for developing evaporation sources [11].

Thermal evaporation is commonly used to deposit good quality metal films (aluminium, silver,

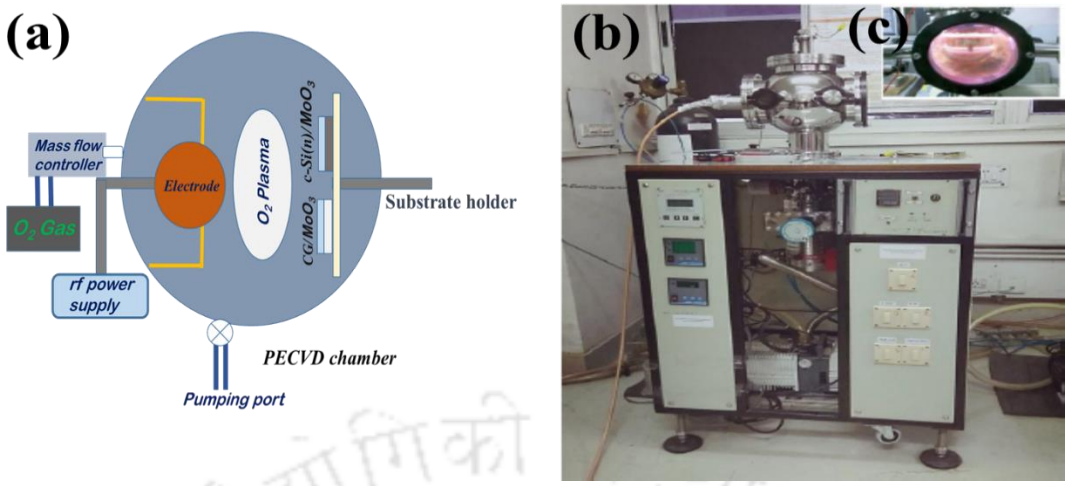

Figure 2.3: *(a) Schematic diagram of RF-PECVD, (b) system in our lab and (c) chamber view during the treatment process.*

gold) on optical accessories, solar cell, transistor and may more. It is also used to deposit organic compounds, oxides and ceramics. The thickness of the deposited films can be controlled by monitoring the deposition rate, which is determined by factors like the temperature of the source material, the distance between the source and substrate, and the deposition time. One of the important factor which determines the properties of thin films is the rate of evaporation (r_e) [11]. This requires heating of the source material to a temperature to produce the desired vapour pressure.

$$r_e = 3.513 \times 10^{22} \frac{P_e}{\sqrt{MT}} \frac{molecules}{cm^2 - sec} \quad \text{---------- (2.1)}$$

Here, P_e is the equilibrium vapour pressure in torr at temperature T and M refers to vapour species molecular weight.

In this thesis, aluminium electrode is deposited using aluminium wire placed in tungsten filament as evaporation source and for depositing molybdenum oxide films, molybdenum boat is used. The thermal evaporator set up in our lab is presented in Figure 2.2b.

2.1.3 RF-Plasma Enhanced Chemical Vapour Deposition

Radio frequency Chemical Vapour Deposition (rf-PECVD) is commonly used technique for

thin film deposition and to perform plasma treatment of deposited thin film to remove surface contaminants or to improve the bonding at surface. In this technique, plasma is used to provide the energy to reacting gases for thin film deposition, hence it is called plasma enhanced CVD. A typical design of a PECVD set up is shown in Figure 2.3a. The setup consists of two parallel plates which acts as electrodes and uses voltage in the radio frequency domain (13.56-200 MHz) to create glow discharge plasma. The commonly used rf frequency is 13.56 MHz. The rf-PECVD system we have in our lab is shown in Figure 2.3b. The rf-PECVD chamber during deposition/treatment is shown in Figure 2.3c. We have employed this method to treat thermally evaporated molybdenum oxide films (MoO_{3-x}) with oxygen plasma. Due to plasma, the oxygen (O_2) gas dissociates and radicals are generated. The dissociation of O_2 gas takes place as $O_2 + e^- \rightarrow 2O + e^-$. The generated active oxygen reacts with oxygen deficient MoO_{3-x} deposited by thermal evaporation to fill the oxygen vacancy forming nearly stoichiometric molybdenum oxide films. The radicals generated due to glow discharge also react with surface adsorbed organic contaminants to clean the film surface.

2.2 Preparation of MoO_{3-x} and ITO thin films

MoO_{3-x} films are dposited on corning 1737 glass (CG) substrates and n-type crystalline silicon wafers (c-Si (n)). Prior to deposition, CG substrates are cleaned using soapy solution to remove impurities and dirt and then sonicated in Reverse Osmosis (RO) water, de-ionized (DI) water and iso-propanol for 15 minutes sequentially to remove organic impurities and dried using the fast flow of dry nitrogen gas.

The c-Si (n) wafers are at first sonicated for 10 minutes in DI water and then dipped in 2% diluted Hydrofluoric (HF) acid to remove native oxide. Dry nitrogen gas is then used for drying the cleaned silicon substrates.

2.2.1 MoO_{3-x} films deposited using rf-sputtering

Using radio frequency sputtering, MoO_{3-x} thin films are deposited on CG substrates. MoO_{3-x} films deposition conditions are optimised to tune the optoelectronic features of these films. Three series of samples are prepared by varying the following parameters: (1) the rf-power from 60 W to 80 W; (2) the substrate temperature from 100 °C to 400 °C; and (3) the gaseous environment which includes use of argon gas only, argon + oxygen gases and oxygen gas solely during the deposition process.

2.2.2 MoO_{3-x} films deposited using thermal evaporation

Thin films of MoO_{3-x} are deposited on CG and c-Si (n) substrates by thermal evaporation technique. MoO_{3-x} films are prepared at two deposition temperatures, room temperature and 100 °C. Films deposited at room temperature are annealed for 30 minutes at 130 °C and 150 °C under high vacuum (10^{-6} mbar) to analyse its impact on different properties of MoO_{3-x}.

2.2.3 Oxygen Plasma Treatment of MoO_{3-x} films

Thermally evaporated molybdnum oxide films deposited on CG and c-Si (n) substrates are treated with oxygen plasma using rf-PECVD technique to investigate how this treatment affects the optoelectronic properties of MoO_{3-x} films. A sequential optimisations of oxygen plasma tretament (OPT) conditions are carried out. For this, at first, rf power during OPT is varied from 20 W to 80 W, then oxygen gas flow rate is varied from 10 SCCM to 30 SCCM. Subsequently, the optimised parameters from the first two series are employed and only OPT time is varied from 10 minutes to 30 minutes and its influence on properties of thermally evaporated MoO_{3-x} films are investigated.

2.2.4 Indium tin oxide films deposited using rf-sputtering

Indium tin oxide (ITO) films are deposited on corning glass 1737 substrates using rf sputtering technique. Two series of samples are prepared by varying the process pressure from 9.3×10^{-3} mbar, 5.3 $\times10^{-3}$ mbar to 3.8×10^{-3} mbar keeping parameters fixed at 7 SCCM argon flow rate (AFR), 150 °C substrate temperature and 30 minutes deposition time. In the second series, substrate temperature is varied from 130 °C to 200 °C at process pressure of 3.8×10^{-3} mbar keeping rest parameters constant as first series.

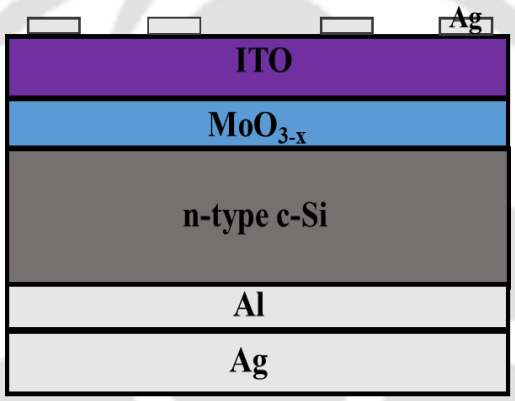

Figure 2.4: *Schematic device structure of MoO_{3-x}/c-Si (n) solar cell.*

2.3 Fabrication of Solar Cells

The device structure which is used for fabrication of MoO_{3-x}/c-Si(n) solar cells is shown in Figure 2.4. In this structure, MoO_{3-x} is used as hole selective layer (HSL). Double side polished (100) oriented c-Si (n) (CZ) wafers of resistivity ~5-10 Ωcm and thickness ~275-325 μm have been used for solar cell fabrication. Several solar cells with active area of 0.07 cm^2 are fabricated on 1×1 $inch^2$ Si wafers. Si wafers are cleaned using the procedure developed by Radio Corporation of America (RCA) laboratory. The standard RCA-1 and RCA-2 cleaning process are followed for removal of organic/insoluble contaminants and ionic/heavy metal atomic contaminants respectively. The cleaning procedure steps are discussed below:

2.3.1 RCA-1 Silicon wafer cleaning

In RCA-1, the solution consists of mixture of 5 parts of de-ionized water, 1 part of ammonium hydroxide (NH_4OH) and 1 part of hydrogen peroxide (H_2O_2) [12-14]. The mixture of 100 ml of DI water and 20 ml of NH_4OH (27%) in Pyrex beaker is heated on hot plate at 80 °C for 10 min to increase the activation of reaction. Then, 20 ml of H_2O_2 (30%) is added to hot solution. c-Si wafer is soaked in the solution for 15 min when the solution started to bubble vigorously. c-Si wafer is then rinsed in DI water to remove residues from the surface, and then immersed in 2% diluted HF acid for 1 minute to remove the oxide layer.

2.3.2 RCA-2 Silicon wafer cleaning

In RCA-2, the solution consists of mixture of 6 parts of de-ionized water, 1 part of hydrogen chloride (HCl) and 1 part of hydrogen peroxide (H_2O_2) [12-14]. The mixture of 120 ml of DI water and 20 ml of HCl (27%) is heated on hot plate at 80 °C for 10 min. Then, 20 ml of H_2O_2 (30%) is added to it. When the solution started to bubble rigorously, c-Si wafer is soaked in it for 15 minutes. c-Si (n) wafers are then rinsed with DI water and dipped in 2% diluted HF acid for 1 min to remove the native oxide.

Subsequently, RCA cleaned wafers are transferred to the thermal evaporation chamber for depositing aluminium (Al) on rear side of c-Si (n) wafer. The c-Si (n) wafer is subsequently loaded in rf-sputtering system and annealed at 400 °C for 60 minutes under a high vacuum (10^{-6} mbar) condition to diffuse Al into c-Si (n) wafer. Afterwards, c-Si (n) wafer is loaded in a different thermal evaporation system to deposit MoO_{3-x} on the front side. ITO is deposited on the top of MoO_{3-x} and Ag is deposited on the rear side by rf-sputtering technique. The front electrode grids are made using silver paste. Layer by layer optimisations are done in order to fabricate efficient solar cells. First, appropriate back electrodes are selected. The impact of ITO

and HSL deposition parameters on MoO_{3-x}/c-Si(n) solar cells performance is next examined. The effects of multiple heat treatments on the properties of the MoO_{3-x} layer and the performance of dopant-free solar cells are also studied, since the MoO_{3-x} layer is sensitive to post-deposition treatments.

2.4 Thin film characterization techniques

The characterization techniques used to study structural, optical and electrical properties of MoO_{3-x} and ITO films are discussed below.

2.4.1 Raman Spectroscopy

Raman spectroscopy is an effective analytical technique for investigating the vibrational and rotational modes of a material for understanding its molecular and crystal structures. This technique is based on the inelastic scattering of monochromatic light (often laser light) as it interacts with a material. The scattered photons can either lose or gain energy compared to the incident photons, resulting in a Raman spectrum. The energy shifts correlate to the sample molecules' vibrational and rotational energy levels, revealing information about their chemical bonding and structure. Raman spectra of MoO_{3-x} thin films deposited on CG substrates are recorded using "Horiba JobinYvon LabRam HR" spectrometer with 633 nm laser wavelength (He-Ne) to gain more insight into structural properties. The spectral range of the recorded Raman shift is 200 - 950 cm^{-1}, with a resolution of 1 cm^{-1}. The spot size of the laser beam, the laser power and acquisition time are 1 µm, 13.5 mW and 20 seconds respectively. Because of the large size difference between the molybdenum and oxygen atoms, the vibrations in molybdenum oxide are primarily caused by the involvement of lighter oxygen atoms. The Raman peak detected in the region 950-600 cm^{-1} are caused by MoO_6 octahedral stretching modes and the bands from 400 to 200 cm^{-1} are caused by MoO_6 octahedral bending vibrations

and lattice modes [15-17]. The characteristics peak of the most stable orthorhombic phase α-MoO_3 is obtained at ~820 cm^{-1} which represents symmetric stretching of doubly coordinated oxygen atoms with molybdenum atoms (Mo-O-Mo) [15-17] whereas peak at 850 cm^{-1} represents the formation of a metastable monoclinic phase β-MoO_3 [15].

2.4.2 X-ray Diffraction

X-ray diffraction (XRD) is an effective analytical method for examining the crystallographic structure of materials. The working principle of this technique is based on the theory of x-ray diffraction by crystal planes present in a material. This technique provides information on the type and nature of a material (amorphous or crystalline), structural phases (orthorhombic, monoclinic, hexagonal, etc.), crystallite orientation, mean crystallite size, unit cell parameters, micro strain, dislocation density, phase transition, and defects present. In this thesis, room temperature XRD measurements are carried out by "Rigaku Smartlab" diffractometer using CuK_α radition of wavelength (λ) 1.54 Å. The measurements are performed in thin film mode with a scanning rate of 1°/min and a step size of 0.02° at a grazing angle of 0.5° for all samples. The Scherer's formula is used for finding crystallite size peak corresponding to highest intensity given as in [18, 19].

$$D = \frac{0.9\lambda}{\beta cos\theta} \quad \text{---------- (2.2)}$$

where λ is the wavelength of X-ray used, β is the full-width at half maximum (FWHM) of peak which has maximum intensity and θ is the Bragg's angle.

The crystallite size is also calculated using the Williamson-Hall equation (considering all the peaks). It is based on the concept that peak broadening of an XRD peak can happen as a result of changes in crystallite size (D) and strain (ε) produced during sample preparation [18, 19].

The approximate formulae for size broadening, B_L and strain broadening, B_e, vary quite differently with respect to Bragg angle, θ:

$$B_L = \frac{0.9\lambda}{Dcos\theta} \quad \text{---------- (2.3)}$$

$$B_e = C\varepsilon tan\theta \quad \text{---------- (2.4)}$$

The summation gives the contribution of both crystallite size and strain in peak broadening

$$B_{Total}cos\theta = \frac{0.9\lambda}{D} + C\varepsilon sin\theta \quad \text{---------- (2.5)}$$

Where, B_{Total} is FWHM of peak obtained at each Bragg's angle.

The intercept of the linear plot of $B_{Total}cos\theta$ vs. $sin\theta$ plot gives the average crystallite size.

2.4.3 Field emission tranmission electron microscopy

The micro-structure properties of MoO_{3-x} are studied using Field Emission Tranmission Electron Microscopy (FETEM). Transmission Electron Microscopy is a powerful imaging technique used to investigate the interior structure of nanoscale materials. It relies on the transmission of electrons through a thin specimen to create high-resolution images and gather detailed structural information. FETEM can be used for imaging, diffraction and spectroscopy, providing information about sample shape, crystal structure, and chemical composition. TEM, selected area electron diffraction (SAED) patterns and high resolution TEM (HRTEM) images of MoO_{3-x} are captured using "JEOL-2100" microscope. For this study, MoO_{3-x} films are deposited on carbon coated copper mesh TEM grid keeping the thickness < 30 nm. During the measurements, the electron beam is accelerated at voltage of 200 KV. The inter-planar spacing is calculated from HRTEM image and SAED pattern using the "ImageJ" software.

2.4.4 Field emission scanning electron microscopy

Field-Emission Scanning Electron Microscopy (FESEM) is an advance microscopy technique utilised for high-resolution imaging of the surface of materials at the nano-scale. FESEM operates on electron microscopy principles. It scans the surface of a specimen with a focused beam of high-energy electrons [20]. The term "field emission" refers to the emission of electrons from a sharp, pointed electrode (usually a tungsten tip) when exposed to a high electric field. This produces a highly focused electron beam. FESEM produces a clearer image with resolution <2 nm. Surface morphology of MoO_{3-x} and ITO films are acquired using "FESEM Zeiss Sigma 300" microscope. FESEM imaging is done at electron high tension voltage (EHT) in the range of 3 kV to 10 kV using InLens detector and aperture of 30 µm. To avoid the charging effect during the analysis, all the films are coated with gold layer of thickness 2-5 nm using sputtering before mounting the sample for FESEM imaging.

2.4.5 Atomic force microscopy

The surface morphology and surface roughness of the films are studied using Atomic Force Microscopy (AFM). AFM is a high resolution surface scanning microscopy technique used to obtain morphological information from films surface. The "Oxford instruments Cypher S" atomic force microscope in non-contact mode is used to generate AFM images by moving a sharp tip mounted on a cantilever across the sample surface. Surface forces (such as van der Waals, electrostatic, and chemical forces) interact with the tip as it moves across the surface of the sample [21]. The cantilever deflection caused by these interactions is monitored using a focused laser beam and used to generate high-resolution topographic images of the sample surface. AFM can be operated in various modes, including non-contact and contact modes. The most often utilised mode is non-contact/tapping mode, in which the AFM tip makes intermittent contact with the sample surface. The "Oxford instruments Cypher S" AFM

microscope is used to obtain the topographic images for scanning area of 5µm × 5 µm in non-contact mode. WSxM software is used to analyse the obtained AFM data.

2.4.6 Ultra-Violet visible Spectroscopy

Ultra-Violet visible (UV-Vis) spectroscopy is a widely used analytical technique for measuring the absorbance, transmittance and reflectance of ultraviolet and visible light by molecules in a sample. UV-Vis spectroscopy is based on the principle that molecules absorb light in the ultraviolet and visible ranges which further causes excitation of electrons from the ground state to a higher energy state. The intensity of the transmitted light is reduced as a result of this absorption and the spectrophotometer records this reduction as transmittance/absorbance. In this thesis, "Perkin-Elmer Lambda 950" spectrometer is used to record the transmission spectra of MoO_{3-x} and ITO films deposited on CG substrates in the range of 200-850 nm. Transmission spectra of each sample is measured with the respect to air. The band gap is calculated using the Taucs' relation [22]:

$$\alpha h\nu^{\frac{1}{n}} = A\left(h\nu - E_g\right) \quad \text{---------- (2.6)}$$

where, α is the absorption coefficient (cm^{-1}), $h\nu$ is the energy of incident photons (eV), A is proportionality constant. The exponent value n are 2 for indirect and $\frac{1}{2}$ for direct band gap material, and α is given as:

$$\alpha = \frac{1}{d} \times \ln\left(\frac{1}{T}\right) \quad \text{---------- (2.7)}$$

where, d is thickness (cm) and T is transmittance.

The band gap of MoO_{3-x} films is calculated from the $\alpha h\nu^{1/n}$ vs. $h\nu$ plot in the strong absorption region, where n = 2.

Thickness of the ITO films is estimated by the Swanepoel's method [23] using equation 2.8

$$d = \frac{\lambda_1 \lambda_2}{2(\lambda_1 n_2 - \lambda_2 n_1)} \quad \text{---------- (2.8)}$$

where, n_1 and n_2 are the refractive indices at two adjacent maxima or minima corresponding to λ_1 and λ_2 in transmission spectra near transparent region respectively.

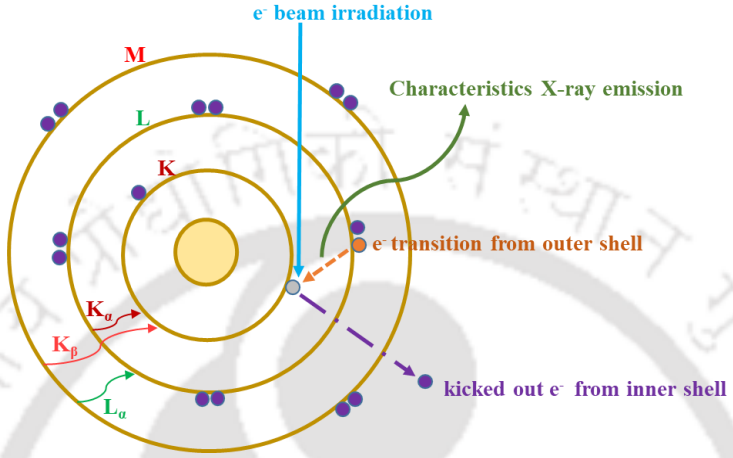

Figure 2.5: *Mechanism of Energy Dispersive X-ray spectroscopy.*

2.4.7 Energy dispersive X-ray spectroscopy

Energy Dispersive X-ray Spectroscopy (EDS) is a technique used to analyse the elemental composition of a sample in materials science. In EDS, presence of an element is identified by the energy of produced X-ray [24]. When electron beam strikes the specimen, it knocks out the electron (e^-) present in inner shells (lower energy shells) creating vacancy. The vacancy is filled by the electron placed in outer shells (high energy shells), while this displacement some amount of energy is released which produces characteristics X-rays. The released X-ray energy helps in the identification of an element. The transition of e^- from outer shell to particular inner shell is categorized by different series like K-series, L-series and M-series [24, 25]. The mechanism of EDS measurements is depicted in Figure 2.5. The energy supplied while EDS analysis has to be more than the energy required to remove electron from particular inner shell of an element. In EDS, energy of electron beam is controlled by the accelerating voltage [26]. In our case, 20 kV of accelerating voltage in SE2 mode is used for EDS analysis to detect the atomic

percent of Mo and Oxygen atoms present in the MoO_{3-x} films deposited on CG and c-Si (n) substrates.

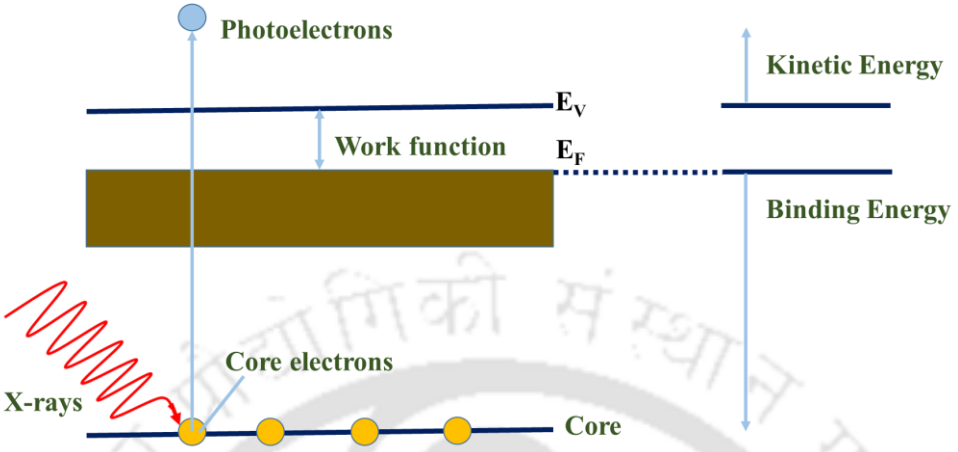

Figure 2.6: *Schematic diagram of working principle XPS.*

2.4.8 X-ray photoelectron spectroscopy

X-ray photoelectron spectroscopy (XPS) is an analytical technique for determining the elemental composition, chemical state, and electronic state of elements on the surface of a material. It is highly surface senistive technique and can extract information from 10 nm depth from surface of a sample. However, depth profiling can be done using sputtering of the top surface to gain more information about the variation of elemental composition from surface to bulk. In XPS, an X-ray beam is used to excite molecules on the surface of a sample, resulting in the release of photoelectrons. We can gain important elemental and chemical binding information about a material's surface by analysing the energy of these photoelectrons. Since XPS employs a low-energy electron beam with a photon energy of 200-2000 eV to generate a constant charge state at the surface, it can be used to examine the surface composition of non-conducting materials. The principle of XPS is depicted in Figure 2.6. The binding energy (*BE*) of core electron is given by the Einstein relation:

$$KE = h\nu - BE - \Phi_A \qquad \text{---------- (2.9)}$$

where, hv is the energy of incident X-ray, KE is the photoelectron kinetic energy and Φ_A is the work function of the spectrometer. Thus, kinetic energy is measured and the emitted atom can be identified from the collected characteristic electron energy spectra.

XPS are carried out using PHI 5000 Versa Probe III spectrometer (Make: M/s Physical electronics, USA). The excitation source of aluminium K-alpha (Al-K) radiation (1486.7 eV) is used for XPS measurements. XPS spectra of MoO_{3-x} films are collected at 0.125 eV step size, 25 eV pass energy, 45° electron emission angle and from 0.1×0.1 mm^2 area. Samples are not etched before measurement. Charge compensation is carried out using a turnkey twin beam charge neutralisation system. The method suggested by G. Greczynski et al. is applied for binding energy scale referencing [27, 28]. The corrected carbon 1s peak is determined using the relation, $E_B = 289.58\, eV - \Phi_{sample}$, where Φ_{sample} refers to the work function of samples. The base pressure is maintained at 10^{-9} mbar during each measurement. Peak fitting of respective element is done for the quantitative analysis. For XPS peak fitting, background subtraction is done using Shirley method and Gaussian/Lorentzian peak nature is used to get good fit. Peak area ratio of Mo $3d_{3/2}$ and $3d_{5/2}$ doublets are maintained to be in 2:3 ratios due to degeneracy of spin states [29]. All MoO_{3-x} films are stored in vacuum before and after XPS measurements as sample storage condition also affects the chemistry of materials [30].

2.4.9 Kelvin Probe Force Microscopy

Local work function (Φ) of thermally evaporated MoO_{3-x} films is studied using Kelvin Probe Force Microscopy (KPFM). The term local work function is used because the measurements are carried out in ambient conditions and any absorbents on surface can alter Φ. Using KPFM, contact potential difference (CPD) between sample and conducting tip is measured which is then used to find the work function of sample [31].

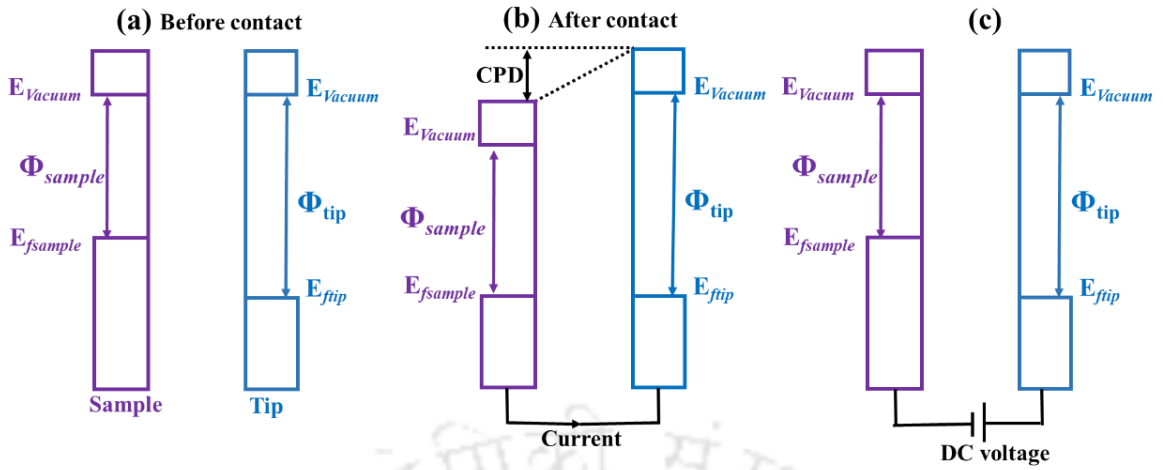

Figure 2.7: *Schematic diagram showing different energy levels of tip and sample for finding contact potential difference using KPFM.*

$$eCPD = \Phi_{tip} - \Phi_{sample} \quad \text{---------- (2.10)}$$

here, Φ_{tip} refers to the work function value of tip and Φ_{sample} represents work function value of sample and e is the electronic charge.

Φ of tip is calculated using highly oriented pyrolytic graphite (HOPG) work function (Φ_{HOPG}) in the equation 2.11. HOPG is often used as a reference because it is not sensitive to contamination and does not form dipoles.

$$\Phi_{tip} = \Phi_{HOPG} + eCPD \quad \text{---------- (2.11)}$$

Using equation (2.10) and (2.11), work function of a sample can be found using [32, 33] –

$$\Phi_{sample} = 4.6\ eV + CPD_{HOPG} - CPD_{sample} \quad \text{---------- (2.12)}$$

The schematic diagram displayed in Figure 2.7 explains the operating mechanism of KPFM. Figure 2.7a shows Fermi level (E_f) and work function of sample and tip with reference to vacuum energy level (E_{vacuum}) when there is no interaction between the sample and tip. When conducting tip is brought near sample, electron tunnelling can happen which requires the position of $E_{fsample}$ and E_{tip} to be at the same energy level to maintain equilibrium [31]. As there is an electrical contact between tip and sample, flow of electrons helps to attain the equilibrium

by aligning E_f. The Fermi energy level alignment causes shift in vacuum energy levels and thus a contact potential difference is generated, as shown in Figure 2.7b. CPD also produces an electrical force, which is nullified by providing external bias DC voltage equal and in opposite direction to CPD [32, 33]. Thus, the fermi energy level return to its initial position as shown in Figure 2.7c. Externally applied DC voltage is equal to CPD and is the difference between work function of sample and tip. The value of CPD is used in the equation 2.12 to find the work function of molybdenum oxide films. This measurement requires preparation of films on conducting substrates and as our objective focuses on fabrication of MoO_{3-x}/c-Si(n) solar cells, thin films of MoO_{3-x} are prepared on c-Si (n) substrate (275 - 325 µm, 1 - 10 Ωcm). In this thesis, Oxford Instruments, Cypher S microscope is used to find the work function of as deposited, oxygen plasma treated and heat treated MoO_{3-x} films.

2.4.10 Conductivity Measurements

In order to gain insight into electrical properties of molybdenum oxide films, conductivity measurements are performed. To carry out this measurement, silver electrodes are prepared in coplanar geometry. Silver electrodes are made on the top surface of MoO_{3-x} film deposited on corning 1737 glass substrates using conducting silver paste (purity 99.99%) and dried in vacuum before measurements. Electrode length and separation are 4 mm and 1 mm respectively. For supplying voltage and measuring current at room temperature and at different temperatures, Keithley source measure unit 2450 is used. All the measurements are done in vacuum. The conductivity (σ) of MoO_{3-x} are given by equation 2.13 [34, 35]:

$$\sigma = \frac{I \times t}{V \times l \times d} \qquad \text{---------- (2.13)}$$

here, d is the film thickness, V is the applied voltage between the silver electrodes of length l separated by the distance t and I is the measured current.

In order to perform temperature dependent conductivity measurements, MoO_{3-x} films are placed inside high vacuum chamber (10^{-5}-10^{-6} mbar) and heated from 30 °C up-to 100 °C under high vacuum. The temperature of MoO_{3-x} films is measured with the help of a platinum resistance thermometer (PT-100). The activation energy (E_a) is calculated from temperature dependent dark conductivity (σ_d) data using Arrhenius equation. The Arrhenius relation is given by equation 2.14 [34, 35]:

$$\sigma_d = \sigma_O \times \exp\left(\frac{-E_a}{k_B \times T}\right) \quad \text{---------- (2.14)}$$

Here, σ_o is the prefactor, k_B is the Boltzmann constant and T is the temperature in Kelvin.

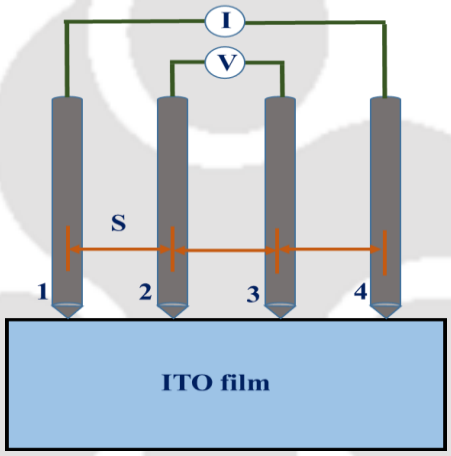

Figure 2.8: *Schematic diagram of four probe measurement.*

2.4.11 Four Probe Current Voltage Measurements

The sheet resistance of ITO films are measured using the four probe current voltage measurements. The schematic diagram of four probe measurement set up is shown in Figure 2.8. This measurement comprises four probes placed along a line, each with equal spacing between them. A current flows between the outer two probes (1 and 4), generating a voltage drop between the inner two probes (2 and 3). The sheet resistance can then be estimated by measuring the voltage change. The sheet resistance R_{sheet} is given by the equation 2.15 [36, 37]:

$$R_{sheet} = \frac{\rho}{t} \qquad \text{---------- (2.15)}$$

Here, ρ is the resistivity of film and *t* corresponds to the thickness of film.

The sheet resistance of ITO films on corning glass is measured using a four-point probe apparatus Ossila, T2001A.

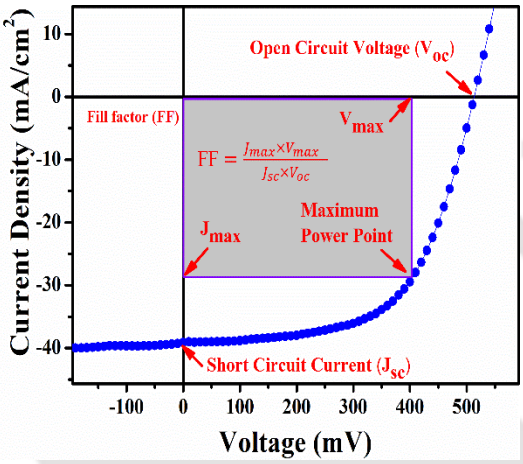

Figure 2.9: *J-V characteristics of a solar cell.*

2.5 Solar cell characterization

2.5.1 Current density and Voltage measurement

The performance of fabricated MoO_{3-x}/c-Si(n) silicon heterojunction solar cells is determined from Current density and Voltage (*J-V*) measurement. The *J-V* characteristics measurements of solar cells are performed using Sciencetech solar simulator with AM 1.5 condtions and 100 mW/cm^2 incident power density. To apply bias voltage and mesure the corresponding current from solar cell, Keithley 2450 source-measure unit has been used. Figure 2.9 shows the *J-V* characteristics of solar cell under illumination conditions. The short circuit current density (J_{sc}), open circuit voltage (V_{oc}), fill factor (*FF*) and efficiency (η) are determined from *J-V* characteristics. The solar cell efficiency (η) is defined as the ratio of maximum electrical energy

output to the incident photons on the cell. The η % is given by the following expression [38, 39]:

$$\eta\ (\%) = \frac{FF \times J_{sc} \times V_{oc}}{P_{in}} \quad \text{---------- (2.16)}$$

and, $$FF = \frac{I_{max} \times V_{max}}{I_{sc} \times V_{oc}} = \frac{P_{max}}{I_{sc} \times V_{oc}} \quad \text{---------- (2.17)}$$

where, J_{sc}, V_{oc}, *FF and* P_{in} are current density, open circuit voltage, fill factor and incident power respectively.

J_{sc} is the current density at which the voltage across the solar cell is zero. The V_{oc} is the maximum voltage at which no current flows through the external circuit (i.e. J_{sc} = 0). FF represents the squareness of *J-V* curve and describes the operating point at which solar cell delivers maximum power to the attached load. In a solar, cell series (R_s) and shunt resistance (R_{sh}) are two important factors which significantly affect the performance of a solar cell and can be obtained from the *J-V* characteristic curve using the following expressions [40, 41]:

$$\frac{1}{R_s} = \left\{\frac{dJ}{dV}\right\}_{J=0} \quad \text{---------- (2.18)}$$

$$\frac{1}{R_{sh}} = \left\{\frac{dJ}{dV}\right\}_{V=0} \quad \text{---------- (2.19)}$$

2.6 Details of simulation studies on MoO_{3-x}/c-Si (n) solar cells using AFORS-HET software

AFORS-HET simulation software is used to perform the simulation studies for MoO_{3-x}/c-Si (n) heterojunction solar cells. This software is widely used for the theoretical studies on performance of silicon heterojunction solar cells [42-44]. It uses one-dimensional Poisson and two carrier continuity equations to perform the numerical studies about cell performance [43].

The standard illumination condition air mass 1.5 (AM 1.5), 300 K with power density of 100 mW/cm^2 is used for analysis. The device structure used for the simulation study is *Ag/ITO/MoO_{3-x}/c-Si (n)/Ag*. We employed MoO_{3-x} as the hole transport layer and altered its work function from 4.7 eV to 5.2 eV to investigate its effect on the *J-V* characteristics of simulated solar cells. A thin silicon oxide (SiO_x) layer is inserted between the MoO_{3-x} and c-Si (n), to study its impact on the performance of MoO_{3-x}/c-Si(n).

2.7 References

[1] M. Nayak, S. Mudgal, S. Mandal, S. Singh, V.K. Komarala, Electrical characterization and defect states analysis of Ag/ITO/MoO_x/n-Si/LiF_x/Al carrier selective contact solar cells processed at room-temperature, 15th International Conference on Concentrator Photovoltaic Systems (CPV-15), (2019).

[2] I.A. de Castro, R.S. Datta, J.Z. Ou, A. Castellanos-Gomez, S. Sriram, T. Daeneke, K. Kalantar-Zadeh, Molybdenum Oxides - From Fundamentals to Functionality, Adv Mater, 29 (2017) 1701619.

[3] N. Lopez-Pinto, T. Tom, J. Bertomeu, J.M. Asensi, E. Ros, P. Ortega, C. Voz, Deposition and characterisation of sputtered molybdenum oxide thin films with hydrogen atmosphere, Applied Surface Science, 563 (2021) 150285.

[4] J. Kumari, P. Agarwal, Optimization of deposition conditions to tune optoelectronic properties of MoO_{3-x} films prepared by RF-sputtering technique, Vacuum, 216 (2023) 112485.

[5] M.F. Al-Kuhaili, S.M.A. Durrani, I.A. Bakhtiari, Pulsed laser deposition of molybdenum oxide thin films, Applied Physics A, 98 (2009) 609-615.

[6] A.S. Etman, Aqueous exfoliation of Transition Metal Oxides for Energy Storage and Photocatalysis Applications, Thesis, (2019).

[7] G.R. Mutta, S.R. Popuri, J.I.B. Wilson, N.S. Bennett, Sol-gel spin coated well adhered

MoO_3 thin films as an alternative counter electrode for dye sensitized solar cells, Solid State Sciences, 61 (2016) 84-88.

[8] N. Zhao, H. Fan, M. Zhang, J. Ma, Z. Du, B. Yan, H. Li, X. Jiang, Simple electrodeposition of MoO_3 film on carbon cloth for high-performance aqueous symmetric supercapacitors, Chemical Engineering Journal, 390 (2020) 124477.

[9] M. Ohring, Chapter 4 - Discharges, Plasmas, and Ion–Surface Interactions, in: M. Ohring (Ed.) Materials Science of Thin Films (Second Edition), Academic Press, San Diego, 2002, pp. 145-202.

[10] A. Bashir, T.I. Awan, A. Tehseen, M.B. Tahir, M. Ijaz, Chapter 3 - Interfaces and surfaces, in: T.I. Awan, A. Bashir, A. Tehseen (Eds.) Chemistry of Nanomaterials, Elsevier 2020, pp. 51-87.

[11] M. Ohring, Chapter 3 - Thin-Film Evaporation Processes, in: M. Ohring (Ed.) Materials Science of Thin Films (Second Edition), Academic Press, San Diego, 2002, pp. 95-144.

[12] Kern W and Puotinen D. A, Cleaning solutions based on hydrogen peroxide for use in silicon semiconductor technology RCA Rev., 31 (1970) 187-206.

[13] W. Kern, The Evolution of Silicon Wafer Cleaning Technology, Journal of The Electrochemical Society, 137 (1990) 1887 -1891.

[14] F.W.K. Mitsushi Itano, Jr., Masayuki Miyashita and Tadahiro Ohmi, Particle Removal from Silicon Wafer Surface in Wet Cleaning Process, IEEE Transactions on Semiconductor Manufacturing, 6 (1993) 258-267.

[15] M. Diskus, O. Nilsen, H. Fjellvag, S. Diplas, P. Beato, C. Harvey, E. van Schrojenstein Lantman, B.M. Weckhuysen, Combination of characterization techniques for atomic layer deposition MoO_3 coatings: From the amorphous to the orthorhombic α-MoO_3 crystalline phase, Journal of Vacuum Science & Technology A, 30 (1) (2012) 01A107.

[16] D. Liu, W.W. Lei, J. Hao, D.D. Liu, B.B. Liu, X. Wang, X.H. Chen, Q.L. Cui, G.T. Zou,

J. Liu, S. Jiang, High-pressure Raman scattering and x-ray diffraction of phase transitions in MoO_3, Journal of Applied Physics, 105 (2009) 0235513.

[17] M. Dieterle, G. Mestl, Raman spectroscopy of molybdenum oxides, Physical Chemistry Chemical Physics, 4 (2002) 822-826.

[18] G.K.W.a.W.H. Hall, X-ray line broadening from filed Aluminium and Wolfram, Acta Metallurgica 1(1953) 22-31.

[19] B.E. Warren, X-ray Diffraction. Dover, New York, 253 (1990).

[20] A. Mayeen, L.K. Shaji, A. K. Nair, N. Kalarikkal, Chapter 12 - Morphological Characterization of Nanomaterials, Characterization of Nanomaterials, Elsevier (2018), 335-364.

[21] S. Gowri, T. Umasankareswari, R. Joseph Rathish, S. Santhana Prabha, S. Rajendran, A. Al-Hashem, G. Singh, C. Verma, Chapter 8 - Atomic force microscopy technique for corrosion measurement, in: J. Aslam, C. Verma, C. Mustansar Hussain (Eds.) Electrochemical and Analytical Techniques for Sustainable Corrosion Monitoring, Elsevier (2023) 121-140.

[22] J.L. Ye Zhao, Ya Zhou, Zhengjun Zhang, Yonghua Xu, H Naramoto, S Yamamoto, Preparation of MoO_3 nanostructures and their optical properties, J. Phys.: Condens. Matter 15 (2003) L547–L552.

[23] R. Swanepoel, Determination of the thickness and optical constants of amorphous silicon, Journal of Physics E: Scientific Instruments, 16 (1983) 1214.

[24] DeenaTitus, E. J. J. Samuel, S. M. Roopan, Chapter 12 - Nanoparticle characterization techniques, Green Synthesis, Characterization and Applications of Nanoparticles, Micro and Nano Technologies, Elsevier (2019) 303-319.

[25] George N. Dolenko, Oleg KhPoleshchuk and Jolanta N. Latosinska, Encyclopedia of Spectroscopy and Spectrometry (Third Edition), (2017) 691-694.

[26] Y. Hua, Estimating Method for Electron Beam Accelerating Voltage Used in Energy

Dispersive X Ray Microanalysis Application in Failure Analysis of Wafer Fabrication, Instrumentation Science & Technology, 32 (2004) 115–126.

[27] G. Greczynski, L. Hultman, C1sPeak of Adventitious Carbon Aligns to the Vacuum Level:Dire Consequences for Material's Bonding Assignment by Photoelectron Spectroscopy, ChemPhysChem 18 (2017) 1507 –1512.

[28] G. Greczynski, L. Hultman, X-ray photoelectron spectroscopy: Towards reliable binding energy referencing, Progress in Materials Science 107 (2020) 100591.

[29] M. Ponce-Mosso, M. Perez-Gonzalez, P.E. Garcia-Tinoco, H. Crotte-Ledesma, M. Morales-Luna, S.A. Tomas, Enhanced photocatalytic activity of amorphous MoO_3 thin films deposited by rf reactive magnetron sputtering, Catalysis Today, 349 (2020) 150-158.

[30] G. Greczynski, L. Hultman, Impact of sample storage type on adventitious carbon and native oxide growth: X-ray photoelectron spectroscopy study, Vacuum, 205 (2022) 111463.

[31] W. Melitz, J. Shen, A.C. Kummel, S. Lee, Kelvin probe force microscopy and its application, Surface Science Reports, 66 (2011) 1-27.

[32] P. Maiti, P. Guha, R. Singh, J.K. Dash, P.V. Satyam, Optical band gap, local work function and field emission properties of MBE grown β-MoO_3 nanoribbons, Applied Surface Science, 476 (2019) 691-700.

[33] D.A. Kowalczyk, M. Rogala, K. Szalowski, D. Belic, P. Dabrowski, P. Krukowski, I. Lutsyk, M. Piskorski, A. Nadolska, P. Krempinski, M. Le Ster, P.J. Kowalczyk, Two-Dimensional Crystals as a Buffer Layer for High Work Function Applications: The Case of Monolayer MoO_3, ACS applied materials & interfaces, 14 (2022) 44506-44515.

[34] M. Balaji, J. Chandrasekaran, M. Raja, Role of substrate temperature on MoO_3 thin films by the JNS pyrolysis technique for P–N junction diode application, Materials Science in Semiconductor Processing, 43 (2016) 104-113.

[35] A. Boukhachem, C. Bouzidi, R. Boughalmi, R. Ouerteni, M. Kahlaoui, B. Ouni, H.

Elhouichet, M. Amlouk, Physical investigations on MoO_3 sprayed thin film for selective sensitivity applications, Ceramics International, 40 (2014) 13427-13435.

[36] M. Naftaly, S. Das, J. Gallop, K. Pan, F. Alkhalil, D. Kariyapperuma, S. Constant, C. Ramsdale, L. Hao, Sheet Resistance Measurements of Conductive Thin Films: A Comparison of Techniques, Electronics, 10 (8) (2021) 960.

[37] l.D. Michal Mazur, Danuta KaczmarekI, Sarfaraz Moh and Frank Placido, Sheet resistance and optical properties of ITO thin films deposited by magnetron sputtering with different O_2/ Ar flow ratio, 2010 International Students and Young Scientists Workshop "Photonics and Microsystems, (2010) 60-63.

[38] T. Markvart, L. CastaÑer, IIa-1 - Principles of Solar Cell Operation, in: T. Markvart, L. Castaner (Eds.) Practical Handbook of Photovoltaics, Elsevier Science, Amsterdam, (2003) 71-93.

[39] E.A. Fagen, Solar cell device physics: Stephen J. Fonash. Academic Press, New York (1981), Materials Research Bulletin, 17 (1982) 1349-1350.

[40] W. Zeng, K.S. Yong, Z.M. Kam, Z.-k. Chen, Y. Li, Effect of MoO_3 as an interlayer on the performance of organic solar cells based on ZnPc and C60, Synthetic Metals, 161 (2012) 2748-2752.

[41] J. Cho, N. Nawal, A. Hadipour, M. Recaman Payo, A. van der Heide, H.S. Radhakrishnan, M. Debucquoy, I. Gordon, J. Szlufcik, J. Poortmans, Interface analysis and intrinsic thermal stability of MoO_x based hole-selective contacts for silicon heterojunction solar cells, Solar Energy Materials and Solar Cells, 201 (2019) 110074.

[42] V. Kanneboina, The simulated performance of c-Si/a-Si:H heterojunction solar cells with nc-Si:H, µc-Si:H, a-SiC:H, and a-SiGe:H emitter layers, Journal of Computational Electronics, 20 (2020) 344-352.

[43] R.S. A. Froitzheim, L. Elmer, M. Kriegel, W. Fuhs, AFORS-HET: A Computer-program

for the simulation of heterojunction solar cells to be distributed for public use, 3rd World Conference on Photovolfaic Energv Conversion May 11-18.2003 Osaka. Japan, (2003) 279-282.

[44] H. Deka, A.K. Sunaniya, P. Agarwal, Simulation studies on MoS_2(n)/a-Si:H(i)/c-Si (p)/MoO_3 heterojunction solar cells using one sided short diode approximation, Solar Energy, 263 (2023) 111943.

CHAPTER 3

Optimization of deposition conditions to tune optoelectronic properties of MoO_{3-x} films prepared by rf-sputtering technique

As molybdenum oxide (MoO_{3-x}) find its wide use in electronics, catalysis, chemical and gas sensing, optoelectronic properties of this material need to be tuned accordingly. Rf-sputtering provides wide prospects to tune optical, electrical and structural properties of TMOs by changing the deposition parameters like substrate temperature, process pressure, rf-power and gaseous atmosphere. Thus, optimisation of deposition parameters are necessary to obtain required optoelectronics properties. In this chapter, rf-sputtering technique is used to prepare MoO_{3-x} films and optoelectronic properties are tuned by optimising deposition conditions. For this, three series of samples are prepared by varying the deposition parameters; rf power (60 W to 80 W), substrate temperature (100 °C to 400 °C) and gaseous atmosphere (Argon gas and Argon + Oxygen gases) during the deposition of MoO_{3-x} films. The optical and electrical properties are studied using UV-Vis spectroscopy and conductivity measurements. X-ray photoelectron spectroscopy (XPS) and Energy dispersive X-ray spectroscopy (EDS) analysis are also carried out to know how different deposition parameters affect the composition of

MoO_{3-x} films. The optimised deposition parameters have led to formation of (a) highly conducting MoO_{3-x} films which are suitable for catalysis application and (b) films having higher transparency, wide band gap and low conductivity suitable for application in solar cell.

3.1 Experimental details

Molybdenum oxide (MoO_{3-x}) thin films were deposited on corning glass 1737 substrate by radio frequency (rf) sputtering technique. MoO_3 target having 99.99% purity, 2-inch diameter and 0.25-inch thickness was used for preparing thin films. Before inserting the substrates inside the vacuum chamber, these were cleaned using the standard procedures described in Chapter 2, section 2.2. The cleaned substrates were loaded in the chamber and pumped up to the base pressure of 5.5×10^{-5} mbar prior to each film preparation. The structural, optical and electrical properties were tuned by changing the deposition parameters like rf-power, gas flow rate, substrate temperature, gaseous environment etc. Three series of films were deposited by varying one parameter at a time as presented in following section. For each series, substrate to target distance was kept constant at 5 cm.

Series 1

For this series of films, rf power was varied while keeping other parameters constant. The detailed deposition conditions are listed in Table 3.1.

Table 3.1: *Deposition parameters for MoO_{3-x} films deposited at different rf power.*

Fixed Deposition parameters	rf power (W) (Variable)
Deposition time = 30 minutes Substrate temperature = 100 °C Argon flow rate = 7 SCCM Process pressure = 1.8×10^{-2} mbar	60 70 80

Series 2

In this series, MoO_{3-x} films were deposited at different substrate temperature (T_s) (100 °C, 200

°C, 300 °C and 400 °C) and other parameters were kept constant as mentioned in Table 3.2.

Table 3.2: *Deposition parameters for MoO_{3-x} films deposited at different substrate temperature.*

Fixed Deposition parameters	Substrate temperature (°C) (Variable)
Deposition time = 30 minutes RF power = 80W Argon flow rate = 10 SCCM Process pressure = 9.6×10^{-3} mbar	100 200 300 400

Series 3

In this series, we had studied the influence of different gaseous environment during deposition of MoO_{3-x} films. Thin films of MoO_{3-x} were deposited in presence of argon (Ar) gas, argon+ oxygen ($Ar + O_2$) gases and oxygen (O_2) gas only. Deposition parameters used for preparing thin films of MoO_{3-x} are mentioned in Table 3.3.

Table 3.3: *Deposition parameters for MoO_{3-x} films prepared under different gaseous environment.*

Fixed Deposition parameters	Gases used	Flow rate (SCCM) (Variable)
Substrate temperature – 400 °C Process pressure- 9.5×10^{-3} mbar RF - 80 W Deposition time - 30 minutes	O_2 $Ar+O_2$ Ar	10 10 (Ar) +1.2 (O_2) 10

3.2 Results and discussion

3.2.1 Properties of MoO_{3-x} films prepared at different rf-powers (Series 1)

3.2.1.1 XRD studies

XRD patterns of MoO_{3-x} films prepared at different rf powers are shown in Figure 3.1 (a). Peak at $2\theta = 25.37°$ corresponds to (040) plane of α-MoO_3. The broad XRD peak indicates that MoO_{3-x} films are mostly amorphous in nature, which is attributed to the fact that crystallization of molybdenum oxide is not initiated on the glass substrates even at high power density of 3.8 W/cm^2 corresponding to 80 W [7]. Though, the peak broadening may also be due to underlying amorphous glass substrate as film thickness is less, however the broad peak due to bare

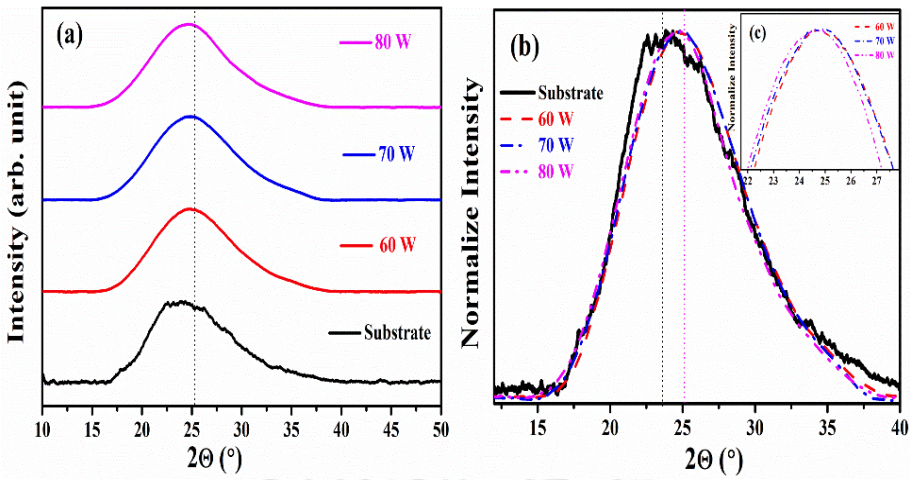

Figure 3.1: *(a) XRD patterns and (b) normalized XRD patterns of CG substrate and MoO_{3-x} films deposited at different rf powers.*

substrate is slightly shifted towards low 2θ value (Figure 3.1a). Normalised XRD (normalized with respect to maximum intensity) patterns and its zoomed view is shown in Figure 3.1b and inset graph 3.1c respectively. A small shift in 2θ value towards smaller angle is observed when rf-power is increased. Shift in the peak position towards lower 2θ value represents the elongation of interlayer distance of α-MoO_3 because of the formation of oxygen vacancy [8, 9]. The observed shift in 2θ value, though very small with increasing rf power could be an indication of increase in oxygen vacancies in these films.

3.2.1.2 Raman spectroscopy

Figure 3.2 shows the Raman spectra of corning glass substrate and MoO_{3-x} films deposited at different rf powers. Raman spectra is deconvoluted (Figure 3.2b) to identify different Mo-O modes present in the film. Raman peaks corresponding to Mo-O bending mode (200-600 cm^{-1}) and Mo-O stretching mode (600-1000 cm^{-1}) are observed. Raman peaks present at 239 cm^{-1} and 338 cm^{-1} are assigned to deformation modes (OMo_2) and (OMo_3) respectively and peaks at 422 cm^{-1} and 750 cm^{-1} represent the formation of sub-stoichiometric molybdenum oxide (MoO_{3-x}) [9-15]. Raman peak at 422 cm^{-1} for 60 W and 70 W films has shifted to a lower value (397 cm^{-1}) for 80 W films, indicating the formation of the MoO_2 phase at higher rf power [16].

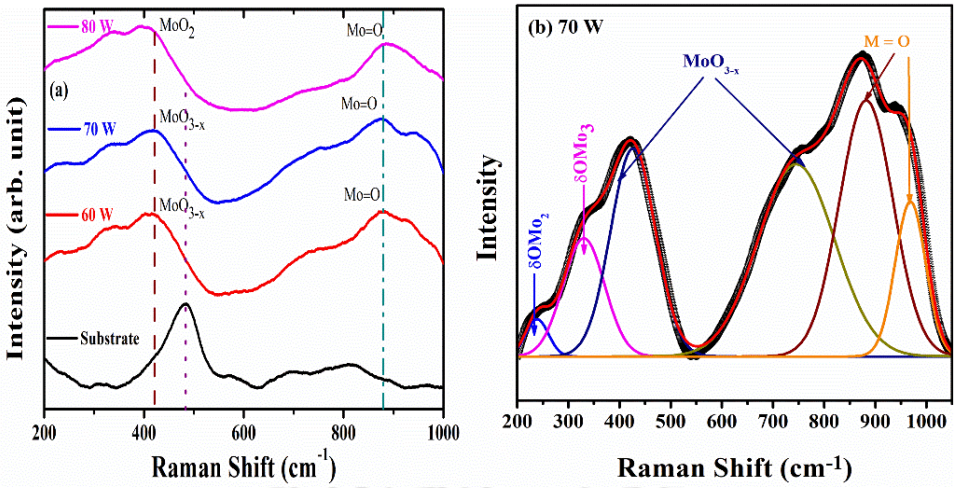

Figure 3.2: *(a) Raman spectra of corning substrate and MoO_{3-x} films deposited at different rf powers and (b) deconvoluted Raman spectra of 70 W films.*

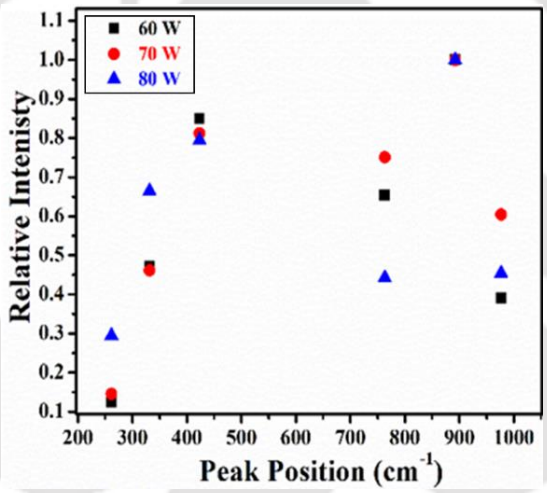

Figure 3.3: *Relative intensity of Raman peaks at different rf powers.*

Relative intensity of peak ($\frac{I_{peak}}{I_{880\ cm^{-1}}}$) is calculated by dividing the respective peak intensity by intensity of peak at 880 cm^{-1} corresponding to stretching mode (Mo=O). The relative intensity(Figure 3.3) of peaks at 239 cm^{-1} and 338 cm^{-1} (MoO_2 phase) has increased with increasing rf power, whereas the relative intensity of peaks at 422 cm^{-1} and 750 cm^{-1} (MoO_{3-x} phase) has decreased, indicating that at higher rf power, the formation of oxygen deficient MoO_2 phase has increased [17]. The broad Raman peaks are due to amorphous nature of sputtered MoO_{3-x} films.

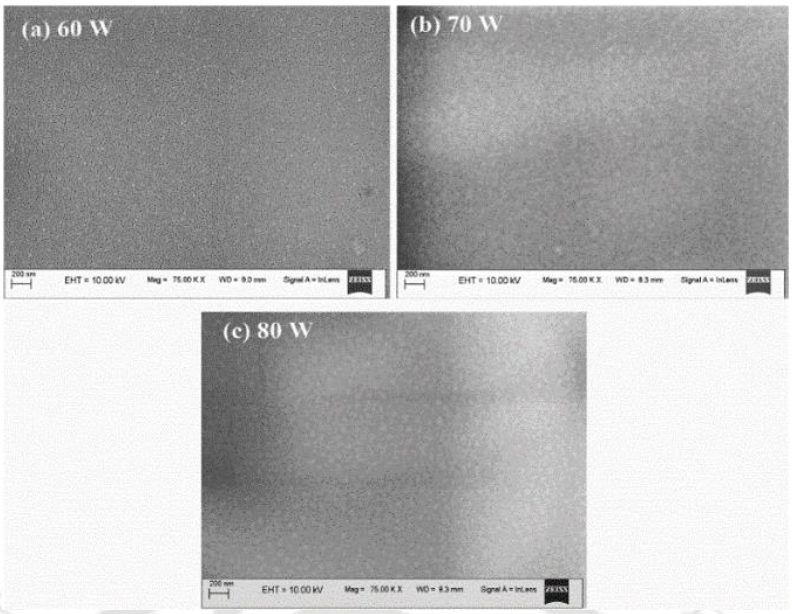

Figure 3.4: *FESEM images of MoO_{3-x} films deposited at (a) 60 W, (b) 70 W and (c) 80 W rf power.*

Table 3.4: *Atomic percent of oxygen and molybdenum (Mo) atoms in MoO_{3-x} films deposited at different rf powers.*

RF power	Oxygen (%)	Molybdenum (%)	Silicon (%)	Aluminium (%)
60	69.6	7.3	17.0	6.2
70	71.1	9.6	14.5	4.8
80	68.7	11.2	15.8	4.3
Corning	70.4		22.3	7.3

3.2.1.3 FESEM and EDS studies

FESEM images of molybdenum oxide films deposited at different rf power are shown in Figure 3.4. Uniform distribution of grains and void free surface are observed for all MoO_{3-x} films. Both XRD and Raman data suggest qualitative decrease in oxygen concentration with increase in rf power. To further confirm, the change in oxygen concentration, EDS measurements are done on these films. As MoO_{3-x} film thickness is relatively low, presence of silicon (Si) and aluminium (Al) from CG substrate are also observed. A part of total oxygen observed is thus also from the substrate. Table 3.4 shows oxygen and molybdenum atoms concentration acquired from EDS data. Mo atoms concentration has increased in MoO_{3-x} films as rf power increased however not much change in oxygen concentration is noticed indicating the formation of oxygen deficient MoO_{3-x} films at high rf power.

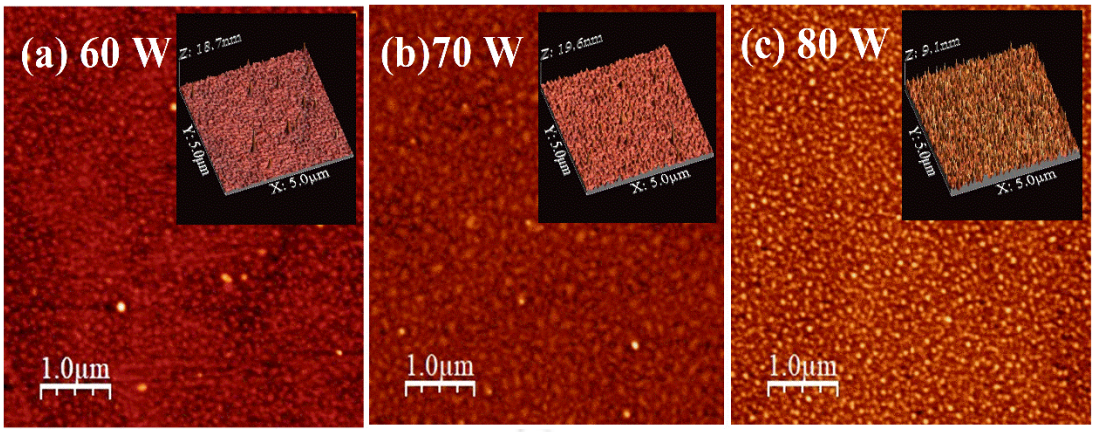

Figure 3.5: *AFM images of MoO_{3-x} films deposited at different rf powers.*

3.2.1.4 AFM studies

Surface topology of films deposited at 60 W, 70 W and 80 W is studied using atomic force microscopy (AFM). AFM 2D and 3D images are shown in figure 3.5. No noteworthy change in growth pattern and surface roughness of MoO_{3-x} films are observed for rf variation series.

3.2.1.5 UV-Vis studies

UV-Vis-NIR transmission spectra of MoO_{3-x} films deposited at different RF power is shown in Figure 3.6a. A red shift in the absorption edge is witnessed at higher rf power, which is attributed to formation of sub-stoichiometric MoO_{3-x} films. The reason of red shift is also associated to creation of oxygen anion vacancies [18]. The optical band gap of films has decreased from 3.12 eV to 2.94 eV with increase of rf power from 60 W to 80 W. The obtained band gap values are within the range reported in literature [19, 20]. Thickness of MoO_{3-x} films are measured with stylus profilometer. Variation of band gap and thickness for all samples are presented in Figure 3.6b. An increase in deposition rate from 2.5 nm/min at 60 W to 4.1 nm/min at 80 W is observed [21]. Maximum transmission of MoO_{3-x} films has dropped from 70% for 60 W to 30% for 80 W. The decrease in transmittance is due to increase in thickness as well as shift of absorption edge towards higher wavelength. Change in electrical conductivity can also

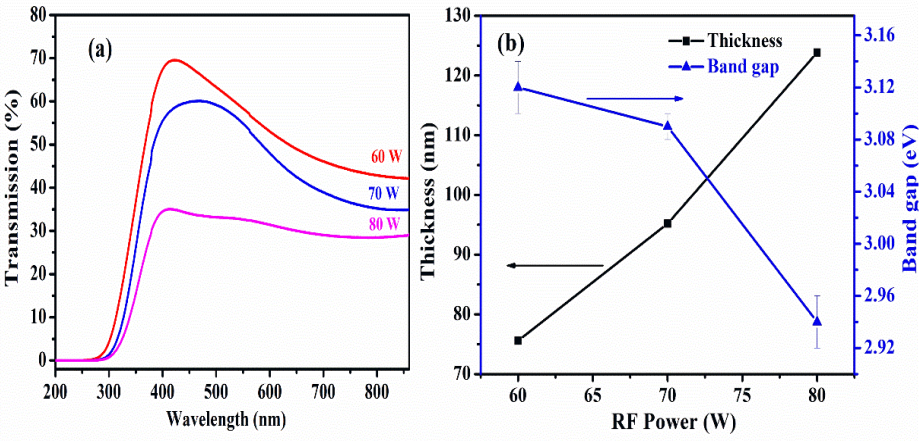

Figure 3.6: *(a) Transmission spectra, (b) band gap and thickness of MoO_{3-x} films deposited at different rf powers.*

Table 3.5: *Thickness, band gap, dark conductivity and activation energy of MoO_{3-x} films deposited at different rf powers.*

RF power	Thickness (nm)	Band gap (eV)	Dark Conductivity at RT ($\Omega^{-1}cm^{-1}$)	Activation Energy (E_a) eV
60	75	3.12±0.01	1.01×10^{-7}	0.548±0.030
70	95	3.09±0.01	7.19×10^{-4}	0.242±0.009
80	124	2.94±0.02	15.18	*0.026±0.001

**Note: This value is closer to the thermal voltage i.e. kT/q at room temperature.*

be a cause of decreased transmission. Also, change in colour of MoO_{3-x} films from light blue to deep blue is observed when rf-power is varied from 60 W to 80 W, which indicates a change in oxidation state of Mo atoms from Mo^{+6} to Mo^{+5} [18, 19].

3.2.1.6 Electrical properties

Room temperature (RT) and temperature dependent conductivity (σ) of prepared films are shown in Figure 3.7. An increment by 3-4 orders of magnitude (10^{-7} $\Omega^{-1}cm^{-1}$ for 60 W, 10^{-4} $\Omega^{-1}cm^{-1}$ for 70 W and 15 $\Omega^{-1}cm^{-1}$ for 80 W) in room temperature dark conductivity $\sigma_d(RT)$ is noticed every time the rf- power is increased by 10 W. Since conductivity of metal oxides are prominently influenced by presence of oxygen vacancies [22], the enhancement in $\sigma_d(RT)$ is allied to increase in oxygen vacancies at higher rf power, which is in line with both EDS and UV-Vis analysis. No photosensitivity is observed for these films under halogen lamp due to wide band gap (3.12 eV - 2.94 eV) of MoO_{3-x} films and poor photon flux in this range.

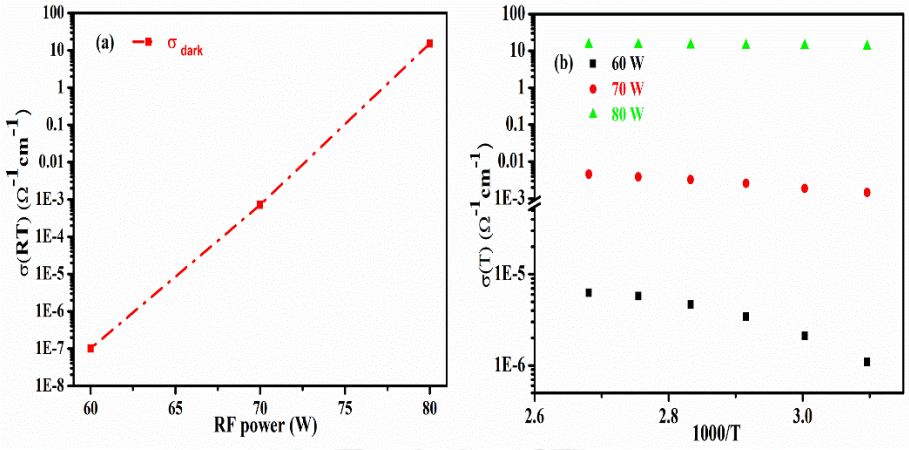

Figure 3.7: *(a) Room temperature dark conductivity and (b) Temperature dependent conductivity of MoO_{3-x} films at rf power 60 W, 70 W and 80 W.*

Temperature dependent conductivity $\sigma_d(T)$ measurements are performed on molybdenum oxide films in coplanar geometry. For rf power of 60 W, conductivity increases with temperature whereas $\sigma_d(T)$ remains almost constant for 70 W and 80 W films, which have higher conductivity. The Arrhenius equation as described in Chapter 2, section 2.4.10, is used for calculating the activation energy (E_a), which is a measure of energy difference between donor/trap level and conduction band edge [23]. E_a value has decreased from 0.548 eV to 0.026 eV as the rf power increased from 60 W to 80 W. Activation energy of 0.026 eV ($\sim kT/q$) suggests that donor state level almost overlapped with conduction energy band and charge carriers are present in thermal equilibrium with conduction band for 80 W films. The oxygen vacancies act as n-type doping in transition metal oxides [24] and shift the defect energy level closer to the conduction band because of the increase in electrons concentration. Thus, decrease in activation energy, further confirms the increase in oxygen vacancies in the films deposited at high rf power. E_a of all MoO_{3-x} films are listed in Table 3.5.

3.2.1.7 XPS studies

XPS survey spectra of MoO_{3-x} films prepared at different rf power is shown in Figure 3.8a. Characteristics peaks corresponding to Mo 3s (508.24 eV), Mo 3p (doublet) (415.48 eV for

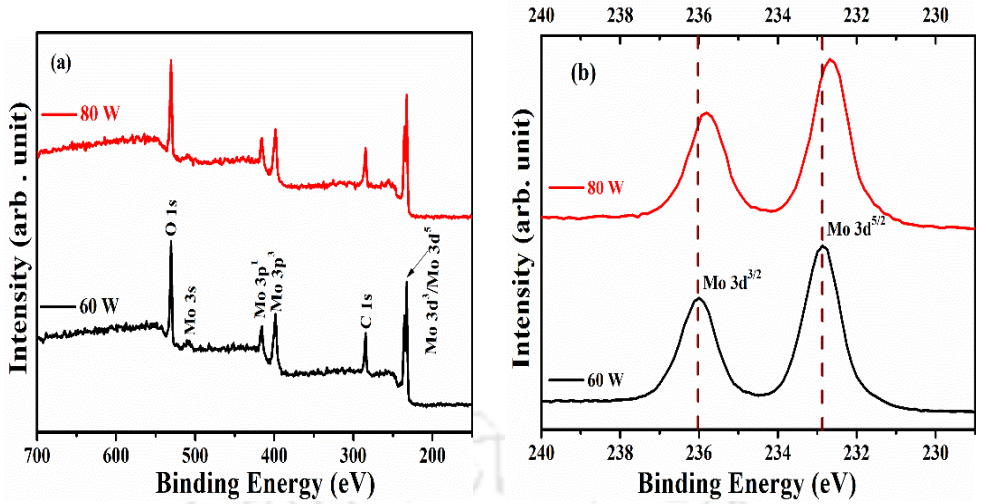

Figure 3.8: *(a) Survey spectra and (b) High resolution XPS spectra of MoO_{3-x} films at rf power 60 W and 80 W.*

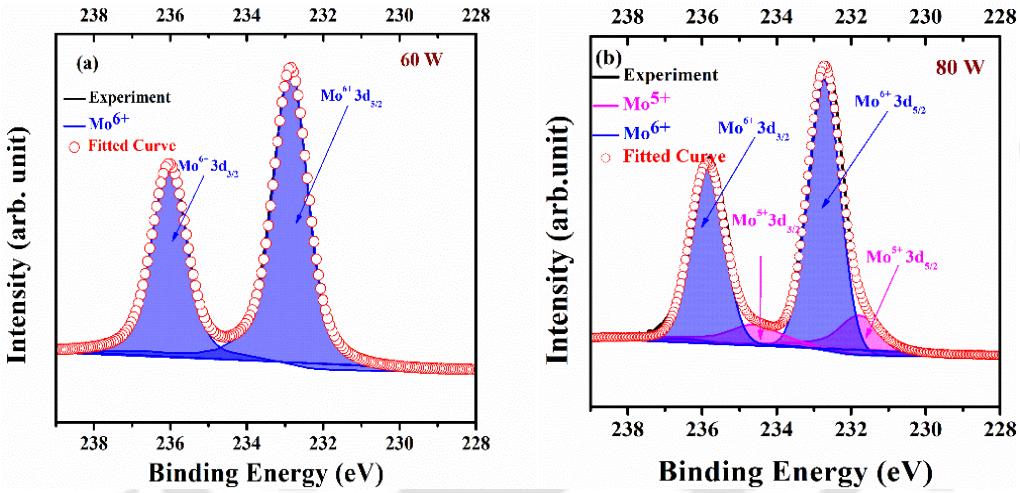

Figure 3.9: *Deconvoluted XPS spectra of MoO_{3-x} films prepared at (a) 60 W and (b) 80 W respectively.*

$3p_{1/2}$, 398.49 eV for $3p_{3/2}$) and Mo 3d (doublet) (235.95 eV for $3d_{3/2}$, 232.85 eV for $3d_{5/2}$) are observed [25-27]. In addition, peak corresponding to O 1s and C 1s are also observed at 530.72 eV and 284.83 eV respectively. C 1s peak is due to surface exposure of MoO_{3-x} films to ambient environment while loading it to XPS chamber. Small shift (~0.15 eV) towards lower binding energy (BE) in Figure 3.8b also suggest the presence of Mo atoms in lower oxidation state for 80 W MoO_{3-x} films [28]. For quantitative studies, Mo 3d and O1s XPS peaks are deconvoluted. The fitting details used for deconvolution are described in Chapter 2, sections 2.4.8 [23-25]. The deconvoluted spectrum in Figure 3.9b shows an additional peak corresponding to Mo^{5+}

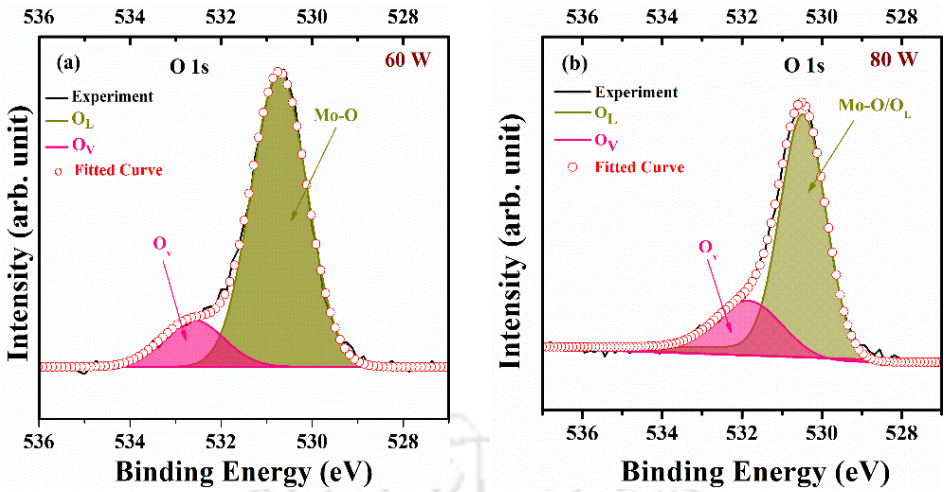

Figure 3.10: *O 1s XPS spectra for (a) 60 W and (b) 80 W MoO_{3-x} films respectively.*

state along with Mo^{6+} state for 80 W film further confirming that high rf power has increased percent of non-stoichiometric MoO_{3-x} inside prepared films [29, 30]. The relation between binding energy of oxygen and molybdenum atoms ($\Delta = O\ 1s - Mo\ 3d_{5/2}$) is used for finding the dominant oxidation state [31, 32]. The doublet separation of 3.10 eV and $\Delta = 297.87\ eV$ confirms dominancy of Mo^{6+} for all MoO_{3-x} films [33]. The amount of Mo atoms contributing to its Mo^{5+} oxidation is obtained by area ratio (Area of Mo^{5+}/(Area of Mo^{5+} + Area of Mo^{6+})) [34]. Among both Mo^{6+} and Mo^{5+}, about 20% of molybdenum atoms are found to be in Mo^{5+} state. Deconvoluted O 1s spectra of 60 W and 80 W MoO_{3-x} films are shown in Figure 3.10. O 1s peak at ~530.72 eV corresponds to molybdenum-oxygen (Mo-O) bond in MoO_{3-x} termed as lattice oxygen (O_L) and peak located at ~532 eV refers to oxygen vacancies (O_v) or molybdenum sub oxides bond [35]. Oxygen vacancies are observed for both 60 W and 80 W films but contribution from O_v peak is more for 80 W films. Only 15% contribution is observed from O_v for films prepared at low rf power whereas it has increased to 22% for 80 W films. Reduction in band gap, colouration of MoO_{3-x} films and enhanced conductivity of 80 W films are due to the presence of molybdenum atoms in two different oxidation states; Mo^{6+} and Mo^{5+} and more oxygen vacancies in these films compared to 60 W films. Similar observations are reported by M.P.Mosso et. al for MoO_{3-x} films deposited at 80 W and 10×10^{-3} mbar pressure

[31].

For this series, we have observed that change in rf power from 60 W to 80 W has reduced the band gap from 3.12 eV to 2.94 eV. Increase in conductivity of MoO_{3-x} films by several orders of magnitude along with decrease in activation energy is also observed for films deposited at high RF power. Thus, films deposited at high RF power (80 W) have low band gap and high conductivity. The high rf power is used for preparing MoO_{3-x} films for the next study.

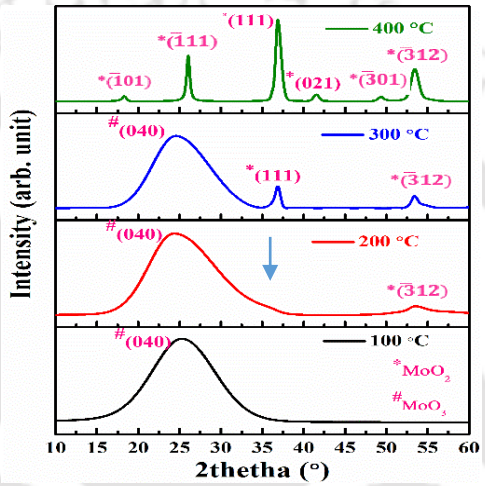

Figure 3.11: *XRD patterns of MoO_{3-x} films deposited at different substrate temperatures.*

3.2.2 Properties of MoO_{3-x} films deposited at different substrate temperatures (Series 2)

3.2.2.1 XRD studies

In this study, the substrate temperature is varied from 100 ℃ to 400 ℃ with increment of 100 ℃ at 80 W rf power. Deposition conditions are mentioned in Table 3.2. From XRD patterns shown in Figure 3.11, it is noticed that MoO_{3-x} films deposited at 100 ℃ have a broad peak at 2θ = 25.27° corresponding to (040) plane for MoO_3 (α-phase). XRD peak obtained at 2θ = 25.27°, shows little shift towards lower angle for T_s = 200 ℃ and T_s = 300 ℃ because of presence of oxygen anion vacancies in these samples [36]. Small humps at 36.89° and 53.48° are noticed indicating the nucleation of MoO_2 phase at 200 ℃. As substrate temperature is

increased above 200 °C, peaks corresponding to MoO_2 phase have become significant; confirming the increase in oxygen vacancies with T_s. When T_s is raised to 400 °C, peak corresponding to MoO_{3-x} phase has disappeared and replaced by sharp peaks at 2θ = 25.98°, 36.89°, 41.55°, 49.40° and 53.50° corresponding to $(\bar{1}11)$, (111), (021), $(\bar{3}01)$, and $(\bar{3}12)$ planes of monoclinic MoO_2 respectively (JCPDS card no. 00-032-0671). For high temperature films (T_s > 200 °C), the preferential growth is along (111) plane of MoO_2 phase. The average crystallite size calculated using W-H plot is found 13.55 nm for T_s = 400 °C. Using the Scherrer equation, the crystallite size corresponding to the MoO_2 phase's (111) plane is determined to be 11.10 nm. The crystallite size calculated using the Williamson-Hall equation (considering all the peaks) and Scherrer formula for peak corresponding to highest intensity as described in Chapter 2, section 2.4.2 [34, 35].

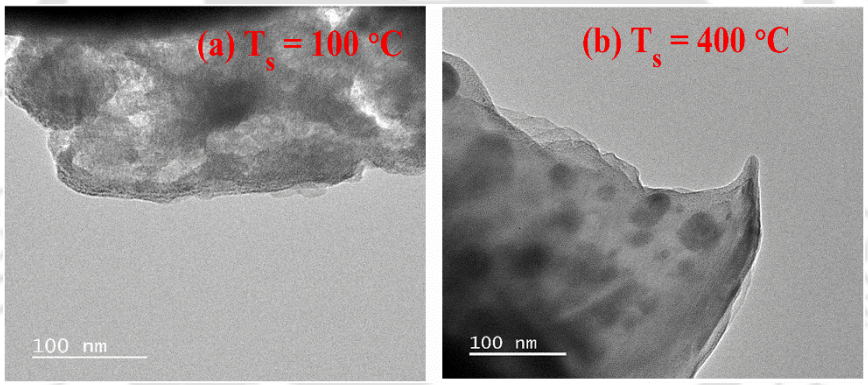

Figure 3.12: *TEM images of MoO_{3-x} films prepared at (a) T_s = 100 °C and T_s = 400 °C.*

3.2.2.2 FETEM studies

Figures 3.12 shows TEM images of MoO_{3-x} films, simultaneously grown on TEM grids at substrate temperatures of 100 °C and 400 °C. From these images, it appears that the films consist of nano sheets with multilayer edges at the periphery. Selected area diffraction pattern (SAED) shown in Figure 3.13a for low temperature film indicates that both amorphous and polycrystalline phases of α-MoO_3 corresponding to different planes are present in these films. The lattice arrangement of MoO_{3-x} nano sheets is portrayed in the HRTEM image (Figure 3.13

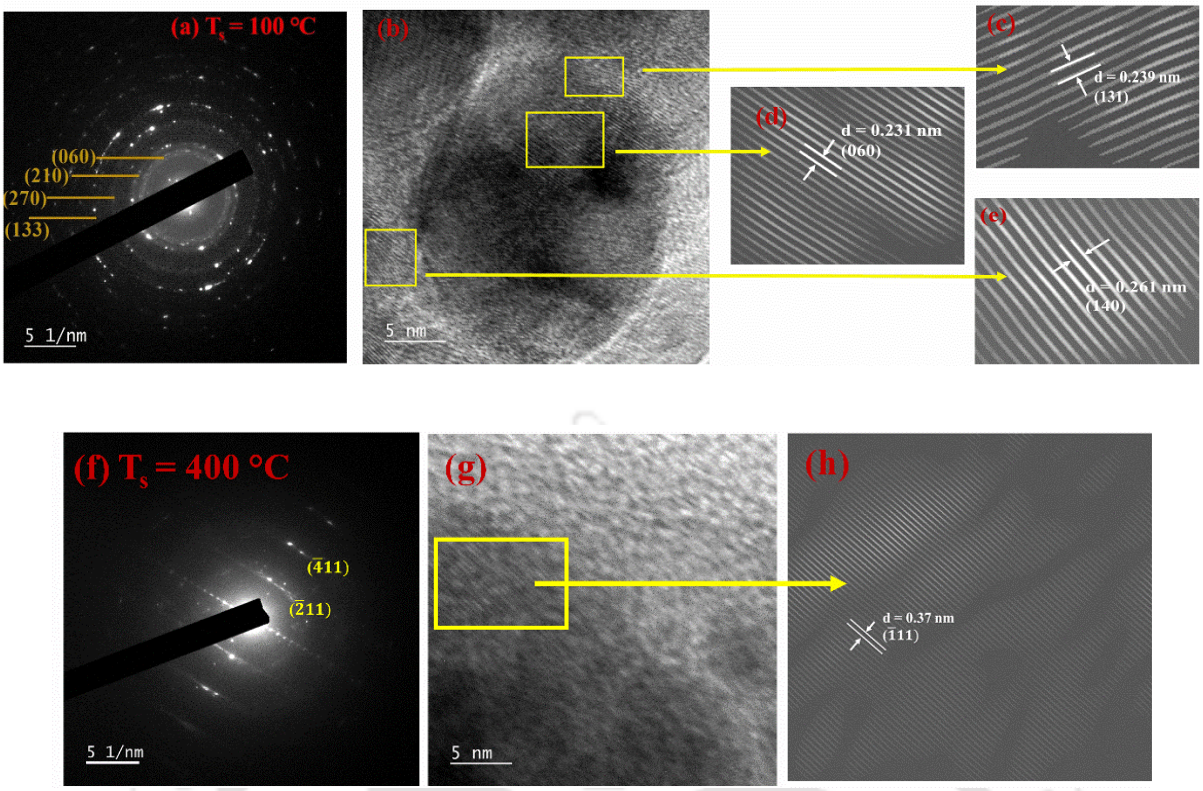

Figure 3.13: *(a) SAED pattern and (b), (c), (d) and (e) HRTEM images of MoO_{3-x} films prepared at T_s = 100 °C and (f) SAED pattern and (g), (h) HRTEM images of MoO_{3-x} films prepared at T_s = 400 °C.*

b), which also illustrates the presence of several lattice planes, confirming the polycrystalline nature of MoO_{3-x} film at 100 °C. The lattice spacing of 0.239 nm (Figure 3.13c), 0.231 nm (Figure 3.13d), and 0.261 nm (Figure 3.13e), correspond to lattice planes (131), (060), and (140) of α-MoO_3 respectively. Lattice spacing dissimilarities from the standard values are indicative of the presence of defects in the MoO_{3-x} film.

For the films deposited at higher temperature (400 °C), SAED pattern shown in Figure 3.13f, reveal that films are mostly crystalline in nature [37]. Corresponding HRTEM image presented in Figure 3.13g depicts the presence of single lattice plane ($1\bar{1}1$) having lattice spacing of 0.37 nm of MoO_2 confirming the crystalline nature of 400 °C film. The planes recognized from SAED patterns and HRTEM for both 100 °C and 400 °C films match well with the XRD results of MoO_{3-x} films deposited on glass substrates.

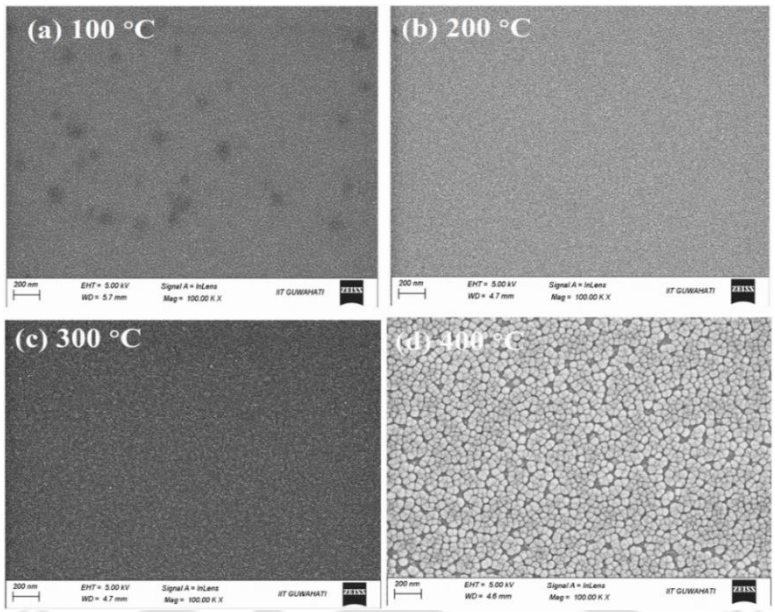

Figure 3.14: *FESEM images of molybdenum oxide thin films deposited at substrate temperature of (a) 100 °C, (b) 200 °C, (c) 300 °C and 400 °C respectively.*

Table 3.6: Atomic percent of Oxygen (O) and molybdenum (Mo) atoms in MoO_{3-x} films deposited at different substrate temperatures.

Temperature (°C)	O atoms (%)	Mo atoms (%)	Si atoms (%)	Al atoms (%)
100	60.4	3.5	27.2	8.9
200	59.0	5.0	27.5	8.4
300	56.6	8.6	26.6	8.2
400	53.2	10.2	28.8	7.8
Corning	70.4		22.3	7.3

3.2.2.3 FESEM and EDS studies

Surface morphology of MoO_{3-x} samples are studied using FESEM. Figure 3.14a shows the presence of small patches along with small grains at the surface of film prepared at 100 °C. As the substrate temperature is increased to 200 °C, small patches disappeared and only small grains are present on surface (Figure 3.14b). Smooth and uniform surface is observed for 100°C and 200 °C. Surface of films prepared at 300 °C (Figure 3.14c) consists of small and large grains forming non-uniform surface. Further, presence of spherical shaped grains (Figure 3.14 d) is observed for MoO_{3-x} films deposited at 400°C. Atomic percent of oxygen atoms and molybdenum atoms obtained from EDS are mentioned in Table 3.6. The Mo concentration has

increased but O atoms concentration has decreased when T_s is raised from 100 °C to 400 °C. Though some contribution from substrate is observed, the EDS data indicate a significant decrease in O/Mo ratio with increase in substrate temperature. These results confirm assessments made from XRD analysis that high substrate temperature results in oxygen deficient MoO_{3-x} film.

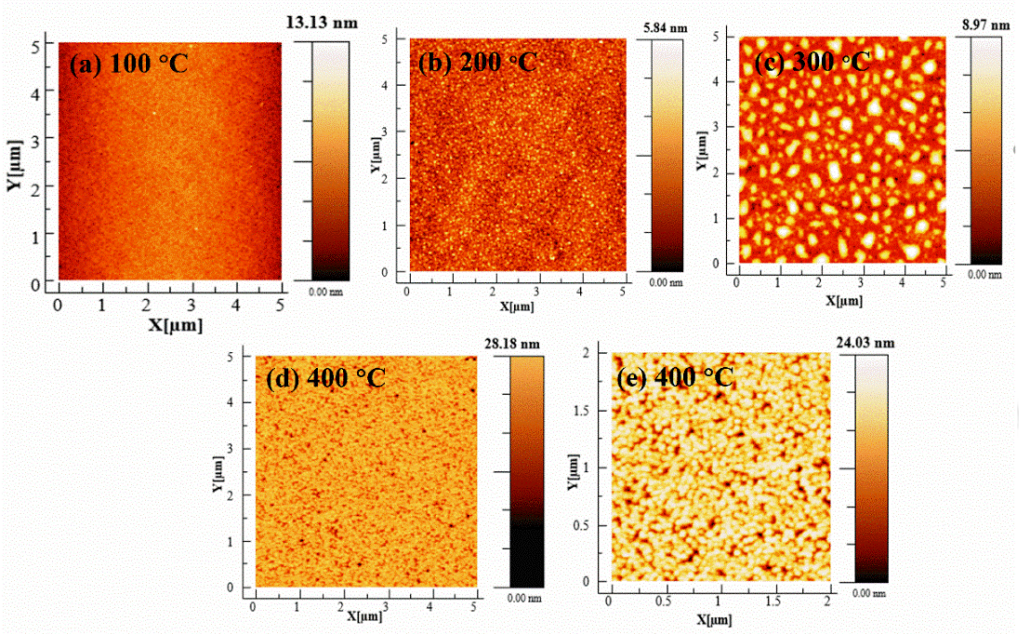

Figure 3.15: *AFM images of MoO_{3-x} films deposited at (a) 100 °C, (b) 200 °C, (c) 300 °C and (d), (e) 400 °C respectively.*

3.2.2.4 AFM studies

Surface roughness of rf-sputtered MoO_{3-x} films are measured using AFM. The 2D AFM images of molybdenum oxide thin films are shown in Figure 3.15. AFM images (Figure 3.15) show that films prepared at substrate temperature of 100 °C and 200 °C are smooth and uniform as compared to high temperature films. From AFM image (Figure 3.15c), different growth pattern is observed for T_s = 300 °C. Presence of both large grains along with smaller grains have increased roughness of these films to 1.40±0.28 nm. Further increase in substrate temperature have formed larger grains throughout the surface increasing surface roughness from 1.40±0.28 nm for T_s = 300 °C to 2.34±0.55 nm for T_s = 400 °C [38]. These observation supports XRD

data where sharp peak corresponding to (111) plane of MoO_2 are observed at T_s = 300 °C and 400 °C. From AFM analysis, it is concluded that substrate temperature of 400 °C has led to growth of uniformly distributed spherical shaped grains as shown in Figure 3.15e. FESEM images have also shown the same growth morphology.

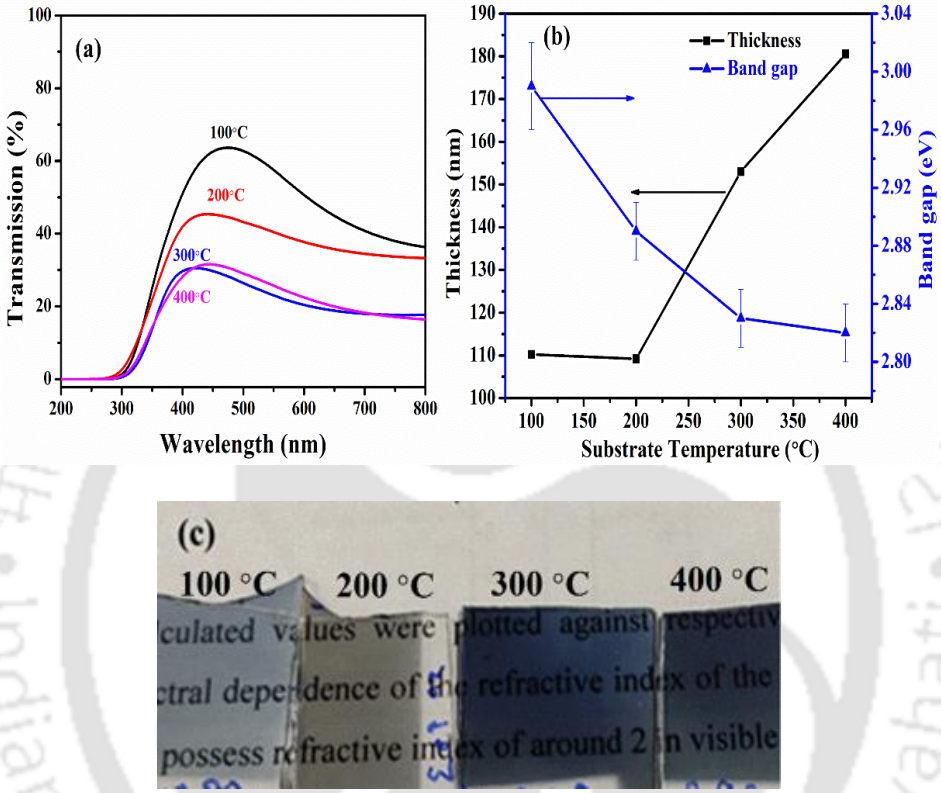

Figure 3.16: *(a) Transmission spectra and (b) band gap and thickness of rf sputtered MoO_{3-x} films deposited on corning glass substrate and (c) appearance of films at different substrate temperatures.*

3.2.2.5 UV-Vis studies

Transmission spectra of MoO_{3-x} films prepared at different subsrate temperature is presented in Figure 3.16a. Thickness and band gap variation with temperature is shown in Figure 3.16b. Deposition rate for films prepared at 100 °C and 200 °C remain almost constant i.e. 3.6 nm/min, which has increased to 5.1 nm/min and 6.0 nm/min for 300 °C and 400 °C substrate temperature respectively. A decrease in maximum transmission (T_{max}) and shift towards higher wavelength (λ) in absorption edge is observed as (substrate temperature) T_s is increased. Broad peak in

Table 3.7: *Thickness, band gap, dark conductivity and E_a of MoO_{3-x} films prepared at different substrate temperatures.*

Temperature (°C)	Thickness (nm)	Band gap (eV)	Dark Conductivity at RT ($\Omega^{-1}cm^{-1}$)	Activation Energy (E_a) eV
100	110	2.99±0.03	1.81×10^{-3}	0.226±0.005
200	109	2.89±0.02	30.65	*0.025±0.001
300	153	2.83±0.02	00.13	0.062±0.007
400	180	2.82±0.02	207.30	*0.016±0.002

**Note: This value is closer to the thermal voltage i.e. kT/q at room temperature.*

transmission spectra shows maxima at 468 nm for 100 °C which shifts to 427 nm for 200 °C. In this case, since thickness of two films are same, a change in refractive index due to change in oxygen vacancies is more likely reason for this shift in T_{max} position along with decrease in T_{max} value [39]. The change in composition of films also shifts the absorption edge towards higher wavelength. Films deposited at 400 °C are MoO_2 rich and an absorption edge is not expected in this case because of metallic nature of MoO_2 [40]. However in our case, presence of absorption edge in transmission spectra indicates the existence of MoO_{3-x} phase along with MoO_2 crystallites. Band gap is calculated using Tauc' plot and found to decrease as temperature is increased from 100 °C to 400 °C. The obtained band gap values are within the range reported in literature [19, 20]. All these observations further confirm that higher T_s results in increase in oxygen vacancies and lower oxidation state of Mo atoms which is also supported by XRD and EDS results. In MoO_{3-x} film, oxygen vacancies basically act as donor states and form a forbidden gap below the conduction band which extend into the band gap and thus reduce the optical band gap of this TMO, along with reduction of transmission of MoO_{3-x} films [41]. The decrease in transmittance is due to increase in thickness as well as shift of absorption edge towards higher wavelength. Meanwhile, when T_s is increased from 100 °C to 400 °C, colour change of MoO_{3-x} films is noticed. Figure 3.16c shows the transparency and colour change of MoO_{3-x} films produced at different substrate temperatures. At higher T_s (300 °C and 400 °C), the coloration behaviour is representative of the thermochromic properties of MoO_{3-x} films, due to the increase in oxygen vacancies and shift in Mo atom oxidation state from Mo^{+6} to

Mo^{+5} [18, 19, 42]. In literature, it is reported that post-deposition treatment upto 300 °C forms dark blue colour MoO_{3-x} films due to formation of oxygen vacancies and bleaching starts when post-deposition treatment temperature is increased to 400 °C [27, 42, 43]. Nevertheless, the thermochromic effect is observed in this work even at 400 °C and is not dependent on any post-deposition treatment.

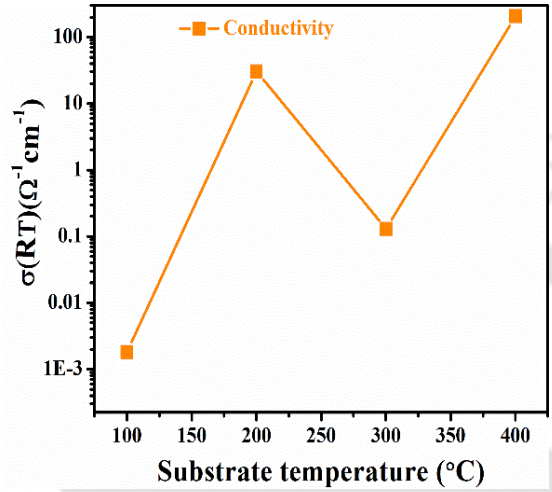

Figure 3.17: *Dark conductivity of MoO_{3-x} films measured at room temperature.*

3.2.2.6 Electrical properties

The effect of substrate temperature on conductivity of rf-sputtered molybdenum oxide films is also investigated. Figure 3.17 represents room temperature dark conductivity ($\sigma_d(RT)$) of MoO_{3-x} films. $\sigma_d(RT)$ of samples prepared at different substrate temperature is listed in Table 3.7. Here, dark conductivity is increased from 10^{-3} $\Omega^{-1}cm^{-1}$ for 100 °C to 30.65 $\Omega^{-1}cm^{-1}$ for 200 °C due to increase in oxygen vacancies. Also, XRD results have shown that formation of MoO_2 has initiated at T_s = 200 °C, confirming the transformation of semiconducting MoO_{3-x} towards metallic oxide which could also be the reason for significant rise in $\sigma_d(RT)$. However, a decrease in conductivity is observed for films deposited at 300°C. The surprising decrement in conductivity for 300 °C film could be due to different growth pattern as confirmed from AFM study (Figure 3.15c). Films deposited at T_s = 300 °C, consist of non-uniformly distributed larger

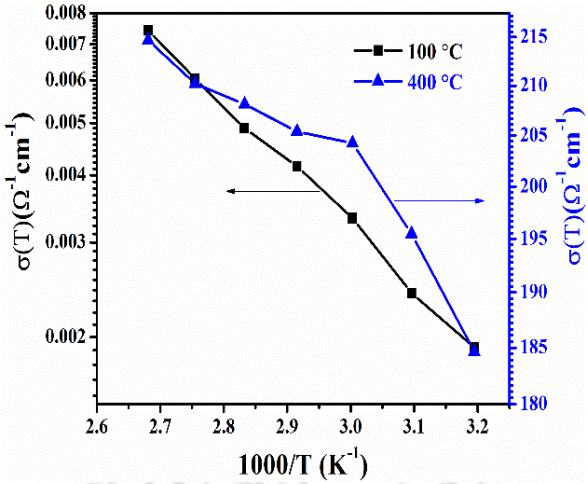

Figure 3.18: *Temperature dependent conductivity of MoO_{3-x} films prepared at 100 °C and 400 °C.*

grains of MoO_2 phase and smaller MoO_{3-x} grains throughout the surface. Thus, presence of grain boundaries will hinder the electron conduction and reduce the conductivity of MoO_{3-x} films. Though, a further increase in T_s to 400 ℃ has led to improvement in $\sigma_d(RT)$ to 207.30 $\Omega^{-1}cm^{-1}$ which can be related to highly crystalline nature of these films dominated by MoO_2 phase as observed in XRD (Figure 3.11). Increase in crystallite size leads to the formation of compact crystals allowing efficient movement of free charge carriers. Excluding the $\sigma_d(RT)$ for films deposited at 300 ℃, the change in conductivity with T_s show similar trend as reported in literature [44-47]. No photosensitivity is observed for these films under halogen lamp due to wide band gap (2.99 eV - 2.82 eV) of MoO_{3-x} films and poor photon flux in this range.

Temperature dependent conductivity variation of molybdenum oxide films prepared at 100 ℃ and 400 ℃ are shown in Figure 3.18. About one order change in conductivity is noticed when measurement temperature is raised from 313 K to 373 K for films deposited at T_s = 100 ℃ whereas for samples deposited at 400 ℃, a very small change in σ (< 10%) is observed in similar temperature range. The small change in σ with temperature for 400 ℃ film could be due to higher conductivity and also change in trapping and emission rates from shallow traps states which are within a few kT/q from the conduction band edge.

E_a of samples prepared at different substrate temperature is listed in Table 3.7. E_a is highest (0.226 eV) for films deposited at T_s =100 ℃ and lowest (0.016 eV i.e. ~ kT/q) for 400 ℃. For 400 ℃ films, E_a is 0.046 eV near room temperature (300 K) and decreases to 0.016 eV around 350 K. 400 ℃ films have more free electrons concentration because of higher oxygen vacancies as confirmed by XRD and EDS analysis. Increase in free charge carriers shifts the defect states level closer to conduction band and thus electrons require less energy to reach conduction band resulting in very low activation energy [48].

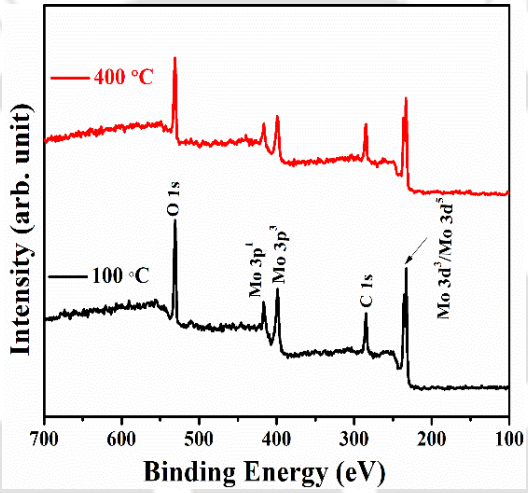

Figure 3.19: *XPS spectra of MoO_{3-x} films prepared at 100 ℃ and 400 ℃.*

3.2.2.7 XPS studies

XPS survey spectra of MoO_{3-x} films prepared at different T_s are shown in Figure 3.19. Characteristics peaks corresponding to Mo 3s, Mo 3p (doublet) ($3p_{1/2}$ and $3p_{3/2}$) and Mo 3d (doublet) ($3d_{3/2}$ and $3d_{5/2}$) are observed [25-27]. In addition, peaks corresponding to O 1s and C 1s are also observed at 530.72 eV and 284.83 eV respectively. Deconvoluted spectra of MoO_{3-x} films prepared at substrate temperature of 100 ℃ and 400 ℃ are presented in Figure 3.20. Films deposited at substrate temperature of 400 ℃ show asymmetric widening of Mo $3d_{5/2}$ and $3d_{3/2}$ peaks. After fitting, peaks are obtained for Mo^{6+} and Mo^{5+} valence states for both lower T_s = 100 ℃ and higher T_s= 400 ℃, confirming the existence of non-stoichiometric MoO_{3-}

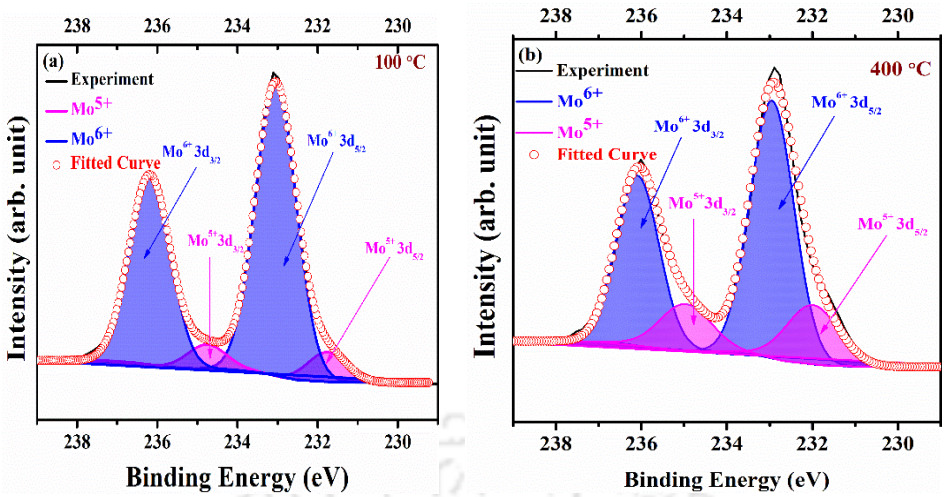

Figure 3.20: *De-convoluted XPS spectra of MoO_{3-x} films prepared at (a) 100 °C and (b) 400 °C respectively.*

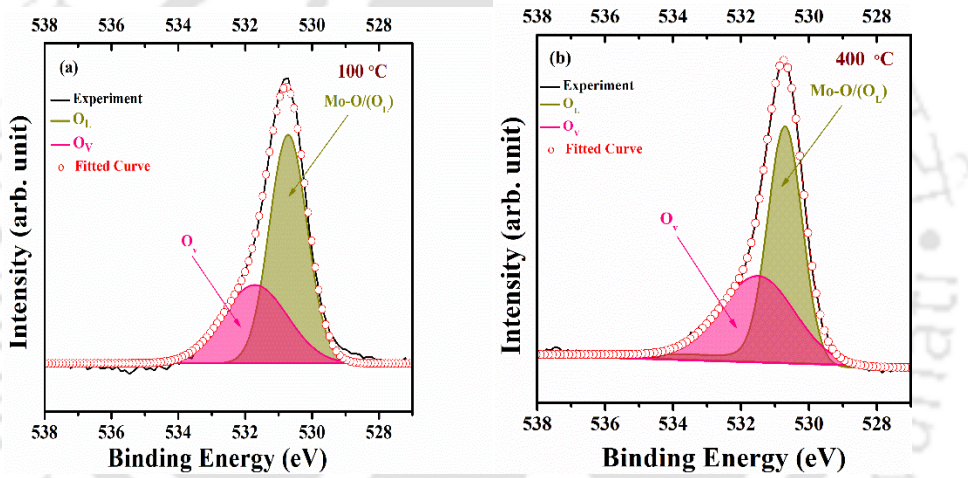

Figure 3.21: *O 1s XPS spectra of MoO_{3-x} films prepared at (a) 100 °C and (b) 400 °C respectively.*

$_x$ inside prepared films [29, 30]. The doublet separation of 3.11 eV confirms dominancy of Mo^{6+} for all MoO_{3-x} films [33]. The contribution of Mo^{5+} oxidation state inside MoO_{3-x} films are found to be ~10 % for T_s = 100 °C which increases to 23% for 400 °C, still Mo^{6+} state is dominant for both 100 °C and 400 °C MoO_{3-x}. Mo^{4+} is not observed for any of MoO_{3-x} films probably, since XPS collects the information only from very thin (~10 nm) layer from the surface. Asymmetric O 1s spectra are also observed for both low temperature (100 °C) and high temperature (400 °C) films and are shown in Figure 3.21a. After fitting O 1s spectra, two peaks are obtained at ~530.79 eV and ~531.74 eV corresponding to Mo-O bond in MoO_3 and

O_V respectively [35]. A small shift of 0.12 eV is observed when T_s is raised from 100 ℃ to 400 ℃. The peak representing Mo-O bond is found to be the dominant one. MoO_{3-x} films prepared at 100 ℃ contain oxygen vacancies of about 32% whereas for 400 ℃ films it is found to be 43%. These observations further confirm that films deposited at high T_s have more oxygen vacancies and more molybdenum atoms present in oxygen deficient Mo^{5+} state. This is the reason for getting lower band gap, deep blue colour and higher conductivity of films deposited at 400 ℃. According to published reports, MoO_{3-x} oxygen vacancies also cause a decrease in work function [24].

These studies further confirm that high substrate temperature of 400 ℃ leads to formation of oxygen deficient conducting and crystalline MoO_{3-x} film suitable for gas sensing and catalysis application.

3.2.3 Properties of MoO_{3-x} films prepared under different gaseous environment (Series 3)

In this section, our focus is to optimise deposition conditions to obtain transparent and low conducting molybdenum oxide films which can be used as hole transport layer (HTL) in solar cells. Optimized conditions (rf power = 80 W, T_s = 400 ℃) of previous studies and different gaseous environment (Argon (Ar) gas, Oxygen (O_2) gas, and Argon + Oxygen (Ar + O_2) gases) are used to deposit MoO_{3-x} thin films. Deposition conditions maintained to carry out this study are listed in Table 3.3. The effect of different gaseous environment is studied in detail.

3.2.3.1 XRD studies

XRD pattern of films prepared using different environment are presented in Figure 3.22. As discussed earlier, the presence of MoO_2 is observed for films prepared at 400 ℃ using argon gas only. As the oxygen is incorporated during deposition, peak corresponding to MoO_2 phase disappeared and new XRD peak appeared at $2\theta = 12.77°$, which represents (020) plane of

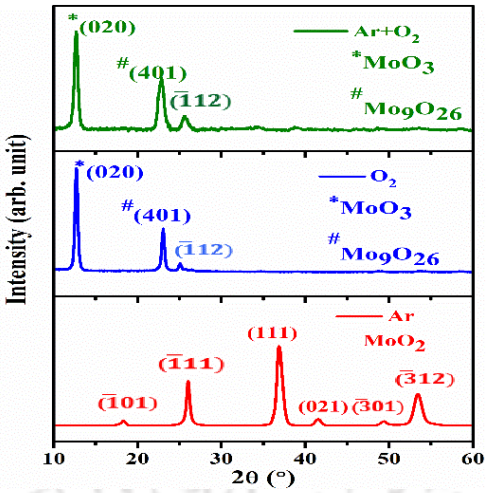

Figure 3.22: *XRD patterns of thin films prepared in different gaseous environment.*

orthorhombic phase of MoO_3 (JCPDS card no - 05-0508). Apart from this, signature of Mo_9O_{26}, an intermediate oxide is also observed with XRD peak at $2\theta = 22.88°$ and 25.68° corresponding to (401) and $(\bar{1}12)$ planes (JCPDS card no - 05-0441) respectively. These results show that O_2 gas present while deposition has led to the formation of MoO_3 along with Mo_9O_{26} which is an intermediate oxide [49]. Average crystallite size obtained using W-H plot is found to be 35.30 nm and 20.18 nm for samples prepared using $Ar+O_2$ and only O_2 gases respectively, whereas for films deposited in presence of Ar only, it is 13.55 nm. Oxygen gas has led to the formation of MoO_3 phase with increase in crystallinity and crystallite size. Crystallite size calculated for (020) plane using Scherer formula from the most intense peak is found to be 15.47 nm and 19.42 nm for samples prepared using $Ar+O_2$ and O_2 respectively.

3.2.3.2 FESEM and EDS studies

From FESEM images shown in Figure 3.23, it can be seen that different gaseous environment has also changed the surface morphology. Presence of spherical shaped grains along with large flakes are noticed on surface of MoO_{3-x} films prepared under O_2 environment. These results are in good agreement with XRD studies which show increment in crystallinity and size of MoO_3 particles deposited under O_2 atmosphere only. The change in growth morphology is due to the

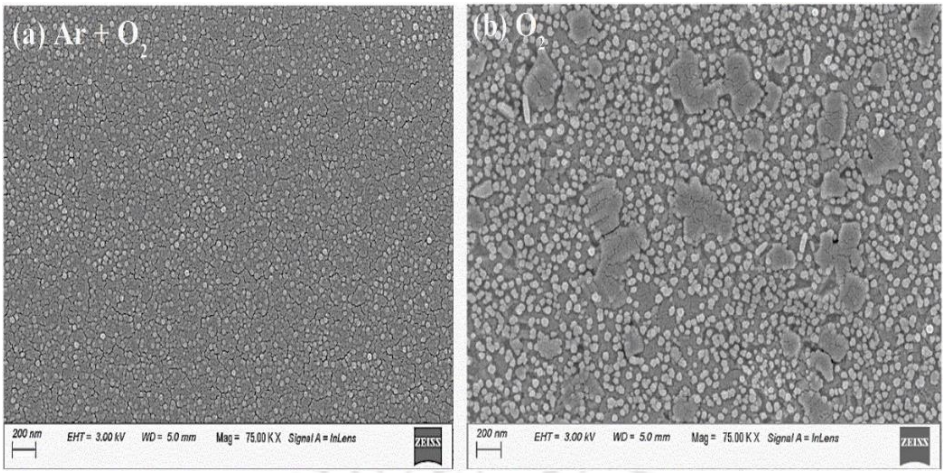

Figure 3.23: *FESEM images of samples prepared under different gaseous atmosphere.*

Table 3.8: *Atomic percent of Oxygen (O) and molybdenum (Mo) atoms in MoO_{3-x} films prepared under different gaseous atmosphere.*

Gaseous Environment	O atoms (%)	Mo atoms (%)	Si atoms (%)	Al atoms (%)
Ar	53.2	10.2	28.8	7.8
Ar + O_2	63.8	2.2	26.3	7.7
O_2	65.3	1.8	25.5	7.4
Corning	70.4		22.3	7.3

reaction taking place between rf-sputtered MoO_3 molecules and chemically reactive oxygen species present in gas phase inside the deposition chamber. The atomic percent of Mo, O, Si and Al atoms present in films prepared under Ar, Ar+O_2 and O_2 environment are listed Table 3.8. An increase in oxygen atoms concentration along with decrease in Mo atoms concentration is observed for films deposited using Ar + O_2 and O_2 gases indicating the transformation of sub stoichiometric MoO_{3-x} closer to stoichiometric MoO_3 films.

3.2.3.3 AFM studies

Effect of gaseous environment on surface morphology is analysed using AFM studies. Presence of Ar+O_2 gases while deposition has initiated the formation of MoO_{3-x} crystallites which can be clearly seen in Figure 3.24a. The surface of films deposited in Ar+O_2 environment looks compact and uniform, whereas film surface is damaged harshly (Figure 3.24b) when only O_2

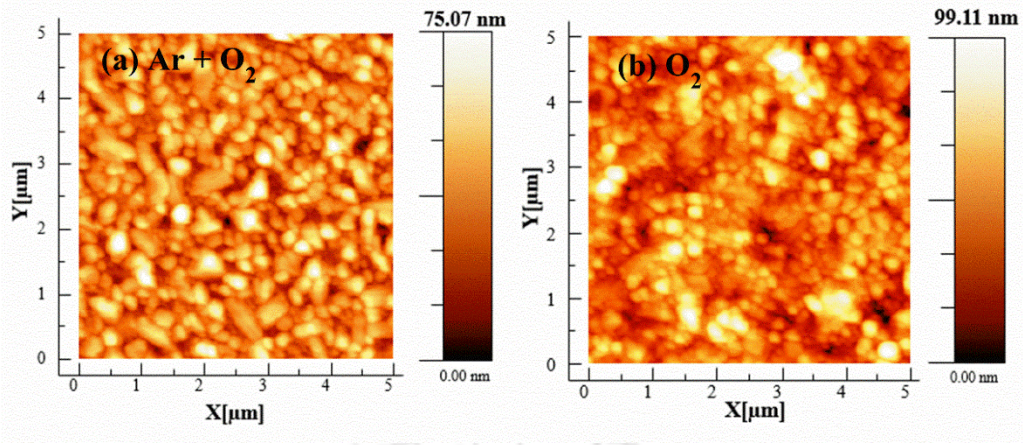

Figure 3.24: *AFM images of samples prepared under different gaseous environment.*

gas is present during deposition increasing the surface roughness from 10.47±1.15 nm (for $Ar+O_2$ atmosphere) to 13.66±2.05 nm (for O_2 atmosphere). Surface damage may happen because of the dissociation of O_2 molecules which increase the active oxygen concentration inside the chamber. Thus, the rate at which reaction takes place between active oxygen and sputtered molybdenum oxide atoms also increase. The highly energetic particles may strike the surface in haphazard manner and damage the film surface.

3.2.3.4 UV-Vis studies

From transmission spectra shown in Figure 3.25a, it is observed that MoO_{3-x} films prepared in presence of argon gas have low transmission (~ 20-30%). However, when oxygen is added during deposition, transparency of films increases. Also, films deposited in $Ar+O_2/O_2$ plasma show blue shift in absorption edge as compared to MoO_{3-x} films deposited using Ar gas only. Highest transmission ~ 85% is observed in the range of 500 nm to 750 nm for samples prepared in presence of $Ar+O_2$ environment. This refers to occupancy of oxygen vacancies by supplied active oxygen [50]. Thickness variation for different gaseous environment is shown in Figure 3.25b. Inclusion of oxygen during sputtering also resulted in decrease in deposition rate of the films due to formation of active oxygen (O^0) species ($O_2 + e^- \rightarrow O^0$) which cause the poisoning of target when adsorbed on the surface [51]. Effect of gaseous environment on band gap is

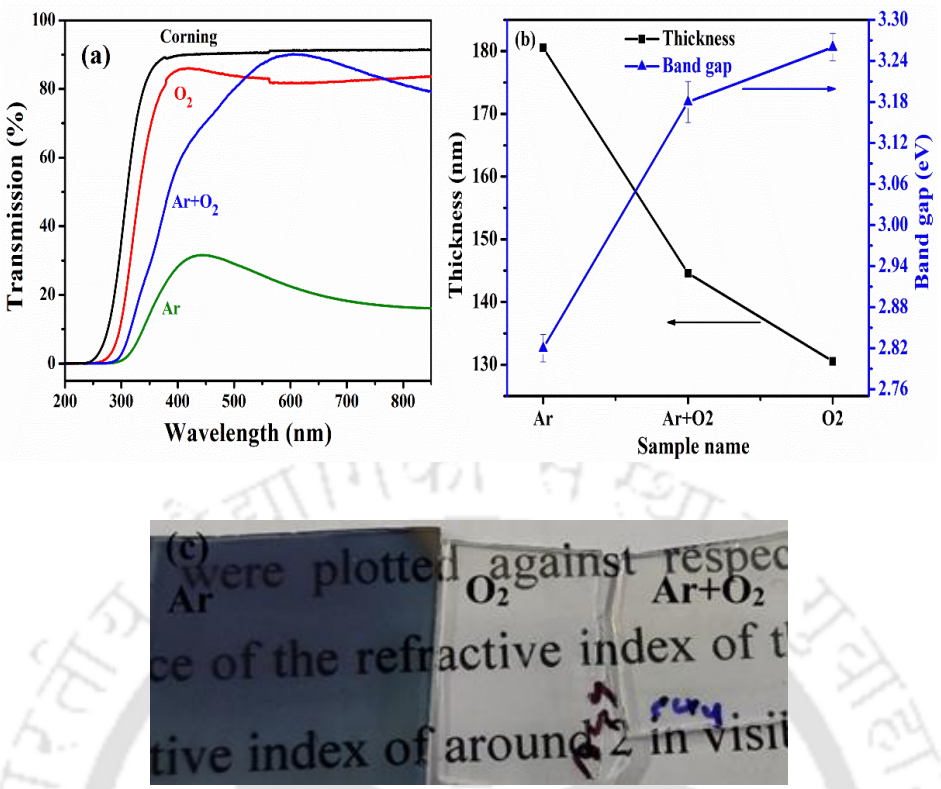

Figure 3.25: *(a) UV-Vis transmission spectra, (b) thickness and band gap variation and (c) colour variation of thin films prepared under different gaseous environment.*

Table 3.9: *Thickness, band gap, dark conductivity and E_a of MoO_{3-x} films prepared in presence of different gaseous atmosphere.*

Gaseous atmosphere	Thickness (nm)	Band gap (eV)	Dark Conductivity at RT ($\Omega^{-1}cm^{-1}$)	Activation Energy (E_a) eV
Ar	180	2.82±0.02	207.30	0.016±0.002
$Ar+O_2$	144	3.18±0.03	2.15×10^{-6}	0.389±0.070
O_2	130	3.26±0.01	2.09×10^{-6}	0.183±0.023

shown in Figure 3.25b. Increase in band gap and shift in absorption edge towards high energy confirms the formation of stoichiometric films due to filling of oxygen vacancies by adding O atoms during deposition [41]. The colour change is also noticed for these samples. Films prepared using only argon gas have deep blue colour as shown in Figure 3.25c whereas transparent films are obtained when mixture of argon and oxygen gases are used for deposition. A change is colour suggest the bleaching of MoO_{3-x} in the presence of oxygen which changes the oxidation state of Mo atoms from Mo^{+5} to Mo^{+6}, Mo^{+4} to Mo^{+5} [41]. These observations suggest that it is possible to deposit highly transparent oxygen rich molybdenum oxide films

by introducing oxygen during deposition.

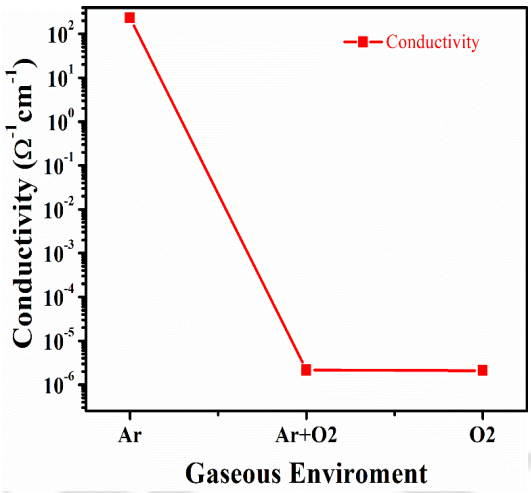

Figure 3.26: *Effect of different gaseous environment on dark conductivity measured at room temperature.*

3.2.3.5 Electrical properties

Electrical properties of MoO_{3-x} films are studied using conductivity measurements. Dark conductivity of all films, measured at room temperature are mentioned in Table 3.9 and graphical representation of $\sigma_d(RT)$ is shown in Figure 3.26. Conductivity of films prepared in presence of oxygen gas is found to drop by nearly 8 orders of magnitude. This major decrement in $\sigma_d(RT)$ is due to the conversion of MoO_2 closer to stoichiometric MoO_3. When oxygen is incorporated for preparation of MoO_{3-x} films, increase in transmission and band gap whereas decrease in conductivity is observed. These findings further confirm that supplied oxygen has filled the oxygen vacancies and shifted sub-stoichiometric ratio of O and Mo atoms towards stoichiometric ratio.

Increase in E_a is also observed for films deposited using oxygen. A higher activation energy indicates shift in trap/defect level away from the conduction band for films deposited in presence of O_2. Here, conduction band reference is considered because MoO_3 is inherently an n-type semiconductor [52]. This shift results in an increase in work function value which further improves the hole selectivity of MoO_{3-x} and makes this material appropriate for its

application as HTL [25, 52].

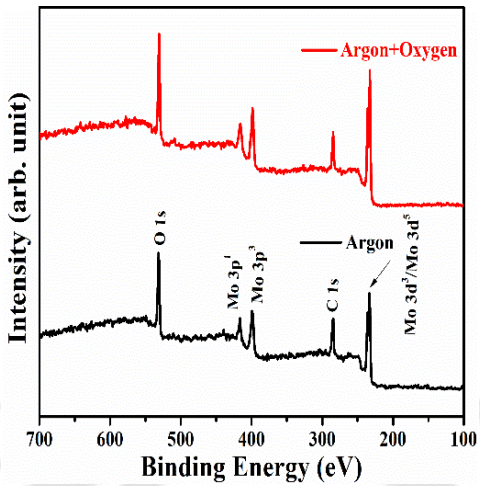

Figure 3.27: *Survey spectra of MoO_{3-x} films prepared in presence of Ar and Ar+O_2 atmosphere.*

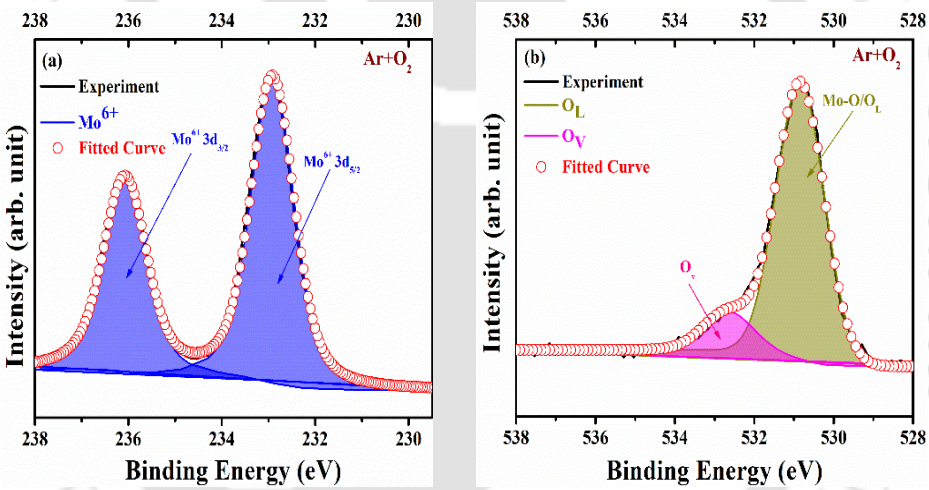

Figure 3.28: *Deconvoluted XPS spectra of (a) Mo 3d and (b) O 1s of MoO_{3-x} films prepared in presence of argon and oxygen atmosphere.*

3.2.3.6 XPS studies

From survey spectra displayed in Figure 3.27, it is observed that MoO_{3-x} films prepared under different atmosphere do not contain trace of any other elements except Mo, O and C atoms. Figure 3.28a and 3.28b show fitted Mo 3d and O 1s XPS spectra for MoO_{3-x} films prepared in Ar+O_2 atmosphere respectively. Use of Ar+O_2 while deposition has removed the shoulder peaks which appeared at 231.59 eV and 234.89 eV in Mo 3d XPS spectra as shown in Figure

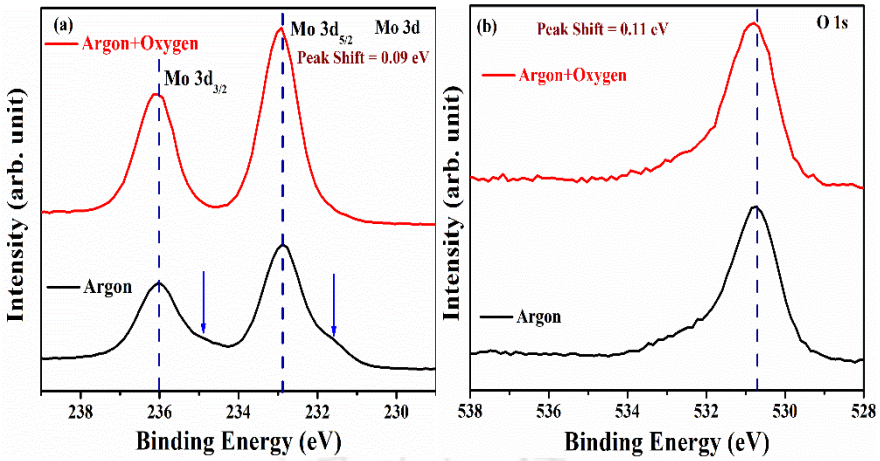

Figure 3.29: *(a) Mo 3d and (b) O 1s XPS spectra for MoO_{3-x} films prepared in the presence of Argon + Oxygen gases and Argon only at 400 ℃.*

3.29a for films prepared using Ar gas only. Peaks corresponding to Mo^{6+} $3d_{5/2}$ and $3d_{3/2}$ are observed for $Ar+O_2$ environment with no signature of Mo^{5+} oxidation state. Comparative O 1s spectra is depicted in Figure 3.29b. Mo-O bond contribution is found to be 57 % for Ar environment and 87% for $Ar+O_2$ atmosphere. Also, presence of oxygen while deposition, has reduced oxygen vacancies contribution from 43% (for Ar atmosphere) to 13% (for $Ar+O_2$ atmosphere). This confirms that supplied oxygen has filled the vacancies present inside MoO_{3-x} films and also reduced Mo^{5+} formation which have resulted in developing transparent and resistive MoO_{3-x} films. These results are consistent with the findings concluded from other characterization techniques results.

In Series 2 and Series 3, we discovered that the substrate temperature and gaseous environment affect the rate at which MoO_{3-x} films are deposited. Because of this, a variation in thickness is obtained when films are deposited at different T_s and gaseous environment. To distinguish between the observed changes in optoelectronic properties of films arising due to variation in thickness and variation in deposition conditions, a few more samples are made at temperatures of 100 °C in presence of Ar gas only and at 400 °C in presence of $Ar+O_2$ gases keeping a constant film thickness of 180 nm (same as that for films deposited at 400 °C in presence Ar

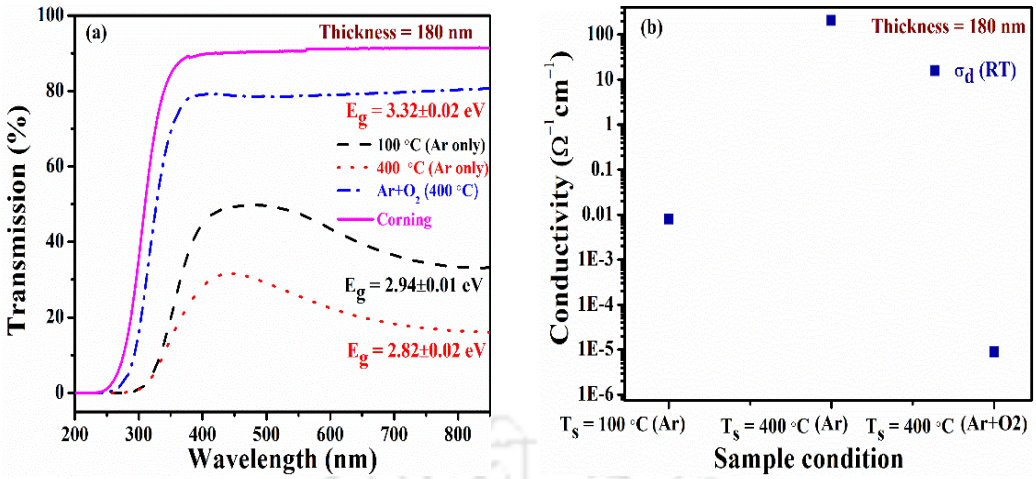

Figure 3.30: *(a) Transmission spectra and (b) room temperature dark conductivity of MoO_{3-x} films prepared under different conditions keeping thickness constant (180 nm).*

gas only) and their optical and electrical properties are examined. Figure 3.30a shows the transmission spectra of 180 nm thick MoO_{3-x} films deposited under different conditions. Even with the same thickness, films deposited in Ar atmosphere only at 100 °C had a higher transmission and band gap than films deposited at 400 °C under similar atmosphere. The transparency of MoO_{3-x} film has increased from 30% (for Ar atmosphere at T_s = 400 °C) to 80% for the same thickness when oxygen was introduced during deposition together with Ar gas. Additionally, it is found that for same thickness (180 nm), $\sigma_d(RT)$ (Figure 3.30b) of films deposited in pure Ar atmosphere at 100 °C is 7-9×10^{-3} $\Omega^{-1}cm^{-1}$, but for those deposited at 400 °C, it increases by 5 orders ($\sigma_d(RT)$ = 207-210 $\Omega^{-1}cm^{-1}$). However, $\sigma_d(RT)$ again decreases to 8-10×10^{-6} $\Omega^{-1}cm^{-1}$ for MoO_{3-x} films prepared in the presence of Ar+O_2 gases at T_s = 400 °C. These observations support that the optoelectronic properties of molybdenum oxide films are strongly influenced by the deposition conditions, such as substrate temperature and gaseous environment.

3.3 Conclusion

In this work, MoO_{3-x} films are prepared by rf- sputtering technique and deposition conditions

are optimised in sequential manner to prepare highly conducting MoO_{3-x} films which make this TMO suitable for their use as catalysis for different chemical processes. Later on, different combination of gaseous environment is used to deposit transparent and non-conducting MoO_{3-x} films for their application as HTL in organic/inorganic solar cells. It is observed that incorporation of oxygen gas while deposition has led to the formation of MoO_{3-x} closer to its stoichiometric ratio. Films prepared using $Ar+O_2$ and O_2 have ~ 80% transmission in the UV and visible region and have low conductivity. Temperature dependent conductivity measurements suggest that presence of oxygen has increased the activation energy and hence increased the work function of molybdenum oxide making it suitable for its use as HTL. This study provides a possible way to tune the electrical and optical properties of molybdenum oxide films prepared using rf-sputtering technique. Optimised conditions for preparing conducting films are: high T_s (400 °C), high rf power (80 W) and pure Argon atmosphere. However, by introducing oxygen during deposition, transparent and resistive MoO_{3-x} films are deposited at high T_s = 400 °C. Such a high conductivity of MoO_{3-x} film at substrate temperature of 400 °C is not achieved yet. After, introducing oxygen gas along with argon gas during deposition, transparent MoO_{3-x} films having wide band gap and low conductivity of order 10^{-6} $\Omega^{-1}cm^{-1}$ could be deposited at substrate temperature of 400 °C for hole transport layer application in heterojunction solar cells. Optimized conditions of these studies allow the preparation of both coloured and conducting as well as transparent and resistive molybdenum oxide films by changing the gaseous environment during the deposition of MoO_{3-x} films.

3.4 References

[1] B.E. Warren, X-ray Diffraction. Dover, New York, 253 (1990).

[2] G.K.W.a.W.H. Hall, X-ray line broadening from filed aluminium and wolfram, Acta Metallurgica, 1 (1953) 22-31.

[3] M.L. Edita Vernickaite, Natalia Tsyntsaru, Vidas Pakstas, Henrikas Cesiulis, XPS studies on the Mo oxide-based coatings electrodeposited from highly saturated acetate bath, CHEMIJA, 31 (2020) 203-209.

[4] Grzegorz Greczynski and L. Hultman, C1sPeak of Adventitious Carbon Aligns to the Vacuum Level: Dire Consequences for Material'sBonding Assignment by Photoelectron Spectroscopy, ChemPhysChem 18 (2017) 1507 –1512.

[5] Grzegorz Greczynski and L. Hultman, X-ray photoelectron spectroscopy: Towards reliable binding energy referencing, Progress in Materials Science 107 (2020) 100591.

[6] J.L. Ye Zhao, Ya Zhou, Zhengjun Zhang, Yonghua Xu, H Naramoto, S Yamamoto, Preparation of MoO_3 nanostructures and their optical properties, J. Phys.: Condens. Matter 15 (2003) L547–L552.

[7] I. Navas, R. Vinodkumar, A.P. Detty, V.P.M. Pillai, Growth of MoO_3 nanorods on glass substrates by R F magnetron sputtering, IOP Conference Series: Materials Science and Engineering, 2 (2009) 1-5.

[8] H.S. Kim, J.B. Cook, H. Lin, J.S. Ko, S.H. Tolbert, V. Ozolins, B. Dunn, Oxygen vacancies enhance pseudocapacitive charge storage properties of MoO_{3-x}, Nat Mater, 16 (2017) 454-460.

[9] M. Dieterle, G. Weinberg, G. Mestl, Raman spectroscopy of molybdenum oxides, Physical Chemistry Chemical Physics, 4 (2002) 812-821.

[10] T. He, J. Yao, Photochromism of molybdenum oxide, Journal of Photochemistry and Photobiology C: Photochemistry Reviews, 4 (2003) 125-143.

[11] E.T.-G. L.O. Alema-Vazquez, J.R. Villagomez-Ibarra, J. L. Cano-Domınguez, Effect of the particle size on the activity of MoO_xC_y catalysts for the isomerization of heptane, Catalysis Letters, 100 (2005) 219-226.

[12] C.J. G. A. Nazri, Far-infrared and Raman studies of orthorhombic MoO_3 single crystal, Solid State Ionics, 53.56 (1992) 376-382.

[13] B. Hui, G. Li, X. Zhao, L. Wang, D. Wu, J. Li, B.K. Via, h-MoO_3 microrods grown on wood substrates through a low-temperature hydrothermal route and their optical properties, Journal of Materials Science: Materials in Electronics, 28 (2016) 3264-3271.

[14] O. Lupan, V. Trofim, V. Cretu, I. Stamov, N.N. Syrbu, I. Tiginyanu, Y.K. Mishra, R. Adelung, Investigation of optical properties and electronic transitions in bulk and nano-microribbons of molybdenum trioxide, Journal of Physics D: Applied Physics, 47 (2014).

[15] L. Kumari, Y.-R. Ma, C.-C. Tsai, Y.-W. Lin, S.Y. Wu, K.-W. Cheng, Y. Liou, X-ray diffraction and Raman scattering studies on large-area array and nanobranched structure of 1D MoO_2 nanorods, Nanotechnology, 18 (2007) 115717.

[16] M.A. Camacho-Lopez, L. Escobar-Alarcon, M. Picquart, R. Arroyo, G. Cordoba, E. Haro-Poniatowski, Micro-Raman study of the m-MoO_2 to α-MoO_3 transformation induced by cw-laser irradiation, Optical Materials, 33 (2011) 480-484.

[17] P.A.S.a.N.S. McIntyre, Thermal Reduction of MoO_3, J. Phys. Chem. , 96 (1992) 9029-9035.

[18] V. Madhavi, P. Kondaiah, S.S. Rayudu, O.M. Hussain, S. Uthanna, Properties of MoO_3 films by thermal oxidation: Annealing induced phase transition, Materials Express, 3 (2013) 135-143.

[19] S. Subbarayudu, V. Madhavi, S. Uthanna, Growth of MoO_3 Films by RF Magnetron Sputtering: Studies on the Structural, Optical, and Electrochromic Properties, ISRN Condensed Matter Physics, 2013 (2013) 1-9.

[20] V.K. Sabhapathi, O.M. Hussain, S. Uthanna, P.J. Reddy, Structural and Electrical-Properties of Electron-Beam Evaporated Molybdenum Trioxide Films, Materials Letters, 20 (1994) 175-178.

[21] V. Nirupama, S. Uthanna, Influence of sputtering power on the physical properties of magnetron sputtered molybdenum oxide films, Journal of Materials Science: Materials in

Electronics, 21 (2009) 45-52.

[22] O.M.H. V.K. Sabhapathi, S. Uthanna, B.S. Naidu, P.J. Reddy, C. Julien, M. Balkanski A.c. conductivity studies on Al/MoO_3/Al sandwich structures, Materials Science and Engineering B32 (1995) 93-97.

[23] L.F. Mao, H. Ning, C. Hu, Z. Lu, G. Wang, Physical Modeling of Activation Energy in Organic Semiconductor Devices based on Energy and Momentum Conservations, Sci Rep, 6 (2016) 24777.

[24] M.T. Greiner, L. Chai, M.G. Helander, W.-M. Tang, Z.-H. Lu, Transition Metal Oxide Work Functions: The Influence of Cation Oxidation State and Oxygen Vacancies, Advanced Functional Materials, 22 (2012) 4557-4568.

[25] K. Crowley, G. Ye, R. He, K. Abbasi, X.P.A. Gao, α-MoO_3 as a Conductive 2D Oxide: Tunable n-Type Electrical Transport via Oxygen Vacancy and Fluorine Doping, ACS Applied Nano Materials, 1 (2018) 6407-6413.

[26] Y. Jiang, S. Cao, L. Lu, G. Du, Y. Lin, J. Wang, L. Yang, W. Zhu, D. Li, Post-annealing Effect on Optical and Electronic Properties of Thermally Evaporated MoO_x Thin Films as Hole-Selective Contacts for p-Si Solar Cells, Nanoscale Res Lett, 16 (2021) 87.

[27] M. Morales-Luna, S.A. Tomas, M.A. Arvizu, M. Perez-Gonzalez, E. Campos-Gonzalez, The evolution of the Mo^{5+} oxidation state in the thermochromic effect of MoO_3 thin films deposited by rf magnetron sputtering, Journal of Alloys and Compounds, 722 (2017) 938-945.

[28] G.B.-C. C. Castillo, C. Manzur, N.Yutronic, R. Sierpe, G. Cabello and B. Chornik, Molybenum Trioxide Thin Films Doped with Gold Nanoparticles Grown by a sequential Methodology: Photochemical Metal-Organic Deposition (PMOD) and DC-Magnetron Sputtering, J. Chil. Chem. Soc., 61 (2016).

[29] S.O.G.a.L.J. Matienzo, X-Ray Photoelectron Spectroscopy of Inorganic and Organometallic Compounds of Molybdenum, Inorganic Chemistry, 14 (1975) 1015.

[30] C.A.H. M. Anwar, R. Bulpett, Effect of substrate temperature and film thickness on the surface structure of some thin amorphous films of MoO_3 studied by X-ray photoelectron spectroscopy (ESCA), Journal of Materials Science, 24 (1989) 3087-3090.

[31] M. Ponce-Mosso, M. Perez-Gonzalez, P.E. Garcia-Tinoco, H. Crotte-Ledesma, M. Morales-Luna, S.A. Tomas, Enhanced photocatalytic activity of amorphous MoO_3 thin films deposited by rf reactive magnetron sputtering, Catalysis Today, 349 (2020) 150-158.

[32] C.V. Ramana, V.V. Atuchin, V.G. Kesler, V.A. Kochubey, L.D. Pokrovsky, V. Shutthanandan, U. Becker, R.C. Ewing, Growth and surface characterization of sputter-deposited molybdenum oxide thin films, Applied Surface Science, 253 (2007) 5368-5374.

[33] H. Mehmood, G. Bektaş, I. Yıldız, T. Tauqeer, H. Nasser, R. Turan, Electrical, optical and surface characterization of reactive RF magnetron sputtered molybdenum oxide films for solar cell applications, Materials Science in Semiconductor Processing, 101 (2019) 46-56.

[34] G.D. Khattak, M.A.Salim, A.S.A-Harthi, David J. Thompson and L.E. Wenger, Structure of molybdenum-phosphate glasses by X-ray photoelectron spectroscopy (XPS), Journal of Non-Crystalline Solids 212 (1997) 180-191.

[35] V.R. Sreelakshmi, A. Anu Kaliani, M. Jithin, Photochromic and hydrophilic self-cleaning nature of MoO_3 thin films, Journal of Materials Science: Materials in Electronics, 33 (2022) 9525-9537.

[36] B. Yusuf, M.M. Halim, M.R. Hashim, M.Z. Pakhuruddin, Structural, optical, and electrical properties of spray-pyrolyzed MoO_3 thin films by varying precursor molarity, as hole-selective contact for silicon-based heterojunction devices, Journal of Materials Science: Materials in Electronics, 31 (2020) 21802-21812.

[37] T.H. Chiang, H.C. Yeh, The Synthesis of alpha-MoO_3 by Ethylene Glycol, Materials (Basel), 6 (2013) 4609-4625.

[38] D. Divya, K.V. Madhuri, Effect of Substrate Temperature on the Growth of Molybdenum

Trioxide Thin Films, Crystallography Reports, 65 (2020) 792-797.

[39] V. Nirupama, S. Uthanna, Investigations on morphological and electrical studies of sputtered MoO_3 films, Journal of Materials Science: Materials in Electronics, 27 (2015) 3668-3674.

[40] O. de Melo, Y. Gonzalez, A. Climent-Font, P. Galan, A. Ruediger, M. Sanchez, C. Calvo-Mola, G. Santana, V. Torres-Costa, Optical and electrical properties of MoO_2 and MoO_3 thin films prepared from the chemically driven isothermal close space vapor transport technique, J Phys Condens Matter, 31 (2019) 295703.

[41] K.H. Krishna, O.M. Hussain, C. Guillen, Photo- and Electrochromic Properties of Activated Reactive EvaporatedMoO_3 Thin Films Grown on Flexible Substrates, Research Letters in Nanotechnology, 2008 (2008) 1-5.

[42] V.R. Sreelakshmi, A.A. Kaliani, M. Jithin, Study of thermochromic and photocatalytic properties of MoO_3 thin films, Superlattices and Microstructures, 161 (2022).

[43] S.A. Tomas, M.A. Arvizu, O. Zelaya-Angel, P. Rodriguez, Effect of ZnSe doping on the photochromic and thermochromic properties of MoO_3 thin films, Thin Solid Films, 518 (2009) 1332-1336.

[44] B.A. Samad, C. Duguay, The dependence of electrical properties of Molybdenum Trioxide Thin Films on substrate temperature, 2021 Photonics North (PN), 2021, pp. 1-4.

[45] H.M. Martineza, J. Torres, L.D. Lopez Carrenoa, M.E. Rodriguez-Garcia, Effect of the substrate temperature on the physical properties of molybdenum tri-oxide thin films obtained through the spray pyrolysis technique, Materials Characterization, 75 (2013) 184-193.

[46] O Lupan, V Trofim, V Cretu, I Stamov, N N Syrbu, I Tiginyanu, Y K Mishra, R Adelung, Investigation of optical properties and electronic transitions in bulk and nano-microribbons of molybdenum trioxide, Journal of Physics D: Applied Physics, 47 (2014) 1-8.

[47] S. Zhou, M. Yahaya, M.M. Salleh, I.A. Talib, N.M. Nor, Y. Wang, Y.-X. Chen, S. Mao,

Preparation and physical properties of MoO_3 thin films, Third International Conference on Thin Film Physics and Applications, (1998) 42-46.

[48] P.R. Huang, Y. He, C. Cao, Z.H. Lu, Impact of lattice distortion and electron doping on alpha-MoO_3 electronic structure, Sci Rep, 4 (2014) 7131.

[49] S. Yazdani, R. Kashfi-Sadabad, T.D. Huan, M.D. Morales-Acosta, M.T. Pettes, Polyelectrolyte-Assisted Oxygen Vacancies: A New Route to Defect Engineering in Molybdenum Oxide, Langmuir, 34 (2018) 6296-6306.

[50] Y. Li, H. Yu, X. Huang, Z. Wu, M. Chen, A simple synthesis method to prepare a molybdenum oxide hole-transporting layer for efficient polymer solar cells, RSC Advances, 7 (2017) 7890-7900.

[51] N. Lopez-Pinto, T. Tom, J. Bertomeu, J.M. Asensi, E. Ros, P. Ortega, C. Voz, Deposition and characterisation of sputtered molybdenum oxide thin films with hydrogen atmosphere, Applied Surface Science, 563 (2021) 150285.

[52] H. Peelaers, M.L. Chabinyc, C.G. Van de Walle, Controllingn-Type Doping in MoO_3, Chemistry of Materials, 29 (2017) 2563-2567.

CHAPTER 4

Impact of deposition temperature and heat treatment on properties of molybdenum oxide thin films deposited by thermal evaporation technique

Thin films of MoO_{3-x} can be prepared by physical vapour deposition methods such as thermal evaporation [1], rf-sputtering (non-reactive or reactive) [2, 3] and other methods like electrochemical (cathodic electro deposition) [4], spin coating [5] and many more. Two of the most common procedures are sputtering and thermal evaporation. According to comparative research on MoO_{3-x} films made by thermal evaporation and sputtering processes, thermal evaporation develops more resistive MoO_{3-x} films with a high work function value [6]. As a result, the thermal evaporation method is the most extensively utilised method for developing dopant-free asymmetric hetero contacts. The optoelectronic properties (transparency, band gap, work function) of molybdenum oxide are sensitive to the presence of oxygen vacancies (O_v), which further depends on methodology and conditions used for film preparation. Post-heat treatment like annealing also affects the structural, morphological, optical and electrical properties of MoO_{3-x} [7, 8]. As, MoO_{3-x} is subjected to various heat treatments during the

preparation of other layers such as the transparent conducting oxide layer and back/front electrodes while fabricating solar cells, it is essential to select the annealing temperature at which the optical and electrical properties of MoO_{3-x} can be retained without compromising their properties when compared to as-deposited films.

In this chapter, the effects of deposition temperature and subsequent heat treatment on various properties of MoO_{3-x} films deposited by thermal evaporation of MoO_3 powder are investigated in detail. The oxygen vacancy concentration and work function of the as-deposited and vacuum-annealed MoO_{3-x} films are analysed using XPS and KPFM, respectively.

4.1 Experimental details

Molybdenum oxide (MoO_{3-x}) thin films were deposited on Corning glass (CG) 1737 and n type crystalline silicon (c-Si (n)) substrates using thermal evaporation. Pure MoO_3 powder (99.99%) purchased from Sigma Aldrich was used for preparing thin films. CG and c-Si (n) substrates were cleaned following the standard cleaning methods as mentioned in Chapter 2, section 2.2. Two sets of films were deposited, one at room temperature (RT) and another at 100°C keeping thickness in the range of ~22-28 nm and its effect on different properties of MoO_{3-x} were thoroughly investigated. Subsequently, films prepared at RT were annealed under high vacuum condition at 130 °C and 150 °C respectively for 30 minutes each to investigate how the heat treatment affects the structural, optical and electrical properties of MoO_{3-x} films.

4.2 Results and discussion

4.2.1 Effect of deposition temperature (T_s) on MoO_{3-x} properties

4.2.1.1 FESEM studies

Field emission scanning electron microscopy (FESEM) images of MoO_{3-x} films deposited at RT and 100 °C are shown in Figure 4.1. FESEM images confirmed the formation of compact

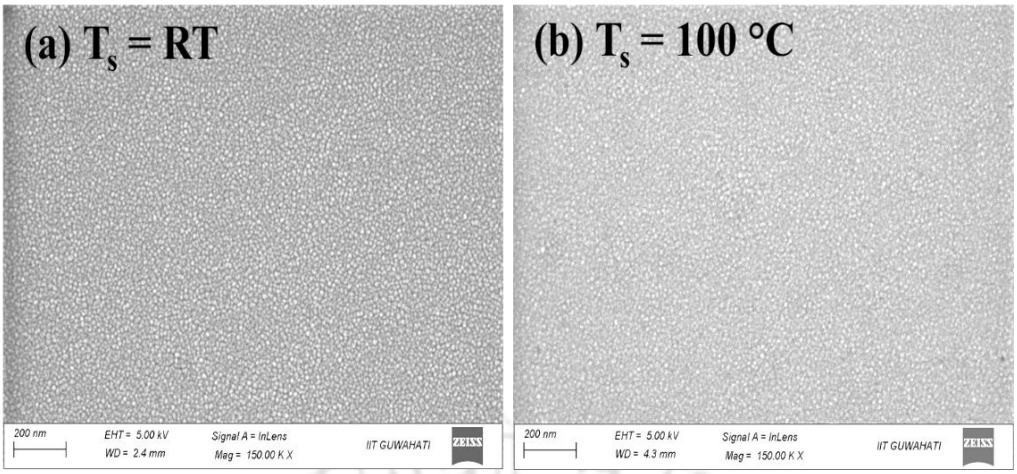

Figure 4.1: *FESEM images of molybdenum oxide films deposited on CG substrates at (a) room temperature and (b) 100 ℃.*

and uniform surface for films prepared at both temperatures.

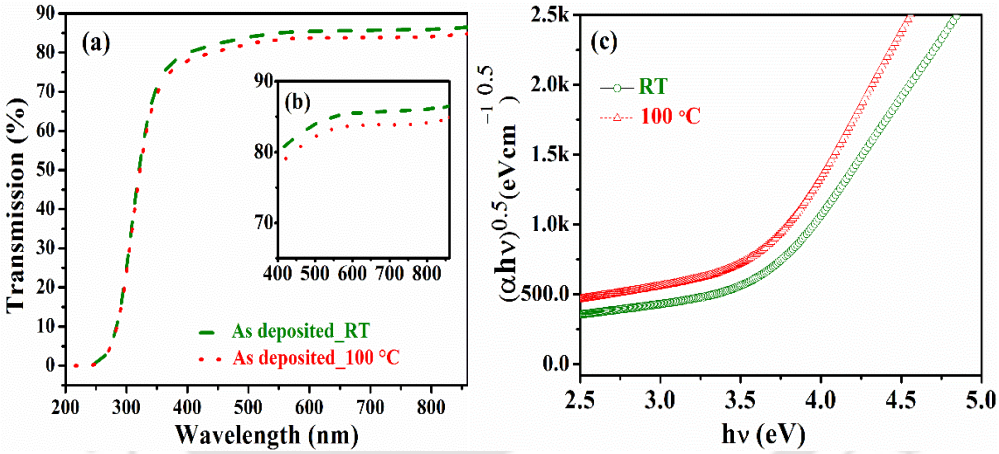

Figure 4.2: *Transmission spectra of molybdenum oxide films deposited on CG substrates (a) at room temperature and 100 ℃ (b) zoomed inset image showing transmission variation for different deposition temperatures in visible range and (c) Taucs' plot of MoO_{3-x} films deposited at RT and 100 ℃.*

4.2.1.2 UV-Vis studies

The transmission spectra of the MoO_{3-x} films deposited on corning glass substrates at room temperature (RT) and 100 °C are shown in Figure 4.2a and its enlarged view is shown as inset image in Figure 4.2b. Using profilometry, the thickness of films is found to be 28±5 nm for room temperature and 23±4 nm for 100 °C. Even though the thickness of RT film is slightly

more, a small increase in transmission is noticed for this film in the visible range. Though no evident shift in the absorption edge is observed in transmission spectra, Tauc plot predicted a small change in band gap of films deposited at two different temperatures (3.35±0.02 eV for 100 °C and 3.41±0.04 eV for RT).

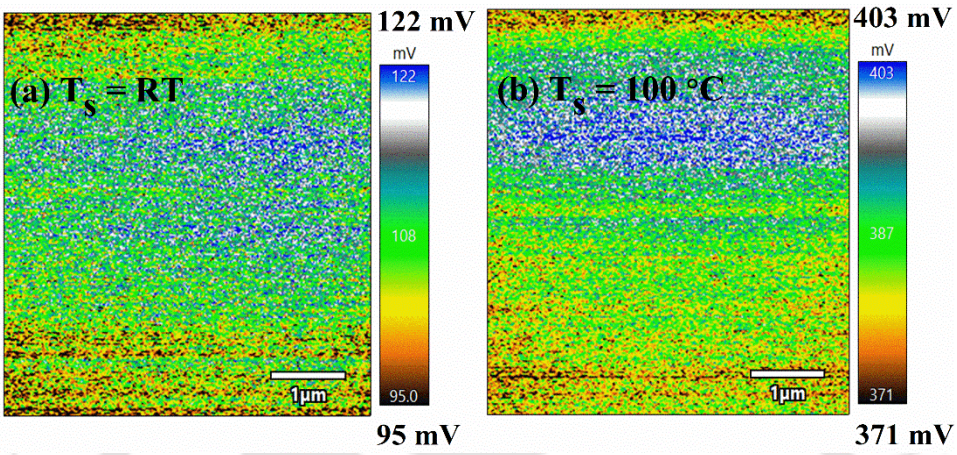

Figure 4.3: *KPFM images of molybdenum oxide films deposited on c-Si (n) substrates at (a) room temperature and (b) 100 °C.*

4.2.1.3 KPFM studies

Work function of molybdenum oxide depends on the stoichiometry ratio (O/Mo) and oxygen anion (O^{2-}) concentration in MoO_{3-x} matrix and these two factors are influenced by the temperature at which MoO_{3-x} is deposited and subsequently annealed. By measuring contact potential difference (CPD) between tip and MoO_{3-x} using Kelvin probe force microscopy (KPFM), the effect of deposition temperature on work function (Φ) is examined. Figure 4.3 shows CPD mapping of as deposited films prepared at RT and 100 °C. The work function values of all MoO_{3-x} films deposited on silicon substrates (c-Si (n)) are determined using Chapter 2, equation 2.12 [9]. The average CPD has increased with a change in the deposition temperature from RT to 100 °C, resulting in a decrease in effective work function from 4.75±0.02 eV to 4.47±0.01 eV for films deposited at high T_s. Apart from the development of oxygen vacancies and metal cations in lower oxidation states, another possible cause of change

in work function is the growth of surface diploes on film surface [10]. In order to determine the exact cause of the work function reduction, XPS measurements are carried out and discussed in following section.

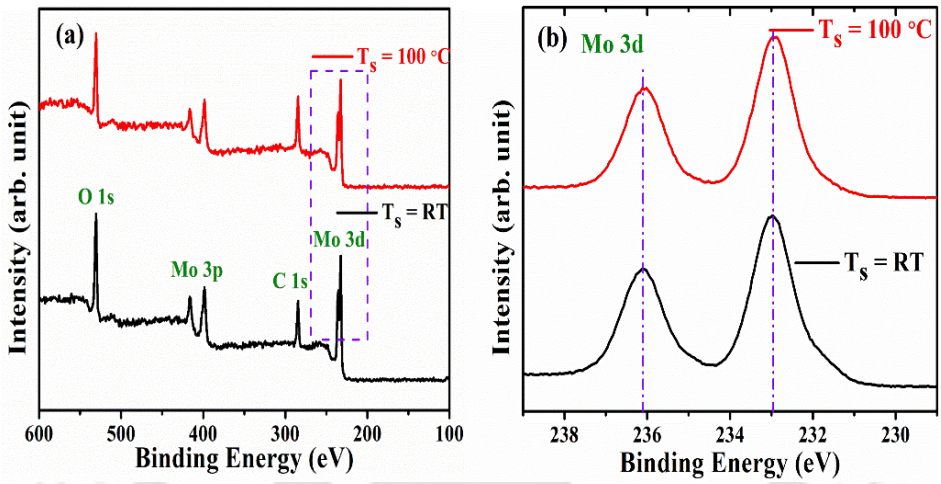

Figure 4.4: *(a) All core level XPS spectra and (b) Mo 3d spectra of molybdenum oxide films deposited on corning glass substrates at RT and 100 ℃.*

4.2.1.4 XPS studies

According to the XPS spectra shown in Figure 4.4a, the existence of oxygen (O 1s), molybdenum (Mo 3p, Mo 3d), and carbon (C 1s) atoms are confirmed [11]. The XPS spectra show absence of any other element's signature. Carbon contamination is inevitable because samples are exposed to air during its loading into vacuum chamber for XPS measurements. Further fitting of the recorded XPS spectra is done to investigate the quantitative changes [12]. The deconvoluted O 1s and Mo 3d spectra are shown in Figure 4.5. Mo 3d doublets: $3d_{5/2}$ and $3d_{3/2}$ peaks are observed at 236.10 eV and 232.95 eV respectively [13]. Peak at 530.79 eV in the O 1s spectra (Figure 4.5a and 4.5b) denotes the contribution of oxygen atoms bonded to molybdenum atoms (Mo-O). However, the peak at 531.74 eV indicates that MoO_{3-x} films have oxygen vacancies [14]. This peak also suggests the formation of a Mo-OH bond, which is composed of molybdenum atoms bonded to a hydroxyl group [14-16]. Figure 4.6 shows the relative contribution of Mo^{6+}, Mo^{5+}, Mo-O and oxygen vacancy obtained from the fitted

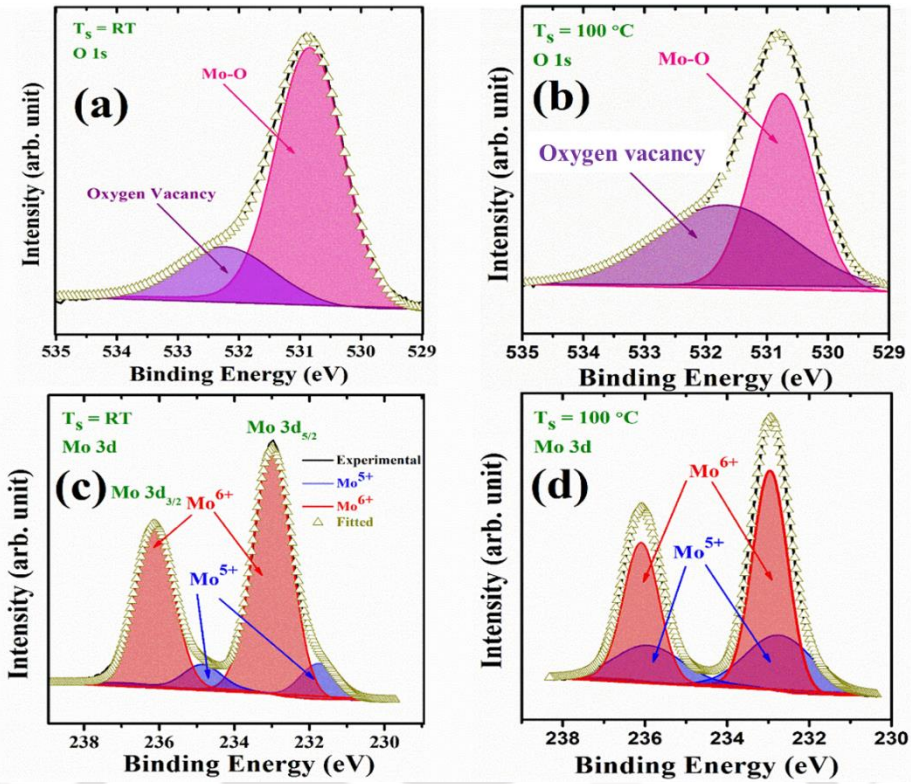

Figure 4.5: *(a) O 1s and (c) Mo 3d spectra of molybdenum oxide films deposited at RT and (b) O 1s and (d) Mo 3d spectra of films deposited at 100 ℃.*

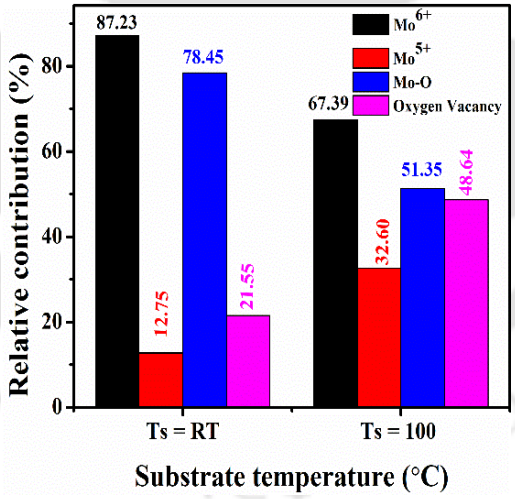

Figure 4.6: *Relative concentration of MoO_{3-x} films deposited on CG substrates at RT and 100 ℃.*

spectra. Higher deposition temperature has enhanced O_v/Mo-O ratio (0.27 for RT deposition and 0.94 for 100 °C deposition) and Mo^{5+}/Mo^{6+} ratio (0.15 for RT deposition and 0.48 for 100 °C deposition) suggesting the oxygen vacancy to be the main cause of reduction of work function for high T_s films.

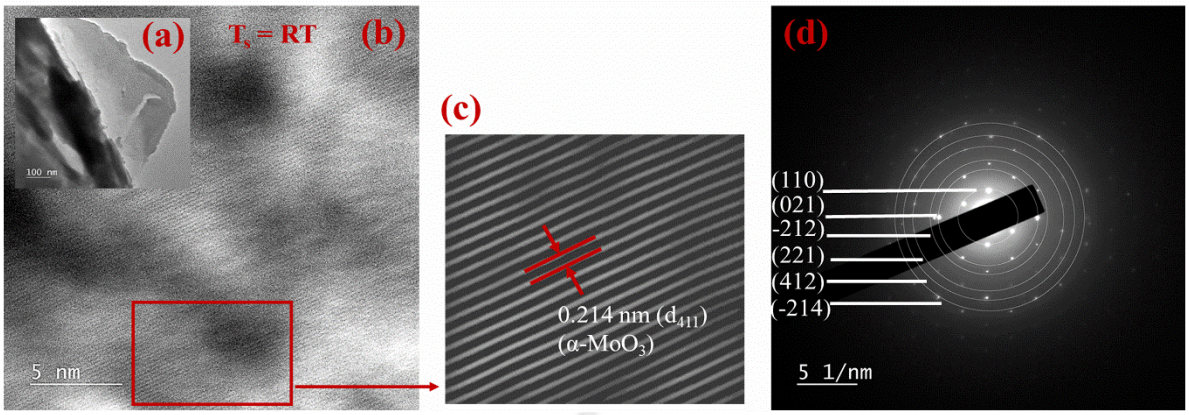

Figure 4. 7: *(a) TEM image (b) HRTEM, (c) respective plane images and (d) SAED pattern of molybdenum oxide films deposited at RT.*

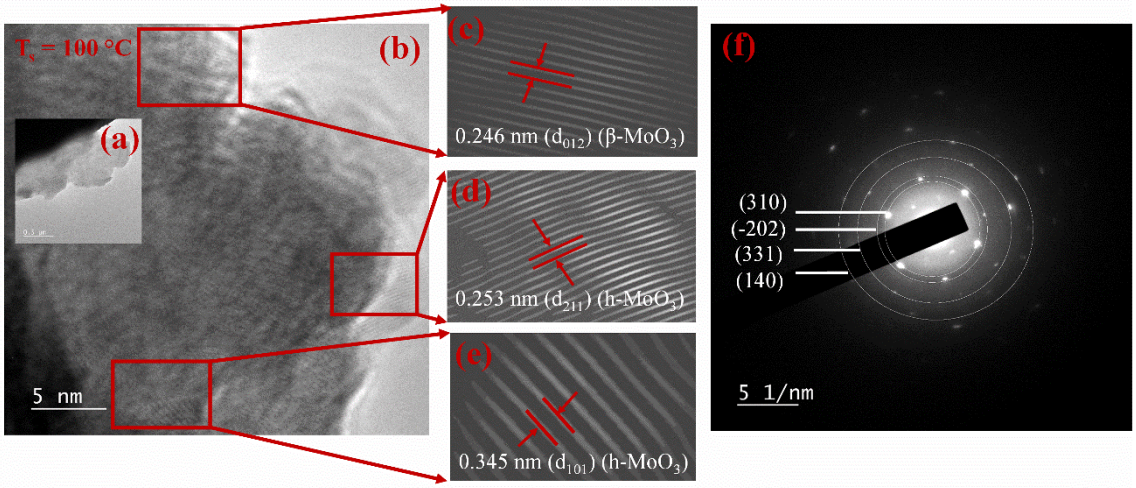

Figure 4.8: *(a) TEM image (b) HRTEM, (c), (d), (e) respective plane images and (f) SAED pattern of molybdenum oxide films deposited at 100 °C.*

4.2.1.5 FETEM studies

Oxygen vacancies not only affect the optoelectronic properties of MoO_{3-x} films but also induce some structural changes [17]. Field emission transmission electron microscopy (FETEM) is performed to get more information about the role of deposition temperatures on structural properties of MoO_{3-x} films. For FETEM analysis, MoO_{3-x} films are directly grown on TEM grids. Nano-sheets of MoO_{3-x} films are obtained for both RT film as well as 100 °C film as confirmed from TEM images shown in Figure 4.7a and 4.8a respectively. The formation of mixed phases (monoclinic: β-MoO_3 and orthorhombic: α-MoO_3) of molybdenum oxide

is confirmed by high resolution transmission electron microscopy (HRTEM) image (Figure 4.7b) and selected area electron diffraction (SAED) pattern (Figure 4.7d). Planes (110), (021), (-212), and (412) obtained in SAED correspond to β-MoO_3, whereas planes (221) and (-214) correspond to α-MoO_3. Planes corresponding to the hexagonal (h-MoO_3) phase and the β phase are obtained in the HRTEM image (Figure 4.8b) of 100 °C film. The formation of h-MoO_3 and β-MoO_3 for T_s = 100 °C is further confirmed by the SAED pattern presented in Figure 4.8f. Planes (310) and (331) correspond to h-MoO_3 whereas planes (-202) and (140) belong to β phase of MoO_3. From FETEM study, it is concluded that RT deposited films consist of stable phase of MoO_3 (α-MoO_3) along with its metastable monoclinic phase whereas 100 °C films consist of MoO_3 in its metastable monoclinic and hexagonal phases. Thus, the mixed metastable phases of MoO_3 and the creation of an oxygen-deficient film at this temperature can both contribute to the drop in work function observed for high temperature MoO_{3-x} film [17]. At high T_s, MoO_{3-x} particles have high energies and are less tightly bonded so there is a chance that energetic and loosely bonded oxygen atoms, may escape the surface when T_s is high [18]. As the deposition temperature rises, this causes an increase in oxygen vacancies and the formation of less resistant MoO_{3-x} films.

4.2.2 Influence of post annealing on MoO_{3-x} properties

During the fabrication of MoO_{3-x}/c-Si (n) heterojunction solar cell, MoO_{3-x} layer is subjected to heat treatment while depositing other layers such as indium tin oxide (ITO) and back electrode. As the work function and optical properties are sensitive to heat treatment such as annealing temperature, so it is necessary to study how the optoelectronic properties of MoO_{3-x} are affected during deposition of ITO and back electrode. To investigate the effects of heat treatment on the characteristics of MoO_{3-x} films, post-annealing of RT-deposited MoO_{3-x} films is performed at 130 °C (A_130 °C) and 150 °C (A_150 °C) for 30 minutes under high vacuum.

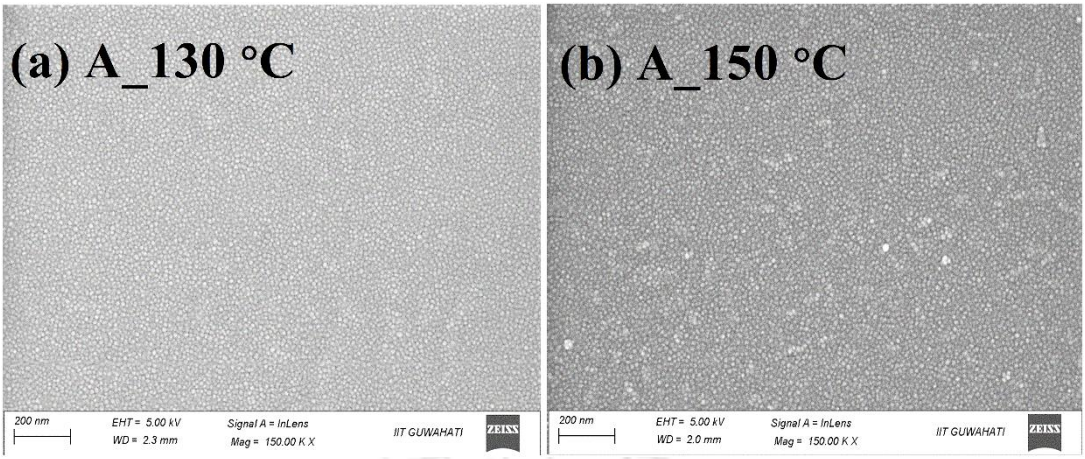

Figure 4.9: *FESEM images of molybdenum oxide films deposited on CG substrates at RT and annealed for 30 minutes at (a) 130 ℃ and (b) 150 ℃.*

4.2.2.1 FESEM studies

FESEM images for heat treated MoO_{3-x} films are shown in Figure 4.9. When MoO_{3-x} films deposited at room temperature have undergone heat treatment at 130 ℃, no noticeable variation in surface morphology (Figure 4.9a) is observed when compared with as deposited film. When the annealing temperature is raised to 150 °C, coalescence began and a rough MoO_{3-x} film is formed, as illustrated in Figure 4.9b, which can affect device performance when MoO_{3-x} is being used as a hole selective layer in silicon-based solar cells [19].

4.2.2.2 UV-Vis studies

Post-annealing of MoO_{3-x} films not only changed the surface morphology but also a decrease in transmission is observed as annealing temperature is increased. The maximum transmission of 87 % is observed for as deposited films which decreased to 80% and 76% for films annealed at 130 °C and 150 °C respectively (Figure 4.10b) which is also accompanied by a shift in absorption edge (Figure 4.10c). Reduced transmission and red shift in absorption edge with an increase in post-annealing temperature is due to the presence of larger grains and rough surface for films annealed at 150 °C as confirmed from FESEM study. The band gap of films decreased

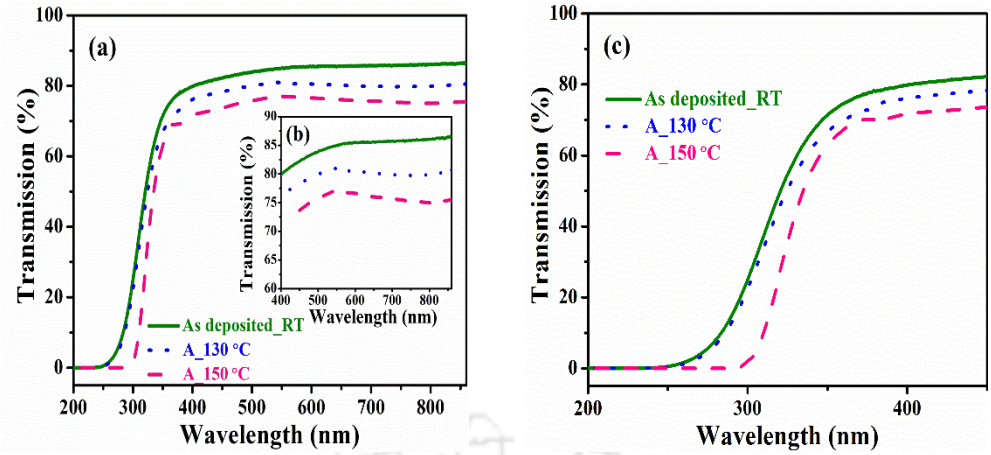

Figure 4.10: *Transmission spectra of molybdenum oxide films (a) deposited at room temperature and annealed at 130 ℃ and 150 ℃ (zoomed inset image (b) shows the transmission variation of as deposited and annealed MoO_{3-x} films in visible range), (c) transmission spectra in the range of 200 nm-450 nm to visualize absorption edge shift of MoO_{3-x} films deposited at RT and annealed at 130 ℃ and 150 ℃. All films are on CG substrates.*

from 3.41±0.04 eV (as deposited) to 3.38±0.02 eV and 3.25±0.05 eV for films annealed at 130 °C to 150 °C respectively. The decrease in transparency and band gap from the values observed for as deposited MoO_{3-x} film may also be caused by the reduction of Mo atoms to lower valence states and/or the development of oxygen vacancies in MoO_{3-x} films during heat treatment [7, 18, 20, 21]. Oxygen vacancies behave as donor centres and appear as trap states between the conduction and valence bands, lowering the molybdenum oxide's band gap.

4.2.2.3 KPFM studies

For this study, MoO_{3-x} films are deposited at RT on c-Si (n) substrates, then annealed for 30 minutes at 130 °C and 150 °C, respectively. KPFM imaging with maximum and minimum CPD values of annealed MoO_{3-x} films are displayed in Figure. 4.11. The Φ values (Figure 4.12) of MoO_{3-x} are noticed to decrease from 4.75±0.02 eV for as deposited film to 4.66±0.02 eV and 4.54±0.03 eV for films annealed at 130 °C and 150 °C respectively. The present study confirmed that heat treatment affects the work function of MoO_{3-x}. A decrease in the work function after annealing reflects the formation of more oxygen vacancies as the annealing temperature is raised [22, 23]. To further confirm these results, XPS analysis of annealed

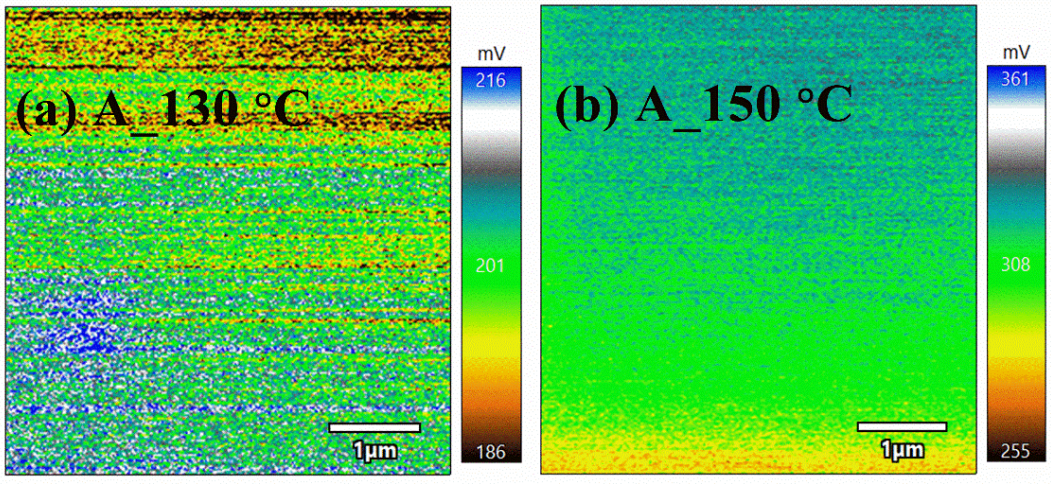

Figure 4.11: *KPFM images of molybdenum oxide films deposited on c-Si (n) at RT and annealed for 30 minutes at (a) 130 ℃ and (b) 150 ℃.*

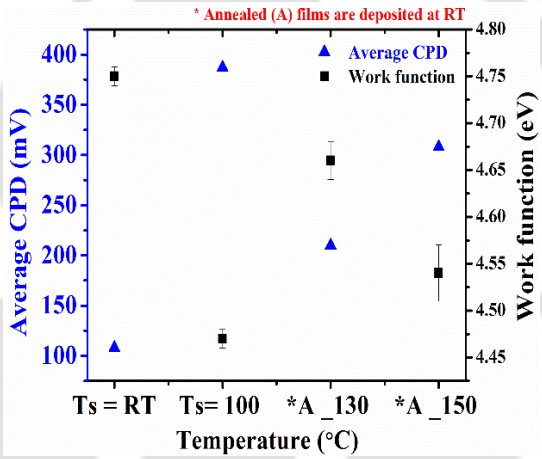

Figure 4.12: *Average CPD and work function of films prepared at RT, 100 ℃ and annealed at 130 ℃ and 150 ℃ for 30 minutes.*

MoO_{3-x} films are performed.

4.2.2.4 XPS studies

O 1s XPS spectra for annealed films are shown in Figures 4.13. Oxygen vacancies contribution is found to increase from 21.55% for as deposited film to 28.30% and 36.98% for films annealed at 130 ℃ and 150 ℃ respectively, which is responsible for decrease in Φ of annealed films [1, 10, 24]. From Mo 3d spectra (Figures 4.13), it is observed that annealing has also enhanced the transformation of Mo^{6+} to Mo^{5+} because of increase in O_v. The relative

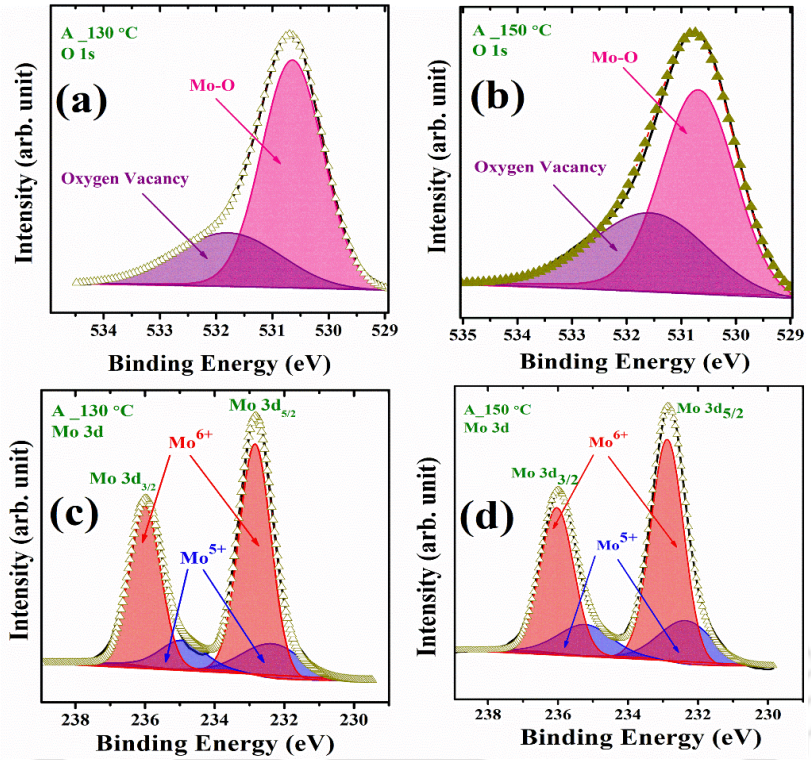

Figure 4.13: *(a) O 1s and (c) Mo 3d spectra of molybdenum oxide films deposited on CG substrates at RT and annealed at 130 ℃ (b) O 1s and (d) Mo 3d spectra of films deposited at RT and annealed at 150 ℃.*

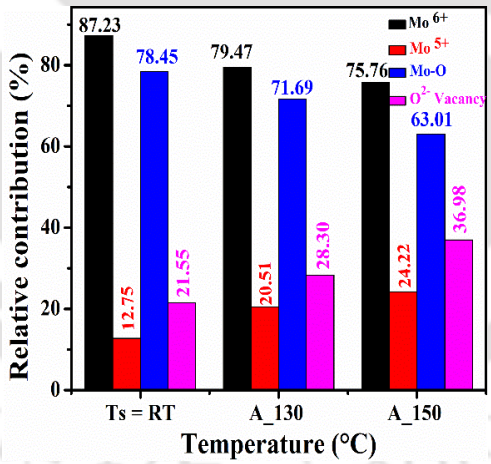

Figure 4. 14: *Relative contribution of MoO_{3-x} films deposited at RT and 100 ℃ and annealed at 130 ℃ and 150 ℃.*

contribution of Mo^{6+}, Mo^{5+}, Mo-O bond and O_v vacancies are shown in Figure 4.14.

4.2.2.5 FETEM studies

FETEM analysis is carried out to investigate the impact of annealing temperature on structural properties of molybdenum oxide films. From SAED pattern shown in Figure 4.15, it is

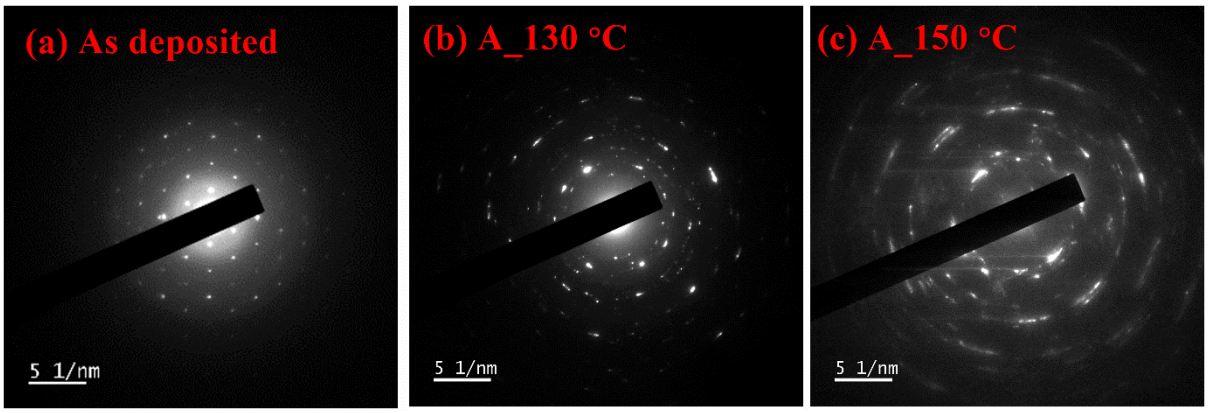

Figure 4.15: *SAED patterns of MoO_{3-x} film (a) deposited at T_s = RT, (b) annealed at 130 ℃ and (c) annealed at 150 ℃ respectively.*

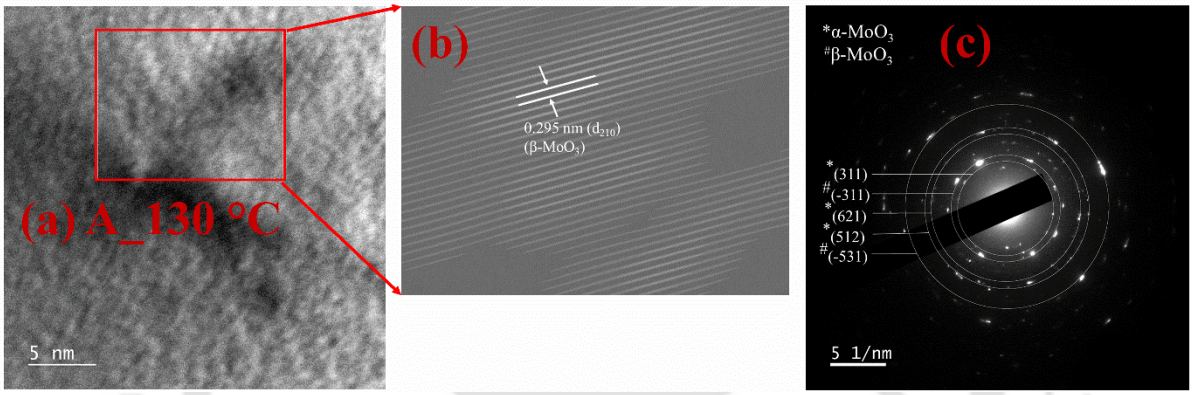

Figure 4.16: *(a) HRTEM images, (b) respective plane and (c) SAED pattern of MoO_{3-x} film annealed at 130 ℃ respectively.*

identified that as deposited films show well-organized diffraction patterns (Figure 4.15a), whereas annealed films exhibit distortion (Figure 4.15b and 4.15c). These differences could be the result of rearrangement of atoms and oxygen vacancies produced during annealing. For film that has been annealed at 150 ℃, SAED pattern (Figure 4.15c) is composed of diffused and coalesced diffraction points, which show that the oxygen vacancies created during the annealing process have accumulated. These vacancies modify the interatomic distance and orientation of the MoO_6 octahedra, changing the lattice properties of the MoO_3 unit cell [25]. In all cases (Figure 4.7, Figure 4.16 and Figure 4.17) whether it is as deposited and post-annealed, formation of α and β phases of MoO_3 are observed. For as deposited and 130 ℃ annealed film, single lattice plane is present in HRTEM images (Figure 4.7b and Figure 4.16

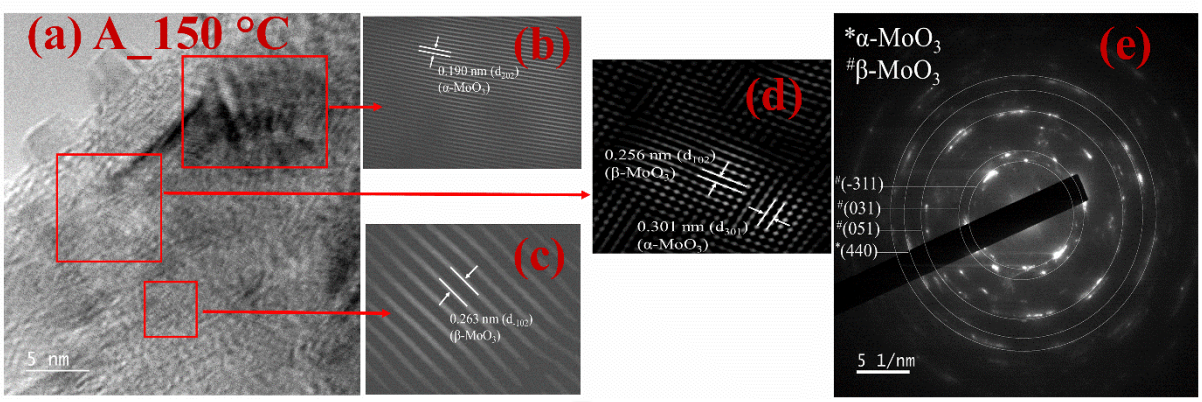

Figure 4.17: *(a) HRTEM images, (b), (c), (d) respective planes and (e) SAED pattern of MoO_{3-x} film annealed at 150 °C respectively.*

a). However, HRTEM image of 150 °C annealed film shows the presence of different distorted lattice planes (Figure 4.17d) confirming the transition of crystalline nature of MoO_{3-x} to polycrystalline.

These results suggest that low deposition temperature and low heat treatment temperature are desired for the preparation of MoO_{3-x} films with fewer oxygen vacancies making it suitable for use as hole selective layer in semiconductor devices especially in solar cells.

4.3 Conclusion

Because of the sensitivity of MoO_{3-x} film properties to deposition temperature and subsequent heat treatment such as annealing, it is essential to investigate how these factors affect the different properties of MoO_{3-x} which further impact the performance of dopant free MoO_{3-x}/c-Si (n) solar cells. That's why the influence of deposition temperature (RT and 100 °C) and heat treatment (vacuum annealing at 130 °C and 150 °C) on the optical, electrical and structural properties of MoO_{3-x} films is thoroughly investigated in this work. With an increase in deposition and annealing temperatures, a decrease in transmission and band gap of MoO_{3-x} films are noticed. When the deposition temperature is increased to 100 °C, the work function decreased by ~0.28 eV, according to KPFM study. Moreover, the annealing has also reduced

Φ value, changing from 4.75±0.02 eV for film deposited at RT to 4.54±0.03 eV for film annealed at 150 °C. According to XPS analysis, the causes of the considerable drop in work function values are increase in oxygen vacancies and Mo^{5+} cations concentration in annealed MoO_{3-x} films.

4.4 References

[1] Y. Jiang, S. Cao, L. Lu, G. Du, Y. Lin, J. Wang, L. Yang, W. Zhu, D. Li, Post-annealing Effect on Optical and Electronic Properties of Thermally Evaporated MoO_x Thin Films as Hole-Selective Contacts for p-Si Solar Cells, Nanoscale Res Lett, 16 (2021) 87.

[2] X. Fan, G. Fang, P. Qin, N. Sun, N. Liu, Q. Zheng, F. Cheng, L. Yuan, X. Zhao, Deposition temperature effect of RF magnetron sputtered molybdenum oxide films on the power conversion efficiency of bulk-heterojunction solar cells, Journal of Physics D: Applied Physics, 44 (2011) 045101.

[3] J. Kumari, P. Agarwal, Optimization of deposition conditions to tune optoelectronic properties of MoO_{3-x} films prepared by RF-sputtering technique, Vacuum, 216 (2023) 112485.

[4] T.M. McEvoy, K.J. Stevenson, J.T. Hupp, X.J. Dang, Electrochemical preparation of molybdenum trioxide thin films: Effect of sintering on electrochromic and electroinsertion properties, Langmuir, 19 (2003) 4316-4326.

[5] G.R. Mutta, S.R. Popuri, J.I.B. Wilson, N.S. Bennett, Sol-gel spin coated well adhered MoO_3 thin films as an alternative counter electrode for dye sensitized solar cells, Solid State Sciences, 61 (2016) 84-88.

[6] J. Sun, Q. Zheng, S. Cheng, H. Zhou, Y. Lai, J. Yu, Comparing molybdenum oxide thin films prepared by magnetron sputtering and thermal evaporation applied in organic solar cells, Journal of Materials Science: Materials in Electronics, 27 (2015) 3245-3249.

[7] R. Sivakumar, M. Jayachandran, C. Sanjeeviraja, Effect of Annealing on Structural, Surface

and Optical Properties Of PVD-EBE α-MoO_3 Thin Films For Electrochromic Devices, Surface Engineering, 20 (2013) 385-390.

[8] H. Mehmood, G. Bektaş, İ. Yıldız, T. Tauqeer, H. Nasser, R. Turan, Electrical, optical and surface characterization of reactive RF magnetron sputtered molybdenum oxide films for solar cell applications, Materials Science in Semiconductor Processing, 101 (2019) 46-56.

[9] W. Melitz, J. Shen, A.C. Kummel, S. Lee, Kelvin probe force microscopy and its application, Surface Science Reports, 66 (2011) 1-27.

[10] M.T. Greiner, L. Chai, M.G. Helander, W.-M. Tang, Z.-H. Lu, Transition Metal Oxide Work Functions: The Influence of Cation Oxidation State and Oxygen Vacancies, Advanced Functional Materials, 22 (2012) 4557-4568.

[11] M.A.S. G.D. Khattak , A.S. A-Harthi, David J. Thompson and L.E. Wenger, Structure of molybdenum-phosphate glasses by X-ray photoelectron spectroscopy (XPS), Journal of Non-Crystalline Solids 212 (1997) 180-191.

[12] A.K.-V. Alexander V. Naumkin, Stephen W. Gaarenstroom, and Cedric J. Powell, NIST X-ray Photoelectron Spectroscopy Database, NIST Standard Reference Database 20, National Institute of Standards and Technology, Gaithersburg MD, 20899 (2000).

[13] G.G.a.L. Hultman, C1sPeak of Adventitious Carbon Aligns to the Vacuum Level:Dire Consequences for Material'sBonding Assignment by Photoelectron Spectroscopy, ChemPhysChem 18 (2017) 1507 –1512.

[14] V.R. Sreelakshmi, A. Anu Kaliani, M. Jithin, Photochromic and hydrophilic self-cleaning nature of MoO_3 thin films, Journal of Materials Science: Materials in Electronics, 33 (2022) 9525-9537.

[15] A. Saha, A. Paul, D.N. Srivastava, A.B. Panda, Porous carbon incorporated β-Mo_2C hollow sphere: An efficient electrocatalyst for hydrogen evolution reaction, International Journal of Hydrogen Energy, 43 (2018) 21655-21664.

[16] Q. Wei, P. Song, Z. Li, Z. Yang, Q. Wang, Enhanced triethylamine gas sensing performance of the PbS nanoparticles-functionalized MoO_3 nanobelts, Journal of Materials Science: Materials in Electronics, 30 (2019) 2898-2907.

[17] N. Kodan, A.P. Singh, M. Vandichel, B. Wickman, B.R. Mehta, Favourable band edge alignment and increased visible light absorption in β-MoO_3/α-MoO_3 oxide heterojunction for enhanced photoelectrochemical performance, International Journal of Hydrogen Energy, 43 (2018) 15773-15783.

[18] N. Lopez-Pinto, T. Tom, J. Bertomeu, J.M. Asensi, E. Ros, P. Ortega, C. Voz, Deposition and characterisation of sputtered molybdenum oxide thin films with hydrogen atmosphere, Applied Surface Science, 563 (2021) 150285.

[19] S. Touihri, A. Arfaoui, Y. Tarchouna, A. Labidi, M. Amlouk, J.C. Bernede, Annealing effect on physical properties of evaporated molybdenum oxide thin films for ethanol sensing, Applied Surface Science, 394 (2017) 414-424.

[20] M. Rellan-Pineiro, N. Lopez, One Oxygen Vacancy, Two Charge States: Characterization of Reduced alpha-MoO_3 (010) through Theoretical Methods, J Phys Chem Lett, 9 (2018) 2568-2573.

[21] S. Subbarayudu, V. Madhavi, S. Uthanna, Growth of MoO_3 Films by RF Magnetron Sputtering: Studies on the Structural, Optical, and Electrochromic Properties, ISRN Condensed Matter Physics, 2013 (2013) 1-9.

[22] A. Lakshmi-Narayana, O.M. Hussain, C.V. Ramana, M. Camacho-Lopez, A. Abdel-Ghany, A. Hashem, A. Mauger, C.M. Julien, Molybdenum-Suboxide Thin Films as Anode Layers in Planar Lithium Microbatteries, Electrochem, 1 (2020) 160-187.

[23] D. Xiang, C. Han, J. Zhang, W. Chen, Gap states assisted MoO_3 nanobelt photodetector with wide spectrum response, Sci Rep, 4 (2014) 4891.

[24] S.-Y. Lin, Y.-C. Chen, C.-M. Wang, P.-T. Hsieh, S.-C. Shih, Post-annealing effect upon

optical properties of electron beam evaporated molybdenum oxide thin films, Applied Surface Science, 255 (2009) 3868-3874.

[25] D.E. Diaz-Droguett, A. Zuniga, G. Solorzano, V.M. Fuenzalida, Electron beam-induced structural transformations of MoO_3 and MoO_{3-x} crystalline nanostructures, Journal of Nanoparticle Research, 14:679 (2012).

CHAPTER 5

Oxygen Plasma Treatment on MoO_{3-x} films deposited by thermal evaporation technique

This chapter discusses the effect of oxygen plasma treatment on structural, optical, electrical and compositional properties of thermally evaporated MoO_{3-x} films. Thermal evaporation method is the commonly used method for depositing molybdenum oxide films because its forms good quality MoO_{3-x} films having high band gap and high transparency. For its use as hole selective layer (HSL) in c-Si heterojunction solar cells, MoO_{3-x} should have wide band gap, high work function and high trap density. All these factors are strongly influenced by oxygen deficiency, metal cation concentrations and stoichiometric ratio of O/Mo. In MoO_{3-x} films, these factors are sensitive towards the techniques used for its synthesis, deposition and annealing temperatures, which we have already discussed in previous chapters. Literature reports that work function of MoO_{3-x} decreases by ~1 eV on exposure to ambient conditions. For efficient and stable devices, it is necessary to recover the decrease in work function by subsequent treatments. So, with the motivation to improve or recover the work function of MoO_{3-x}, oxygen plasma treatment (OPT) using plasma enhanced chemical vapor deposition technique (PECVD) is carried out on MoO_{3-x} films deposited by thermal evaporation. Here,

sequential optimization of OPT conditions are done. For this at first, rf power is varied, followed by oxygen flow rate (OFR) and OPT duration and its effect on different properties are studied in detail. Further, the optimized OPT conditions are used to improve the work function of thin films (14 nm and 23 nm) suitable for MoO_{3-x}/c-Si(n) solar cells.

5.1 Experimental Details

Molybdenum oxide films were deposited on corning glass 1737 substrates and n-type silicon (c-Si (n)) wafers using thermal evaporation technique. MoO_3 powder (99.99%) purchased from Sigma Aldrich is used for preparing MoO_{3-x} films. Both types of substrates were cleaned using separate cleaning process as described in Chapter 2, section 2.2. After completion of cleaning process, both substrates were dried using dry nitrogen and then loaded to the deposition chamber. The MoO_{3-x} films were deposited at substrate temperature of 100 °C and pressure of 5×10^{-6} mbar. After deposition, MoO_{3-x} films were transferred to PECVD chamber for oxygen plasma treatment. OPT was performed at room temperature and 1 mbar pressure. Treatment parameters such as rf power, oxygen flow rate and oxygen plasma treatment time were varied to study the effect of these parameters on structural, compositional and electrical properties. Initially, rf power was varied from 20 W, 40 W, 60 W to 80 W at fixed oxygen flow rate (OFR) of 10 SCCM; then, OFR was varied from 15 SCCM, 20 SCCM, 25 SCCM to 30 SCCM at fixed rf power of 80 W. Using the optimized conditions obtained from these two series, OPT time was varied from 20 minutes to 30 minutes.

5.2 Results and discussion-

5.2.1 OPT on thick MoO_{3-x} films

5.2.1.1 Raman studies

Figure 5.1a shows the recorded Raman spectra of ~500 nm thick as deposited (untreated)

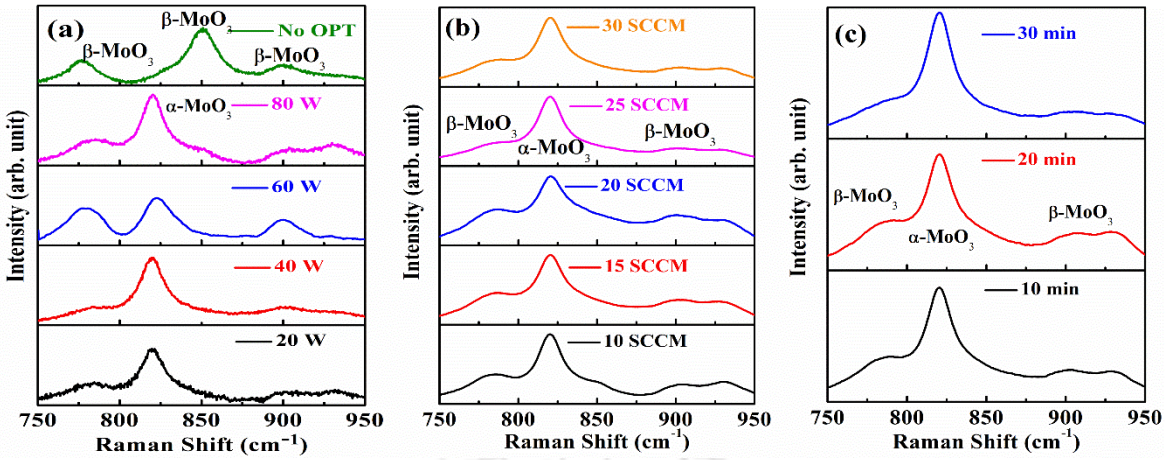

Figure 5.1: *Raman spectra of MoO_{3-x} films treated using oxygen plasma at (a) different rf-power values(OFR 10 SCCM, time 10 min), (b) different oxygen gas flow rates (OPT at 80 W for 10 min) and (c) different OPT times (rf 80 W, OFR 30 SCCM).*

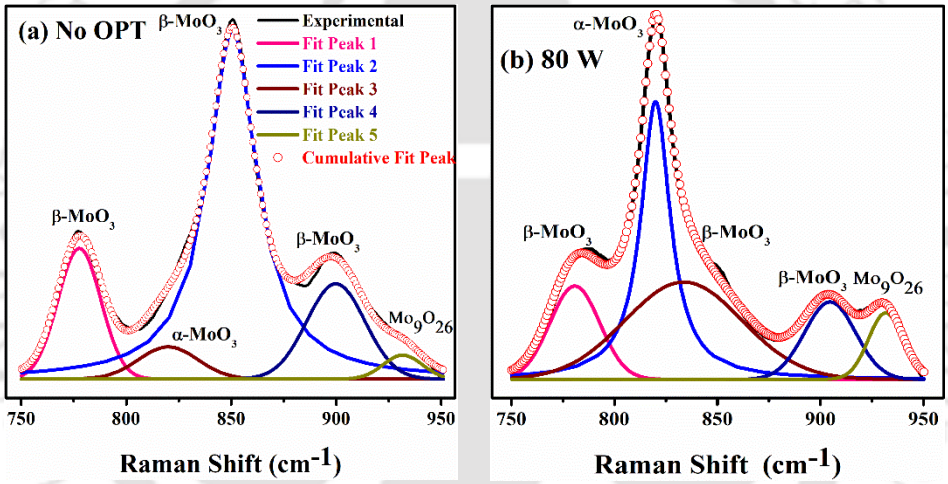

Figure 5.2: *Deconvoluted Raman spectra for (a) untreated MoO_{3-x} film deposited at 100 °C and (b) OPT performed at 80 W.*

MoO_{3-x} films and those treated with oxygen plasma at different rf-power values. The broadness of Raman peaks confirms the amorphous nature of as deposited and OP-treated films. From Raman spectra shown in Figure 5.1a, it is observed that untreated films have a broad and intense peak at 850 cm^{-1} that represents the formation of β phase of MoO_3 i.e. a metastable monoclinic phase [1]. After oxygen plasma treatment, the peak is shifted to ~820 cm^{-1}, which is the characteristics peak of the most stable orthorhombic phase of MoO_3 (α-MoO_3) [1-3]. Raman spectra are deconvoluted to extract information about small peaks present along with the characteristics MoO_3 peak. To get an adequate fit, five peaks are used during the fitting process.

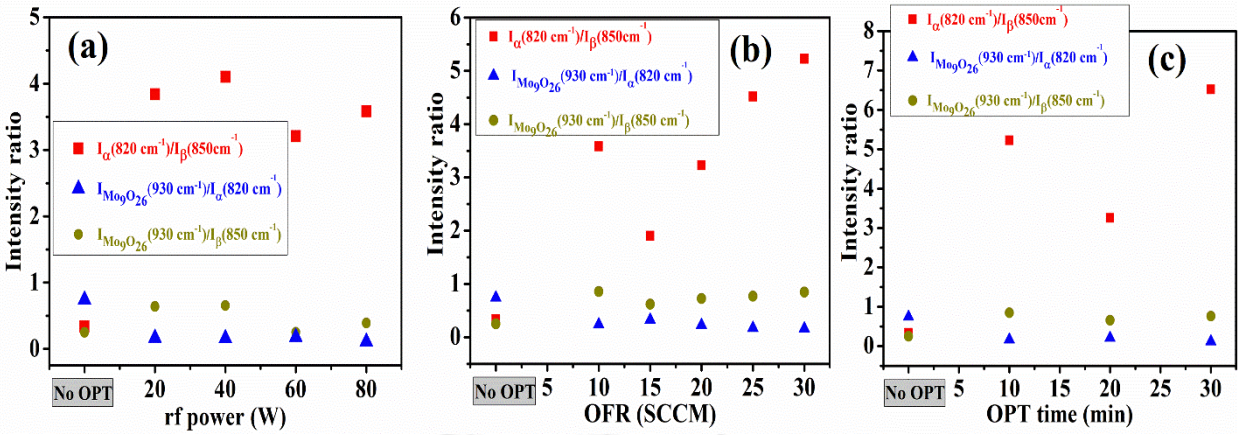

Figure 5.3: *Intensity ratio of Raman peaks of as deposited MoO_{3-x} films and after OPT (a) at different rf-powers value (OFR = 10 SCCM, time = 10 min), (b) at different oxygen gas flow rates (OFR) (rf power = 80 W, time = 10 min) and (c) at different OPT times (rf power = 80 W, OFR = 30 SCCM).*

The deconvoluted spectra of as-deposited films (Figure 5.2a) show most intense peak at 850 cm^{-1} along with small peaks at 780 cm^{-1} and 904 cm^{-1} corresponding to different bonding modes of β-phase and a small intensity peak at 820 cm^{-1} corresponding to α-phase [4, 5]. However, after OPT, the peak corresponding to α-phase is the most dominating whereas the intensity of different β-peaks (850 cm^{-1}, 780 cm^{-1}, 904 cm^{-1}) is reduced. The peak intensity at 930 cm^{-1}, corresponding to the intermediate oxide Mo_9O_{26}, is found to be higher in OP-treated films than as deposited films. [6]. A significant increase in intensity ratio $\left(\frac{I_\alpha(820\ cm^{-1})}{I_\beta(850\ cm^{-1})}\right)$ is observed for OP-treated films (Figure 5.3a). This suggests that oxygen plasma has triggered the reaction among oxygen radicals and MoO_{3-x} causing phase transformation of MoO_3 from β to α phase [1]. Formation of Mo_9O_{26} (Figure 5.3a) is observed to be more for OP-treated films.

Raman spectra of OP-treated films for different oxygen flow rate (OFRs) are also recorded and are shown in Figure 5.1b. For this series also, all the plasma-treated films have a broad and intense peak at ~ 820 cm^{-1}, the characteristics peak of α-MoO_3. From the deconvolution data, it is observed that MoO_{3-x} films treated using different OFRs also consist of Mo_9O_{26} and mixed phase of MoO_3 (α and β). The ratio of $\left(\frac{I_\alpha(820\ cm^{-1})}{I_\beta(850\ cm^{-1})}\right)$ (Figure 5.3b) has initially decreased when

OFR is increased from 10 SCCM to 15 SCCM, however, an improvement in peak intensity ratio has taken place with further increase in OFR, confirming the dominance of α phase for all OP- treated films. The contribution of Mo_9O_{26} phase has slightly increased at the expenses of β phase of MoO_{3-x} when the oxygen flow rates have increased from 10 SCCM during OPT.

Raman spectra of films undergone plasma treatment for different time are shown in Figure 5.1c. Similar to the previous series, peak deconvolution is done using five peaks to obtain good fitting, which further confirmed the presence of orthorhombic and monoclinic phases of MoO_3. An increase in peak intensity ratio is observed (Figure 5.3c) when OPT time is increased from 10 minutes to 30 minutes, most likely due to an increased reaction probability between molybdenum oxide and oxygen radicals, which leads to a major conversion of β phase to α phase.

5.2.1.2 XRD studies

XRD patterns of as deposited MoO_{3-x} films and after oxygen plasma treatment at different rf power values are presented in Figure 5.4a. These spectra show that as-deposited and OP-treated films are amorphous in nature, having a broad peak at 2θ ~ 25.68° for all set of samples. This peak represents the formation of the most stable phase of molybdenum oxide i.e. orthorhombic (α-MoO_3) and refers to (040) plane (JCPDS card no - 05-0508) [7]. Apart from this, two humps are observed in XRD spectra. To get more insight into it, the deconvolution of XRD data is done using three peaks to achieve an appropriate fit (R^2 = 0.998). Deconvoluted XRD of as deposited and OP-treated films at 80 W are shown in Figure 5.5a and 5.5b respectively. As deposited as well as OP-treated MoO_{3-x} films exhibit the XRD peaks for Mo_9O_{26} at 2Θ = 33.29° and β-MoO_3 at 2Θ = 51.25° [8, 9]. To figure out how the oxygen plasma treatment affects MoO_3 phase, the intensity ratio is calculated for α-MoO_3, β-MoO_3 and Mo_9O_{26} phases using the relation ($\frac{I_{phase}}{I_\alpha + I_\beta + I_{Mo9O26}}$) and is displayed in Figure 5.6. The development of α-

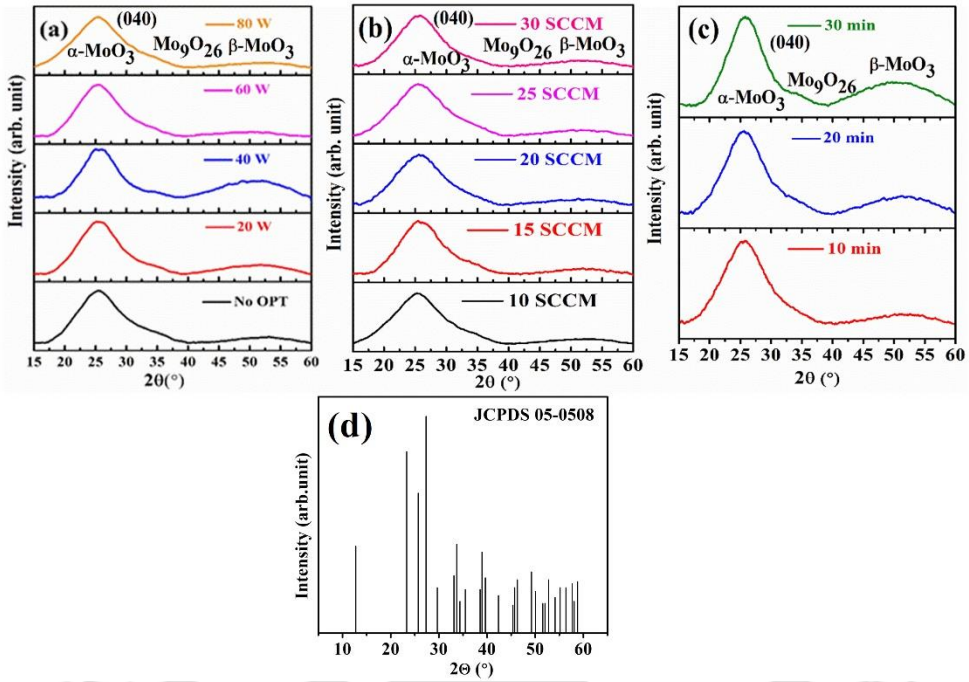

Figure 5.4: *XRD patterns of MoO_{3-x} films treated (a) different rf-power values (OFR 10 SCCM, time 10 min), (b) different oxygen gas flow rates (OPT at 80 W for 10 min) (c) different OPT times (rf 80 W, OFR 30 SCCM) and (d) JCPDS data card- 05-0508.*

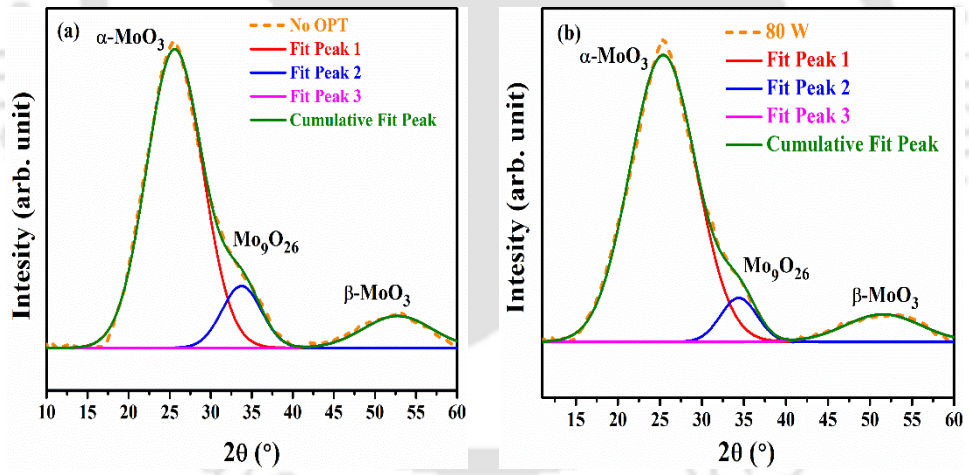

Figure 5.5: *Deconvoluted XRD for (a) untreated MoO_{3-x} film and (b) OP-treated film at 80 W.*

MoO_3 phase and Mo_9O_{26} phase after OPT displayed a linear relationship with rf power at the expense of the β-MoO_3 phase. It is caused by increase in the active oxygen concentration at high rf power, which leads to the formation of stable phase of MoO_{3-x}. XRD results are in good agreement with the outcomes of Raman results.

Figure 5.4b displays the XRD pattern of films treated with various oxygen flow rates. Along with Mo_9O_{26} and β-MoO_3 phase, a broad peak corresponding to the α-MoO_3 phase is seen for

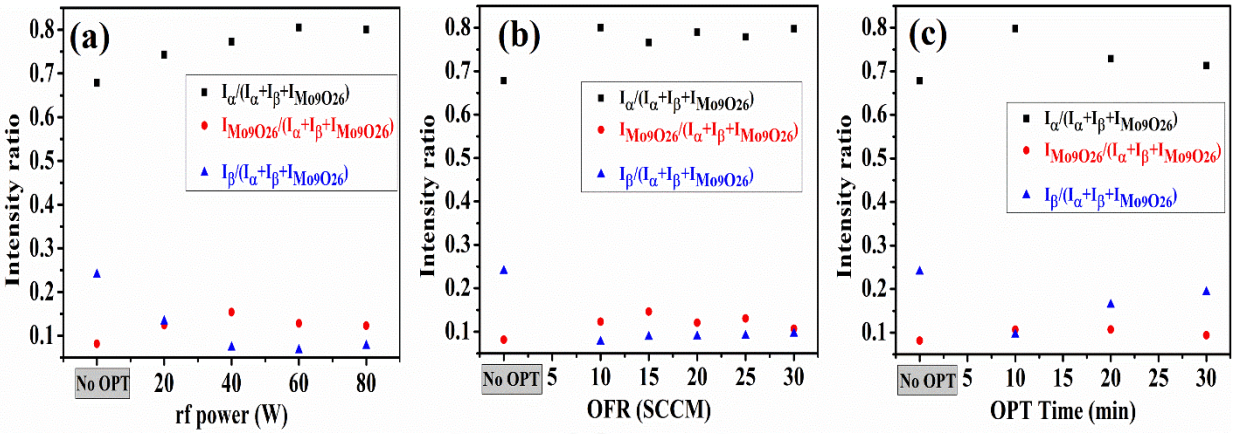

Figure 5.6: *Intensity ratio of different XRD peaks of MoO_{3-x} films treated (a) different rf-power values, (b) different oxygen gas flow rates (c) different OPT times.*

this set of samples as well. The growth of different phases of MoO_3 as displayed in Figure 5.6b has not been affected by an increase in OFR in any discernible ways.

Figure 5.4c shows the XRD patterns of the samples treated for 10, 20 and 30 minutes. All samples exhibit a broad peak at $2\Theta = 25.68°$, indicative of the amorphous nature and formation of the orthorhombic phase of MoO_3. Figure 5.6c shows that longer oxygen plasma treatment initiated the transformation of MoO_3 from stable α-phase to metastable β-MoO_3. This is probably due to the removal of light oxygen vacancies from the surface, which can lead to further structural changes.

5.2.1.3 KPFM studies

The effect of OPT on work function (Φ) is studied using KPFM. Since our objective is to use MoO_{3-x} as hole selective layer with n-type c-Si (c-Si (n)) (the absorber layer) for solar cell fabrication, for these studies MoO_{3-x} films for each conditions are prepared on (c-Si (n)) substrates (275-325 µm, 5-10 Ωcm). Work function is sensitive to the presence of contaminants on the surface of film, surface condition and reaction occurring at surface. Here, the local work function of OP-treated MoO_{3-x} films is measured. The term local work function is used here because the measurements are carried out in ambient conditions near the tip position and any

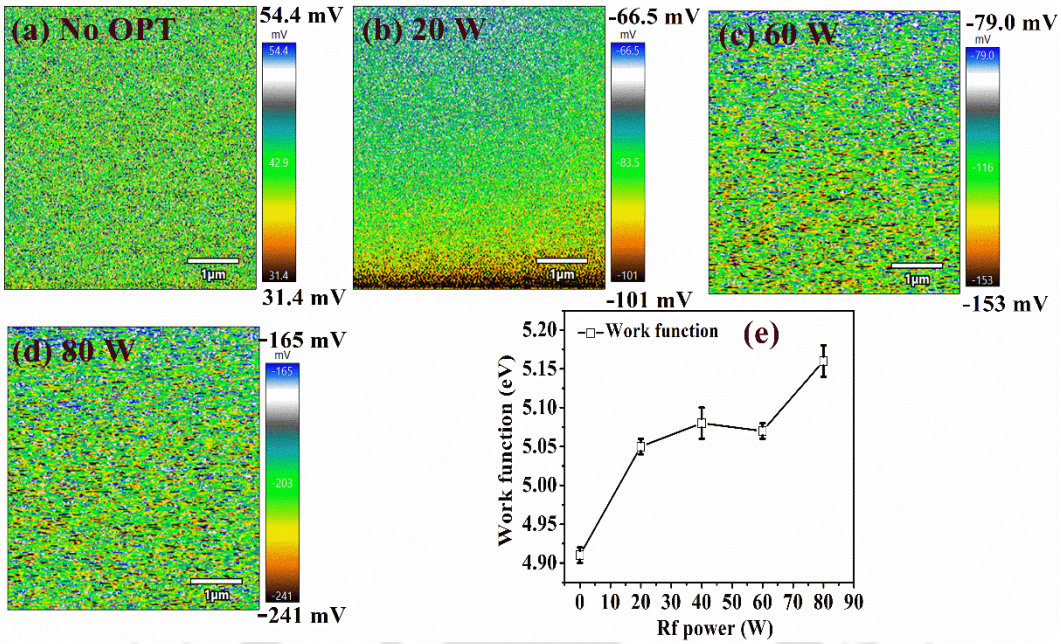

Figure 5.7: *KPFM images of (a) as deposited MoO_{3-x} films and OPT treated films at rf-power of (b) 20 W, (c) 60 W, (d) 80 W and (e) work function variation respectively.*

absorbents on surface can alter Φ. Using KPFM, the contact potential difference (CPD) between MoO_{3-x} and conducting tip is measured, which is then used to find the work function of MoO_{3-x} films using Chapter 2, Equation 2.12 [10-12]. CPD mapping images of MoO_{3-x} films, with and without oxygen plasma treatment, are shown in Figure 5.7. CPD images show that as deposited MoO_{3-x} film (Figure 5.7a) has positive CPD values whereas for OP-treated films, (Figure 5.8b-d) CPD values are negative. An increase in CPD value is observed as rf power is increased from 20 W to 80 W. The increase in CPD between the conducting tip and OP-treated MoO_{3-x} indicates that the resistance of films has increased with rise in rf power, further suggesting that the stoichiometric ratio of O/Mo is shifting closer to 3 [13-15]. OPT performed at higher RF power has increased the concentration of active oxygen (O), which combines with molybdenum oxide to fill oxygen-vacant sites present in MoO_{3-x} films. The dissociation of oxygen atoms and possible reactions between MoO_{3-x} and O are shown in Equation (5.1), (5.2) and (5.3) respectively [16].

$$O_2 + e^- \rightarrow 2O + e^- \quad \text{---------- (5. 1)}$$

$$MoO_{3-x} + O \rightarrow MoO_{3-y}, 3 \geq x > y \quad \text{---------- (5. 2)}$$

$$MoO_{3-x} + O_2 \rightarrow MoO_{3-y}, 3 \geq x > y \quad \text{---------- (5. 3)}$$

Figure 5.7e shows the work function values of as deposited and OP-treated MoO_{3-x} films. The work function has increased from 4.91±0.01 eV for as deposited MoO_{3-x} film to 5.05±0.01 eV for 20 W OP-treated film. The film that has undergone OPT at 80 W has the highest Φ value = 5.16±0.02 eV. KPFM results suggest that oxygen plasma treatment has improved the work function of molybdenum oxide films. The literature reports that a material's work function is sensitive to its roughness [13, 17, 18]. Nevertheless, the surface roughness of MoO_{3-x} films does not change noticeably after OPT. Hence, the work function increase is primarily caused by the filling of oxygen vacancies during OPT.

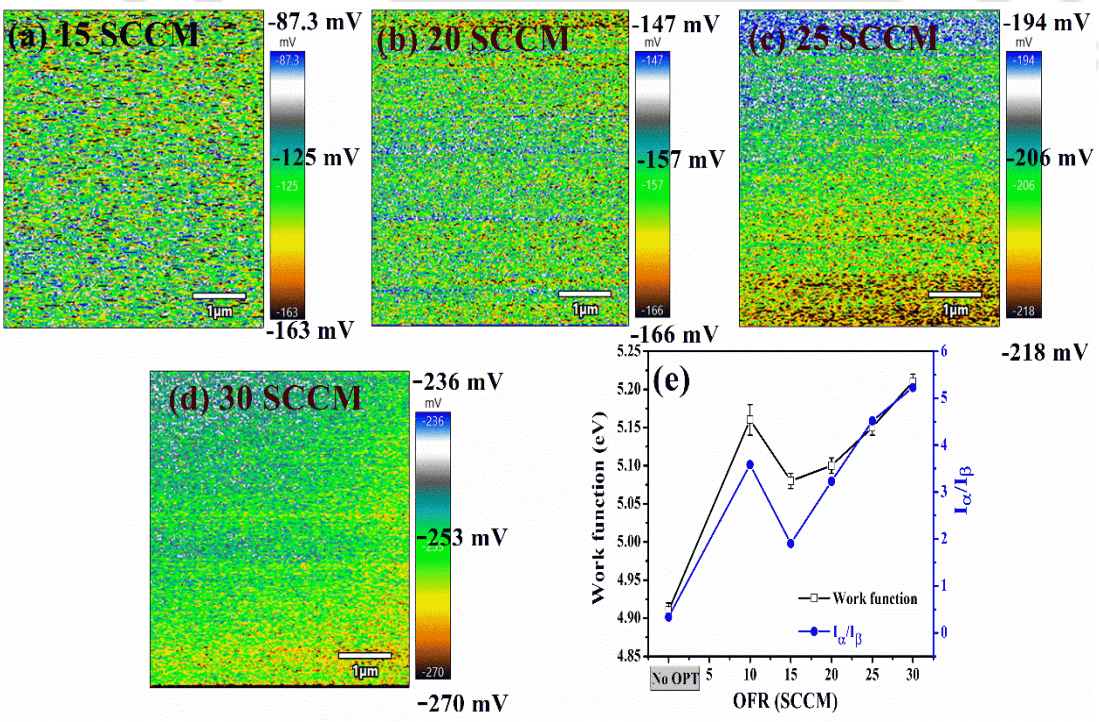

Figure 5.8: *CPD mapping of OP-treated films using (a) 15, (b) 20, (c) 25, (d) 30 SCCM oxygen flow rate (rf 80 W and OPT time 10 minutes) and (e) work function variation of different OFRs.*

The CPD mapping and work function of MoO_{3-x} films treated using different OFRs at 80 W

are presented in Figure 5.8. Initially a small decrease in CPD and Φ is observed when OFR is increased from 10 SCCM (Figure 5.7d) to 15 SCCM (Figure 5.8a). However, subsequent increase in OFR from 15 SCCM to 30 SCCM results in a linear increase in CPD and work function values as shown in Figure 5.8e. This trend is similar to the ratio of $\left(\frac{I_\alpha(820\ cm^{-1})}{I_\beta(850\ cm^{-1})}\right)$ observed in Raman studies suggesting that the work function decrease for 15 SCCM is due to the increased β-phase of molybdenum oxide at the expense of α-phase [13, 19]. The variation in Φ values depending on phases of MoO_3 is also observed by Kodan et al. group [19]. By varying OFR during OPT, we have been able to increase the work function of MoO_{3-x} films from 5.16±0.02 eV for 10 SCCM to 5.22±0.02 eV for 30 SCCM of OFR.

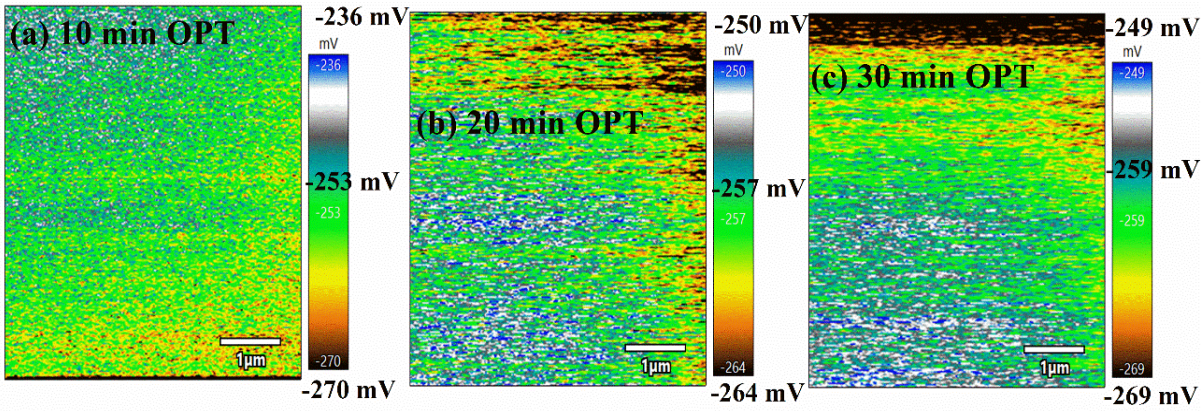

Figure 5.9: *CPD mapping of OP-treated MoO_{3-x} films for (a) 10, (b) 20 and (c) 30 min (rf 80 W and OFR 30 SCCM).*

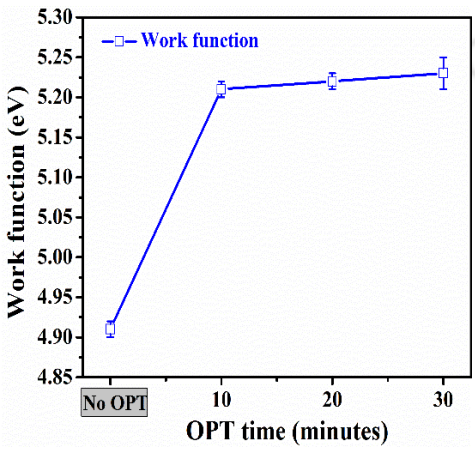

Figure 5.10: Work function variation of MoO_{3-x} films treated (a) using different oxygen flow rates and (b) for *different OPT times.*

Figure 5.9 shows CPD images of OPT carried out at different times. Work function values have remained almost the same for all cases as shown in Figure 5.10. Also, when the OPT time is increased from 10 to 30 minutes, no noticeable differences in the roughness of the MoO_{3-x} films are observed.

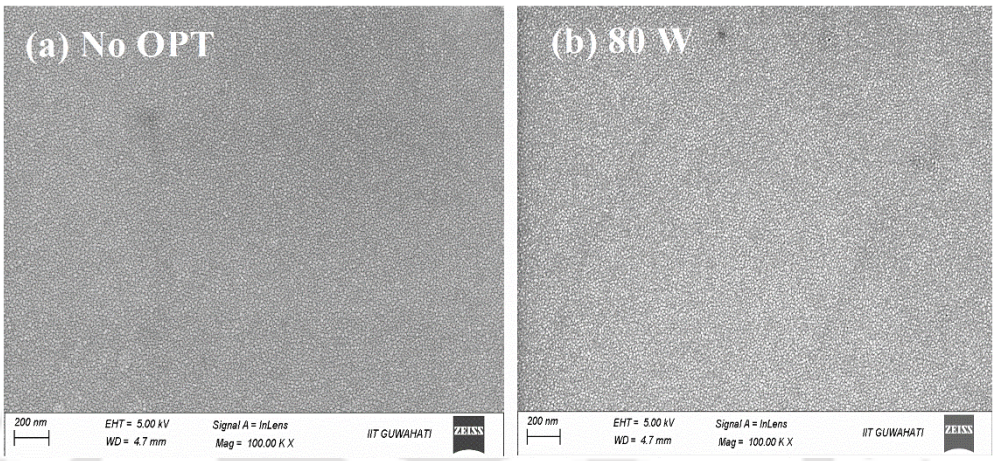

Figure 5.11: *FESEM images of (a) as deposited MoO_{3-x} film and (b) OP-treated film at rf-power of 80 W respectively.*

Table 5.1: *Atomic percent of Oxygen (O), Molybdenum (Mo) and Silicon (Si) atoms in as deposited and MoO_{3-x} films treated at different rf-powers.*

rF power (W)	With substrate contribution				No substrate contribution		
	O	Mo	Si	O/Mo ratio	O	Mo	O/Mo ratio
No OPT	34.3	20.3	45.4	1.68	69.1	30.9	2.23
20 W	37.2	19.8	43.1	1.87	71.0	29.0	2.44
40 W	37.0	19.4	43.6	1.90	71.3	28.7	2.48
60 W	36.0	18.5	47.3	1.94	72.0	28.0	2.57
80 W	39.1	19.2	41.7	2.03	72.5	27.5	2.63

5.2.1.4 FESEM + EDS studies

To establish that the increase in work function of MoO_{3-x} films after OPT is due to change in O/Mo stoichiometry ratio, EDS studies are performed. Presence of Si from substrate is detected along with the Mo and O. For all the films after OPT, Mo and Si atomic % is reduced, whereas O atomic % has increased. Compositional information for as deposited and OPT treated

molybdenum oxide films with and without substrate contribution is mentioned in Table 5.1. We have not taken into consideration the possibility of silicon oxide formation at the MoO_{3-x}/c-Si(n) interface while calculating the stoichiometric ratio. O/Mo ratio estimated from EDS data is found to be 2.33 for as deposited films and 2.63 for films treated at 80 W. The stoichiometric ratio has increased with increase in rf power confirming that OPT treatment has increased O atoms concentration inside MoO_{3-x} films and improved the O/Mo ratio. This could be a reason for getting Mo_9O_{26} and stable phase of MoO_3 in XRD and Raman spectra. X. Liu has reported that OPT treated MoO_{3-x} films can have thin layer of O_2 absorbents on its surface [17]. So, it is possible that the surface oxygen atoms are also detected in EDS analysis. Since MoO_{3-x} films deposited on Si substrates have a thickness of around 500 nm and EDS has a maximum penetration depth of 2 μm [20, 21], oxygen atoms can be collected from both the bulk and the surface. So, the increased oxygen atom concentration confirmed that OPT has filled the oxygen vacancies present throughout the bulk of OP-treated MoO_{3-x} films and improved the stoichiometry. These findings also match the KPFM measurement results.

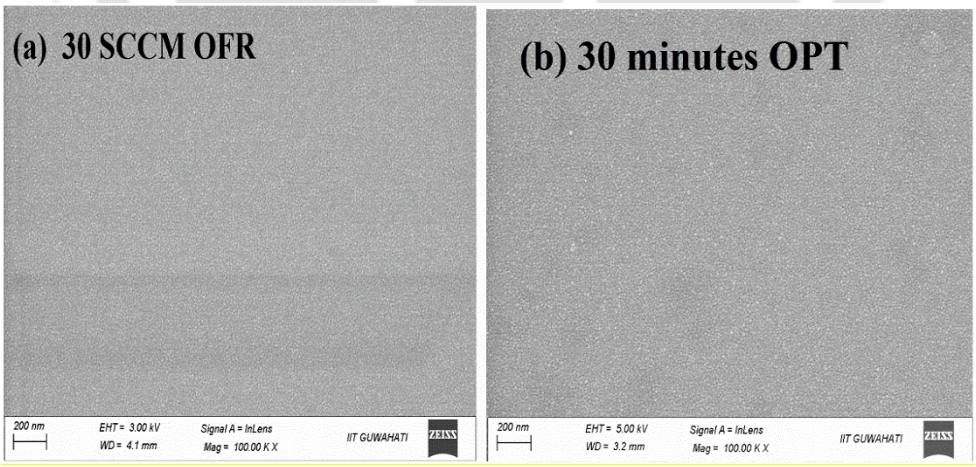

Figure 5.12: *FESEM images of films treated (a) using 30 SCCM OFR at 80 W and 10 min and (b) for 30 min at 80 W and 30 SCCM OFR.*

Table 5.2 shows the compositional details of MoO_{3-x} films treated using different O_2 gas flow rates. Increase in OFR resulted in an improvement in O/Mo ratio. An increase in oxygen atom

Table 5.2: *Atomic percent of Oxygen (O), Molybdenum (Mo) and Silicon (Si) atoms in MoO_{3-x} films treated using different OFRs.*

OFR (SCCM)	With substrate contribution				No substrate contribution		
	O	Mo	Si	O/Mo ratio	O	Mo	O/Mo ratio
10	39.1	19.2	41.7	2.03	72.5	27.5	2.63
15	54.9	21.6	23.5	2.54	74.0	26.0	2.84
20	57.9	22.0	20.1	2.63	74.3	25.7	2.89
25	59.8	20.8	19.4	2.87	75.9	24.1	3.14
30	59.6	20.4	20.0	2.92	76.6	23.4	3.27

Table 5.3: *Atomic percent of Oxygen (O), Molybdenum (Mo) and Silicon (Si) atoms in MoO_{3-x} films treated for different times.*

OPT Time (minutes)	With substrate contribution				No substrate contribution		
	O	Mo	Si	O/Mo ratio	O	Mo	O/Mo ratio
10	59.6	20.4	20.0	2.92	76.6	23.4	3.27
20	59.7	21.0	19.3	2.84	74.8	25.2	2.96
30	55.4	17.4	27.1	3.18	78.2	21.8	3.58

concentration inside the treatment chamber amplifies the reaction between oxygen and molybdenum atoms, forming MoO_{3-x} closer to its stoichiometry.

Atomic concentration of Mo, O and Si atoms for different OPT time are listed in Table 5.3. When plasma treatment time is varied keeping rf power = 80 W and OFR = 30 SCCM, no proper trend in stoichiometric ratio change is noticed. FESEM images confirmed that high rf power (80 W) (Figure 5.11b), high OFR (30 SCCM) (Figure 5.12a) and long OPT time (30 minutes) (Figure 5.12b) have not damaged MoO_{3-x} films surface.

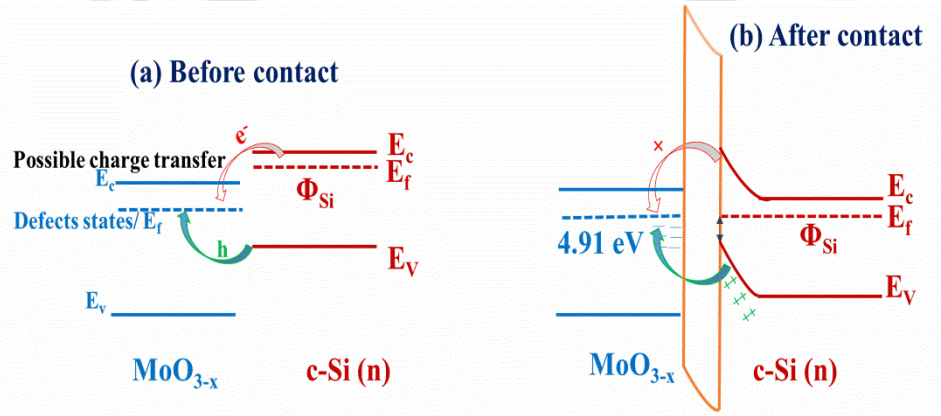

Figure 5.13: *Energy band diagram between as deposited MoO_{3-x} films and c-Si (n) (a) before contact and (b) after contact. The depicted interface layer is silicon oxide (SiO_x) layer.*

5.2.1.5 Charge carrier transfer mechanism

Figure 5.13 shows the energy band diagram between as deposited MoO_{3-x} and c-Si (n). Electron affinity (χ_c), band gap (E_g) and work function of silicon substrate is taken from literature and are 4.05 eV, 1.12 eV and 4.25 eV respectively [22]. The energy barrier faced by electrons ($E_{bn}(eV) = \Phi_{MoO_{3-x}} - \chi_{c-Si(n)}$) and holes ($E_{bp}(eV) = (E_g + \chi)_{c-Si(n)} - \Phi_{MoO_{3-x}}$) are calculated using the expression mentioned by H. Mehmood et. al [22]. For as deposited MoO_{3-x}, E_{bp}=0.26 eV < E_{bn}=0.86 eV (Figure 5.13b), so holes transfer from valence band (E_v) of c-Si (n) to conduction band (E_c) of MoO_{3-x} is more probable as compared to transfer of electrons. Also, at MoO_{3-x}/c-Si(n) interface, nature of n type c-Si has changed to p-type (i.e. inversion layer formation) which further supports the flow of holes. Because the hole transport from E_v of c-Si (n) to E_c of MoO_{3-x}, the charge transfer mechanism in MoO_{3-x}/c-Si(n) devices is different. Literature reports that this material inherently has n-type nature due to oxygen vacancy. But it favors hole transfer because of high Φ and presence of deep trap states [23]. When MoO_{3-x} is treated with oxygen plasma, Φ value has increased from 4.91±0.01 eV (for No OPT) to 5.05±0.01 eV and 5.16±0.02 eV, for 20 W and 80 W OPT treated films respectively. The Φ increment has increased E_{bn} from 1.00 eV for 20 W to 1.11 eV for 80 W and reduced E_{bp} from 0.12 eV for 20 W to 0.01 eV for 80 W. The low E_{bp} suggests that ohmic-type hole transport is possible at Φ = 5.16±0.02 eV, however, electrons flow from c-Si (n) to MoO_{3-x} layer is blocked by the high energy barrier. Figure 5.14b displays the energy band diagram for this case. These results suggest that OPT treatment have improved the hole selectivity of MoO_{3-x} films by improving Φ of MoO_{3-x}, which is very important when MoO_{3-x} is used as hole selective contact in silicon heterojunction solar cells or any organic solar cells. The Φ values and the respective E_{bn} and E_{bp} obtained at different rf powers and OFRs are listed in Table 5.4. The increase in plasma treatment time has resulted in Fermi level pinning due to easier transport of holes from c-Si (n) to MoO_{3-x} side as the position of Fermi level in MoO_{3-x}

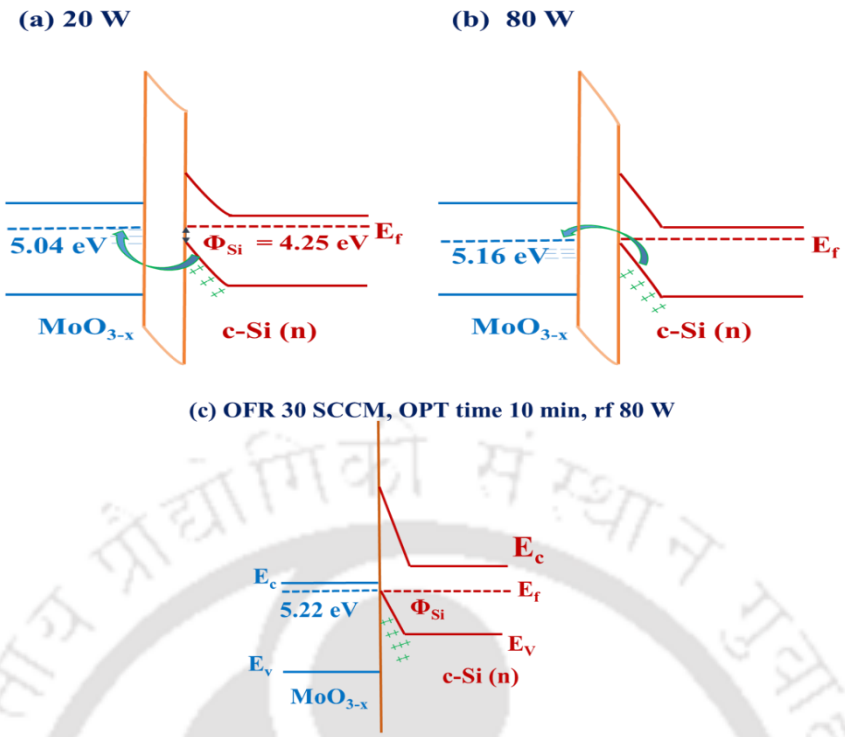

Figure 5.14: *Energy band diagram of c-Si (n) and MoO_{3-x} films undergone OPT at (a) 20 W, (b) 80 W and (c) OFR 30 SCCM, OPT time 10 min and rf 80 W respectively. The depicted interface layer is SiO_x layer.*

Table 5.4: *Values of calculated Φ, E_{bn} and E_{bp} of as deposited and OP treated MoO_{3-x} films.*

OPT RF power (W)	Constant parameters	Φ (eV)	E_{bn}(eV)	E_{bp}(eV)
No OPT	OFR=10SCCM, Treatment time=10min	4.91±0.01	0.86	0.26
20		5.05±0.01	1.00	0.12
40		5.07±0.02	1.02	0.10
60		5.06±0.01	1.01	0.11
80		5.16±0.02	1.11	0.01
OFR (SCCM)				
10	Rf power = 80W Treatment time = 10min	5.16±0.01	1.11	0.01
15		5.04±0.01	0.99	0.13
20		5.10±0.01	1.05	0.07
25		5.15±0.01	1.10	0.02
30		5.22±0.02	1.17	-0.05

lies at ~ 5.22 eV which is nearby the valence band of c-Si (n) [22]. This would form a strong p-type inversion layer across the interface and hinder electrons flow as shown in Figure 5.14c.

5.2.2 OPT on thin MoO_{3-x} films

Solar cells require a thin hole selective layer, so thin films (14 nm & 23 nm) of MoO_{3-x} are prepared on corning glass and c-Si (n) substrates at substrate temperature of 100 ℃ and also

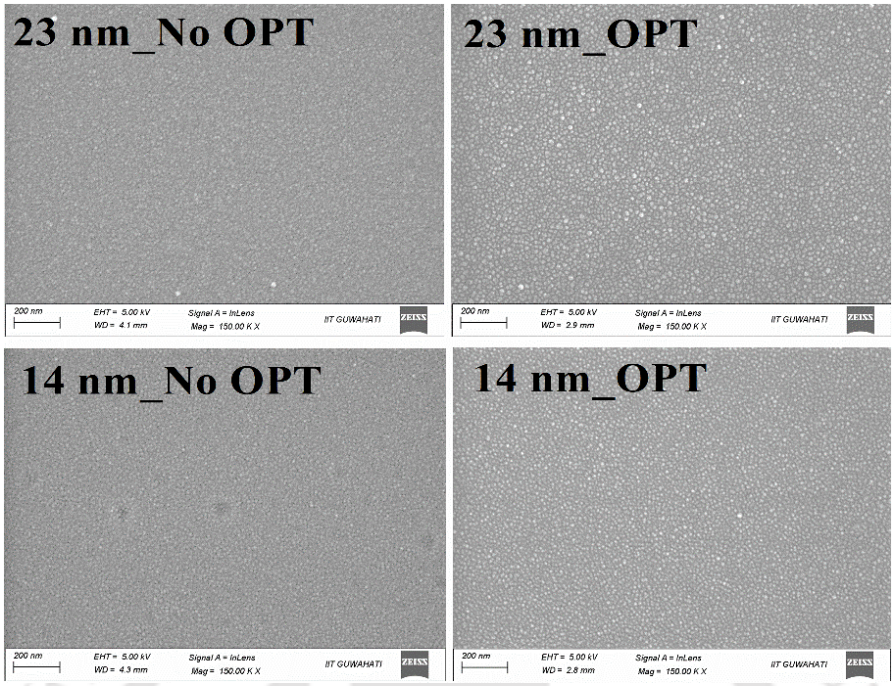

Figure 5.15: *FESEM images of untreated and oxygen plasma treated films of MoO_{3-x}.*

Table 5.5: *Atomic percent of O, Mo and Si atoms present in thin MoO_{3-x} films.*

Sample name	With substrate contribution		
	O	Mo	Si
23 nm_No OPT	7.0	1.7	91.3
23 nm_OPT	12.0	2.1	85.9

treated with oxygen plasma to study its effect on work function of thin MoO_{3-x} films. The OPT conditions used for these studies are: rf-power 80 W, OFR = 30 SCCM and time 5 minutes, which are chosen based on the previous studies on thick MoO_{3-x} films.

5.2.2.1 FESEM + EDS studies

FESEM images of MoO_{3-x} films prepared on silicon substrates, displayed in Figure 5.15, demonstrated that OPT has not caused any surface damage to thin films. However, a small increase in grain size is observed after OPT for both 23 nm and 14 nm thin MoO_{3-x} films. EDS analysis shows an increase in O atom concentration after OPT (Table 5.5). Since, molybdenum oxide films are very thin, a considerable portion of Si atoms are yielded by the EDS measurements.

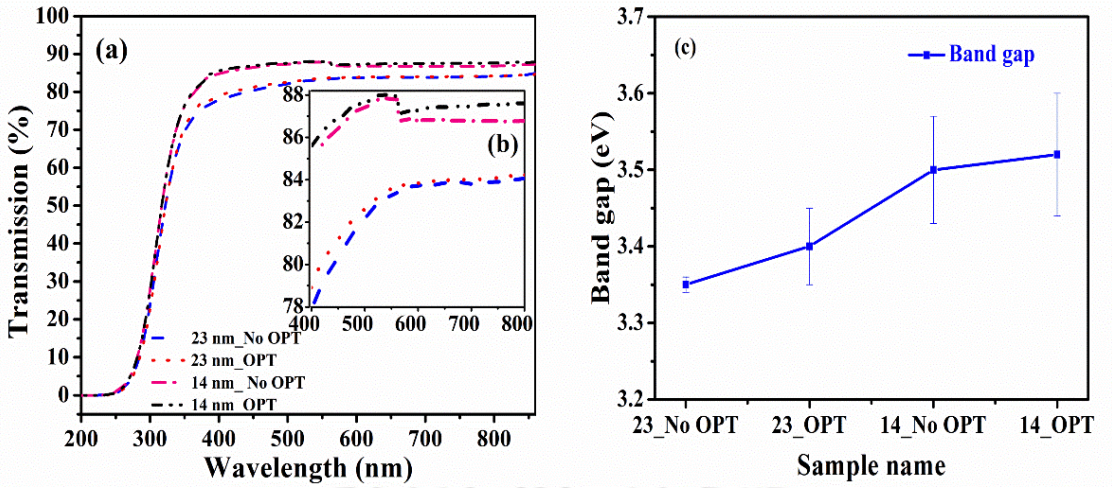

Figure 5.16: *(a) Transmission spectra, (b) zoomed view of transmission (inset image) and (c) band gap values of untreated and oxygen plasma treated thin films of MoO_{3-x}.*

5.2.2.2 UV-Vis studies

Figure 5.16a shows the transmission spectra of untreated and oxygen plasma treated 23 nm and 14 nm thin MoO_{3-x} films deposited on corning glass substrates. Because of lower thickness, transmission of 14 nm film is higher as compared to 23 nm MoO_{3-x} film. After OPT, both films show a slight increase in transmission (Figure 5.17b) and band gap (Figure 5.17c) due to the filling of oxygen vacancies by oxygen plasma treatment; this is further supported by EDS analysis (Table 5.5).

5.2.2.3 KPFM studies

Figure 5.17 shows the CPD mapping of untreated and OP-treated thin MoO_{3-x} films deposited on c-Si (n) substrates. The average CPD value for both films changes from positive to negative after OPT, indicating that OPT has improved the work function of thin films. MoO_{3-x} can react with oxygen atoms during plasma treatment, altering the surface dipole by filling oxygen vacancies within the material and subsequently altering the oxidation state of the Mo cations [17]. OPT also helps in removal of surface contaminants, which can also be one of the reasons for observed increment in work function. Work function is increased from 4.47±0.01 eV (No

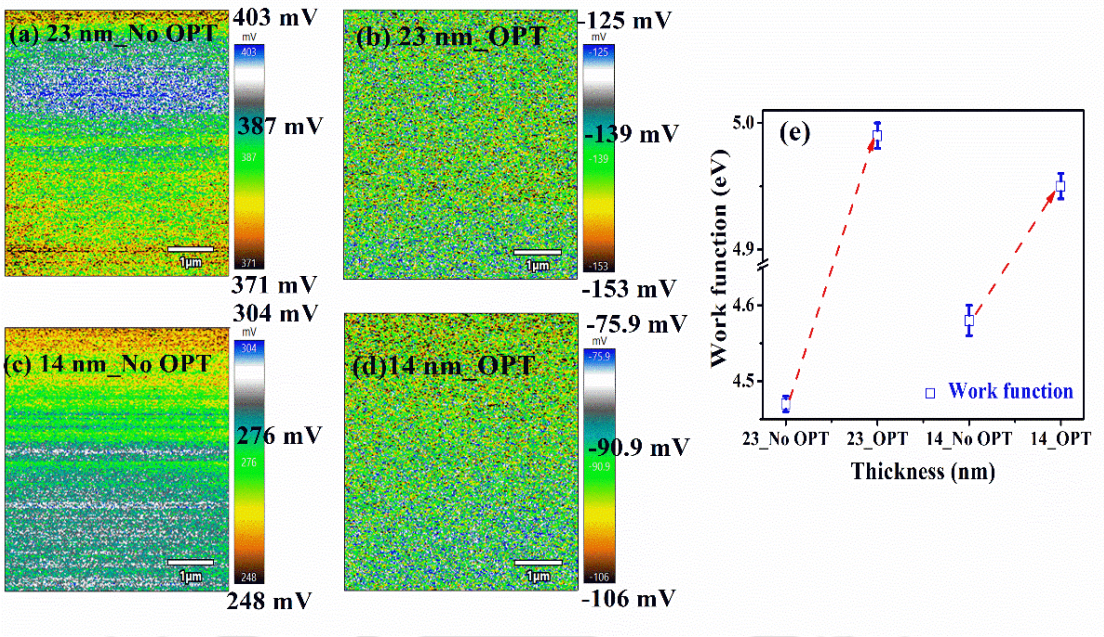

Figure 5.17: *CPD mapping of untreated (a) 23 nm and (c) 14 nm thin MoO_{3-x} films and oxygen plasma treated (b) 23 nm and (d) 14 nm MoO_{3-x} films and (e) work function of untreated and OP-treated thin MoO_{3-x} films.*

Table 5.6: *Work function of MoO_{3-x} films before and after OPT.*

Thickness (nm)	Without OPT		With OPT	
	Average CPD (mV)	Φ (eV)	Average CPD (mV)	Φ (eV)
23 nm	387	4.47±0.01	-139	4.99±0.01
14 nm	276	4.58±0.02	-90	4.95±0.01

OPT) to 4.99±0.01 eV (OPT) for 23 nm films whereas from 4.58±0.02 eV (No OPT) to 4.95±0.01 eV (OPT) for 14 nm films. The *Φ* of thin films is smaller compared to that of thicker films, however, in both cases, OPT has improved the *Φ* significantly. The *Φ* increase is more for thin MoO_{3-x} films. Table 5.6 shows the CPD and work function values of thin MoO_{3-x} films before and after OPT.

5.2.2.4 XPS studies

The full XPS spectra of MoO_{3-x} films prepared on c-Si (n) substrates, shown in Figure 5.18, affirm the presence of oxygen atoms (O 1s), molybdenum atoms (Mo 3s, Mo 3p doublet peaks, Mo 3d doublet peaks) and traces of carbon atoms (C 1s).

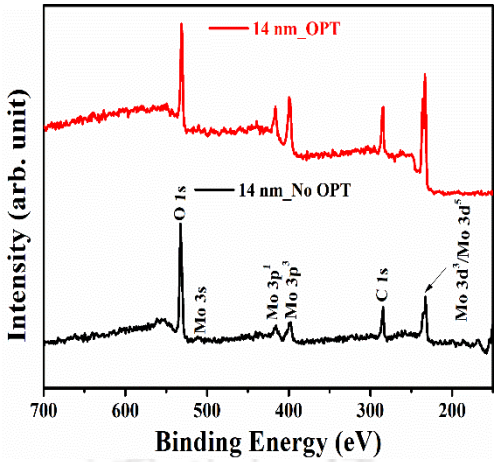

Figure 5.18: *XPS spectra of untreated and OP-treated 14 nm MoO_{3-x} films.*

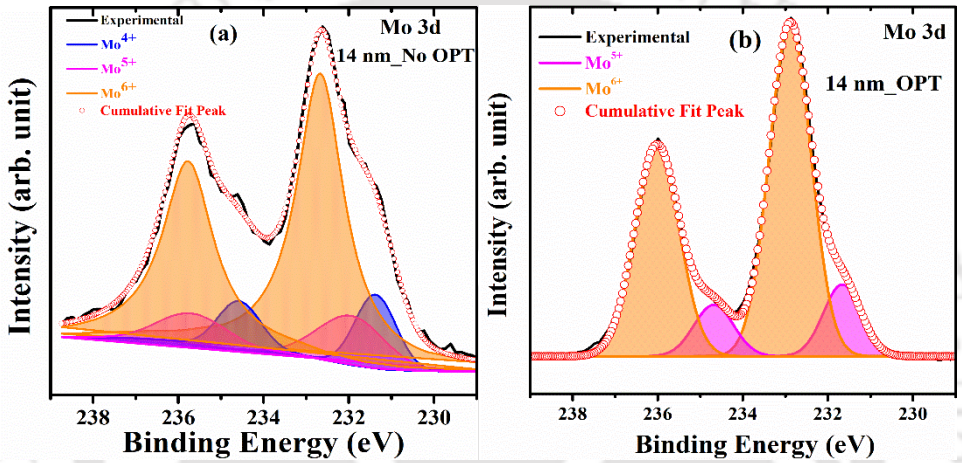

Figure 5.19: *High resolution Mo 3d XPS spectra of (a) untreated and (b) OP-treated 14 nm MoO_{3-x} films.*

Figures 5.19a and 5.19b show the high resolution Mo 3d XPS spectra of as deposited and OP-treated 14 nm MoO_{3-x} films deposited on c-Si (n) substrates. It can be seen that XPS spectra of as deposited thin films are more asymmetric and centered towards lower binding energy compared to the oxygen plasma treated films; Mo^{6+}, $3d_{3/2}$ peak shifts from 235.75 eV to 236.00 eV, $3d_{5/2}$ peak shifts from 232.64 eV to 232.87 eV after OPT confirming the presence of Mo atoms in its higher oxidation states [23]. For as-deposited MoO_{3-x} films, the Mo^{5+} and Mo^{4+} states are observed in addition to Mo^{6+} state (Figure 5.19a), whereas for films treated with OP, only the Mo^{5+} signature is observed in conjunction with Mo^{6+} state (Figure 5.19b) [24]. Asymmetry is also evident in the high-resolution O 1s XPS spectra displayed in Figure 5.20, which suggests the presence of Mo-O bonds (532.68 eV) and oxygen vacancies (O_v) (530.51

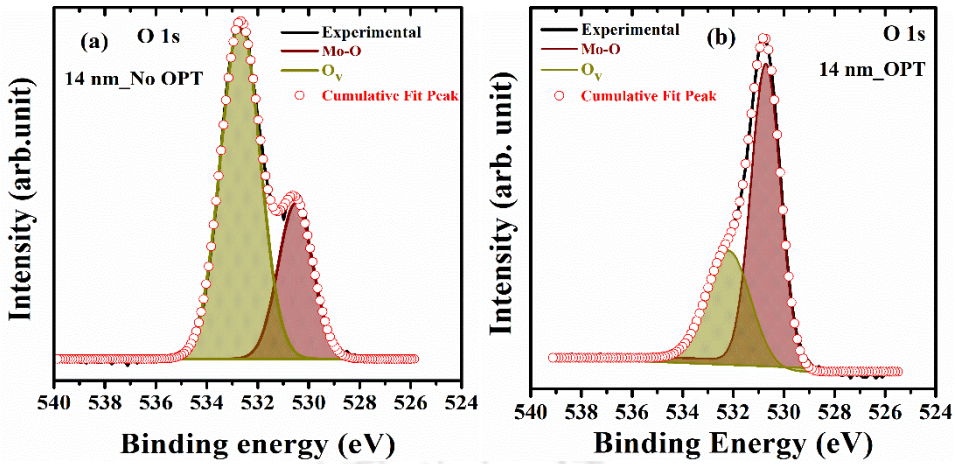

Figure 5.20: *High resolution O1s XPS spectra of (a) untreated and (b) OP-treated 14 nm MoO_{3-x} films.*

eV) in MoO_{3-x} matrix. In as-deposited 14 nm film, the relative contribution of O_v is 71% (Figure 5.20a); however, for OP-treated MoO_{3-x} film, it drops to 35% (Figure 5.20b). This suggests that by filling oxygen vacancies with active oxygen atoms produced during the OPT process, OPT improves the stoichiometry and work function of MoO_{3-x} films. These results provide additional evidence that treating molybdenum oxide with oxygen plasma is an effective way to enhance its work function.

By optimizing the OP treatment conditions, the work function of thicker films improved by 0.31 eV, whereas the work function of thinner films has improved by 0.40 eV to 0.50 eV. The reason for this improvement is filling of greater percentage of O_v in MoO_{3-x} when thinner films are exposed to oxygen plasma, whereas thicker films can only allow filling of O_v from the surface up to a few nm.

5.3 Conclusion

In this chapter, oxygen plasma treatment of thermally evaporated molybdenum oxide films using the PECVD method is explored as an approach to tune the work function of MoO_{3-x}. We are the first to study the OPT effect on structural, optical and electrical properties of MoO_{3-x} films. OPT is done at different rf powers (20 W - 80 W) and it is observed that plasma treatment

at 80 W has improved the work function of MoO_{3-x} films from 4.91 eV for as deposited films to 5.16 eV. For further optimization of OPT conditions, oxygen flow rates and OPT durations are varied. EDS results confirmed that OPT have improved the stoichiometry ratio of O/Mo throughout the bulk resulting in an improvement of work function. Also, a significant improvement in hole selectivity of MoO_{3-x} is inferred for the films treated at 80 W using 30 SCCM oxygen gas for 10 minutes. The increase in OPT timing has caused Fermi level pinning in MoO_{3-x}. As these studies are done on ~500 nm thick MoO_{3-x} films, which are not suitable for its application in photovoltaic devices, thin films (23 nm and 14 nm) of this material are also prepared and treated with OP. Decrease in O_v and enhancement in Φ values by ~0.40 eV are observed when thin MoO_{3-x} films are treated with OP. From these analysis, it is confirmed that oxygen plasma treatment by PECVD technique can be a suitable approach to tune the work function of molybdenum oxide films. As the work function of TMO is sensitive to air contact and synthesis process, this approach can also help to recover or improve the work function of MoO_{3-x} compounds. For solar cells, work function is one of the key parameters which directly affects the device properties. Our studies suggest that oxygen plasma treatment of MoO_{3-x} films will be helpful in improving the performance of c-Si/TMO heterojunction solar cells.

5.4 References

[1] M. Diskus, O. Nilsen, H. Fjellvag, S. Diplas, P. Beato, C. Harvey, E. van Schrojenstein Lantman, B.M. Weckhuysen, Combination of characterization techniques for atomic layer deposition MoO_3 coatings: From the amorphous to the orthorhombic α-MoO_3 crystalline phase, Journal of Vacuum Science & Technology A, 30 (2012) 01A107.

[2] D. Liu, W.W. Lei, J. Hao, D.D. Liu, B.B. Liu, X. Wang, X.H. Chen, Q.L. Cui, G.T. Zou, J. Liu, S. Jiang, High-pressure Raman scattering and x-ray diffraction of phase transitions in MoO_3, Journal of Applied Physics, 105 (2009) 023513.

[3] M. Dieterle, G. Mestl, Raman spectroscopy of molybdenum oxides, Physical Chemistry Chemical Physics, 4 (2002) 822-826.

[4] D.D. Yao, J.Z. Ou, K. Latham, S. Zhuiykov, A.P. O'Mullane, K. Kalantar-zadeh, Electrodeposited α- and β-Phase MoO_3 Films and Investigation of Their Gasochromic Properties, Crystal Growth & Design, 12 (2012) 1865-1870.

[5] B. Hui, G. Li, X. Zhao, L. Wang, D. Wu, J. Li, B.K. Via, h-MoO_3 microrods grown on wood substrates through a low-temperature hydrothermal route and their optical properties, Journal of Materials Science: Materials in Electronics, 28 (2016) 3264-3271.

[6] B. Saravanakumar, R. Shobana, G. Ravi, V. Ganesh, R. Yuvakkumar, Preparation and electrochemical characterization of Mo_9O_{26} nanopowders for supercapacitors applications, Nano-Structures & Nano-Objects, 19 (2019) 100340.

[7] O.M.H. K. Hari Krishna, C. Guillen, Photo- and Electrochromic Properties of Activated Reactive Evaporated MoO_3 Thin Films Grown on Flexible Substrates, Research Letters in Nanotechnology, 2008 (2008) 1-5.

[8] L. Wang, M.-C. Li, G.-H. Zhang, Z.-L. Xue, Morphology evolution and quantitative analysis of β-MoO_3 and α-MoO_3, High Temperature Materials and Processes, 39 (2020) 620-626.

[9] L. Wang, Z.L. Xue, A. Huang, F.F. Wang, Mechanism and Kinetic Study of Reducing MoO_3 to MoO_2 with CO-15 vol % CO_2 Mixed Gases, ACS Omega, 4 (2019) 20036-20047.

[10] P. Maiti, P. Guha, R. Singh, J.K. Dash, P.V. Satyam, Optical band gap, local work function and field emission properties of MBE grown β-MoO_3 nanoribbons, Applied Surface Science, 476 (2019) 691-700.

[11] D.A. Kowalczyk, M. Rogala, K. Szalowski, D. Belic, P. Dabrowski, P. Krukowski, I. Lutsyk, M. Piskorski, A. Nadolska, P. Krempinski, M. Le Ster, P.J. Kowalczyk, Two-Dimensional Crystals as a Buffer Layer for High Work Function Applications: The Case of

Monolayer MoO_3, ACS applied materials & interfaces, 14 (2022) 44506-44515.

[12] K.H. Krishna, O.M. Hussain, C. Guillen, Photo- and Electrochromic Properties of Activated Reactive Evaporated MoO_3 Thin Films Grown on Flexible Substrates, Research Letters in Nanotechnology, 2008 (2008) 1-5.

[13] J.R. Yuzheng Guo, Origin of the high work function and high conductivity of MoO_3, Applied Physics Letters, 105 (2014) 222110-222114.

[14] K. Crowley, G. Ye, R. He, K. Abbasi, X.P.A. Gao, α-MoO_3 as a Conductive 2D Oxide: Tunable n-Type Electrical Transport via Oxygen Vacancy and Fluorine Doping, ACS Applied Nano Materials, 1 (2018) 6407-6413.

[15] M. Vishwakarma, D. Varandani, C. Andres, Y.E. Romanyuk, S.G. Haass, A.N. Tiwari, B.R. Mehta, A direct measurement of higher photovoltage at grain boundaries in CdS/ CZTSe solar cells using KPFM technique, Solar Energy Materials and Solar Cells, 183 (2018) 34-40.

[16] C.A. Wolden, The Role of Oxygen Dissociation in Plasma Enhanced Chemical Vapor Deposition of Zinc Oxide from Oxygen and Diethyl Zinc, Plasma Chemistry and Plasma Processing, 25 (2005) 169-192.

[17] X. Liu, C. Wang, Irfan, S. Yi, Y. Gao, Effect of oxygen plasma treatment on air exposed MoO_x thin film, Organic Electronics, 15 (2014) 977-983.

[18] W. Melitz, J. Shen, A.C. Kummel, S. Lee, Kelvin probe force microscopy and its application, Surface Science Reports, 66 (2011) 1-27.

[19] N. Kodan, A.P. Singh, M. Vandichel, B. Wickman, B.R. Mehta, Favourable band edge alignment and increased visible light absorption in β-MoO_3/α-MoO_3 oxide heterojunction for enhanced photoelectrochemical performance, International Journal of Hydrogen Energy, 43 (2018) 15773-15783.

[20] H.C. J Fournelle, P T Pinard and S Richter, Low voltage EPMA: experiments on a new frontier in microanalysis - analytical lateral resolution, IOP Conference Series: Materials

Science and Engineering, 109 (2016) 012003.

[21] S.B. Manuel Scimeca, Harpreet Kaur Lamsira, Rita Bonfiglio and Elena Bonanno, Energy Dispersive X-ray (EDX) microanalysis: A powerful tool in biomedical research and diagnosis, European Journal of Histochemistry 62 (2018) 2841.

[22] H. Mehmood, H. Nasser, T. Tauqeer, S. Hussain, E. Ozkol, R. Turan, Simulation of an efficient silicon heterostructure solar cell concept featuring molybdenum oxide carrier-selective contact, International Journal of Energy Research, 42 (2018) 1563-1579.

[23] M. Ponce-Mosso, M. Perez-Gonzalez, P.E. Garcia-Tinoco, H. Crotte-Ledesma, M. Morales-Luna, S.A. Tomas, Enhanced photocatalytic activity of amorphous MoO_3 thin films deposited by rf reactive magnetron sputtering, Catalysis Today, 349 (2020) 150-158.

[24] A.K.-V. Alexander V. Naumkin, Stephen W. Gaarenstroom, and Cedric J. Powell, NIST X-ray Photoelectron Spectroscopy Database, NIST Standard Reference Database 20, National Institute of Standards and Technology, Gaithersburg MD, 20899 (2000).

CHAPTER 6

Role of deposition parameters on optoelectronic properties of ITO films

Transparent conducting oxides (TCOs) are the semiconductor materials which are used in various optoelectronic applications such as transparent electrodes for photovoltaic cells [1-3], light-emitting diodes [4], flat panel displays [5], window defrosters [6], etc. A TCO should be highly conductive, have good transmission in the visible range of solar spectrum, be stable, non-toxic and cost-effective [7]. TCOs are high band gap (>3 eV) oxides and are doped with different metal atoms to attain resistivity less than 10^{-4} Ω-cm [8]. Most frequently used TCOs are: Indium oxides or Tin (Sn) doped Indium oxide (ITO) [9-11]; Zinc oxides (ZnO) with different metal dopants like Al-doped ZnO (AZO)[12], boron-doped ZnO [13]; and tin oxides/ fluorine-doped tin oxide (FTO) [14], etc. ITO is the most widely used TCO in solar cells because of its low sheet resistance, high optical transmissivity (>85 %), high optical band gap (3.5-4.3 eV), low resistivity (~10^{-4} Ω-cm) [15] and stability against chemical attacks and time [16]. A few of these properties of ITO thin films are however, influenced by the method of deposition and processing conditions which impact the performance of solar cells. This requires

tuning of deposition conditions to get ITO films with most suitable properties. With this motivation, the deposition parameters are optimised in this chapter for producing good-quality ITO films for use as TCO in solar cells. This chapter investigates the effect of process pressure and substrate temperature on the optoelectronic properties of ITO films.

6.1 Experimental Details

Tin-doped indium oxide films were deposited on Corning 1737 glass substrate using rf-sputtering. The influence of deposition parameters on the structural, optical, and electrical properties of ITO films were explored. ITO (In_2O_3:SnO_2; 95:5wt%) target having purity of 99.99% was used for the deposition. Argon gas is used during the deposition process and gas flow rate was controlled using a mass flow controller (MFC). Corning glass substrates were cleaned and dried before being inserted into the rf-sputtering chamber for deposition. Two series of ITO films were prepared by altering one parameter and keeping other parameters constant. In the first series, process pressure (PP) was varied; 9.3×10^{-3} mbar, 5.3×10^{-3} mbar and 3.8×10^{-3} mbar while other parameters were fixed at 7 SCCM of argon flow rate (AFR), 150 °C of substrate temperature (T_s) and 30 minutes of deposition time (t_d). In second series, substrate temperature (T_s) was altered (130 °C, 150 °C, 170 °C and 200 °C) at process pressure of 3.8×10^{-3} mbar and rest parameters were kept same as the first series.

6.2 Results and discussion

6.2.1 XRD studies

Figure 6.1. shows XRD patterns of ITO films prepared at different process pressures and substrate temperatures. From Figure 6.1a, it is observed that high-pressure films (9.3×10^{-3} mbar and 5.3×10^{-3} mbar) are crystalline in nature with a sharp peak at $2\theta \sim 30°$ corresponding to (222) plane. In contrast, the low-pressure film (3.8×10^{-3} mbar) shows polycrystalline nature

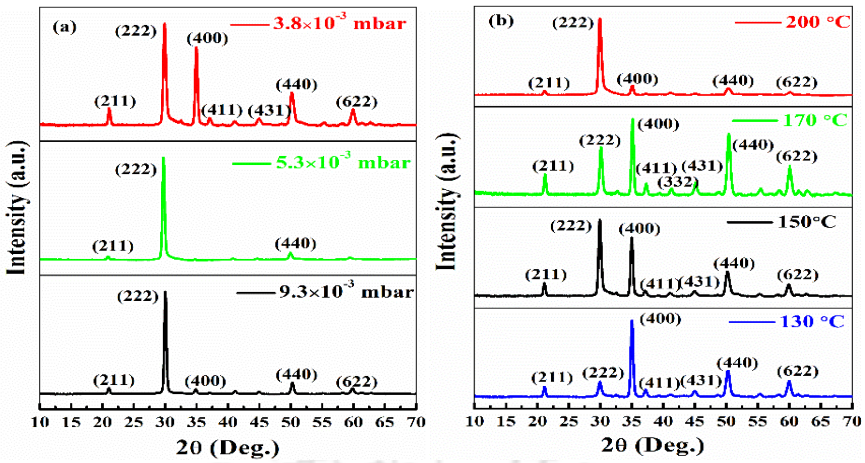

Figure 6.1: *XRD patterns of ITO films on corning substrates prepared at different (a) process pressures and (b) substrate temperatures.*

Table 6.1: *Crystallite sizes for different planes of ITO films at various process pressures.*

Process Pressure (mbar)	Crystallite size (nm)		
	For (222) plane	For (400) plane	For (440) plane
9.3×10^{-3}	20.28	16.85	17.02
5.3×10^{-3}	19.33	16.36	16.34
3.8×10^{-3}	15.59	18.14	11.76

Table 6.2: *Crystallite sizes for different planes of ITO films at various substrate temperatures.*

Substrate temperature (°C)	Crystallite size (nm)		
	For (222) plane	For (400) plane	For (440) plane
130	11.96	17.83	12.32
150	15.59	18.14	11.76
170	14.49	19.24	14.08
200	14.63	15.90	9.99

with peaks at 2θ = 21.07°, 29.90, 34.98°, 37.13°, 44.98°, 50.18° and 59.91° corresponding to planes (211), (222), (400), (411), (431), (440), and (622) respectively and are found in good concurrence with cubic phase of ITO (JCPDS card no.: 06-0416) [17, 18]. All films exhibited an intense peak along the (222) plane, but when the PP is reduced to 3.8×10^{-3} mbar, intensity of the (400) peak has improved significantly. Table 6.1 shows crystallite sizes for dominant planes of ITO films prepared at different process pressures. There was no obvious difference in crystallite size along any of the planes when the pressure is decreased from 9.3×10^{-3} mbar to 5.3×10^{-3} mbar. However, a considerable reduction in the sizes of (222) and (440) aligned

crystallites is due to the favoured growth of the (400) peak [19, 20]. Growth of ITO crystallites along [400] direction is influenced by the energy of sputtered particles striking the substrate surface, which is high at low pressure; so growth along [400] increases when PP is reduced [18, 21]. Furthermore, growing crystallites along the [400] direction can increase the deposition rate of ITO films because crystallites orientated along the [222] direction are more prone to re-sputtering than crystallites developed along the [400] direction. This is consistent with UV-Vis findings, which revealed an increased deposition rate at low PP and will be discussed in the following section. The similar pattern has been reported for ITO films prepared using various methods [21].

The XRD patterns displayed in Figure 6.1b for the substrate temperature variation series reveal that the ITO films have different preferential growth orientations for different substrate temperatures. Films prepared at T_s = 130 °C showed major grains growth for [400] direction. Increase in T_s to 150 °C and 170 °C resulted in the development of the (222) peak in addition to the preferential growth of (400) peak [22, 23]. Increase in substrate temperature increases the diffusivity of Ad-atoms on the substrate surface initiating preferred alignment along [400] direction [23]. At T_s = 200 °C, a decrease in oxygen vacancies within ITO films most likely initiated a shift in growth orientation from [400] to [222] [21, 23]. High substrate temperatures might provide oxygen atoms sufficient energy to get bonded in the ITO matrix and fill the oxygen vacancy. This could explain why, at T_s >130 °C, the peak intensity of the (222) plane increases at the expense of the intensity of the (400) plane [23]. Table 6.2 shows crystallite sizes for dominant planes of ITO films prepared at different substrate temperatures.

6.2.2 FESEM studies

FESEM images of ITO films deposited on corning glass substrates for different deposition parameters are shown in Figure 6.2. Figure 6.2a and 6.2c show FESEM images of films

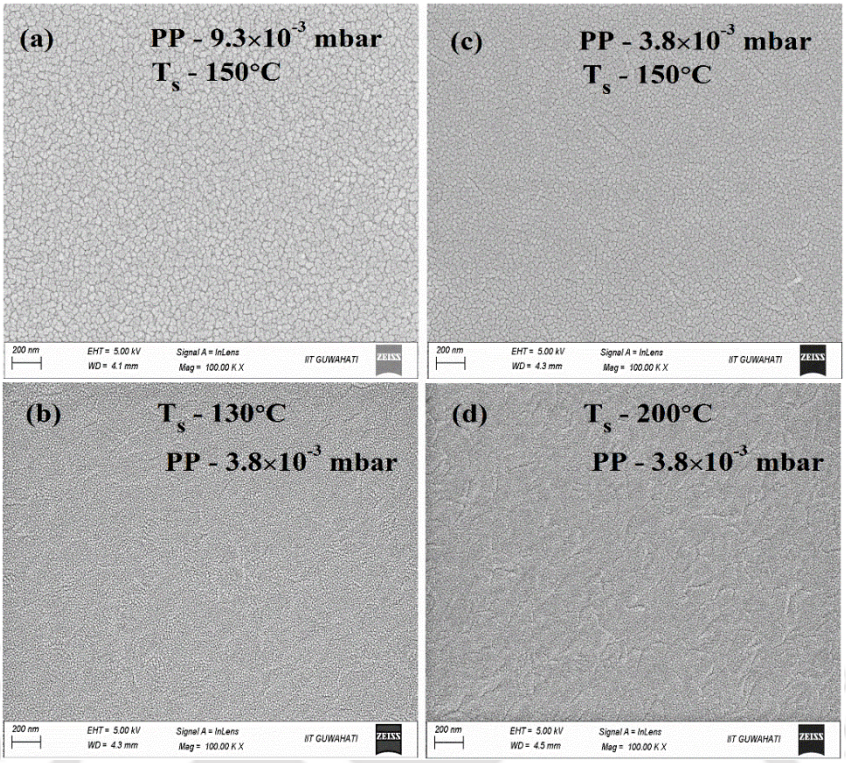

Figure 6.2: *FESEM micrograph for ITO films of (a,c) process pressure variation and (b,d) substrate temperature variation.*

deposited at 9.3×10^{-3} mbar and 3.8×10^{-3} mbar pressure respectively. The high pressure film consisted of more grain boundaries, whereas the grain boundaries decreased at low pressure, forming a compact film. All ITO films are observed to have pinhole-free surface.

Figure 6.2b, 6.2c and 6.2d show the FESEM images of the ITO films deposited at different substrate temperatures (130 ℃, 150 ℃ and 200 ℃ at 3.8×10^{-3} mbar PP). Films prepared at low temperature (130 ℃) have small size grains, whereas at T_s = 150 ℃, an increase in grain size is observed. A further increase in T_s to 200 ℃ resulted in a decrease in grain size and detoriated the film quality, as shown in Figure 6.2d. Films deposited at T_s = 130 ℃, 150 ℃ and 200 ℃ are compact yet have rough surface.

6.2.3 AFM studies

Figure 6.3 shows 3D AFM images of ITO films deposited at various process pressures and

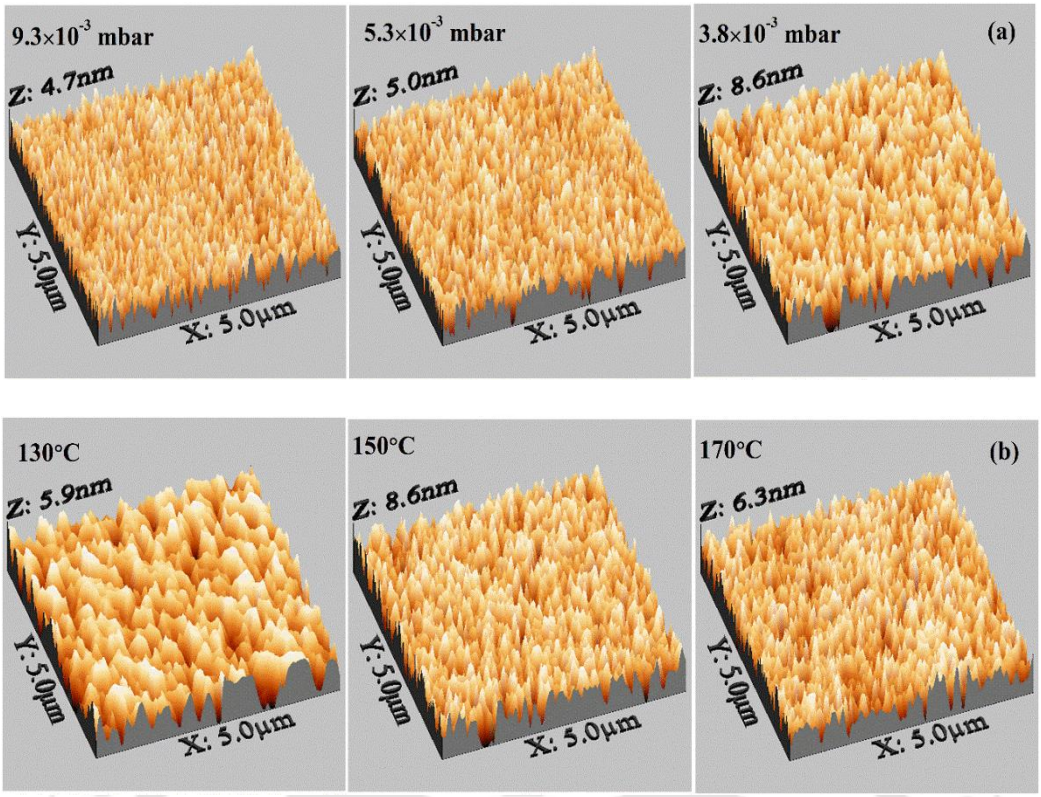

Figure 6.3: *AFM images of ITO films deposited at different (a) process pressure (T_s = 150 °C), and (b) substrate temperature (PP = 3.8×10^{-3} mbar).*

Table 6.3: *rms roughness of ITO films prepared at different process pressures.*

Process Pressure (mbar)	rms roughness (r_{rms}) (nm)
9.3×10^{-3}	1.12
5.3×10^{-3}	1.15
3.8×10^{-3}	1.68

Table 6.4: *rms roughness of ITO films prepared at different substrate temperatures.*

Temperature (°C)	rms roughness (r_{rms}) (nm)
130	1.38
150	1.68
170	1.45
200	1.52

substrate temperatures. AFM images (Figure 6.3a) show that, films prepared at high pressures (9.3×10^{-3} mbar and 5.3×10^{-3} mbar) have uniformly distributed grains of ITO. However, low-pressure films (3.8×10^{-3} mbar) are composed of different-sized ITO grains. The rms roughness of ITO films deposited at different PP are listed in Table 6.3. Films deposited at 3.8×10^{-3} mbar have higher rms roughness because of the existence of smaller and larger grains altogether for (222), (400) and (440) planes, as observed in XRD studies. This property is beneficial for TCO

because it also functions as an antireflective layer in a solar cell, and a rougher surface can help in reducing the reflection losses at the surface [18].

Fig. 6.3b and Table 6.4 present AFM images and roughness of ITO films deposited at different T_s, respectively. The films deposited at T_s = 130 °C have the lowest surface roughness (1.38 nm) and increasing T_s to 150 °C produced rougher ITO films with surface roughness of 1.68 nm. Further increases in T_s above 150 °C results in decrease in surface roughness of ITO films.

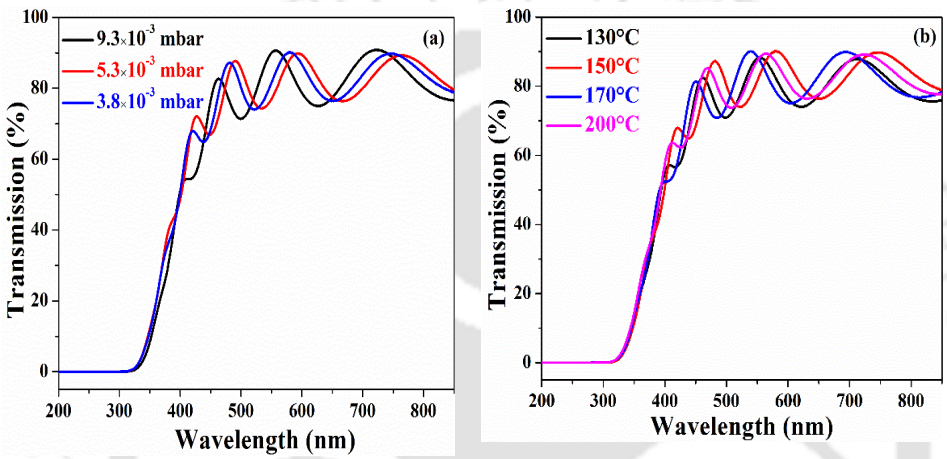

Figure 6.4: *UV-Vis transmission spectra of ITO films deposited at different (a) process pressures and (b) substrate temperatures.*

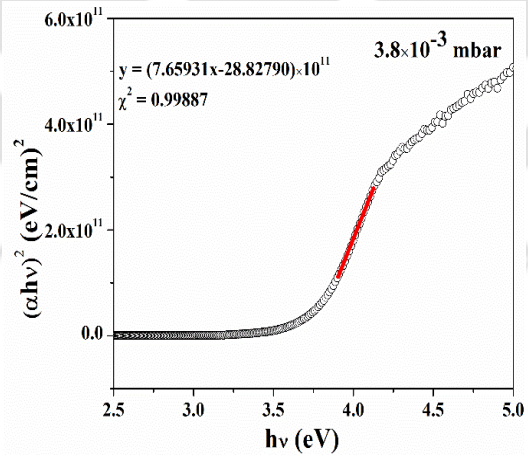

Figure 6.5: *$(\alpha h\nu)^2$ vs. hν plot for ITO film prepared at a process pressure of 3.8×10^{-3} mbar.*

6.2.4 UV-Vis studies

Figure 6.4a shows the UV-Vis transmission spectra of ITO films prepared at different process pressures. All the films have interference fringes in the visible region with good transparency

Table 6.5: *Thickness, deposition rate (r_d), and optical band gap (E_g) for the ITO films prepared at varied process pressure estimated from UV-Vis transmission spectra along with thickness measured by surface profilometer.*

Process Pressure (mbar)	Thickness from UV-Vis transmission spectra (nm)	Thickness from profilometer (nm)	E_g (eV)	r_d (Å/s)
9.3×10^{-3}	327	345±12	3.72±0.01	1.92±0.13
5.3×10^{-3}	555	538±15	3.75±0.01	3.00±0.17
3.8×10^{-3}	621	624±8	3.76±0.02	3.50±0.09

Table 6.6: *Thickness, deposition rate (r_d), and optical band gap (E_g) for the ITO films prepared at varied substrate temperatures estimated from UV-Vis transmission spectra along with thickness measured by surface profilometer.*

Substrate temperature (°C)	Thickness from UV-Vis transmission spectra (nm)	Thickness from profilometer (nm)	E_g (eV)	r_d (Å/s)
130	560	592±10	3.73±0.01	3.30±0.11
150	621	624±8	3.76±0.02	3.50±0.09
170	643	630±12	3.68±0.02	3.50±0.13
200	585	598±5	3.73±0.02	3.32±0.06

~85% (maximum transmission ~91%). Film thicknesses calculated using the Swanepoel method and profilometer are listed in Table 6.5 [24]. The thicknesses determined by the profilometer and the Swanepoel method yielded closer values. Increase in deposition rate (r_d) is observed from 1.9 Å/s to 3.5 Å/s when PP is lowered from 9.3×10^{-3} mbar to 3.8×10^{-3} mbar respectively. At high pressure, a large number of argon ions remain in the chamber, increasing the collision frequency and lowering the energy of the argon ions striking the ITO target. This reduces the number of sputtered atoms/molecules emitted from the ITO target, resulting in decreased deposition rate. On the other hand, because of the lower collision frequency at low pressure conditions, argon ions retain more energy. When these highly energetic ions collide with the ITO target, more ITO molecules sputter from the target and reach the substrate, increasing the deposition rate of ITO films [18, 25]. The optical band gap (E_g) of ITO films is calculated by plotting $(\alpha hv)^2$ vs. hv as shown in Figure 6.5 and listed in Table 6.5 [26]. Band gap is found to be nearly same (~3.74 eV) for all PP varied ITO films.

Figure 6.4b shows the UV-Vis transmission spectra of ITO films deposited at different substrate temperatures. The transmission of each film is in the range of ~85% in the visisble

range with interference fringes. Table 6.6 shows the thickness, deposition rate and band gap of all substrate temperature-varied films. Not much variation is noticed in thickness, band gap, and deposition rate values with change in substrate temperature.

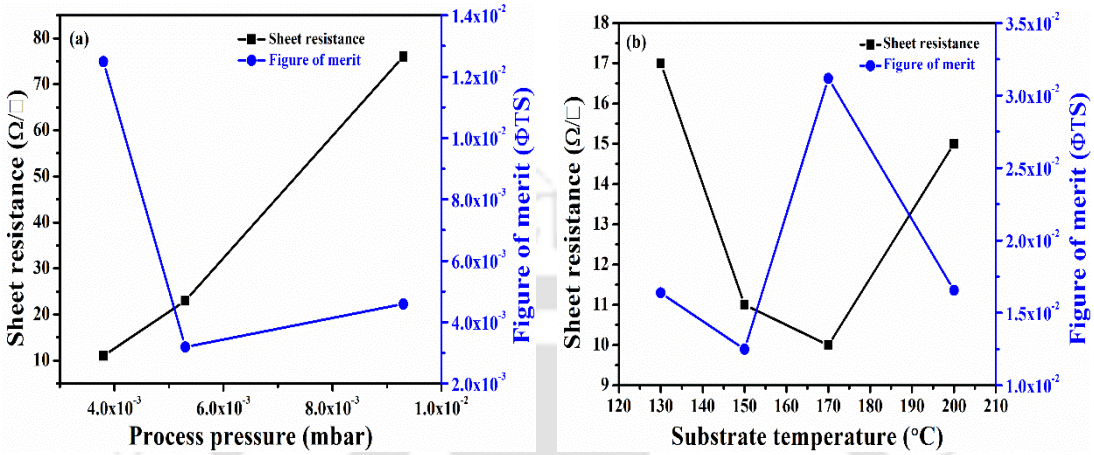

Figure 6.6: *The sheet resistance and figure of merit values for (a) different process pressures and (b) substrate temperature.*

6.2.5 Sheet Resistance Studies

The sheet resistance (R_{sheet}) of ITO films deposited on corning glass is measured using four-point probe method as described in Chapter 2, Equation 2.15 [27].

When electrical sheet resistance and optical transmission properties are known, the performance of TCOs can be compared by calculating its figure of merit. Thus, to quantitatively evaluate the performance of ITO films deposited at different process pressures and substrate temperatures, figure of merit *(ΦTS)* is calculated using the equation 6.1 [28]

$$\text{Figure of Merit } (\Phi TS) = \frac{T^{10}}{R_{sheet}} \qquad \text{---------- (6.1)}$$

where T is the transmittance of ITO film at 550 nm, and R_{sheet} is the sheet resistance.

Figure 6.6 shows the sheet resistance and figure of merit values for different process pressures and susbtrate temperatures. Low PP films have lower sheet resistance value (Figure 6.6a) than high pressure films. ITO films having orientation along [222] and [400] directions exhibit high

Table 6.7: *Sheet resistance and the figure of merit of ITO films prepared at different process pressures.*

Process pressure (mbar)	Transmittance at 550 (nm)	Sheet resistance (Ω/□)	The figure of merit (ΦTS)
9.3×10^{-3}	0.90	76	4.59×10^{-3}
5.3×10^{-3}	0.77	23	3.19×10^{-3}
3.8×10^{-3}	0.82	11	12.49×10^{-3}

Table 6.8: *Sheet resistance and the figure of merit of ITO films prepared at different substrate temperatures.*

Substrate temperature (°C)	Transmittance at 550 (nm)	Sheet resistance (Ω/□)	The figure of merit (ΦTS)
130	0.88	17	16.38×10^{-3}
150	0.82	11	12.49×10^{-3}
170	0.89	10	31.18×10^{-3}
200	0.87	15	16.56×10^{-3}

carrier mobility and high carrier density [29]. The conductivity of ITO is determined by the presence of Sn atoms and oxygen vacancies [29, 30]. As the (222) plane confirms the substiution of Indium (In^{3+}) vacancy by Tin (Sn^{4+}) in In_2O_3 and (400) refers to oxygen vacancy [20], presence of both the planes in adequate ratio is required to attain low resistivity and high transparency of ITO films finding its application in optoelectronic devices. In our case, ITO films prepared at low PP exhibited preferential peaks along both (222) and (400) planes as well as higher thickness, which explain the reason for getting lower sheet resistance at PP of 3.8×10^{-3} mbar. Transmittance of ITO films at 550 nm, respective sheet resistance and ΦTS are mentioned in Table 6.7. The lowest sheet resistance of 11 Ω/□ and highest figure of merit of 12.49×10^{-3} are observed for ITO films prepared at 3.8×10^{-3} mbar process pressure, which suggest that low process pressure is required to prepare good quality ITO films suitable for its use as TCO in solar cells.

Table 6.8 shows the sheet resistance and the figure of merit values of ITO films prepared at various substrate temperatures. Sheet resistance is lowest for films deposited at 170 °C (10 Ω/□) and 150 °C (11 Ω/□) temperatures due to formation of thicker ITO films. Films deposited at 170°C have highest figure of merit, primarily because these ITO films have lowest sheet resistance and highest transmittance. A plot of sheet resistance and figure of merit for various

T_s is shown in Figure 6.6b.

6.3 Conclusion

ITO films are deposited on corning glass substrates at different process pressures and substrate temperatures using rf-sputtering technique. In the first series, process pressure is varied from 5.3×10^{-3} mbar to 3.8×10^{-3} mbar and its effect on structural, optical and electrical properties is studied. Low PP has resulted in the formation of polycrystalline ITO films with preferential peaks along (222) and (400) planes. ITO films depsoited at low PP exhibited highest deposition rate (3.50 Å/s) , lowest sheet resistance (11 Ω/□) and highest figure of merit (12.49×10^{-3}). In the second series, the substrate temperature is varied from 130 °C to 200 °C at optimized PP of 3.8×10^{-3} mbar pressure. ITO films deposited at T_s = 150 °C and 170 °C are polycrystalline with intense peak along (400) and (222) planes. ITO films deposited at 170 °C have lowest sheet resistance (10 Ω/□) and highest figure of merit (31.18×10^{-3}). These studies suggest that PP of 3.8×10^{-3} mbar and T_s = 150°C/170°C are ideal conditions to deposit ITO films suitable for their application in solar cells.

6.4 References

[1] T. Feng, A.K. Ghosh, C. Fishman, Structure, photovoltaic properties, and angle-of-incidence correlations of electron-beam-deposited SnO_2/n-Si solar cells, Journal of Applied Physics, 50 (1979) 8070-8074.

[2] G.K.B.a.K.B. Sundaram, Electrical and photvoltaic properties of Tin Oxide-Silicon heterojunctions, Thin Solid Films, 63 (1979) 197-201.

[3] Takao Nagatomo, Mitsuo Endo, Osamu Omoto, Fabrication and Characterization of SnO_2/n-Si Solar Cells, Japanese Journal of Applied Physics, 18 (1979) 1103.

[4] H. Kim, A. Pique, J.S. Horwitz, H. Mattoussi, H. Murata, Z.H. Kafafi, D.B. Chrisey, Indium

tin oxide thin films for organic light-emitting devices, Applied Physics Letters, 74 (1999) 3444-3446.

[5] G.S. Chae, A Modified Transparent Conducting Oxide for Flat Panel Displays Only, Japanese Journal of Applied Physics, 40 (2001) 1282.

[6] R.A. Afre, N. Sharma, M. Sharon, M. Sharon, Transparent Conducting Oxide Films for Various Applications: A Review, 53 (2018) 79-89.

[7] W. Beyer, J. Hupkes, H. Stiebig, Transparent conducting oxide films for thin film silicon photovoltaics, Thin Solid Films, 516 (2007) 147-154.

[8] G. Brunin, F. Ricci, V.-A. Ha, G.-M. Rignanese, G. Hautier, Transparent conducting materials discovery using high-throughput computing, npj Computational Materials, 5 (2019) 63.

[9] J. Kumari, P. Basumatary, M.S. Gangwar, P. Agarwal, Molybdenum oxide (MoO_{3-x}) as an emitter layer in silicon based heterojunction solar cells, Materials Today: Proceedings, 39 (2021) 1996-1999.

[10] Z. Yu, I.R. Perera, T. Daeneke, S. Makuta, Y. Tachibana, J.J. Jasieniak, A. Mishra, P. Bauerle, L. Spiccia, U. Bach, Indium tin oxide as a semiconductor material in efficient p-type dye-sensitized solar cells, NPG Asia Materials, 8 (2016) e305-e305.

[11] A. Altuntepe, S. Erkan, O. Hasret, A. Yagmyrov, D. Yazici, M. Tomakin, M.A. Olgar, R. Zan, Performance of Si-based solar cell utilizing optimized Al-doped ZnO films as TCO layer, Journal of Materials Science: Materials in Electronics, 34 (2023).

[12] S. Sinha, S.K. Maurya, R. Balasubramaniam, S.K. Sarkar, Development of Al doped ZnO as TCO by Atomic Layer Deposition, 2015 IEEE 42nd Photovoltaic Specialist Conference (PVSC), (2015).

[13] H.A. Gatz, D. Koushik, J.K. Rath, W.M.M. Kessels, R.E.I. Schropp, Atomic Layer Deposited ZnO: B As Transparent Conductive Oxide for Increased Short Circuit Current

Density in Silicon Heterojunction Solar Cells, Energy Procedia, 92 (2016) 624-632.

[14] H.M. Yates, P. Evans, D.W. Sheel, The Influence of F-Doping in SnO_2 Thin Films, Physics Procedia, 46 (2013) 159-166.

[15] J. Shi, L. Shen, Y. Liu, J. Yu, J. Liu, L. Zhang, Y. Liu, J. Bian, Z. Liu, F. Meng, MoO_x modified ITO/a-Si:H(p) contact for silicon heterojunction solar cell application, Materials Research Bulletin, 97 (2018) 176-181.

[16] W. Gong, G. Wang, Y. Gong, L. Zhao, L. Mo, H. Diao, H. Tian, W. Wang, J. Zong, W. Wang, Investigation of In_2O_3:SnO_2 films with different doping ratio and application as transparent conducting electrode in silicon heterojunction solar cell, Solar Energy Materials and Solar Cells, 234 (2022) 111404.

[17] D. Caudevilla, E. García-Hemme, E. San Andres, F. Perez-Zenteno, I. Torres, R. Barrio, R. García-Hernansanz, S. Algaidy, J. Olea, D. Pastor, A. del Prado, Indium tin oxide obtained by high pressure sputtering for emerging selective contacts in photovoltaic cells, Materials Science in Semiconductor Processing, 137 (2022) 106189.

[18] S. Najwa, A. Shuhaimi, N. Ameera, K.M. Hakim, M. Sobri, M. Mazwan, M.H. Mamat, Y. Yusnizam, V. Ganesh, M. Rusop, The effect of sputtering pressure on structural, optical and electrical properties of indium tin oxide nanocolumns prepared by radio frequency (RF) magnetron sputtering, Superlattices and Microstructures, 72 (2014) 140-147.

[19] L.-j. Meng, M.P. dos Santos, Properties of indium tin oxide (ITO) films prepared by r.f. reactive magnetron sputtering at different pressures, Thin Solid Films, 303 (1997) 151-155.

[20] A.M. Gheidari, F. Behafarid, G. Kavei, M. Kazemzad, Effect of sputtering pressure and annealing temperature on the properties of indium tin oxide thin films, Materials Science and Engineering: B, 136 (2007) 37-40.

[21] C. Guillen, J. Herrero, Polycrystalline growth and recrystallization processes in sputtered ITO thin films, Thin Solid Films, 510 (2006) 260-264.

[22] G.-Y. Tzou, C.-C. Wu, C.-C. Diao, Effects of substrate temperature on the properties of the indium tin oxide thin films deposited by sputtering method, MATEC Web of Conferences, 185 (2018).

[23] M. Nisha, S. Anusha, A. Antony, R. Manoj, M.K. Jayaraj, Effect of substrate temperature on the growth of ITO thin films, Applied Surface Science, 252 (2005) 1430-1435.

[24] R. Swanepoel, Determination of the thickness and optical constants of amorphous silicon, Journal of Physics E: Scientific Instruments, 16 (1983) 1214.

[25] H. Zhang, H. Zhu, T.-h. Zhang, S.-j. Yu, P.-c. Guo, Y.-x. Wang, Z.-s. Yang, Effect of sputtering pressure on the optical and electrical properties of ITO film on fluorphlogopite substrate, Applied Surface Science, 559 (2021) 149968.

[26] M. Thirumoorthi, J. Thomas Joseph Prakash, Structure, optical and electrical properties of indium tin oxide ultra thin films prepared by jet nebulizer spray pyrolysis technique, Journal of Asian Ceramic Societies, 4 (2016) 124-132.

[27] M. Naftaly, S. Das, J. Gallop, K. Pan, F. Alkhalil, D. Kariyapperuma, S. Constant, C. Ramsdale, L. Hao, Sheet Resistance Measurements of Conductive Thin Films: A Comparison of Techniques, Electronics, 10 (2021) 960.

[28] G. Haacke, New figure of merit for transparent conductors, Journal of Applied Physics, 47 (1976) 4086-4089.

[29] S. Ahn, A.H. Tuan Le, S. Kim, C. Park, C. Shin, Y.-J. Lee, J. Lee, C. Jeong, V. Ai Dao, J. Yi, The effects of orientation changes in indium tin oxide films on performance of crystalline silicon solar cell with shallow-emitter, Materials Letters, 132 (2014) 322-326.

[30] S. Yang, B. Sun, Y. Liu, J. Zhu, J. Song, Z. Hao, X. Zeng, X. Zhao, Y. Shu, J. Chen, J. Yi, J. He, Effect of ITO target crystallinity on the properties of sputtering deposited ITO films, Ceramics International, 46 (2020) 6342-635.

CHAPTER 7

Fabrication and characterization of dopant free single sided MoO_{3-x}/c-Si(n) heterojunction solar cells

Sub-stoichiometric MoO_{3-x} is widely used hole selective layer (HSL) in organic and inorganic semiconductor devices due to its wide band gap and high work function value [1-4]. The application of MoO_{3-x} in silicon wafer-based heterojunction solar cells has accelerated due to the excellent results obtained by replacing p-doped amorphous silicon layers with MoO_{3-x} [5-7]. Furthermore, the large band gap of MoO_{3-x} reduces parasitic absorption losses, resulting in increased current density for MoO_{3-x} /c-Si solar cells [8]. However, fill factor and open circuit voltage of dopant-free MoO_{3-x}/c-Si(n) solar cells are being constrained by the MoO_{3-x} material's temperature sensitivity. In this chapter, we have sequentially optimised the different layers' deposition conditions to fabricate an efficient MoO_{3-x}/c-Si(n) solar cells. Initially, devices with different back electrodes are fabricated and their effect on the performance of solar cells is studied. We have also explored the impact of the ITO's deposition conditions on the performance of dopant-free single-sided MoO_{3-x}/c-Si (n) solar cells because MoO_{3-x} films

also suffer sputtering damage during the deposition of transparent conducting oxide (TCO), i.e. indium tin Oxide (ITO). MoO_{3-x} preparation temperature and its subsequent heat treatment during the fabrication of MoO_{3-x}/c-Si (n) solar cell have also been tuned to achieve good device performance. FETEM, FESEM and UV-Vis spectroscopy are used to investigate the effect of various heat treatments on the properties of MoO_{3-x} films.

Using, MoO_{3-x} as the HSL and ITO as TCO layer, solar cells with the configurations *Ag/ITO/MoO_{3-x}/c-Si(n)/Ag* and *Ag/ITO/MoO_{3-x}/c-Si(n)/Al/Ag* are fabricated. The specifications of c-Si (n) wafers (CZ) used for cell fabrication are: thickness ~ 275 -325 µm, resistivity ~ 5-10 Ωcm. Prior to the deposition of different layers, silicon wafers are cleaned using RCA 1 and RCA 2 methods as described in Chapter 2 (section 2.3.1 & 2.3.2), to remove organic based contaminants and metal residues respectively [9] and subsequently dipped in hydrofluoric acid with 2% dilution to remove native silicon oxide layers formed on the surface of silicon wafers. Aluminium (Al) and silver (Ag) are used as back electrodes and deposited using thermal evaporation and rf-sputtering techniques respectively. MoO_{3-x} films (about 22-26 nm) are deposited on double-side polished c-Si (n) wafers using thermal evaporation technique. Afterwards, ITO film (~80 nm) is deposited on top of MoO_{3-x} layer using rf magnetron sputtering. Front metal grids are prepared using silver (Ag) paste (purity 99.99%) on top of ITO for better electrical contacts. Current density-voltage (*J-V*) measurements of fabricated dopant free solar cells are performed in dark and under AM 1.5 illumination at room temperature.

7.1 Fabrication of device using different back electrodes combination

MoO_{3-x}/c-Si (n) solar cells are fabricated (i) with Ag as back electrode and (ii) with Aluminium

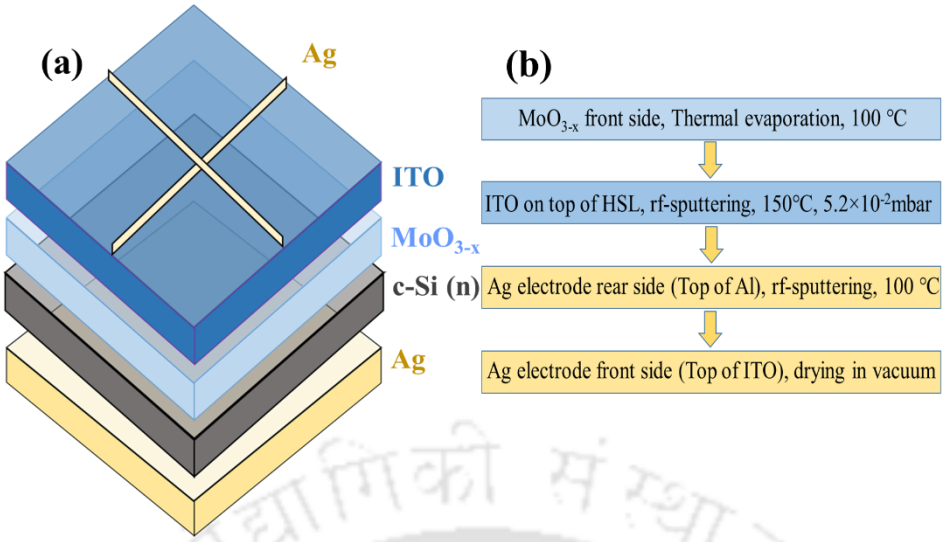

Figure 7.1: *(a) MoO_{3-x}/c-Si (n) device structure with Ag as back electrode and (b) steps for fabrication of respective device.*

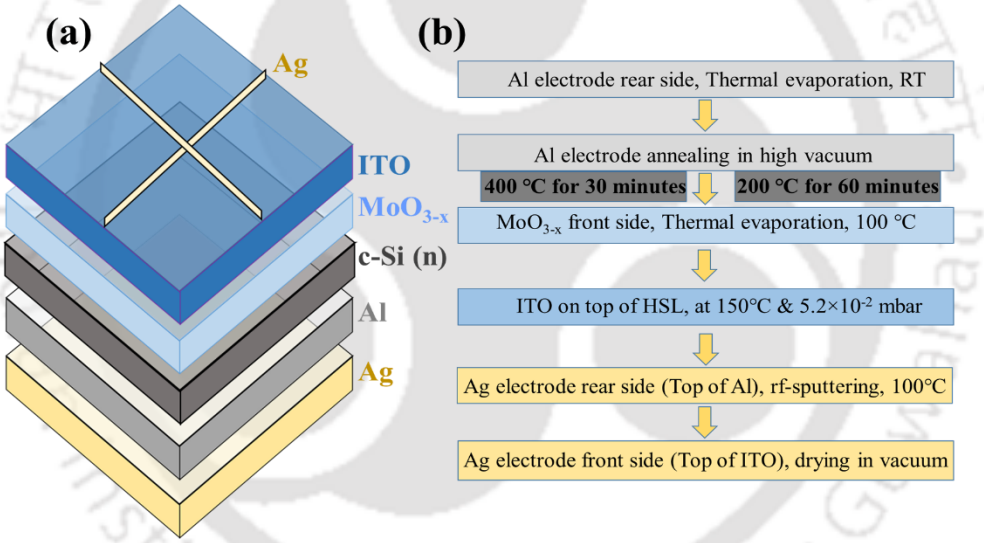

Figure 7.2: *(a) MoO_{3-x}/c-Si (n) device structure with Ag/Al as back electrodes and (b) steps for fabrication of respective device.*

(Al) and Ag as back electrodes. Al electrode is deposited on rear side using thermal evaporation method and Ag is deposited on top of Al using rf magnetron sputtering as back electrode. Figures 7.1 and 7.2 illustrate device configurations with Ag and Ag/Al back electrodes, as well as the corresponding device fabrication steps.

The current density and voltage (*J-V*) characteristic of *Ag/ ITO/MoO_{3-x}/c-Si(n)/Ag* solar cell with Ag as back electrode is shown in Figure 7.3a. This device showed an open circuit voltage

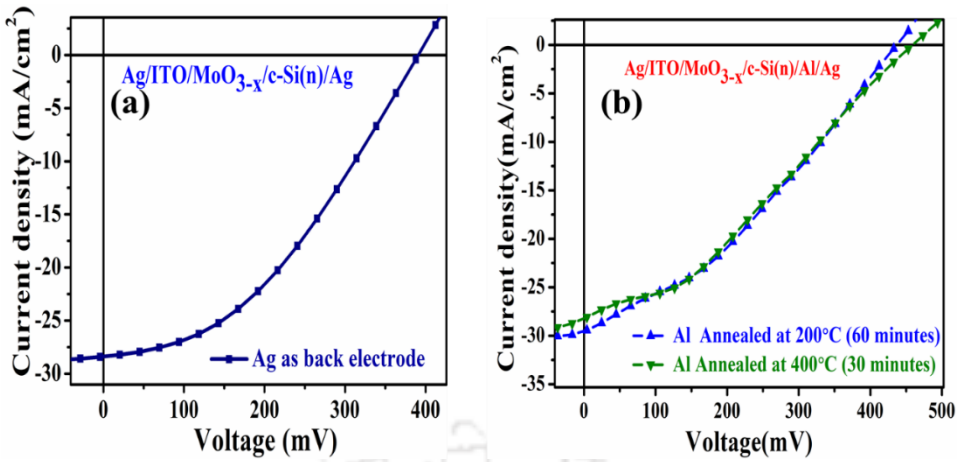

Figure 7.3: *J-V characteristics of fabricated solar cells (a) with Ag as back electrode and (b) Ag/Al as back electrodes.*

Table 7.1: *Calculated solar cell parameters for MoO_{3-x}/c-Si(n) solar cells.*

Cell Structure	J_{sc} (mA/cm^2)	V_{oc} (mV)	FF	η (%)	R_{sh} (Ω.cm^2)	R_s (Ω.cm^2)
Ag/ ITO/MoO_{3-x}/c-Si(n)/Ag	28.44	391	0.40	4.44	155.40	8.75
Ag/ ITO/MoO_{3-x}/c-Si(n)/Al/Ag (Al annealed at 200 °C for 60 minutes)	28.57	437	0.32	3.99	34.14	11.21
Ag/ ITO/MoO_{3-x}/c-Si(n)/ Al/Ag (Al annealed at 400 °C for 30 minutes)	28.14	455	0.30	3.84	29.16	14.86

(V_{oc}) = 391 mV, current density (J_{sc}) = 28.44 mA/cm^2, fill factor (*FF*) = 0.40 and device efficiency (η) = 4.44%. The V_{oc} and *FF* values of this device are relatively low. To increase the device performance, the combination of Al and Ag are used as back electrodes for efficient extraction of photo-generated charge carriers. Al electrodes are deposited on the backside of c-Si (n) wafer using thermal evaporation technique and diffused into the silicon wafer by annealing at 200 °C for 60 minutes for one device and at 400 °C for 30 minutes for the other one, followed by the deposition of HSL, ITO and Ag. Annealing process is carried out under high vacuum (5.5×10^{-5} mbar) condition. The *J-V* characteristics of these cells (*Ag/ ITO/MoO_{3-x}/c-Si(n)/Al/Ag*) are shown in Figure 7.3b. The use of Ag/Al back electrodes have improved V_{oc} from 391 to 455 mV. It is because of improved back contact, which facilitates the extraction of majority carriers from c-Si (n) to metal contacts. However, FF decreased from 0.40 to 0.30. Combination of Ag and Al as back electrodes lowered shunt resistance *(R_{sh})* while increasing series resistance (R_s). The repeated exposure of c-Si (n) wafers in the environment after

annealing can cause adsorption of moisture on surface of the fabricated devices. As MoO_{3-x} is moisture sensitive, it may result in poor junction formation during MoO_{3-x} deposition and a decrease in shunt resistance. No change is J_{sc} is observed for devices prepared using Ag/Al as back electrodes. These results are summarized in Table 7.1.

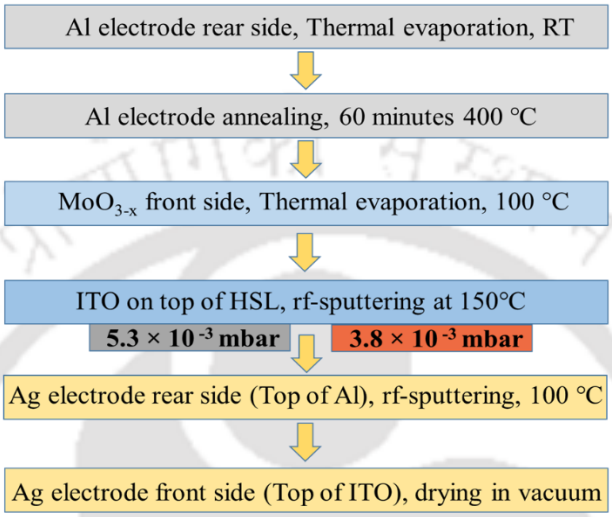

Figure 7.4: *Steps used for fabrication of MoO_{3-x}/c-Si(n) with different ITO preparation conditions.*

7.2 Fabrication of device by varying the process pressure for depositing ITO, the TCO layer

The optimised deposition conditions described in Chapter 6 are used to deposit ITO films with high transparency and low sheet resistance. Solar cells are fabricated using different process pressures for 80 nm ITO film deposition i.e., 5.3×10^{-3} mbar and 3.8×10^{-3} mbar. RCA cleaned c-Si (n) wafers are dried with nitrogen gas and immediately loaded in the thermal evaporation chamber to deposit Al (~200 nm) as back electrode followed by annealing at 400 °C for 1 hour under high vacuum conditions. After annealing, MoO_{3-x} is deposited on front side using thermal evaporation at substrate temperature (T_s) of 100 °C. Afterwards, ITO layer is deposited on top of HSL using rf-sputtering at T_s = 150 °C. Ag (~150 nm) is deposited at 100 °C using rf-sputtering as back electrode on top of diffused Al. Solar cell preparation steps are shown in Figure 7.4. Figure 7.5 shows solar cells' *J-V* characteristics for ITO layer deposited at different

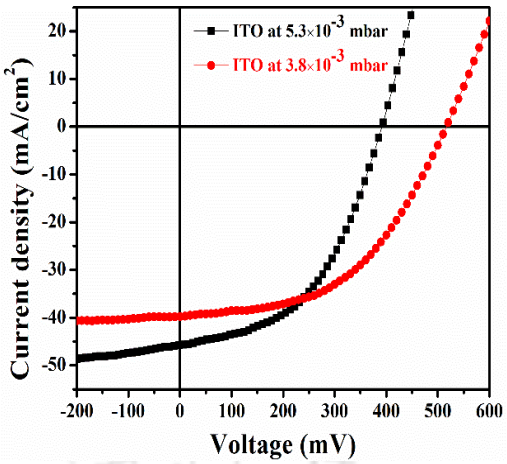

Figure 7.5: *J-V characteristics of the fabricated devices with ITO layers deposited at different process pressure.*

Table 7.2: *Calculated solar cell parameters for MoO_{3-x}/c-Si(n) solar cells (Cell diameter = 3mm).*

ITO process pressure (mbar)	V_{oc} (mV)	J_{sc} (mA/cm^2)	*FF*	η (%)	R_s (Ω.cm^2)	R_{sh} (Ω.cm^2)
5.3×10^{-3}	391	45.71	0.48	8.58	3.99	54.25
3.8×10^{-3}	517	39.71	0.49	10.06	4.13	140.00

process pressures. The solar cell parameters are shown in Table 7.2. The cell open circuit voltage increased from 391 mV to 517 mV and efficiency increased from 8.58% to 10.06% with a decrease in deposition pressure of ITO film from, 5.3×10^{-3} mbar to 3.8×10^{-3} mbar respectively. The improvement in V_{oc} is due to the high R_{sh} value, suggesting the formation of a better ITO/MoO_{3-x} interface at 3.8×10^{-3} mbar pressure. Because of the higher deposition rate (3.5 Å/s) at low deposition pressure (3.0 Å/s at 5.3×10^{-3} mbar pressure) (Chapter 6, section 6.2.4), MoO_{3-x} films are exposed to rf-plasma for a shorter duration [10]. This reduces sputter damage to the films and improves the junction between ITO and MoO_{3-x} [11]. A decrease in current density (J_{sc}) and small increase in series resistance (R_s) (Table 8.2) are observed for solar cell in which ITO is prepared at 3.8×10^{-3} mbar. This difference could be due to the slight variation in thicknesses of MoO_{3-x} films (22 nm for 5.3×10^{-3} mbar and 26 nm for 3.8×10^{-3} mbar) as these devices are fabricated in different batches.

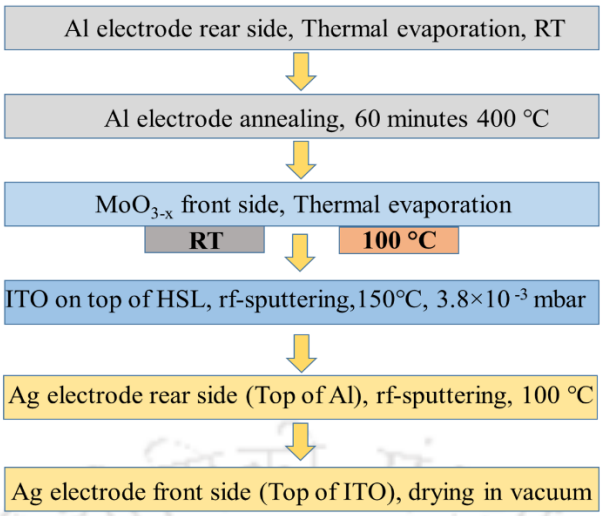

Figure 7.6: *Steps used for fabrication of MoO_{3-x}/c-Si (n) device by varying MoO_{3-x} deposition temperature.*

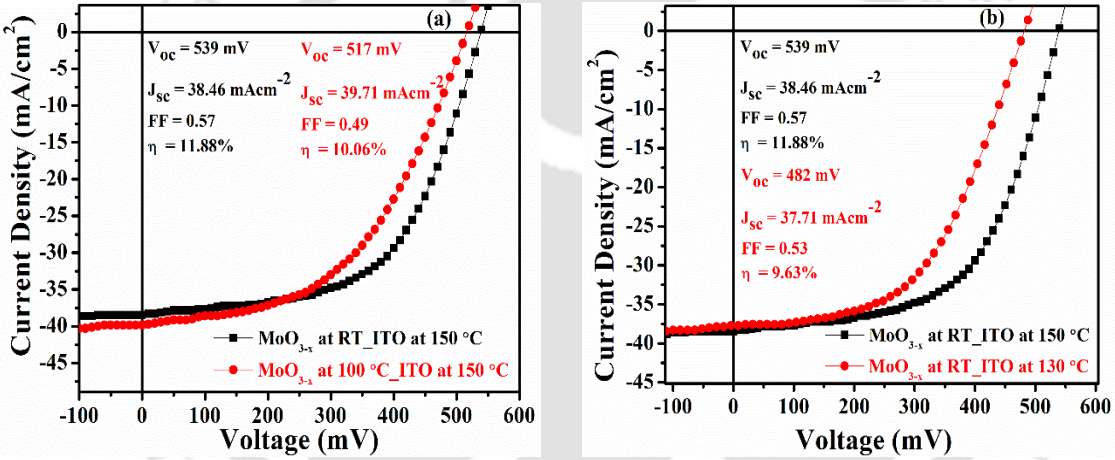

Figure 7.7*: J-V characteristics of fabricated solar cells (a) HSL deposited at different T_s and (b) ITO deposited at different T_s.*

7.3 Fabrication of devices by varying the deposition temperature of MoO_{3-x} and ITO layers

In this study, we have explored how the performance of solar cells is impacted by the deposition temperature of different layers. Deposition conditions of different layers of *Ag/ITO/MoO_{3-x}/c-Si(n)/Al/Ag* solar cells are specified in Figure 7.6. Keeping the device structure and fabrication steps same, devices are prepared in different conditions like preparation of MoO_{3-x} and ITO layers at different deposition temperatures (T_s) and its effect on the device performance is studied. Figure 7.7a depicts the *J-V* characteristics of devices fabricated using MoO_{3-x} as the

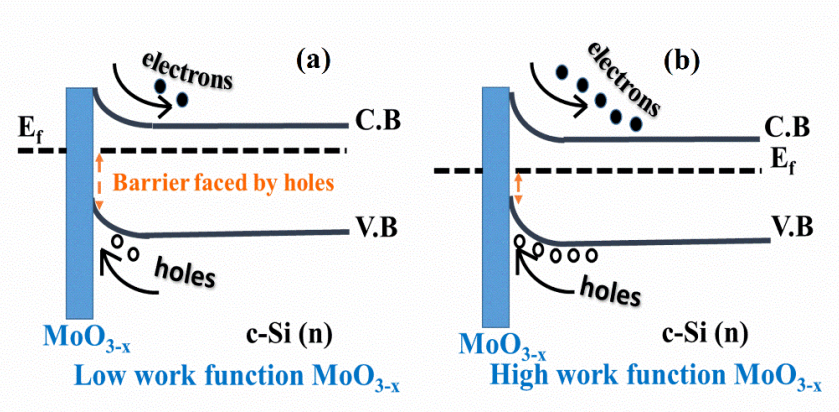

Figure 7.8: *Band diagram of MoO_{3-x}/c-Si (n) solar cells.*

Table 7.3*: Solar cell parameters for different deposition temperatures of MoO_{3-x} and ITO.*

MoO_{3-x} deposition temperature	ITO deposition temperature	V_{oc} (mV)	J_{sc} (mA/cm^2)	*FF*	η (%)	R_s (Ω.cm^2)	R_{sh} (Ω.cm^2)
100 ℃	150 ℃	517	39.71	0.49	10.06	4.13	140
RT	**150 ℃**	539	38.46	0.57	11.88	3.50	175
RT	**130 ℃**	482	37.71	0.53	9.63	4.27	140

HSL, at two different deposition temperatures (RT and 100 °C). Devices with MoO_{3-x} deposited at room temperature perform better than those with HSL deposited at 100 °C. Both open circuit voltage (V_{oc}) and fill factor (*FF*) have improved when the MoO_{3-x} deposition temperature is reduced. This can be related to the higher work function of MoO_{3-x} as noticed in the earlier study Chapter 4, section 4.2.1, for RT film. Higher work function eases hole transport due to reduced hole energy barrier at the MoO_{3-x}/c-Si (n) interface, as depicted in Figure 7.8 [13]. Hence, with reduced recombination at the interface, an efficient hole transport from silicon to the molybdenum oxide layer is possible resulting in better device performance, when MoO_{3-x} is deposited at room temperature. These device results are closer to those obtained in simulation studies using thin SiO_x layer with pin holes, which will be discussed in detail in Chapter 8. These results indicate that SiO_x is unintentionally formed at the MoO_{3-x}/c-Si(n) interface, enabling the transport of photogenerated carriers through pinholes and through SiO_x layer. The probability of SiO_x formation is higher for RT deposited MoO_{3-x} films due to more oxygen atoms concentration inside the film, which is also confirmed by the higher work function

achieved for these films as described in Chapter 4, sections 4.2.1.3 & 4.2.1.4.

Our previous study (Chapter 4, section 4.2.2.3) suggested that MoO_{3-x} films annealed in vacuum at 130 °C have higher work function than the films annealed at 150 °C. So, in the next attempt to further enhance the device's performance, the ITO preparation temperature has been reduced to 130 °C. The *J-V* characteristic of a MoO_{3-x}/c-Si (n) heterojunction solar cell with 130 °C-deposited ITO is displayed in Figure 7.7b. When TCO layer is deposited at 130 °C, there is a considerable drop in V_{oc} from 539 mV to 482 mV, which has further led to an overall decrease in efficiency (η) to 9.63%. This degradation may be caused by changes to the structure and work function of MoO_{3-x} films (described in Chapter 4) and increase in sheet resistance of ITO films (described in Chapter 6) [10]. Solar cell parameters for different deposition temperatures of MoO_{3-x} and ITO are listed in Table 7.3.

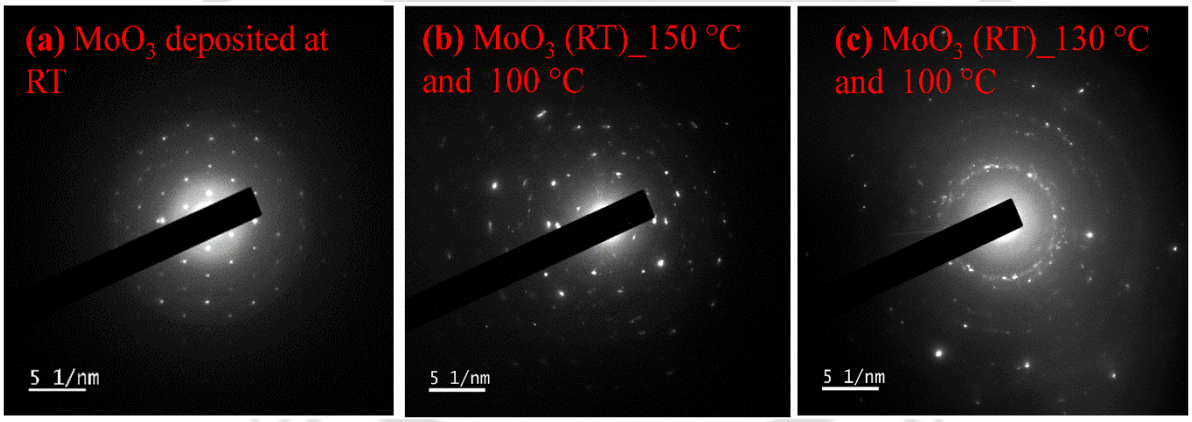

Figure 7.9: *(a) SAED patterns of as deposited MoO_{3-x} and (b), (c) SAED of subsequently two time heat treated MoO_{3-x} films during device fabrication.*

7.3.1.1 Effect of two time heat treatments on properties of MoO_{3-x} films

During the fabrication of MoO_{3-x}/c-Si (n) solar cells, MoO_{3-x} is subjected to heat treatment twice; first during the deposition of ITO at 150°C/130°C and subsequently during the deposition of Ag at 100 °C. So, it is possible that multiple time heat treatment could alter the optoelectronic and structural properties of MoO_{3-x}. To figure out the changes induced by two

time heat treatment (THT); FETEM and FESEM, UV-Vis spectroscopy are performed on MoO_{3-x} films prepared on TEM grids and corning glass substrates respectively and simultaneously subjected to similar heat treatment conditions during device fabrication.

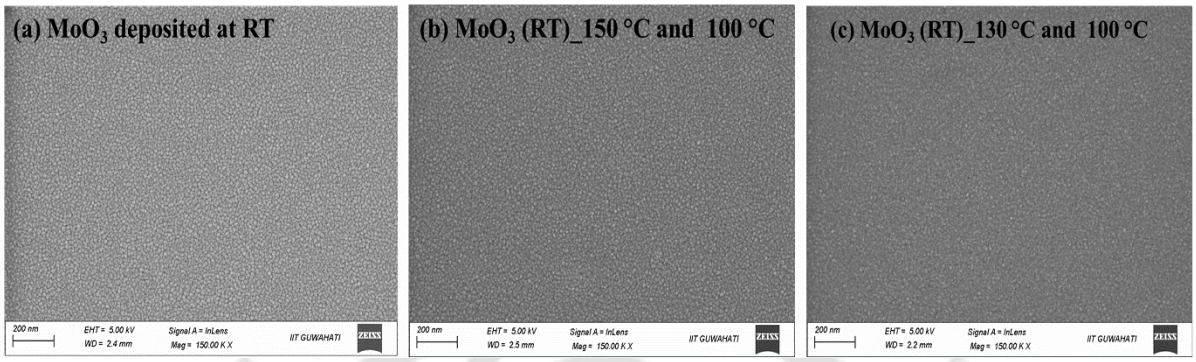

Figure 7.10: *(a) FESEM images of as deposited MoO_{3-x} and (b), (c) FESEM images of subsequently two time heat treated MoO_{3-x} films during device fabrication.*

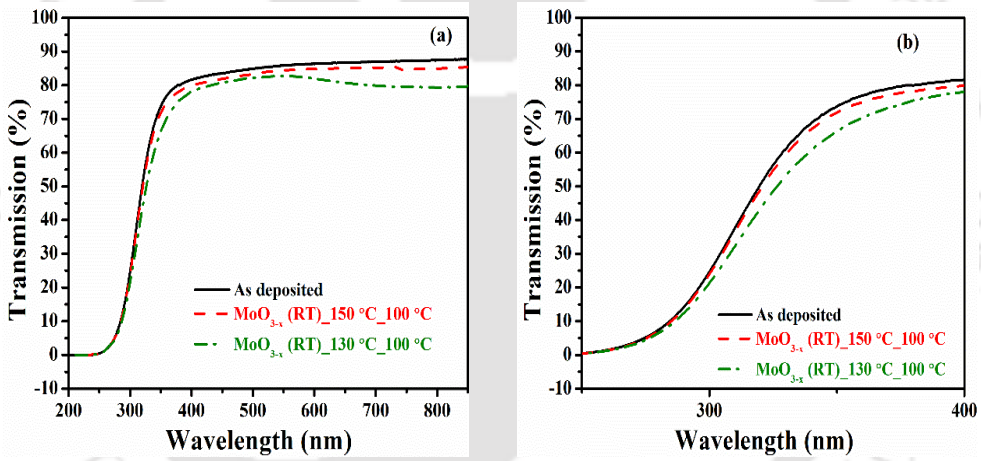

Figure 7.11: *(a) Transmission spectra and (b) its zoomed view of as deposited and two time heat treated MoO_{3-x} films.*

It is evident from Figures 7.9a and 7.9b that SAED patterns have been disturbed by the THT of MoO_{3-x} film at 150 °C and 100 °C. For MoO_{3-x} subjected to THT at 130 °C and 100 °C, the discontinuous and diffused diffraction rings (Figure 7.9c) have formed, indicating the formation of irregularly aligned crystals and grains. However, no morphological changes (Figure 7.10) are noticed for two time heat treated MoO_{3-x} films. Figure 7.11 shows THT has suppressed the transmission and also caused a red shift in the absorption edge. Since the thickness of MoO_{3-x} is kept constant in all conditions, this decrease is mostly attributable to the

creation of oxygen vacancies, which increase the concentration of free electrons inside MoO_{3-x}, which behave like scattering centres and reduce the transmission as well as the band gap of molybdenum oxide films [14, 15]. These results indicate that THT at 130 °C and 100 °C has caused more structural disorder and also generated more oxygen vacancies than THT of MoO_{3-x} film at 150 °C and 100 °C. The deterioration of performance of solar cells fabricated with ITO deposited at 130 °C is due to lower work function of MoO_{3-x} films subjected to THT at 130 °C and 100 °C, because of higher oxygen vacancies in this condition as discussed in Chapter 4.

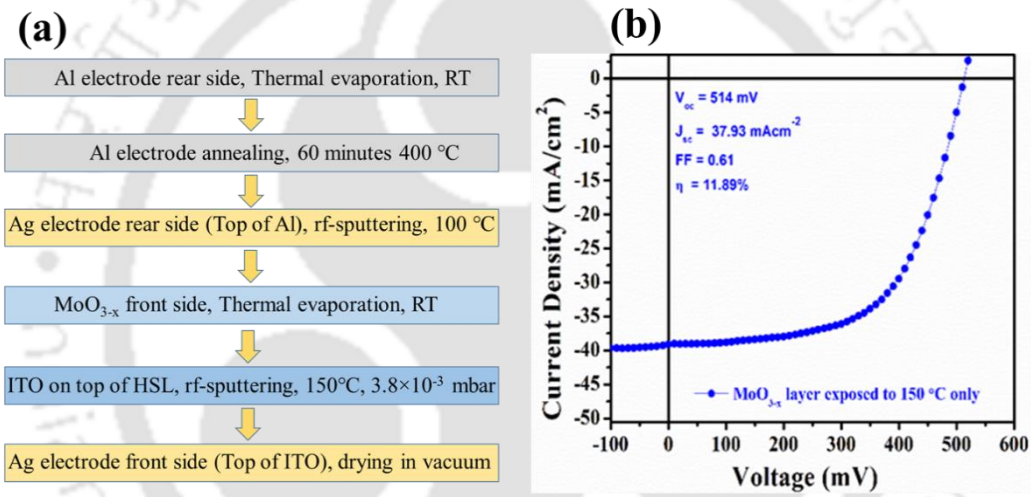

Figure 7.12: *(a) Fabrication steps and (b) J-V characteristics of device in which MoO_{3-x} layer is exposed to 150 °C only (OHT).*

Table 7.4: *Solar cell parameters for different treatment heat treatment conditions of MoO_{3-x}.*

Heat treatment conditions of MoO_{3-x}	V_{oc} (mV)	J_{sc} (mA/cm^2)	FF	η (%)	R_s (Ω.cm^2)	R_{sh} (Ω.cm^2)
THT	539	38.46	0.57	11.88	3.50	175
OHT	514	37.93	0.61	11.89	3.71	164

7.3.1.2 Effect of one time heat treatment on the performance of MoO_{3-x}/c-Si(n) solar cells

As previous study has suggested that THT influences the structural and optical characteristics of HTL, so for the next device fabrication, two times heat treatment (THT) is reduced to one

time heat treatment (OHT). In OHT condition, prior to deposition of MoO_{3-x} film, Ag is deposited at 100 °C on top of diffused Al on rear side of silicon wafer, followed by the deposition of MoO_{3-x} layer on front side at room temperature and an ITO layer at 150 °C. So, the MoO_{3-x} layer is exposed to heat treatment only once during the deposition of ITO at 150 °C. The fabrication steps are depicted in Figure 7.12a

J-V characteristics of device fabricated in OHT condition is shown in Figure 7.12b. Solar cell fabricated in OHT condition has shown η of 11.89%, which is same as device prepared in THT condition (for ITO deposition at 150 °C); however, V_{oc} has decreased by 25 mV and *FF* has improved from 0.57 (THT) to 0.61 in OHT condition (Table 7.4). As the OHT device has nearly the same *FF* and η, further optimisations for the OHT condition are required to improve the device results. The possible cause of V_{oc} drop in OHT condition is decrease in R_{sh} because of exposure of silicon substrates to ambient many times prior to the deposition of MoO_{3-x}, resulting in poor junction formation. The performance of dopant-free single-sided heterojunction MoO_{3-x}/c-Si (n) solar cells can be enhanced by further optimisations for depositing MoO_{3-x} layer and other processes, such as oxygen plasma treatment of HSL as discussed in Chapter 5.

7.4 Conclusion

The fabrication of MoO_{3-x}/c-Si(n) solar cells, in which MoO_{3-x} serves as a hole selective layer, is discussed in this chapter. The appropriate back electrode combinations are first selected, then different deposition conditions are employed to deposit ITO (the TCO layer), to find how it affects the device performance. After that, MoO_{3-x} deposition temperature is varied and the effects of post-deposition heat-treatments on HSL properties and performance of prepared devices are studied. An increase in V_{oc} is observed when Ag/Al back electrode is used for fabricating MoO_{3-x}/c-Si(n) solar cell. This increase is due to the formation of good contact

between c-Si(n)/Al. Solar cell efficiency has increased from 8.58% to 10.06% with the decrease in process pressure from 5.3×10^{-3} mbar to 3.8×10^{-3} mbar for ITO films deposition. Enhancement in cell efficiency and photovoltaic parameters are due to the higher deposition rate of ITO film at low pressure, which reduces damage to the ITO/MoO_{3-x} interface. Later, by changing the deposition temperature of MoO_{3-x}, the HSL, MoO_{3-x}/c-Si(n) solar cells with 11.88% efficiency are fabricated. The increased work function of MoO_{3-x} film accounts for improvements in V_{oc} and *FF* for devices with MoO_{3-x} films deposited at RT. To decrease the temperature at which the MoO_{3-x} film is exposed during device fabrication, the ITO film is deposited at 130 °C, but in this case the device efficiency has dropped from 11.88% (for ITO film deposited at 150 °C) to 9.63%. This is because of the optical and microstructural changes in MoO_{3-x} induced due to THT at 130 °C for ITO preparation and 100 °C for silver electrode preparation on back side. FETEM and UV-Vis studies on two times heat treated MoO_{3-x} films indicated that multiple heat treatments degrade the structural and optical characteristics of molybdenum oxide films. Therefore, it is inferred that the temperature at which MoO_{3-x} is exposed during the fabrication of different layers in solar cells also has an impact on the performance of MoO_{3-x}/c-Si (n) solar cells.

7.5 References

[1] C. Battaglia, X. Yin, M. Zheng, I.D. Sharp, T. Chen, S. McDonnell, A. Azcatl, C. Carraro, B. Ma, R. Maboudian, R.M. Wallace, A. Javey, Hole selective MoO_x contact for silicon solar cells, Nano letters, 14 (2014) 967-971.

[2] L. Gerling, S. Mahato, C. Voz, R. Alcubilla, J. Puigdollers, Characterization of Transition Metal Oxide/Silicon Heterojunctions for Solar Cell Applications, Applied Sciences, 5 (2015) 695-705.

[3] M.T. Greiner, L. Chai, M.G. Helander, W.-M. Tang, Z.-H. Lu, Transition Metal Oxide

Work Functions: The Influence of Cation Oxidation State and Oxygen Vacancies, Advanced Functional Materials, 22 (2012) 4557-4568.

[4] M.T. Greiner, Z.-H. Lu, Thin-film metal oxides in organic semiconductor devices: their electronic structures, work functions and interfaces, NPG Asia Materials, 5 (2013) e55-e55.

[5] J. Dréon, Q. Jeangros, J. Cattin, J. Haschke, L. Antognini, C. Ballif, M. Boccard, 23.5%-efficient silicon heterojunction silicon solar cell using molybdenum oxide as hole-selective contact, Nano Energy, 70 (2020) 104495.

[6] L. Cao, P. Procel, A. Alcaniz, J. Yan, F. Tichelaar, E. Ozkol, Y. Zhao, C. Han, G. Yang, Z. Yao, M. Zeman, R. Santbergen, L. Mazzarella, O. Isabella, Achieving 23.83% conversion efficiency in silicon heterojunction solar cell with ultra-thin MoO_x hole collector layer via tailoring (i)a-Si:H/MoO_x interface, Progress in Photovoltaics: Research and Applications, DOI 10.1002/pip.3638(2022) 1-10.

[7] J. Bullock, Y. Wan, Z. Xu, S. Essig, M. Hettick, H. Wang, W. Ji, M. Boccard, A. Cuevas, C. Ballif, A. Javey, Stable Dopant-Free Asymmetric Heterocontact Silicon Solar Cells with Efficiencies above 20%, ACS Energy Letters, 3 (2018) 508-513.

[8] M. Bivour, J. Temmler, H. Steinkemper, M. Hermle, Molybdenum and tungsten oxide: High work function wide band gap contact materials for hole selective contacts of silicon solar cells, Solar Energy Materials and Solar Cells, 142 (2015) 34-41.

[9] W.K. 1990, The Evolution of Silicon Wafer Cleaning Technology, Journal of The Electrochemical Society, 137 (1990) 1887-1892.

[10] J. Kumari, Rahul, P. Agarwal, Role of deposition parameters on optoelectronic properties of ITO films and its application in MoO_{3-x}/c-Si(n) heterojunction solar cells, Journal of Materials Science: Materials in Electronics, 34:1286 (2023) .

[11] S. Patwardhan, B. Kavaipatti, Effect of ITO capping and its deposition parameters on electrical properties of MoO_3/Si carrier-selective contact solar cell, INAE Letters, 4 (2018)

139-145.

[12] J. Kumari, P. Agarwal, Optimization of deposition conditions to tune optoelectronic properties of MoO_{3-x} films prepared by RF-sputtering technique, Vacuum, 216 (2023) 112485.

[13] H. Mehmood, H. Nasser, T. Tauqeer, S. Hussain, E. Ozkol, R. Turan, Simulation of an efficient silicon heterostructure solar cell concept featuring molybdenum oxide carrier-selective contact, International Journal of Energy Research, 42 (2018) 1563-1579.

[14] D. Divya, K.V. Madhuri, Effect of Substrate Temperature on the Growth of Molybdenum Trioxide Thin Films, Crystallography Reports, 65 (2020) 792-797.

[15] X. Fan, G. Fang, P. Qin, N. Sun, N. Liu, Q. Zheng, F. Cheng, L. Yuan, X. Zhao, Deposition temperature effect of RF magnetron sputtered molybdenum oxide films on the power conversion efficiency of bulk-heterojunction solar cells, Journal of Physics D: Applied Physics, 44 (2011) 045101

CHAPTER 8

Simulation studies on MoO_{3-x}/c-Si(n) hetero-junction solar cells using AFORS-HET software

This chapter presents the simulation studies on MoO_{3-x}/c-Si (n) silicon heterojunction solar cells performed using the AFORS-HET simulation tool. AFORS-HET has been identified as a powerful simulation tool for heterojunction solar cell design [1-5]. This software solves Poisson equation together with two continuity equations and gives thorough information on absorption qualities, band diagrams and electric field distribution across interfaces [2]. MoO_{3-x} is an extensively utilised dopant free hole selective layer (HSL) in silicon heterojunction solar cells [6-8]. Despite being an n-type semiconductor, the high work function of MoO_{3-x} makes it an appropriate HSL [9, 10]. In the previous Chapter, we observed that solar cells fabricated with MoO_{3-x} deposited at room temperature have performed better as compared to devices fabricated with MoO_{3-x} deposited at 100 °C. The improved performance is due to the higher work function achieved with MoO_{3-x} films prepared

at room temperature. We performed simulations studies on MoO_{3-x}/c-Si (n) heterojunction solar cells to better understand the impact of work function on solar cell performance as well as the probable transport mechanism occurring at the MoO_{3-x}/c-Si (n) junction.

8.1 Simulation details of MoO_{3-x}/c-Si(n) heterojunction solar cells

The simulation studies were carried out for device structure; *Ag/ITO/MoO_{3-x}/c-Si(n)/Ag*. In this structure, MoO_{3-x} was used as a hole selective layer and its work function was altered from 4.7 to 5.2 eV. Table 8.1 lists the parameters that were used to conduct the simulation study [4]. After investigating the effect of work function on the performance of dopant-free MoO_{3-x}/c-Si (n) solar cells, tunnelling through the insulator layer was introduced at the interface of MoO_{3-x} and c-Si (n), and its impact on simulated device performance was explored. The standard illumination condition Air mass 1.5 (AM 1.5) at 300 K with a power density of 100 mW/cm^2 was used for simulated cells' current density and voltage *(J-V)* analysis.

Table 8.1: *The parameters used for MoO_{3-x}/c-Si(n) solar cell simulation.*

Parameters (units)	c-Si(n)
Thickness (μm)	300
Dielectric constant	11.9
Electron affinity (eV)	4.05
Band gap(eV)	1.12
Effective conduction band density ($cm^{-3)}$	2.84×10^{19}
Effective valence band density (cm^{-3})	2.68×10^{19}
Electron mobility ($cm^2V^{-1}s^{-1}$)	1107
Hole mobility ($cm^2V^{-1}s^{-1}$)	424.6
Acceptor concentration (cm^{-3})	0
Donor concentration (cm^{-3})	1.5×1^{16}
Thermal velocity of electrons($cm.s^{-1}$)	10^7
Thermal velocity of holes($cm.s^{-1}$)	10^7
Layer density ($g.cm^{-3}$)	2.328

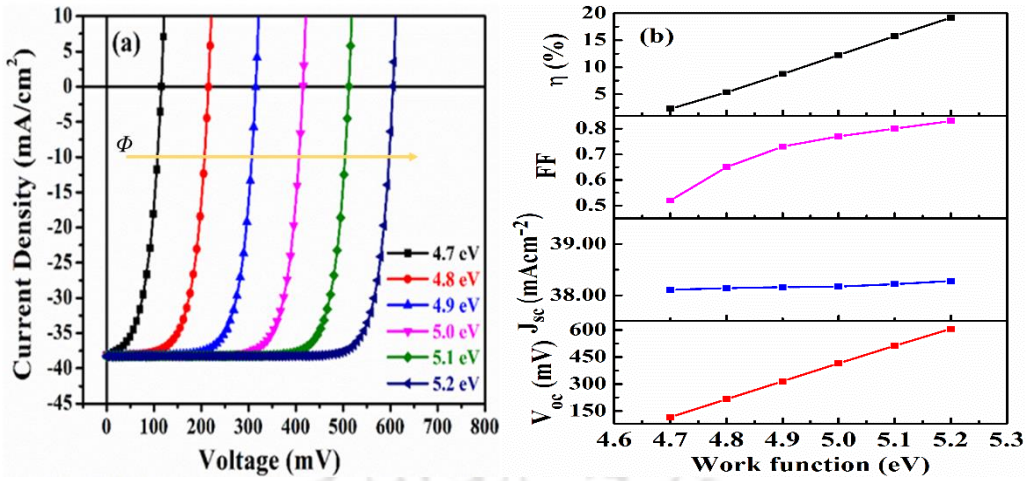

Figure 8.1: *(a) J-V characteristics of MoO_{3-x}/c-Si(n) solar cell and (b) solar cell performance parameters (V_{oc}, J_{sc}, FF and η) variations for different work function of MoO_{3-x}.*

8.2 Results and discussion:

8.2.1 Influence of work function on performance of MoO_{3-x}/c-Si (n) solar cells

The work function, *Φ* of molybdenum oxide (MoO_{3-x}), which is crucial in controlling the contact resistance and charge transfer, has a major impact on the hetero-contact characteristic of the MoO_{3-x}-based solar cells. Figure 8.1 depicts the effect of MoO_{3-x} work function on the *J-V* characteristics and solar cell parameters of dopant-free devices with structure *Ag/ITO/MoO_{3-x}/c-Si(n)/Ag*. The current density (J_{sc}) remains approximately same in all cases. However, there is an increase in the open circuit voltage (V_{oc}) from 115.70 mV to 605.80 mV when work function (*Φ*) of MoO_{3-x} is increased from 4.7 eV to 5.2 eV respectively. Also, the fill factor (*FF*) has shown a considerable increase from 0.52 to 0.82 with the increase of *Φ* from 4.7 eV to 5.2 eV respectively. Because of the pinning of the Fermi level (E_f) away from the valence band (E_v) of c-Si (n) at MoO_{3-x}/c-Si(n) interface, as shown in Figure 8.2a, low work function does not enable the efficient transportation of holes from c-Si (n) to MoO_{3-x} layer, hence for lower work function values lower V_{oc} and FF values are observed. Figure 8.2a shows the band edge shifts in the energy band diagram induced by the increase in MoO_{3-x}'s work

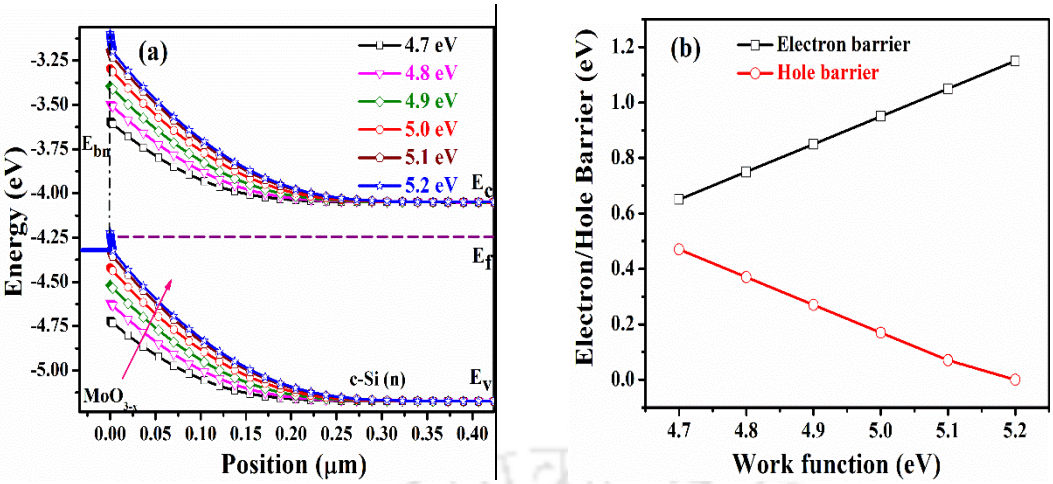

Figure 8.2: *(a) Energy band diagram and (b) values of energy barrier faced by electrons and holes for different work function of MoO_{3-x}.*

Table 8.2: *Solar cell parameters and energy barrier faced by electrons and holes for different work function of MoO_{3-x}.*

Φ (eV)	E_{bn} (eV)	E_{bp} (eV)	V_{oc} (mV)	J_{sc} (mA/cm^2)	*FF*	η (%)
4.7	0.65	0.47	115.70	38.11	0.52	2.30
4.8	0.75	0.37	215.40	38.14	0.65	5.37
4.9	0.85	0.27	315.40	38.22	0.73	8.75
5.0	0.95	0.17	415.20	38.14	0.77	12.25
5.1	1.05	0.07	512.50	38.22	0.80	15.77
5.2	1.15	-0.03	605.80	38.26	0.82	19.18

function at the MoO_{3-x}/c-Si(n) interface. The energy barrier faced by holes (E_{bp}) and electron (E_{bn}) are obtained using equation 8.1 and 8.2 respectively [11].

$$E_{bp} = (E_g + \chi)_{c-Si(n)} - \Phi_{MoO_{3-x}} \quad \text{---------- (8.1)}$$

$$E_{bn} = \Phi_{MoO_{3-x}} - \chi_{c-Si(n)} \quad \text{---------- (8.2)}$$

where, E_g and χ are the band gap and electron affinity of c-Si (n) respectively. Φ is the work function of MoO_{3-x}.

Figure 8.2b shows the graphical representation of E_{bp} and E_{bn} values. E_{bn} is observed to increase with increase in Φ of MoO_{3-x}, whereas E_{bp} is decreased. The lower E_{bp} allows easier transportation of holes from the E_v of c-Si (n) to the HSL side and reduced recombination for the photo-generated minority carriers at the interface due to the higher E_{bn}. These factors

account for the increase in V_{oc} of MoO_{3-x}/c-Si(n) solar cells with increasing MoO_{3-x} work function [12, 13]. Similarly, the increased hole collecting efficiency provided by MoO_{3-x}, boosts the fill factor of devices with a work function rise from 4.7 eV to 5.2 eV [11]. Enhancement in work function has improved the solar cell efficiency (η) from 2.30 % (Φ = 4.7 eV) to 19.18% (Φ = 5.2 eV). Solar cell parameters *and* E_{bn}, E_{bp} values are listed in Table 8.2.

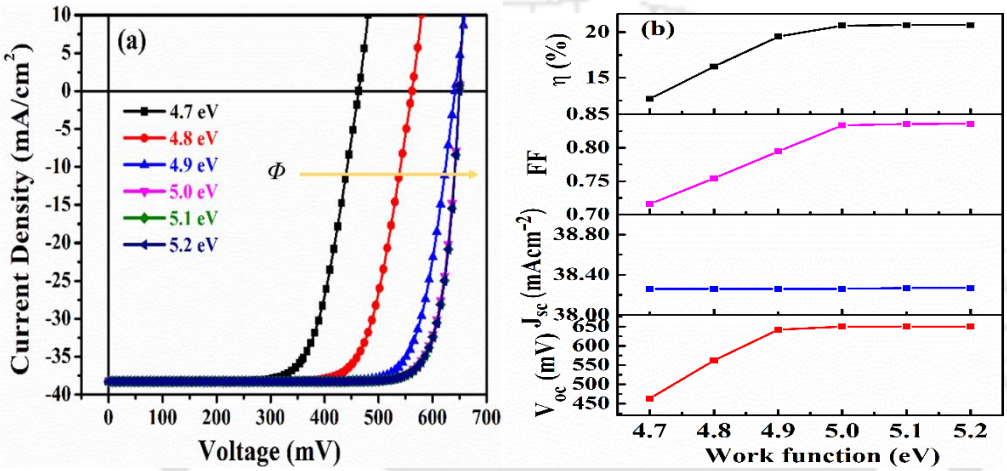

Figure 8.3: *(a) J-V characteristics of MoO_{3-x}/SiO_x/c-Si(n) solar cell and (b) solar cell performance parameters (V_{oc}, J_{sc}, FF and η) for different work function when tunnelling is introduced at MoO_{3-x} and c-Si (n) interface.*

Table 8.3: *Solar cell parameters of MoO_{3-x}/SiO_x/c-Si(n) solar cells when tunnelling is introduced at MoO_{3-x} and c-Si (n) interface.*

Φ (eV)	V_{oc} (mV)	J_{sc} (mA/cm²)	*FF*	η (%)
4.7	463.30	38.26	0.71	12.69
4.8	562.00	38.26	0.75	16.22
4.9	641.90	38.26	0.79	19.51
5.0	649.90	38.26	0.83	20.73
5.1	650.00	38.27	0.83	20.79
5.2	650.00	38.27	0.83	20.79

8.2.2 Influence of tunneling through insulator layer on the performance of MoO_{3-x}/ SiO_x/c-Si(n) solar cells

Assuming the formation of silicon oxide (SiO_x), an insulating layer at the interface of molybdenum oxide and c-Si (n), tunnelling is introduced through SiO_x layer and its influence on the performance of MoO_{3-x}/c-Si(n) solar cell is studied. To perform this study, an insulating

layer of thickness 1 nm, electron affinity of 1 eV and band gap of 9 eV is used. These values are taken from the literature corresponding to SiO_x layer [14-16]. The *J-V* characteristics of MoO_{3-x}/SiO_x/c-Si(n) solar cells are shown in Figure 8.3a. When tunnelling is introduced at MoO_{3-x} and c-Si (n) junction, performance of the simulated devices improves significantly as compared to devices with no tunnelling defined. For work function of 4.7 eV, V_{oc} and FF have improved from 115.70 mV, 0. 52 (for no tunnelling) to 463.30 mV, 0.71 (when tunnelling in introduced) respectively. The rise in V_{oc} and *FF* has increased the device's efficiency from 2.30% to 12.69%. Similarly, improvements in V_{oc}, *FF* and η are also observed for work function values of 4.8 eV, 4.9 eV and 5.0 eV. However, no improvement in device performance is observed for subsequent increases in work function to 5.1 eV and 5.2 eV. Figure 8.3b and Table 8.3, depict graphical representations of solar parameters and their values respectively when tunnelling through the SiO_x layer is included in MoO_{3-x}/c-Si(n) dopant free solar cells. Improvement in V_{oc} is because SiO_x acts as passivation layer at MoO_{3-x} and c-Si (n) interface and also reduce the minority carriers' recombination at the interface by filling the dangling bonds on the surface of silicon wafer which act as recombination centres [17-19].

8.2.3 Influence of thickness of SiO_x, the interfacial layer on the performance of MoO_{3-x}/SiO_x/c-Si(n) solar cells

Since an improvement in device performance was observed by introducing SiO_x layer between MoO_{3-x} and c-Si (n), the next step was to optimise the thickness of SiO_x layer. For this, thickness of SiO_x layer is varied from 0.8 nm to 1.7 nm keeping MoO_{3-x} work function fixed at 4.8 eV and its influence on the performance of MoO_{3-x}/c-Si(n) solar cells are studied.

Figure 8.4 show *J-V* curve and performance parameters of the simulated MoO_{3-x}/SiO_x/c-Si(n) solar cells for different SiO_x layer thicknesses. An increase in open circuit voltage and a decrease in fill factor are observed when the thickness of SiO_x layer is increased from 0.8 nm to 1.7 nm. The poor *FF* is caused by an increase in series resistance with the increase in SiO_x

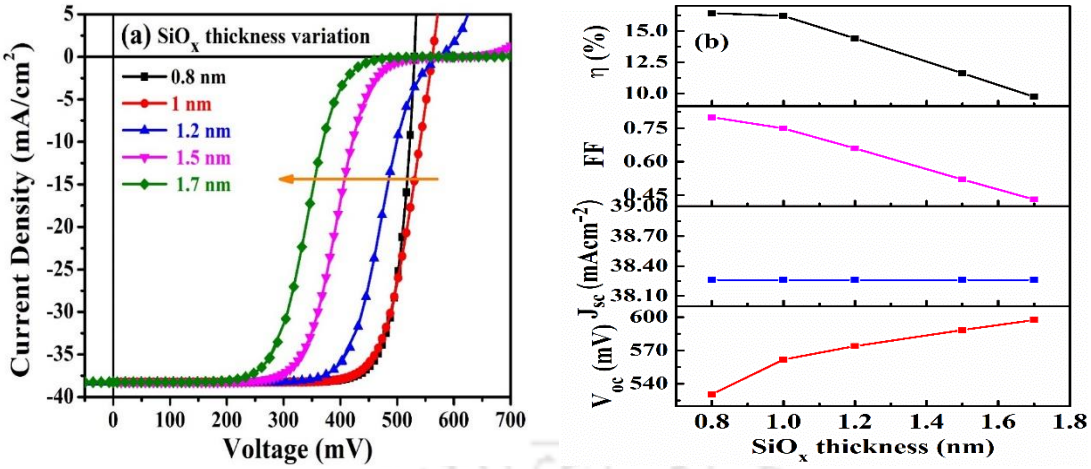

Figure 8.4: *(a) J-V characteristics and (b) performance parameters of MoO_{3-x}/SiO_x/c-Si(n) solar cell for different SiO_x layer thicknesses keeping MoO_{3-x} work function fixed at 4.8 eV.*

Table 8.4: *Performance parameters of MoO_{3-x}/SiO_x/n-Si(c) solar cells for different SiO_x layer thicknesses.*

SiO_x thickness (nm)	V_{oc} (mV)	J_{sc} (mA/cm^2)	*FF*	η (%)
0.8	530.60	38.26	0.80	16.43
1.0	562.00	38.26	0.75	16.21
1.2	573.90	38.26	0.66	14.41
1.4	588.40	38.26	0.52	11.63
1.7	597.50	38.26	0.43	9.74

layer thickness [16]. Table 8.4 lists the solar cell parameters obtained for various SiO_x thicknesses. The study suggests that 1 nm SiO_x layer thickness is preferable for fabricating a good device, because effective carrier transport at the MoO_{3-x}/c-Si(n) interface requires low SiO_x thickness [16]. When the thickness of SiO_x exceeds than what is required, it has a negative influence on device performance as it obstructs photo-generated charge carriers' transport [16, 17]. The simulated device results for the 1.2 nm SiO_x layer are found to be somewhat comparable to the experimental results obtained for MoO_{3-x}/c-Si(n) solar cells fabricated with MoO_{3-x} deposited at room temperature and ITO deposited at 150 °C (Chapter 7, section 7.3, Figure 7.7a).

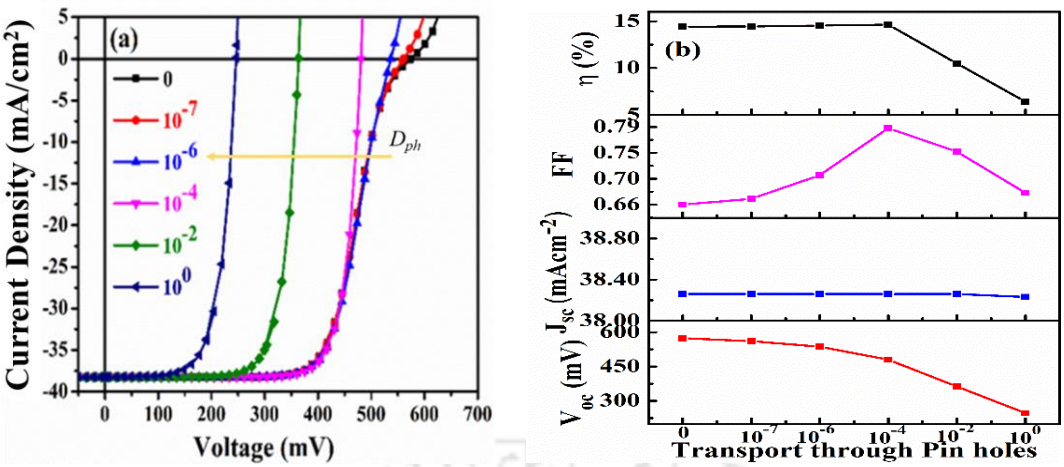

Figure 8.5: *(a) J-V characteristics and (b) solar cell performance parameters of MoO_{3-x}/SiO_x/c-Si(n) solar cell when transport through pin holes are introduced.*

Table 8.5: *Performance parameters of MoO_{3-x}/SiO_x/c-Si(n) solar cell when transport through pin holes (D_{ph}: fraction of pinholes) present at MoO_{3-x}/c-Si(n) interface) are introduced.*

D_{ph}	V_{oc} (mV)	J_{sc} (mA/cm^2)	*FF*	η (%)
0	573.90	38.26	0.66	14.41
10^{-7}	560.70	38.26	0.67	14.43
10^{-6}	537.00	38.26	0.71	14.54
10^{-4}	480.70	38.26	0.79	14.63
10^{-2}	363.26	38.26	0.75	10.49
10^{0}	246.50	38.23	0.68	6.42

8.2.4 Influence of transport through pin holes on the performance of MoO_{3-x}/SiO_x/c-Si(n) solar cells

Since, it is challenging to obtain a uniform SiO_x layer at MoO_{3-x} and c-Si (n) interface, we further investigated how the existence of pin holes in thin SiO_x layer impacts the *J-V* characteristics of MoO_{3-x}/c-Si(n) solar cells. The influence of pin holes on *J-V* characteristics and solar cell performance parameters are depicted in Figure 8.5. Introduction of transport through pin holes at the interface of MoO_{3-x} and c-Si (n) has initially improved the nature of *J-V* curve, fill factor and efficiency of MoO_{3-x}/c-Si(n) solar cells. When pinholes are introduced, the carriers can pass through pinholes in addition to tunnel through SiO_x at MoO_{3-x}/c-Si(n) interface, which reduces series resistance and enhances the FF and η till it reaches its maximum. Increasing the pinhole transport, on the other hand, adds a shunt path, lowering the

V_{oc} of simulated solar cells. Furthermore, excessive pinholes may diminish passivation quality, increase interface recombination and degrade solar cell performance [16, 18]. So, a significant drop in device performance is observed for D_{ph}(fraction of pinholes)>10^{-4}. All the solar cell parameters for transport through pin holes are listed in Table 8.5. This study inferred that an ultrathin layer of SiO_x along with some pin holes between MoO_{3-x} and c-Si(n) in MoO_{3-x}/c-Si(n) solar cell, facilitates quantum tunnelling of photo-generated carriers combined with transport through pinholes.

8.3 Conclusion

MoO_{3-x}'s work function has a substantial impact on device performance when it is used as a hole selective layer in MoO_{3-x}/c-Si(n) solar cells. With this motivation, we have varied the work function of MoO_{3-x} and studied its influence on the performance of MoO_{3-x}/c-Si(n) solar cells. As the performance of simulated MoO_{3-x}/c-Si(n) solar cells are found to be very low than experimentally achieved device results, tunneling through the thin interfacial layer SiO_x is introduced between MoO_{3-x} and c-Si(n). Quantum tunneling through 1 nm SiO_x layer has improved the device performance significantly. The experimental results (V_{oc} = 539 mV, J_{sc} = 38.46 mA/cm^2, FF = 0.57 and η = 11.88%) as described in Chapter 7, Table 7.3 have matched well with the simulation results (V_{oc} = 537 mV, J_{sc} = 38.26 mA/cm^2, FF = 0.71 and η = 14.54%) when transport of carriers are supported by both quantum tunneling and pin holes transport through 1.2 nm thin SiO_x and 10^{-6} pinholes fraction for 4.8 eV of MoO_{3-x} work function. By correlating the simulation studies with experimental results, it is concluded that during the device fabrication process, ultrathin SiO_x layer forms with some pin holes at the MoO_{3-x}/c-Si(n) interface, which acts as passivation layer and also help in the carriers' transportation along with other transport mechanisms.

8.4 References

[1] R.S. A. Froitzheim, L. Elmer, M. Kriegel, W. Fuhs, AFORS-HET: A computer-program for the simulation of heterojunction solar cells to be distributed for public use., 3rd World Conference on Photovolfaic Energv Conversion May 11-18.2003 Osokn. Jopon, IP-D3-34 (2003) 279-282.

[2] V.A. Dao, J. Heo, H. Choi, Y. Kim, S. Park, S. Jung, N. Lakshminarayan, J. Yi, Simulation and study of the influence of the buffer intrinsic layer, back-surface field, densities of interface defects, resistivity of p-type silicon substrate and transparent conductive oxide on heterojunction with intrinsic thin-layer (HIT) solar cell, Solar Energy, 84 (2010) 777-783.

[3] H. Deka, A.K. Sunaniya, P. Agarwal, Simulation studies on MoS_2(n)/a-Si:H(i)/c-Si (p)/MoO_3 heterojunction solar cells using one sided short diode approximation, Solar Energy, 263 (2023) 111943.

[4] L.-C. Hao, M. Zhang, M. Ni, J.-M. Liu, X.-D. Feng, Simulation of high efficiency silicon heterojunction solar cells with molybdenum oxide carrier selective layer, Materials Research Express, 5 (2018) 075504.

[5] V. Kanneboina, The simulated performance of c-Si/a-Si:H heterojunction solar cells with nc-Si:H, µc-Si:H, a-SiC:H, and a-SiGe:H emitter layers, Journal of Computational Electronics, 20 (2020) 344-352.

[6] M. Nayak, K. Singh, S. Mudgal, S. Mandal, S. Singh, V.K. Komarala, Carrier-Selective Contact Based Silicon Solar Cells Processed at Room Temperature using Industrially Feasible Cz Wafers, Physica Status Solidi A, 216 (2019) 1900208.

[7] M.M. Nayak, Sapna Mandal, Sourav Singh, Sonpal Komarala, Vamsi Krishna, Electrical characterization and defect states analysis of Ag/ITO/MoO_x/n-Si/LiF_x/Al carrier selective contact solar cells processed at room-temperature, 15th International Conference on Concentrator Photovoltaic Systems (CPV-15), (2019).

[8] M. Nayak, V.K. Komarala, Thermal Stability Analysis of Molybdenum-Oxide-Based Carrier Selective Contact Silicon Solar Cells, IEEE Transactions on Electron Devices, 69 (2022) 3251-3257.

[9] L. Gerling, S. Mahato, C. Voz, R. Alcubilla, J. Puigdollers, Characterization of Transition Metal Oxide/Silicon Heterojunctions for Solar Cell Applications, Applied Sciences, 5 (2015) 695-705.

[10] L.G. Gerling, S. Mahato, A. Morales-Vilches, G. Masmitja, P. Ortega, C. Voz, R. Alcubilla, J. Puigdollers, Transition metal oxides as hole-selective contacts in silicon heterojunctions solar cells, Solar Energy Materials and Solar Cells, 145 (2016) 109-115.

[11] H. Mehmood, H. Nasser, T. Tauqeer, S. Hussain, E. Ozkol, R. Turan, Simulation of an efficient silicon heterostructure solar cell concept featuring molybdenum oxide carrier-selective contact, International Journal of Energy Research, 42 (2018) 1563-1579.

[12] Y. Zang, J. Huang, H. Li, J. Yu, Y. Jiang, Effect of Molybdenum Oxide Anode Buffer Layer on the Performance of Inverted Small Molecular Organic Solar Cells, Energy Procedia, 12 (2011) 513-518.

[13] C. Messmer, M. Bivour, J. Schon, S.W. Glunz, M. Hermle, Numerical Simulation of Silicon Heterojunction Solar Cells Featuring Metal Oxides as Carrier-Selective Contacts, IEEE Journal of Photovoltaics, 8 (2018) 456-464.

[14] G. Seguini, S. Schamm-Chardon, P. Pellegrino, M. Perego, The energy band alignment of Si nanocrystals in SiO_2, Applied Physics Letters, 99 (2011) 082107.

[15] Z. Li, Z. Zhang, J. Tian, G. Wu, Y. He, B. Yu, F. Zhan, Y. Wang, M. Sun, W. Yang, Z. Li, Q. Chen, P. Yan, X. Wei, Efficient and Dense Electron Emission from a SiO_2 Tunneling Diode with Low Poisoning Sensitivity, Nano letters, 22 (2022) 1270-1277.

[16] Z. Zhang, Y. Zeng, C.-S. Jiang, Y. Huang, M. Liao, H. Tong, M. Al-Jassim, P. Gao, C. Shou, X. Zhou, B. Yan, J. Ye, Carrier transport through the ultrathin silicon-oxide layer in

tunnel oxide passivated contact (TOPCon) c-Si solar cells, Solar Energy Materials and Solar Cells, 187 (2018) 113-122.

[17] Y. Xu, H. Shen, B. Xu, Z. Wang, Y. Li, B. Lai, J. Zhang, High-performance MoO_x/n-Si heterojunction NIR photodetector with aluminum oxide as a tunneling passivation interlayer, Nanotechnology, 32 (2021) 275502.

[18] X.M. Song, Z.G. Huang, M. Gao, D.Y. Chen, Z. Fan, Z.Q. Ma, Y. Li, Role of Interfacial Oxide Layer in MoO_x/n-Si Heterojunction Solar Cells, International Journal of Photoenergy, 2021 (2021) 1-8.

[19] L.G. Gerling, C. Voz, R. Alcubilla, J. Puigdollers, Origin of passivation in hole-selective transition metal oxides for crystalline silicon heterojunction solar cells, Journal of Materials Research, 32 (2016) 260-268.

CHAPTER 9

Summary, Conclusion and future Scope

This chapter summarizes the work reported in the present thesis on the studies of properties of molybdenum oxide (MoO_{3-x}) films and fabrication of dopant free single sided *MoO_{3-x}/c-Si(n)* solar cells. MoO_{3-x} and ITO thin films are fabricated using thermal evaporation and rf-sputtering techniques, respectively and *MoO_{3-x}/c-Si(n)* solar cells are fabricated using the optimised deposition parameters. The motivation of the present thesis work is to optimize the deposition conditions and study the optoelectronic properties of MoO_{3-x} films for its use as hole selective layer in Silicon based solar cells. To accomplish the targeted objective, MoO_{3-x} films are deposited using rf-sputtering and thermal evaporation techniques and the effect of different deposition parameters such as substrate temperature, gaseous environment and post-deposition annealing on structural, optical and electrical properties are investigated. Indium tin oxide (ITO) films are prepared using rf-sputtering technique and deposition parameters are optimised to fabricate ITO films with high transparency and low sheet resistance. The optimised deposition conditions for preparing MoO_{3-x} and ITO films are then utilised to

fabricate dopant free single-sided *MoO_{3-x}/c-Si(n)* solar cells. In addition, we have also performed simulation studies on *MoO_{3-x}/c-Si(n)* heterojunction solar cells using AFORS-HET software to understand the influence of work function of MoO_{3-x} on the performance of *MoO_{3-x}/c-Si(n)* solar cells. The following section presents the overall conclusion of the thesis work as well as future research goals.

9.1 Summary and Thesis conclusion

- The structural, optical and electrical properties of MoO_{3-x} films deposited by rf-sputtering technique depend upon process conditions such as rf-powers and substrate temperatures (T_s). MoO_{3-x} films deposited at low RF power (60 W) have higher band gap (3.12 eV) and lower conductivity (10^{-7} $\Omega^{-1}cm^{-1}$), whereas films formed at high RF power (80 W) have lower band gap (2.94 eV) and higher conductivity (15.18 $\Omega^{-1}cm^{-1}$). Films deposited at low T_s (100 °C) have higher transmittance (0.60-0.65), higher band gap (2.99 eV) and lower conductivity (1.81×10^{-3} $\Omega^{-1}cm^{-1}$) whereas high T_s (400 °C) has formed deep blue colour MoO_{3-x} films with lower band gap (2.82 eV) and higher conductivity (207.30 $\Omega^{-1}cm^{-1}$). X-ray photoelectron spectroscopy (XPS) studies confirmed that the presence of higher oxygen vacancies (O_v) and Mo atoms in lower oxidation states (Mo^{5+}) are the reasons for the formation of coloured and highly conducting MoO_{3-x} films at higher T_s = 400 °C and higher rf power 80 W.
- Transparent MoO_{3-x} films with large band gap of 3.18 eV and low conductivity of order 10^{-6} $\Omega^{-1}cm^{-1}$ are formed when oxygen gas is present along with argon gas during deposition. Oxygen gas supplied during MoO_{3-x} films deposition fills the O_v as confirmed by XPS, and forms transparent and highly resistive MoO_{3-x} films. Optimised conditions for preparing conducting MoO_{3-x} films are high T_s (400 °C), high rf power (80 W) and pure Argon atmosphere. However, transparent and resistive MoO_{3-x} films

can be deposited at high T_s = 400 °C, by using oxygen gas during MoO_{3-x} film deposition.

- Properties of MoO_{3-x} films deposited by thermal evaporation technique are significantly affected by the deposition temperature and post-deposition annealing. The transmission and band gap of MoO_{3-x} films have decreased with the increase in the deposition and annealing temperatures. Increasing the deposition temperature from room temperature (RT) to 100 °C, reduced the work function (Φ) of thermally evaporated MoO_{3-x} films from 4.75 eV to 4.47 eV respectively. Post-deposition vacuum annealing reduced the Φ value from 4.75 eV for as deposited MoO_{3-x} film to 4.54 eV for MoO_{3-x} film annealed at 150 °C. The main cause of the substantial decrease in work function value is: increase in oxygen vacancies and Mo^{5+} concentration in high temperature deposited and vacuum annealed MoO_{3-x} films.
- The oxygen plasma treatment of MoO_{3-x} films by PECVD technique can be a suitable approach to improve or recover the work function of molybdenum oxide films. The work function of MoO_{3-x} increased from 4.91 eV for as deposited films to 5.16 eV after OPT at 80 W. Work function is increased up to 5.22 eV by optimising the OPT conditions, such as rf power, oxygen flow rate, and treatment duration. For OP-treated MoO_{3-x} films at 80 W using 30 SCCM oxygen gas for 10 min, significant improvements in hole selectivity of MoO_{3-x} is observed.
- OPT is established as an effective approach to tune the work function of both thick (~500 nm) as well thin (23 nm and 14 nm) MoO_{3-x} films. An enhancement of ~0.40 eV in Φ values is observed for OP- treated thin MoO_{3-x} films. This approach is useful in restoring or enhancing MoO_{3-x}'s work function, thereby making it appropriate for use as a hole selective layer (HSL) in solar cells.
- The deposition parameters, such as process pressures (*PP*) and substrate temperatures,

have a significant impact on the optoelectronic characteristics of ITO films deposited by rf-sputtering. ITO films are observed to be polycrystalline and have the highest deposition rate of 3.50 Å/s, the lowest sheet resistance of 11 Ω/□ and highest figure of merit of 12.49×10^{-3} when deposited at low process pressure (3.8×10^{-3} mbar). Highly conducting ITO films with figure of merit of 31.18×10^{-3} have been formed when T_s is increased from 130 °C to 170 °C. Dopant free single sided *MoO_{3-x}/c-Si(n)* solar cells are fabricated using the optimised conditions for depositing MoO_{3-x}, the HSL and ITO, the transparent conducting oxide (TCO) layer.

- Use of Ag/Al as back electrodes increased the open circuit voltage (V_{oc}) of fabricated solar cells to 455 mV from 391 mV (for Ag as back electrode). The open circuit voltage (V_{oc}) of solar cells with ITO films deposited at 3.8×10^{-3} mbar increased from 391 mV (for 5.3×10^{-3} mbar) to 516 mV, fill factor (*FF*) increased from 0.48 to 0.49 and efficiency (η) of *MoO_{3-x}/c-Si(n)* solar cell (η) from 8.58% to 10.06%. The improvement in device performance is because of the higher deposition rate (3.5 Å/s) of ITO at 3.8×10^{-3} mbar as compared to 5.3×10^{-3} mbar pressure (3.0 Å/s) which decreased the exposure time of MoO_{3-x} to rf-plasma resulting in the formation of better ITO/MoO_{3-x} interface and increased shunt resistance (R_{sh}) from 775 Ω (for 5.3×10^{-3} mbar) to 2000 Ω.
- Devices fabricated with MoO_{3-x} film prepared at room temperature (RT) have shown better performance (11.88%) as compared to the solar cells with MoO_{3-x} deposited at 100 °C. The formation of SiO_x at *MoO_{3-x}/c-Si(n)* interface and higher work function of MoO_{3-x} films are the probable reasons for the improved device performance when MoO_{3-x} films are deposited at RT during solar cell fabrication. Layer by layer optimisations have improved the device performance from 4.44% to 11.88%.
- The studies carried out on MoO_{3-x} films exposed to two times heat treatment (THT)

corresponding to the deposition of ITO film at 150 °C/130 °C and Ag back electrode at 100 °C, while fabricating MoO_{3-x}/c-Si(n) solar cells, confirmed that multiple heat treatments degrade the structural and optical characteristics of molybdenum oxide films. This has a significant impact on the performance of *MoO_{3-x}/c-Si(n)* solar cells. Thus, fabrication of efficient MoO_{3-x} and silicon-based solar cells necessitates lower deposition temperature and fewer heat treatments of MoO_{3-x}.

- The simulation study confirmed that high work function of MoO_{3-x} is required to fabricate an efficient *MoO_{3-x}/c-Si(n)* solar cells. An increase in Φ from 4.7 eV to 5.2 eV has significantly increased V_{oc}, *FF* and η *of* MoO_{3-x}/c-Si(n) solar cells. Tunnelling through thin SiO_x layer has considerably improved the performance of solar cells.
- Increase in SiO_x thickness from 1 nm to 1.7 nm at Φ = 4.8 eV has increased V_{oc} from 562 mV to 597 mV respectively. However, a drop in *FF* is observed because of the increase in series resistance as SiO_x thickness increased. Simulation results obtained for Φ = 4.8 eV and tunnelling through 1.2 nm SiO_x at the interface of MoO_{3-x}/c-Si(n) are observed to be closer to the results obtained for experimentally fabricated MoO_{3-x} /c-Si(n) solar cells.
- Decrease in V_{oc} is observed as the pin holes increased at the MoO_{3-x} and c-Si(n) interface. However, improvement in *FF* is noticed when pin hole coverage (D_{ph}) is increased from 10^{-7} to 10^{-4} and further increase in D_{ph} has initiated decrease in FF and efficiency.
- By correlating the experimental results and simulation studies, it is inferred that an ultrathin SiO_x layer develops at the MoO_{3-x}/c-Si(n) interface during the fabrication of devices, which serves as a passivation layer and also help in the movement of carriers in addition to other transport mechanisms.

9.2 Scope for future work

The present thesis mainly focuses on the optimisation of properties of different layers to fabricate an efficient dopant free single sided MoO_{3-x}/c-Si(n) heterojunction solar cells. The present work can be extended in several ways, which are discussed below.

- The process of fabrication affects the MoO_{3-x} properties and thermal evaporation is the most commonly used method to deposit MoO_{3-x} films for solar cells. The conditions optimised to fabricate transparent and stoichiometric MoO_{3-x} films using rf- sputtering can be used to make a good *MoO_{3-x}/c-Si(n)* solar cells.
- As OPT has been developed as an effective way to improve the work function. It can be combined along with the optimised deposition conditions to deposit high work function HSL to further enhance the performance of dopant free solar cells
- A good passivation layer such as intrinsic amorphous silicon layer with optimised properties can be inserted between MoO_{3-x} and c-Si (n) to achieve higher V_{oc} and *FF*.
- Using the simulation tool, a dopant free ESL on rear side and thin intrinsic amorphous silicon layer can be integrated between MoO_{3-x} and c-Si (n) to achieve high-efficiency dopant free *MoO_{3-x}/c-Si(n)* solar cells.
- The optimum deposition conditions to fabricate HSL can also be used in organic solar cells and other optoelectronic devices to achieve better results.

List of publications

Part of thesis:

1. **Juhi Kumari**, Pilik Basumatary, Manvendra Singh Gangwar and Pratima Agarwal, "Molybdenum trioxide as an emitter layer in Silicon based heterojunction solar cells", *Material today proceedings, 39, Part 5, 1821-2056, 2021.*
2. **Juhi Kumari**, Rahul, and Pratima Agarwal, "Role of deposition parameters on optoelectronic properties of ITO films and its application in MoO_{3-x}/c-Si(n) heterojunction solar cells", *J Mater Sci: Mater Electron, 2023, 34:1286.*
3. **Juhi Kumari** and Pratima Agarwal, "Optimization of deposition conditions to tune optoelectronic properties of MoO_{3-x} films prepared by RF- sputtering Technique", *Vacuum 216 (2023) 112485.*
4. **Juhi Kumari,** Jai Shree Bhardwaj, Rahul and Pratima Agarwal, "Oxygen Plasma Treatment of thermally evaporated MoO_{3-x} films: An Approach to tune the work function", *ACS Appl. Electron. Mater. 5 (2023) 4103−4113.*
5. **Juhi Kumari**, Rahul, Rohan and Pratima Agarwal, "Impact of heat treatment on molybdenum oxide properties and performance of MoO_{3-x} silicon heterojunction solar cells", (*Submitted).*
6. **Juhi Kumari**, Anterdipan Singh, Rahul, Rohan and Pratima Agarwal, "Preparation of conducting as well resistive MoO_{3-x} films at low substrate temperature", (*Prepared*).
7. **Juhi Kumari**, Anterdipan Singh and Pratima Agarwal, "Simulations studies on dopant free single side MoO_{3-x} and silicon solar cells", (*Prepared*).
8. **Juhi Kumari** and Pratima Agarwal, "Carrier selective contacts in c-Si based heterojunction solar cell", (*Book Chapter, Under Preparation*).

Not a part of thesis:

9. Ramakrishna Madaka, **Juhi Kumari**, Venkanna Kanneboina and Pratima Agarwal, "Hydrogenated amorphous silicon solar cells fabricated at low substrate temperature 110ºC on flexible PET substrate", *AIP Conf. proc. 1953 (2018) 100040.*
10. Vivek Ghritlahre, **Juhi Kumari** and Pratima Agarwal, "Synthesis and study of molybdenum diselenide ($MoSe_2$) by Solvo-thermal method", *AIP Conf. proc. 1953 (2018) 050048.*

11. Asha Yadav, **Juhi Kumari** and Pratima Agarwal, "Role of Interface States on Electron Transport in a-Si:H/nc-Si:H Multilayer Structures", *AIP Conf. proc. 1953 (2018) 100045*.

12. **Juhi Kumari**, Vivek Ghritlahre, and Pratima Agarwal, "Fabrication of $MoSe_2$ and ZnO: Al based heterojunction structure", *AIP Conference Proceedings 2091 (2019) 020015*.

13. Ramakrishna Madaka, **Juhi Kumari**, Venkanna Kanneboina, Himanshu S. Jha, Pratima Agarwal, "Role of chamber pressure on crystallinity and composition of silicon films using silane and methane as precursors in hot-wire chemical vapour deposition technique", *Thin Solid Films 682 (2019) 126–130*.

14. Pilik Basumatary, **Juhi Kumari** and Pratima Agarwal, "Enhancing the performance and stability of $MAPbI_3$ perovskite solar cells by inserting the ITO layer before the Ag electrode", *AIP Conference Proceedings 2369 (2021) 020022*.

15. Pilik Basumatary, **Juhi Kumari** and Pratima Agarwal, "Probing the defects states in $MAPbI_3$ perovskite thin films through photoluminescence and photoluminescence excitation spectroscopy studies", *Optik 266 (2022) 169586*.

16. **Juhi Kumari,** Rahul and Pratima Agarwal, "Modelling of p-a-Si:H/i-a-Si:H/(n)c-Si silicon solar cells by AFORS-HET software", *Book Chapter, NERC 2022: Sustainable Energy Generation and Storage, Springer (2023) 127–133*.

List of papers presented in conferences (National/International)

1. Ramakrishna Madaka, **Juhi Kumari**, Venkanna Kanneboina and Pratima Agarwal, "Hydrogenated amorphous silicon solar cells fabricated at low substrate temperature 110 ºC on flexible PET substrate", *International Conferences on Condensed Matter and Applied Physics'2017 (ICC 2017), Govt. Engineering College, Bikaner, Rajasthan, 24th-25th November 2017.*
2. Asha Yadav, **Juhi Kumari** and Pratima Agarwal, "Role of Interface States on Electron Transport in a-Si:H/nc-Si:H Multilayer Structures", *International Conferences on Condensed Matter and Applied Physics'2017 (ICC 2017), Govt. Engineering College, Bikaner, Rajasthan, 24th-25th November 2017.*
3. **Juhi Kumari**, Vivek Ghritlahre, and Pratima Agarwal, "Fabrication of $MoSe_2$ and ZnO: Al based heterojunction structure", International Conference on Renewable and Alternated Energy'*2018 (ICRAE 2018), Assam Science and Technology University (ASTU), Guwahati, 4th-6th December 2018.*
4. **Juhi Kumari** and Pratima Agarwal "Effect of post annealing on structural, optical and electrical properties of thermally evaporated WO_3 films*", Research Conclave 2019, IIT Guwahati, Guwahati, 14th-17th March 2019.*
7. **Juhi Kumari**, Pilik Basumatary, Manvendra Singh Gangwar and Pratima Agarwal, "Molybdenum trioxide as an emitter layer in Silicon based heterojunction solar cells", 3rd *International Conference on Solar Energy Photvoltaic'2019 (ICSEP 2019), KIIT Bhubaneswar, 19th-22nd December 2019.*
8. 5th International Conference on Emerging Electronics (*IEEE-ICEE 2020),* Indian Institute of Technology Delhi, Delhi, *26th – 28th November 2020.*
9. **Juhi Kumari**, and Pratima Agarwal, "Role of MoO_x work function on performance of MoO_x/n-Si heterojunction solar cells", *21st International Workshop on Physics of Semiconductor Devices (IWPSD 2021), Indian Institute of Technology Delhi, Delhi, 14th -17th December 2021.*
10. **Juhi Kumari**, Rahul, Pratima Agarwal, "Fabrication and simulation studies of MoO_x/n-Si heterojunction solar cells"; *Recent Advances and Innovations in Solar Energy (RAiSE 2021), Indian Institute of Technology Madras, Madras, 2nd-4th December 2021.*

11. **Juhi Kumari**, and Pratima Agarwal, "Effect of substrate temperature on thermally evaporated tungsten tri-oxide films*"*, *North East Research Conclave (NERC 2022), Indian Institute of Technology Guwahati, Guwahati, 20th -22nd May 2022.*
12. **Juhi Kumari**, Rahul and Pratima Agarwal, "Modelling of a-Si:H(p)/a-Si:H(i)/c-Si(n) heterojunction solar cells using AFORS-HET software", *North East Research Conclave (NERC 2022), Indian Institute of Technology Guwahati, Guwahati, 20th -22nd May 2022.*
13. **Juhi Kumari**, Rahul, and Pratima Agarwal, "Fabrication of an efficient single side MoO_{3-x}/n-Si(c) heterojunction solar cells", *International Symposium on Semiconductor Materials and Devices (ISSMD-2022), KIIT (DU), Bhubaneswar, 16th-18th December 2022.*

List of Webinars/workshop attended

1. *National Workshop on NEMS/MEMS & Theranostic Devices 2018*, IIT Guwahati, Guwahati, 26th -28th February 2018.
2. *INUP Familiarization Workshop on "Nanofabrication Technologies",* National Institute of Technology Silchar, Assam, 28th -29th January 2019.
3. Webinar on *"Futuristic Thin films & Semiconductor Devices & Fabrication Process",* 9th-10th September'21.